The synthesis, structural characterisation, and photophysical properties of platinum(IV) complexes with tri- or tetra-dentate ligands

DIKOVA, YANA,MIHAYLOVA

The synthesis, structural characterisation, and photophysical properties of platinum(IV) complexes with tri- or tetra-dentate ligands

Yana Dikova

A thesis submitted for the degree of Doctor of Philosophy

Department of Chemistry

Durham University

September 2024

Abstract

The work in this thesis aims to develop Pt^{IV} complexes incorporating tridentate and tetradentate ligands and to explore their photophysical properties.

The synthesis of Pt^{IV} complexes featuring *NCN*- and *NNC*-coordinating tridentate ligands is detailed in Chapters 2 and 3. Complexes of the type $3+2+1$ were prepared, which incorporate one cyclometallating tridentate ligand, one bidentate ligand (*NC* – cyclometallating or *NN* – coordinating), and a monodentate chloride, as well as the first examples of bis-tridentate Pt^{IV} complexes. The bis-cyclometallated complexes featuring an *NNC* ligand are luminescent in degassed acetonitrile at room temperature with quantum yields ranging from 0.4% to 4%.

Chapter 4 explores further examples of $[Pt(NNC)(NC)Cl]^+$ complexes that incorporate a phenyl substituent at the 6-position of the *NNC* lateral pyridine ring. While their photophysical properties in solution were similar to those of their unsubstituted counterparts, significant enhancements in quantum yield were observed when embedded in PMMA films, likely due to a $\pi - \pi$ interaction between the phenyl substituent on the *NNC* ligand and the pyridine ring of the *NC* ligand.

In Chapter 5 the development of dinuclear complexes featuring rigid, ditopic bis-tridentate pyrimidine-bridged *CNN-NNC* ligands is described. The reactions of these ligands with K_2PtCl_4 yielded mononuclear Pt^{II} complexes. However, further oxidation to Pt^{IV}, followed by reaction with additional K_2PtCl_4, facilitated the formation of dinuclear Pt^{II}/Pt^{IV} complexes. These were further oxidised to yield dinuclear Pt^{IV} complexes. A trace amount of a dinuclear complex of the type $[CNN\text{-}NNC\{Pt(ppy)Cl\}_2]$ was successfully isolated, and found to be luminescent with a quantum yield of 1.6% and a lifetime of 13 µs.

Chapter 6 focuses on the synthesis of tetradentate *NCCN* ligands, incorporating pyridine or quinoline heterocycles and substituted phenyl cyclometallating rings, and their complexation with platinum. Mixtures of Pt^{II} and Pt^{IV} complexes were formed, and in one instance a dimeric Pt^{III} complex. The Pt^{IV} complexes were only emissive at 77 K, but the Pt^{II} complexes were luminescent also at room temperature, with quantum yields reaching up to 67% in CH_2Cl_2 solution.

Declaration

The research described herein was undertaken at the Department of Chemistry at Durham University between October 2020 and March 2024. All of the work is my own, except where specifically stated otherwise. No part of it has previously been submitted for a degree at this or any other university.

Statement of copyright

Acknowledgements

I have thoroughly enjoyed my time at Durham and would like to convey my heartfelt thanks to the people who have been a part of it.

First and foremost, I would like to express my deepest gratitude to my supervisor, Professor Gareth Williams. It has been a privilege to work under your guidance. Your encouragement, patience, and unwavering support have been invaluable throughout these few years.

Being part of the JAGW group has been a true delight and I genuinely believe I have made some incredible friends (forever besties). Amit, Rebecca, and Chris, thank you for being the most welcoming and supportive group I could have joined. Amit, I am grateful for everything you've taught me and for always knowing how to make me laugh. Rebecca, I loved our conversations and never hesitated to get a ride back to college with you, even though walking probably would have been faster. Thank you for being our 'Mother Becky'. Chris, thank you for being so knowledgeable and helpful in the lab, for fitting in so well with the girlies when Amit left, and for always being there to listen to everyone's rants. Special thanks to Lucy and Laura – living and working with you could have been a complete disaster, but you turned out to be some great people to be spending 24/7 with. Lucy, I will miss being silly sausages in the office with you, our evening trips to McDonald's, and watching horror shows together after the lab. Laura, thank you for trusting my opinion in the lab and for putting up with our friendly teasing. Emma, thank you for teaching us so many new things and for your patience in dealing with our quirks. Thanks also to Abbi, David and all of our master's students.

Thanks to my other friends in Durham. Exe, Jaime, Victor and Felipe, thank you for always being there to help and for your friendships. Elizabeth and Sinthujah, thank you for joining us for tea, especially when CG001 got emptier. Thanks to Zoe for being the extroverted friend who dragged me out and with whom I instantly clicked.

Thanks to all of the staff at the department, in particular, Dr Dmitry Yufit and Dr Toby Blundell for solving all of the crystal structures and Dr Juan Aguilar for collecting the NMR of some very dilute samples.

I would also like to thank Dr Piotr Pander for his invaluable assistance with DFT and electrochemistry. A special thanks to Dr Marc Etherington for helping with the preparation of thin films and for his encouragement about that project.

Thanks to my friends back home for being a welcome distraction during the holidays. Special thanks to my best friends Sofi, Eti and Kari for always being there for me, despite the distance. Suny, thank you for all of your help, love, and support. To my mum, Mila and Kamen, thank you for your constant support and for always distracting me with the family drama. Grandma and grandad (dyadka), thank you for always believing in me.

CHAPTER 1

INTRODUCTION

Chapter 1: Introduction

1.1 Introduction to luminescence

To emit light, a molecule must first absorb energy to be electronically excited to a higher energy excited state.[1] Its return to the ground state by the emission of a photon is termed luminescence or radiative decay. This process competes with non-radiative decay processes, e.g., thermal dissipation of the absorbed energy. The key photophysical processes are typically represented by an energy level diagram, usually referred to as a Jablonski diagram (Figure 1.1).

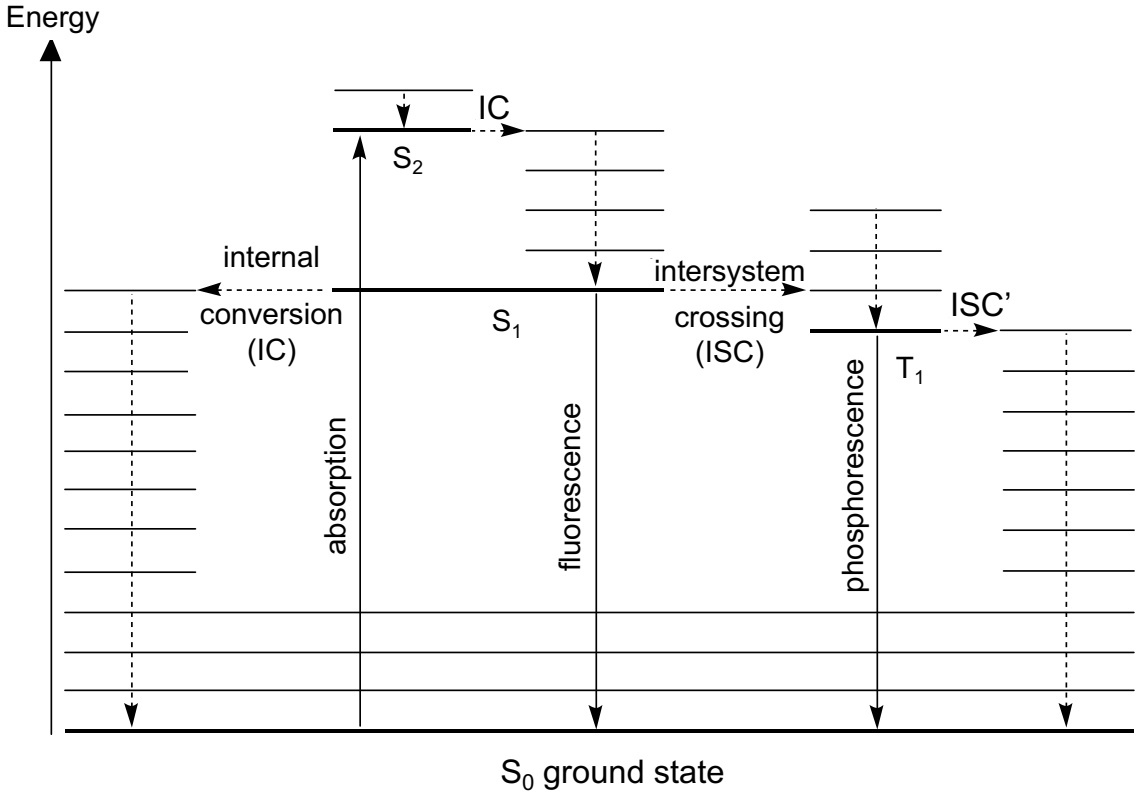

Figure 1.1: *Typical Jablonski diagram showing possible transitions between different states.*

Fluorescence is the spin-allowed radiative relaxation to the ground state ($\Delta S = 0$) and is typical for most organic light-emitting molecules. The simplest example is excitation to S_1, followed by return to S_0 through the emission of light. Often, the molecule is excited to a higher vibrational level of S_1, but quickly relaxes to the lowest vibrational level through internal conversion, prior to significant emission occurring.

Phosphorescence is the spin-forbidden process of radiative relaxation, e.g. $T_1 \rightarrow S_0$. For organic emitters, this process is often very slow and struggles to compete with non-radiative decay processes at room temperature. Second- and especially third-row transition metals have high spin-orbit coupling constants, ξ (ξ increases as Z^4). Introducing such a metal ion that interacts with an organic ligand accelerates inter-system crossing and emission from the triplet state due to relaxation of the spin selection rule through spin-orbit coupling (SOC).

The lifetime of a given excited state is given by:

$$\tau(S_1) = \frac{1}{k_{IC} + k_{fl} + k_{ISC}} \tag{1}$$

$$\tau(T_1) = \frac{1}{k'_{ISC} + k_{ph}} \tag{2}$$

where k_{IC} is the rate of non-radiative internal conversion from S_1 to S_0, k_{fl} the rate of fluorescence, k_{ISC} the rate of intersystem crossing to T_1, k'_{ISC} the rate of non-radiative decay from T_1 and k_{ph} the rate of phosphorescence.

Fluorescence lifetimes are usually short (in the nanosecond range), due to the faster processes involved (e.g., k_{fl} for conjugated organic molecules is $\approx 10^7$–10^8 s^{-1}, corresponding to radiative lifetimes of around 10 ns). On the other hand, phosphorescence lifetimes may be up to minutes or hours, but are reduced to the µs range for heavy metal ion-containing compounds.

The quantum yield is a measure of the efficiency of emission and is defined as the ratio of the number of photons emitted to the number absorbed. The fluorescence and phosphorescence quantum yields are related to the rate constants defined above through the following equations:

$$\Phi_{fl} = \frac{k_{fl}}{k_{IC} + k_{fl} + k_{ISC}} \tag{3}$$

$$\Phi_{ph} = \frac{k_{ph} \cdot k_{ISC}}{(k'_{ISC} + k_{ph}) \cdot (k_{IC} + k_{fl} + k_{ISC})} \tag{4}$$

Possible values of Φ are 0 to 1, but sometimes reported as a %, 0 to 100%. Higher values of Φ indicate more efficient emission.

For transition metal complexes, the molecular orbitals (MOs) can be described as metal-centered or ligand-centered, depending on whether they are mostly localised on the metal or the ligand, respectively. There are four main types of possible transitions – metal-centred (MC) involving only d-orbitals on the metal, ligand-centred (LC), metal-to-ligand charge transfer (MLCT) and ligand-to-metal charge transfer (LMCT). The excited states that arise from each transition are named correspondingly, e.g., MC state. The relative energies of the transitions and therefore the character of the lowest-energy transition depend on the identity and the oxidation state of the metal, as well as on the identity of the ligands. Density functional theory (DFT) is often used to estimate the energy of the lowest energy transitions and to evaluate the relative metal and ligand contributions to the orbitals involved in these transitions.

1.2 Introduction to Pt^{IV} complexes

A vast amount of research has been focused on the development of transition metal complexes with chelating heteroaromatic ligands due to their potential use in various applications such as OLED devices,[2,3] bioimaging probes,[4,5] chemosensors,[6] energy conversion devices,[7] photodynamic therapy photosensitisers[8] and singlet-oxygen generation.[9,10] While there have been innumerable studies on Pt^{II} complexes, research into Pt^{IV} complexes of this type and their photophysical properties is still rather limited. One reason for this might be that back-bonding is not typically favourable for metals in high oxidation states. The high charge also means that the 5d orbitals will be low in energy and may not mix very well with the ligand orbitals to facilitate phosphorescence. Moreover, Pt^{IV} is kinetically a very inert ion, due to its low-spin d^6 configuration and large ligand-field splitting, which could pose more of a challenge to the synthesis of its complexes than those of Pt^{II}.

Pt^{IV} is isoelectronic with Ir^{III}, whose complexes have been extensively explored due to their attractive and versatile photophysical properties.[11] In terms of emission, one of the main differences to have emerged between complexes of these two ions is that there is less metal character in the excited state of Pt^{IV} complexes and therefore weaker SOC, resulting in longer lifetimes. Although this may not be desirable for OLED devices, longer lifetimes offer potential for applications such as time-resolved bioimaging, oxygen sensing and generation of singlet oxygen and reactive oxygen species (ROS).

1.3 Organometallic Pt^{IV} complexes

Cyclometallation

Cyclometallation is the binding of a polydentate ligand to a metal through a covalent carbon-metal bond. Cyclometallated complexes are formally organometallic compounds. The anionic carbon is a strong σ-donor. The strong σ-donation combined with the π-acceptance of the heterocyclic rings of aromatic cyclometallating ligands leads to particularly strong ligand fields. This results in a decrease in the energy of the emitting ^{3}MLCT state and an increase in the energy of the ^{3}MC state of cyclometallated complexes, whose population serves as one of the main deactivation pathways for the complexes of many ions. While the decrease in the energy of the ^{3}MLCT state leads to a red-shift in the emission and should result in a decrease in the luminescence quantum yield according to the 'energy gap law', the opposite has been shown by a number of cyclometallated complexes of different metal ions, at least for blue and green emitters.[12] The change from a nitrogen atom to an anionic carbon also results in a reduction of the overall charge of the complex.

1.3.1 Methods of oxidation

Von Zelewsky and co-workers first started to investigate the oxidative addition reactions of Pt^{II} complexes to form organometallic Pt^{IV} complexes in 1983.[13] Their pioneering work involved the oxidative addition of Br_2 to *cis*–$Pt(ppy)_2$ (ppy = 2-phenylpyridine), by the dropwise addition of a dichloromethane solution of bromine to a dichloromethane solution of the complex. Subsequently, Balzani and von Zelewsky found that $Pt(ppy)_2$ and $Pt(thpy)_2$ (thpy = 2-(2-thienyl)pyridine) underwent oxidative addition reactions by irradiation with light (medium-pressure Hg lamp, $\lambda > 400$ nm) in deaerated chloroform or CH_2Cl_2.[14] The products of these reactions were the first examples of luminescent Pt^{IV} compounds, showing emission in the blue or green part of the visible spectrum, distinct from that of their Pt^{II} precursors. Later work by von Zelewsky explored the thermal and the photochemical oxidative addition of a series of alkyl halides to $Pt(thpy)_2$.[15] An interesting feature of the photoactivated reactions was that out of 11 possible isomers, the enantiomeric pair of *C*,*C*,*C-fac* was the only one observed (Scheme 1.1). Evidence suggested a radical mechanism for the photochemical oxidative addition and an S_N2-type mechanism for the thermal oxidative addition reactions.

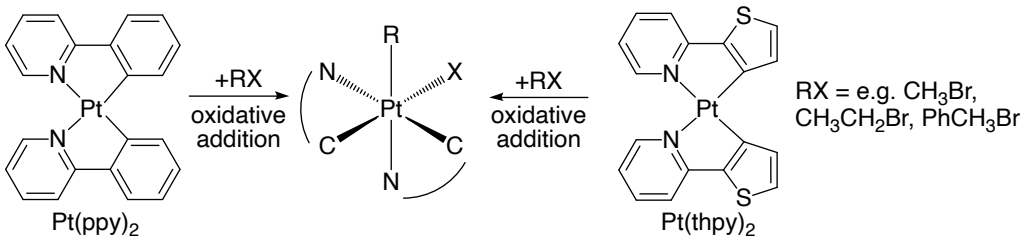

Scheme 1.1: *Structures of Pt(ppy)$_2$ and Pt(thpy)$_2$, and the major Pt^{IV} product (C,C,C-fac isomer) of the oxidative addition reaction with alkyl halides.*

Two types of precursors can be used for the formation of complexes of the type Pt(*NC*)$_2$Cl$_2$ – the aforementioned Pt(*NC*)$_2$, as well as complexes of the type *trans*-*N*,*N*-Pt(*NC*)(*NC*H)Cl with one cyclometallated and one pendant ppy ligand. Pt(*NC*)$_2$Cl$_2$ complexes can form 8 different geometric isomers (Figure 1.2)

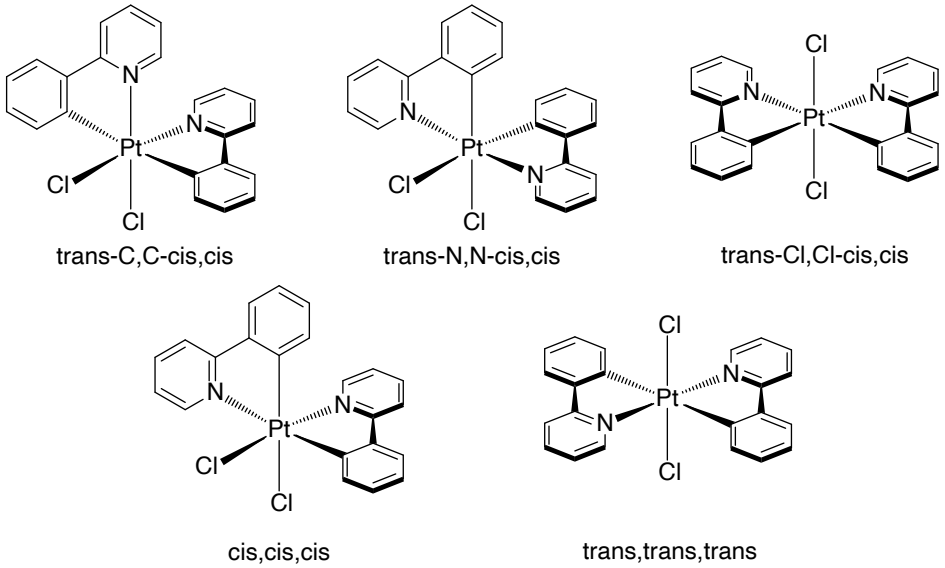

Figure 1.2: *Structures of possible isomers of the complex Pt(ppy)$_2$Cl$_2$.*

Rourke and co-workers first found that they could use *trans*-*N*,*N*-Pt(ppy)(ppyH)Cl, rather than Pt(ppy)$_2$, and oxidise it with hydrogen peroxide to afford Pt(ppy)$_2$Cl$_2$.[16] To study how the oxidation proceeds, the F-substituted ppy derivative 4-fluorophenylpyridine was used and the reaction was monitored by ^{19}F NMR. A mixture of isomers formed initially, but after about a week a single compound was isolated. Single-crystal X-ray diffraction revealed that the final product had a *trans*-*N*,*N*-*cis*,*cis* configuration (Scheme 1.2).

The use of the electrophilic chlorinating reagent PhICl$_2$ was later introduced by Sanford and Whitfield and then took off as one of the main methods to obtain Pt^{IV} complexes.[17] Oxidising Pt(ppy)$_2$ with PhICl$_2$ led to the formation of *cis*,*cis*,*cis*–Pt(ppy)$_2$Cl$_2$

as the main product (Scheme 1.2). However, when Rourke and co-workers used $PhICl_2$ to oxidise the pendant complex Pt(4-F-ppy)(4-F-ppyH)Cl, the exclusive formation of *trans-N,N-cis,cis*-Pt(4-F-ppy)$_2$Cl$_2$ was observed again.[18] This shows that different isomers can be obtained as the main product, depending on the starting material used. An interesting feature of the ^{1}H NMR spectrum is an upfield shift of H* (Scheme 1.2), which experiences a shielding effect from the ring current of the aromatic ring, which is in the plane perpendicular to that containing H*. An effect of this type was first observed and described for a Ru complex.[19]

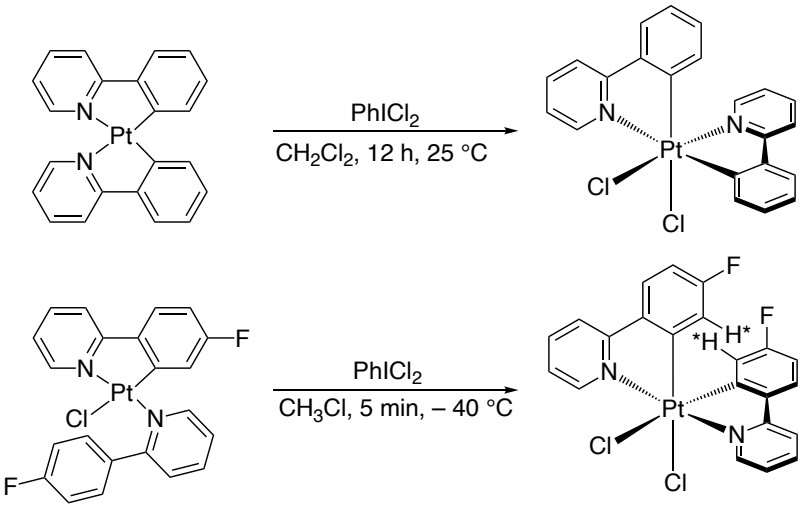

Scheme 1.2: *Oxidative addition of $PhICl_2$ to bis-cyclometallated Pt(ppy)$_2$ and pendant Pt(4-F-ppy)(4-F-ppyH)Cl.*

Parker *et al.*[20] reported the direct synthesis of [Pt(Meppy)$_2$Cl$_2$] (MeppyH = 2-tolylpyridine) by heating K_2PtCl_4 with MeppyH in 2-ethoxyethanol under N_2 in the presence of DMSO. It was suggested that DMSO might be acting as the oxidant in this reaction. A yield of 34% was obtained and the resulting complex was identified as the *trans-N,N-cis,cis* isomer.

A different method was explored by van Koten and co-workers, in which the chemical oxidation of an *NCN* Pt^{II} complex was achieved by a reaction with Cu^{II}X$_2$ in CH_2Cl_2/MeOH,[21–23] giving Pt^{IV}(*NCN*)X$_3$ (X = Cl or Br, Scheme 1.3).

The properties of the Pt^{IV} complex Pt^{IV}(*NCN*)Cl$_3$ were compared to those of its Pt^{II} precursor. The molecular structures revealed an increase in the Pt–Cl, Pt–C and Pt–N bond lengths upon oxidation. A downfield shift of protons 1 was observed in the ^{1}H NMR spectrum of the Pt^{IV} complex, when compared to its Pt^{II} analogue. A decrease was also seen in the ^{3}J coupling constants between ^{195}Pt and protons 1 and 2 for

the oxidised complex, relative to Pt(*NCN*)Cl. In contrast to its Pt^{II} precursor, which is weakly emissive, the Pt^{IV} complex did not show room-temperature emission.

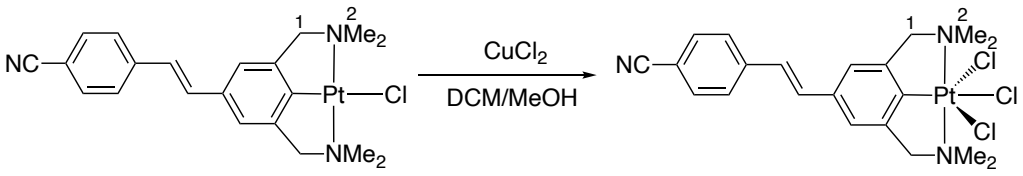

Scheme 1.3: *Oxidation of pincer Pt^{II} NCN complexes with Cu^{II} salts. Relevant protons on both structures are numbered.*

1.3.2 Excited state properties of Pt^{IV} complexes containing two bidentate ligands

Influence of isomerism and ancillary ligands on the emission properties

González-Herrero and co-workers began looking at organometallic Pt^{IV} complexes in 2014[24] and have since then been leading much of the work on complexes of the type [Pt(*NC*)$_2$RX], [Pt(*NC*)$_2$X$_2$] and [Pt(*NC*)$_3$]$^+$.

They explored the influence of isomerism and of the ancillary ligand on the luminescence properties of Pt(ppy)$_2$X$_2$ and Pt(ppy)$_2$MeX.[25] The three different types of compounds that they looked at are shown in Figure 1.3. 'Sym' and 'unsym' were used to denote the relative arrangement of the ppy ligands. The synthesis of sym- and unsym-Pt(ppy)$_2$Cl$_2$ was the same as that shown in Scheme 1.2. Unsym-Pt(ppy)$_2$MeCl was synthesised from [Pt$_2$Me$_4$(μ-SMe$_2$)$_2$] and 4 equiv. of ppyH, affording the pendant complex [Pt(*NC*)(*NC*H)Me].[26] This was followed by oxidation with PhICl$_2$ in the presence of base (*N,N*-diisopropylethylamine, DIPEA). The base is used to trap the HCl produced, preventing the subsequent substitution of the Me ligand by chloride. They looked at different ancillary ligands X$^-$ = F$^-$, Cl$^-$, Br$^-$, I$^-$, AcO$^-$ and TFA$^-$ (trifluoroacetate). Most of these complexes were obtained by using silver trifluoromethanesulfonate (AgOTf), which replaces the Cl ligands with the labile OTf, that are then exchanged by treatment with an appropriate salt (e.g., NaBr).

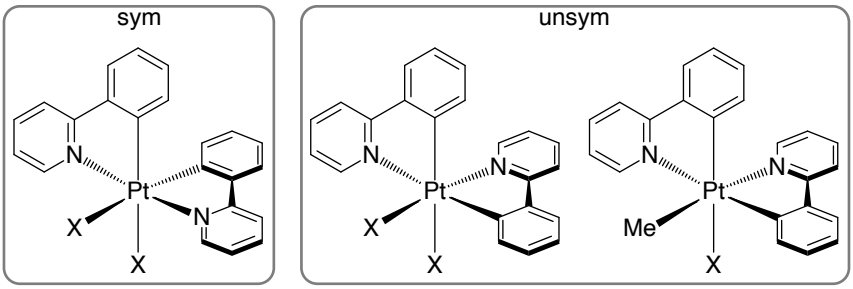

Figure 1.3: *Structures of sym- and unsym-Pt(ppy)$_2$X$_2$, and unsym-Pt(ppy)$_2$MeX. X$^-$ = F$^-$, Cl$^-$, Br$^-$, I$^-$, AcO$^-$, TFA$^-$.*

While all of the sym-X complexes (except sym-I) showed room temperature emission, none of the unsym-X were emissive under these conditions. Irradiation of unsym-Cl with a UVB light in CH_2Cl_2 for 15 h was found to result in the photoisomerisation to sym-Cl. It was suggested that a low-lying LMCT state could be responsible for both the lack of room temperature emission and the photoisomerisation reaction. This hypothesis was supported by a DFT study, which showed that the LUMO of the unsym-X complexes had a much higher percentage of metal orbital contribution, implying the accessibility of a low-energy deactivating ^{3}LMCT state. In contrast, all of the unsym-MeX complexes showed room-temperature emission, with quantum yields of up to 0.63 for unsym-MeBr. This is a result of the strong σ-donating methyl ligand, which ensures that the deactivating states lie at higher energies.

The variation of ancillary ligands showed no significant effect on the emission energies of any of the complexes. However, the emission efficiencies were found to be heavily influenced by it. A decrease in the quantum yield was seen for unsym-X with increasing π-donation in the order F^-, Cl^-, Br^-. Deactivating LLCT or LMCT states could be arising from the higher-lying p(X) orbitals. Interestingly, apart from a lower k_{nr} value, a notably higher k_r value was found for sym-F, suggesting a higher MLCT contribution. This was also supported by the broader and slightly red-shifted emission at 77 K compared to that of the other derivatives. The higher MLCT contribution may be a result of the shorter Pt–C bond and a better energy match and therefore better overlap of the p(F) and d(Pt) orbitals.

Influence of the nature of the bidentate ligands on the emission

The same group also looked at complexes of the type [Pt(*NC*)$_2$MeCl] with different *NC* ligands, some of which are shown in Figure 1.4.[26] All of the complexes in this

series were emissive. The emission was shifted to lower energy along the series dfppy > Meppy > MeOppy > Bppy > flpy > thpy > piq > npy, ranging from 435 to 585 nm. The quantum yield decreased in the same order, consistent with the 'energy gap law', with the exception of [Pt(Bppy)MeCl], which showed the highest quantum yield of 0.81. This behaviour was possibly a result of the bulkiness of the group, making the complex more rigid and therefore reducing k_{nr}.

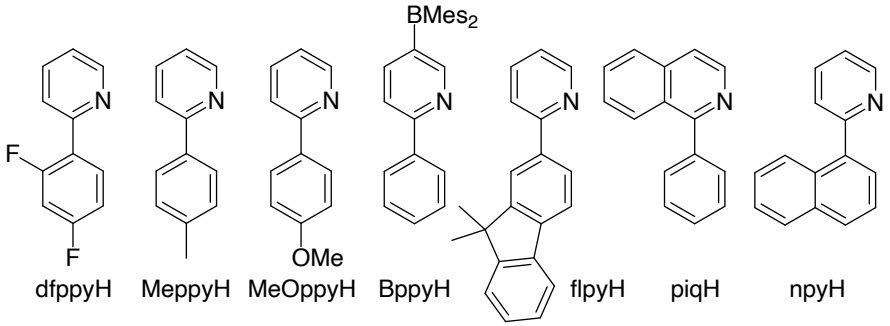

Figure 1.4: *Structures of NCH proligands.*

Heteroleptic complexes of the type unsym-[Pt(*NC*)(*N′C′*)Cl_2] with some of the same ligands (Figure 1.4) were also explored.[27] The two *NC* positions are not equivalent – the pyridine of the *NC* ligand is opposite a Cl, whereas that of the *N′C′* is opposite the phenyl of the *NC* (Figure 1.5). The emission of these complexes arises from the ligand with the lowest $\pi - \pi^*$ transition – thpy < Meppy < dfppy. On comparison of the emission of [Pt(Meppy)(thpy)Cl_2] and [Pt(thpy)(Meppy)Cl_2] it was found that when the chromophoric ligand thpy is in the *NC* position, the emission energy is lower and the emission lifetime is shorter, indicating a higher MLCT contribution to the emitting state. A possible explanation for this could be the shorter Pt–C bond *trans* to N′ and therefore a stronger π–donation and better dπ orbital interaction.

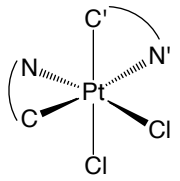

Figure 1.5: *A scheme of unsym-[Pt(NC)(N′C′)Cl_2], showing the two different NC and N′C′ ligand position.*

Abstraction of the chloride ligands from these complexes followed by the addition of a third *NC* ligand was probed as a route to tris-bidentate Pt^{IV} complexes. [Pt(dfppy)(Meppy)Cl_2] was reacted with two equiv. of AgOTf and MeppyH in 1,2-dichlorobenzene at 120°C. Interestingly, an isomerisation reaction to a *trans-N,N* complex was observed, leading to the final formation of two isomers with a meridional

conformation (Scheme 1.4a). An even more intriguing result was achieved upon reacting [Pt(dppyH)(ppy)Cl_2] (where dppyH_2 is 2,6-diphenylpyridine) with MeppyH in 1,2-dichloroethane at 90°C. A reductive C–C coupling was observed leading to the Pt^{II} complex shown in Scheme 1.4b.

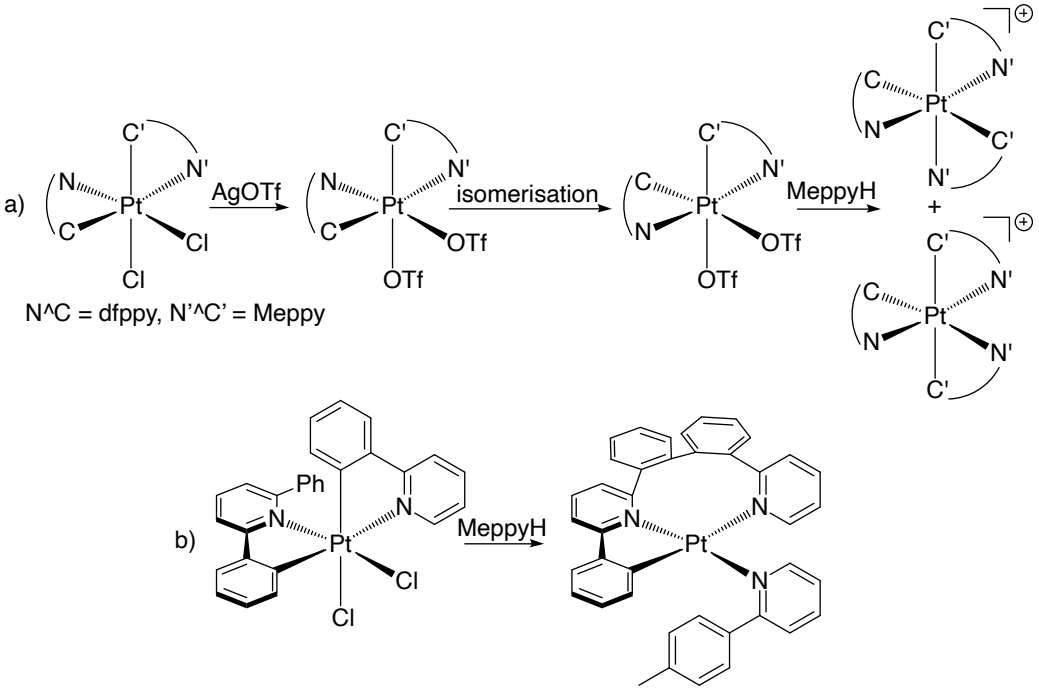

Scheme 1.4: *Reactions of a) [Pt(dfppy)(Meppy)Cl_2] and b) [Pt(dppyH)(ppy)Cl_2] with MeppyH.*

Very recently, the use of a strongly σ-donating aryl-1,2,3-triazolylidene ligand was explored.[28] Mesoionic aryl-NHC ligands are known for their strong σ-donating properties, leading to large ligand field splitting and raising the energy of deactivating MC excited states in Pt^{II} and Ir^{III} complexes.[29,30] A scheme for the synthesis of [Pt(*NC*)(*CC**)Cl_2] is shown in Scheme 1.5 (C* denotes the carbene C). A trans-metallation reaction of [Pt_2(μ-Cl)$_2$(*NC*)$_2$] with the *in situ*-generated AgI(trzH) (trzH = 4-butyl-3-methyl-1-phenyl-1H-1,2,3-triazol-5-ylidene) results in the formation of *trans*-*C*,*C**-[Pt(*NC*)(trzH)]. This is followed by the isomerisation to *trans*-*N*,*C**-[Pt(*NC*)(trzH)] by irradiation with blue LEDs and the subsequent oxidation with $PhICl_2$. Heating the mixture of products in the presence of base ensures the conversion of any non-cyclometallated trzH product [Pt(*NC*)(trzH)Cl_3] to the desired product [Pt(*NC*)(trz)Cl_2].

The complexes with *NC* ligands dfppyH, ppyH, MeppyH and thpyH showed room-temperature emission quantum yields of 0.27, 0.31, 0.26 and 0.046, respectively. In all cases, the transitions were centred on the *NC* ligands, which therefore determine the emission energies. However, the emission efficiencies are shown to be heavily influenced by the presence of the triazolylidene ligand, when compared to the homoleptic [Pt(*NC*)$_2$Cl$_2$]. The biggest difference is seen in the large decrease in the k_{nr} value (32.8×10^3 s^{-1} for [Pt(ppy)$_2$Cl$_2$] decreasing to 6.2×10^3 s^{-1} for [Pt(ppy)(trz)Cl$_2$]), indicating that the strong σ-donation of the carbene of the trz ligand leads to an increase in the energy of the dσ* orbitals and therefore an increase in the energy of the deactivating ^{3}LMCT state.

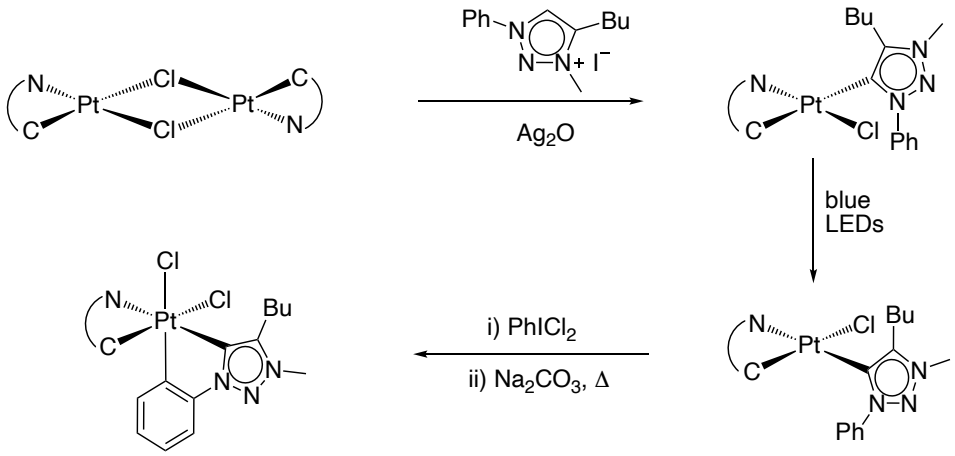

Scheme 1.5: *Synthesis of [Pt(NC)(trz)Cl$_2$].*

1.3.3 Synthesis and excited-state properties of tris-bidentate Pt^{IV} complexes

Bis-cyclometallated complexes

Bernhard and Jenkins[31] showed the first example of a tris-bidentate Pt^{IV} complex by reacting Pt(ppy)$_2$Cl$_2$ with bipyrdine in the presence of Ag$^+$ or Tl$^+$ in acetonitrile/water. By introducing substituents into the 2-phenylpyridine and/or the 2,2'-bipyridine ligands, they investigated the influence of structural modifications on the excited state properties of these complexes (Figure 1.6).

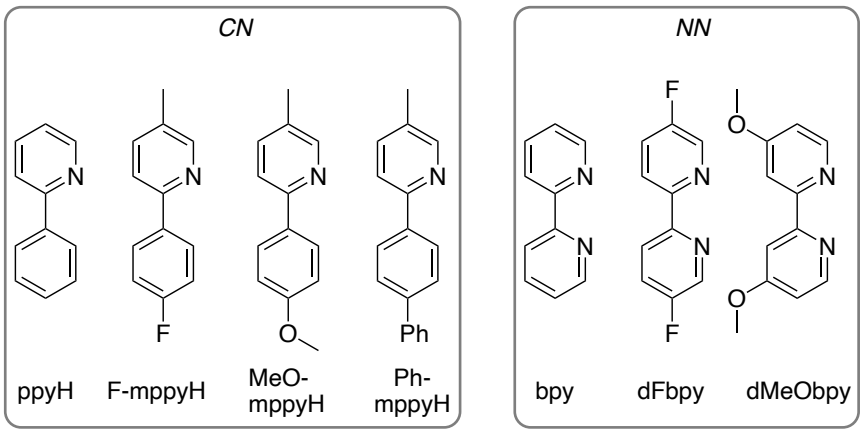

Figure 1.6: *Structures of NCH proligands and NN ligands used by Bernhard and Jenkins.*[31]

While all the complexes containing the ppy, F-mppy and Ph-mppy ligands showed structured room-temperature luminescence in the blue region, none of the complexes containing the MeO-mppy ligands were emissive under these conditions. For those that were emissive, the luminescence lifetimes were between 1.08 and 260 µs and quantum yields between 0.0005 and 0.035. Variation of the *NN* ligand showed almost no effect on the emission maxima, suggesting it had no strong contribution to the emissive state. Varying the *NC* ligand, a red shift was seen in the order ppy, F-ppy, Ph-mppy. Lifetimes and quantum yields increased in the order: dFbpy < bpy < dMeObpy and F-mppy < ppy < Ph-mppy. Contrary to the expectations based on the 'energy gap law', the complexes containing Ph-mppy showed the highest quantum yields. DFT calculations revealed that the lowest-energy excited state for the complexes containing ppy and F-mppy ligands was a ^{3}LC state involving the *NC* ligands. However, for the complexes with a Ph-mppy ligand it was found that the LUMO is localised on the two phenyl groups (cyclometallated and non-cyclometallated) and the HOMO is localised on the pyridine and the cyclometallated phenyl. The transition is described as an intraligand charge transfer ^{3}ILCT. This difference was suggested as a likely explanation for the different excited-state properties shown by these complexes.

Very recently, Lalinde, Moreno and co-workers[32] expanded the series of $[Pt(NC)_2(NN)]^{2+}$ complexes by looking at 2-phenylbenzothiazole (pbtH) as an *NC* ligand and phenanthroline-based *NN* ligand (Figure 1.7). The complexes showed phosphorescence centred on the *NC* ligand with quantum yields between 0.01 and 0.02 in degassed CH_2Cl_2 solution.

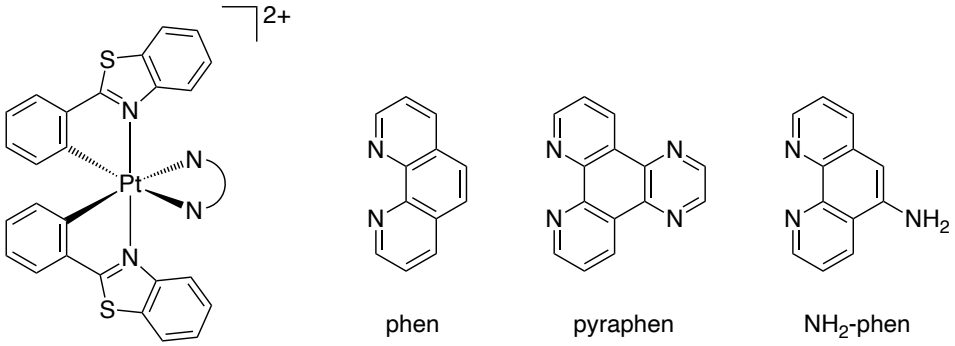

Figure 1.7: *Structures of $[Pt(NC)_2(NN)]^{2+}$ complexes reported by Lalinde, Moreno and co-workers.*[32]

Tris-cyclometallated complexes

Influence of isomerism on the emission properties

González-Herrero and co-workers looked at tris-cyclometallated complexes of the type [Pt(*NC*)$_3$]OTf with the *NC* ligands ppy, Meppy, dfppy and flpy (Figure 1.4, page 9).[24,33] As previously mentioned, the reaction of *cis*-*N*,*N*-[Pt(*NC*)$_2$Cl$_2$] with AgOTf and excess of proligand favours the formation of the *mer*-isomer through an isomerisation step (Figure 1.4). The *mer*-isomer is also formed upon reacting *trans*-*N*,*N*-[Pt(*NC*)$_2$Cl$_2$] under the same conditions. Irradiation of the *mer*-isomer with UV light in MeCN results in the photoisomerisation to the *fac*-isomer (Scheme 1.6). While the *fac*-isomers display room-temperature emission with quantum yields of up to 0.49, the *mer*-isomers of the complexes showed very weak emission, due to competitive photoisomerisation to the more emissive *fac*-isomer. Both isomers showed strong emission at 77 K, indicating that a low-lying non-emissive state (likely LMCT) becomes thermally accessible at room temperature in the *mer* case, leading to non-radiative deactivation. Population of the same state could also be responsible for the photoisomerisation reaction, as for unsym-Pt(*NC*)$_2$X$_2$ (page 7).

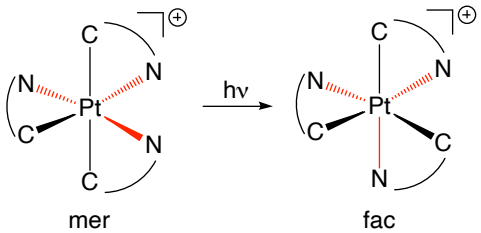

Scheme 1.6: *Photoisomerisation reaction of mer-$[Pt(NC)_3]^+$ to fac-$[Pt(NC)_3]^+$.*

The *mer*-isomer of [Pt(flpy)$_3$]OTf was the only one of the prepared *mer*-complexes that showed measurable emission at room temperature (Φ = 0.08). An explanation for this could be that the ^{3}LC state has a lower energy (due to the lower ligand π–π^* transition energy), compared to that of the other complexes, and therefore there is a larger gap between the emitting and the deactivating ^{3}LMCT state. Inefficient population of the deactivating state meant that little photoisomerisation was observed during the measurement, allowing reliable emission data to be obtained for this complex. Nonetheless, isomerisation to the *fac*-isomer through UV light irradiation was still possible. The *fac*-isomer showed slightly blue-shifted emission (from 520 to 516 nm), compared to the mer with a more than doubled phosphorescence quantum yield of 0.17.

Influence of the nature of the ligands on the emission properties

To probe the influence of the ligand on the excited state properties of Pt^{IV} complexes, [Pt(*NC*)$_3$]$^+$ and [Pt(*NC*)$_2$(*N′C′*)]$^+$ were prepared with different combinations of *NC* and *N′C′* ligands.[34] Attempts to synthesise homoleptic [Pt(*NC*)$_3$]$^+$ complexes with the electron-rich thpy and piq (Figure 1.4, page 9), were unsuccessful, leading to reduction to Pt^{II} complexes. Hence, the *mer*-isomers of the heteroleptic [Pt(dfppy)$_2$(thpy)]OTf, [Pt(dfppy)$_2$(piq)]OTf, [Pt(ppy)$_2$(thpy)]OTf and [Pt(ppy)$_2$(piq)]OTf were prepared. *mer*-[Pt(dfppy)$_2$(ppy)]OTf was also synthesised for comparison.

Irradiation of the heteroleptic complexes with UV light only led to the successful isomerisation to the *fac*-isomer in the case of *mer*-[Pt(dfppy)$_2$(ppy)]OTf. Comparison of the room-temperature emission of the two isomers was consistent with the previously described behaviour – the *mer*-isomer was only weakly emissive, whereas the *fac*-isomer showed strong emission with a quantum yield of 0.43. The *fac*-[Pt(dfppy)$_2$(ppy)]OTf emission spectrum looked very similar to that of *fac*-[Pt(ppy)$_3$)]OTf, indicating that the ppy ligand, which has the smaller $\pi - \pi^*$ transition, is the one responsible for the emission of the complex.

The remaining heteroleptic complexes with a *mer*-configuration showed weak emission with quantum yields in the range 0.02 – 0.07. The two complexes containing a thpy ligand had identical emission spectra, which suggests that the transition is centred on the thpy ligand. The same is observed for the two complexes containing a

piq ligand. [Pt(dfppy)$_2$(piq)]OTf and [Pt(ppy)$_2$(piq)]OTf showed emission in the orange region, as well as an additional band at a higher energy, which could be ascribed as fluorescence on the basis of a small Stokes shift and short lifetime (<0.2 ns).

More recently, tris-cyclometallated complexes of the type *mer*-[Pt(trz)$_2$(*NC*)]$^+$, incorporating one bidentate *NC* ligand and two bidentate mesoionic aryl-NHC ligands (Figure 1.8), were studied.[35] All of the prepared Pt^{IV} complexes were stable to photoisomerisation. Despite their *mer* configuration, the complexes were emissive in CH_2Cl_2 solution with quantum yields between 0.10 and 0.34. TD-DFT calculations revealed that the emission is centred on the *NC* ligand, and the strong σ-donation from the aryl-NHC ligand likely serves to push the deactivating excited states to higher energy.

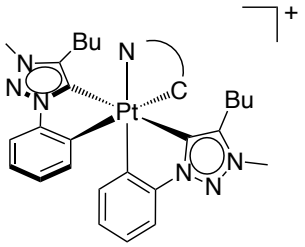

Figure 1.8: *Structure of [Pt(CC*)$_2$(NC)]$^+$ complexes.*

Alternative method for the synthesis of tris-bidentate Pt^{IV} complexes

Although the synthesis of [Pt(*NC*)$_3$]$^+$ and [Pt(*NC*)$_2$(*N′C′*)]$^+$ using the method described above was somewhat easily achieved in some cases, it proved to be problematic in others. In particular, the reaction of [Pt(*NC*)$_2$Cl$_2$] with an excess of *NC*H in the presence of AgOTf did not lead to the successful isolation of a tris-bidentate complex when the electron-rich thpyH and piqH were used.

A new method was introduced which used 2-(2-pyridyl)-arenediazonium salts as the precursor to the third ligand. Such compounds were previously known to oxidatively add to Au^I and other metal ion species.[36–38] The reaction proceeded with the oxidative addition of 2-(2-pyridyl)-arenediazonium tetrafluoroborate (e.g., piqN$_2$BF$_4$) to *cis*-[Pt(*NC*)$_2$] in MeCN or MeOH, followed by the photochemical or thermal elimination of N_2 (Scheme 1.7). The photochemical method involved irradiation with blue LEDs for 24 h and led to the formation of mixtures of isomers, whereas the thermal method resulted in the selective formation of the *fac*-isomer by heating in the solid state at 150 °C for 3 h.

This new procedure afforded the synthesis of the *fac*-isomers of [Pt(*NC*)$_3$]$^+$ and [Pt(*NC*)$_2$(*N′C′*)]$^+$ complexes containing ligands with low-energy $\pi - \pi^*$ transitions.

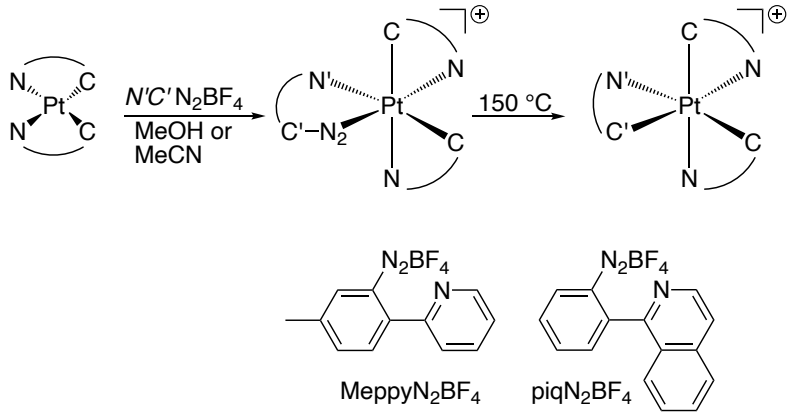

Scheme 1.7: *Alternative synthesis of tris-bidentate Pt^{IV} complexes.*

These complexes showed red-shifted emission, dictated by the ligand of the lowest energy $\pi - \pi^*$ transition energy and quantum yields between 0.02 and 0.06, decreasing in an order consistent with the 'energy gap law'.

1.3.4 Synthesis and excited state properties of Pt^{IV} complexes containing a tridentate ligand

One of the potential advantages of complexes with tridentate ligands, over those with bidentate ligands, is that the former are more usually rigid. When there is less distortion upon transition to an excited state, there is less overlap between the vibrational wavefunctions of the ground and excited states and therefore lower probability of non-radiative decay (Fermi Golden Rule) (Figure 1.9).

When it comes to six-coordinate pseudo-octahedral complexes, there is another benefit of having one or two tridentate ligands, as opposed to three bidentate ligands. Tris-bidentate complexes are chiral and require resolution if a single enantiomer is sought. Molecules incorporating two or more such units will form a mixture of diastereomers. In contrast, their analogues with symmetric tridentate ligands are typically achiral.

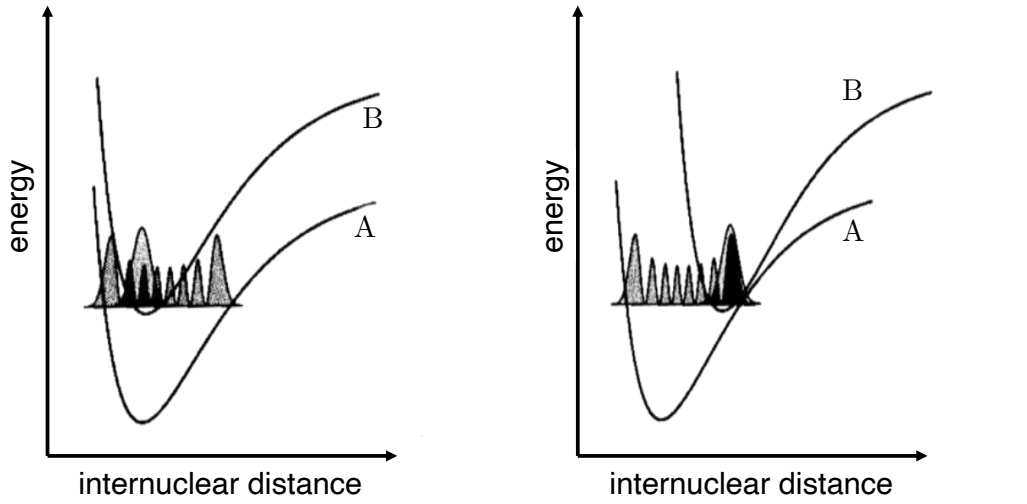

Little or no displacement of excited state PES compared to ground state

Large displacement of excited state PES compared to ground state

Figure 1.9: *Correlation between excited-state potential energy surface distortion relative to the ground state and vibrational wavefunction overlap. On the left, there is little distortion between the ground state (A) and the excited state (B) and little overlap of the vibrational wavefunctions. The opposite scenario of large distortion is shown on the right.*

There are few examples of organometallic Pt^{IV} complexes with tridentate ligands in the literature. González-Herrero and co-workers explored the formation of a complex containing one 2,6-bis(*p*-tolyl)pyridine (*CNC*) and one trz ligand (*CC**).[39] Two Pt^{II} precursors were probed for the reaction – [Pt(*CNC*)(DMSO)] and [Pt_2(μ-Cl)$_2$(*CNC*H)$_2$] (Scheme 1.8). The transmetallation reaction of [Pt(*CNC*)(DMSO)] with AgI(trzH) led to the direct formation of [Pt(*CNC*)(trzH)]. The formation of this complex from the dichloro-briged dimer was achieved by photoisomerisation of *trans*-*C*,*C**-[Pt(*CNC*H)(trzH)Cl] to its *cis*-*C*,*C**-isomer and the subsequent treatment with base, leading to the cyclometallation of the *CNC* ligand. The oxidation step results in the cyclometallation of the phenyl of the trz and decyclometallation of one of the tolyls of the *CNC* ligand. Heating in the presence of base yields the final tridentate + bidentate + Cl complex.

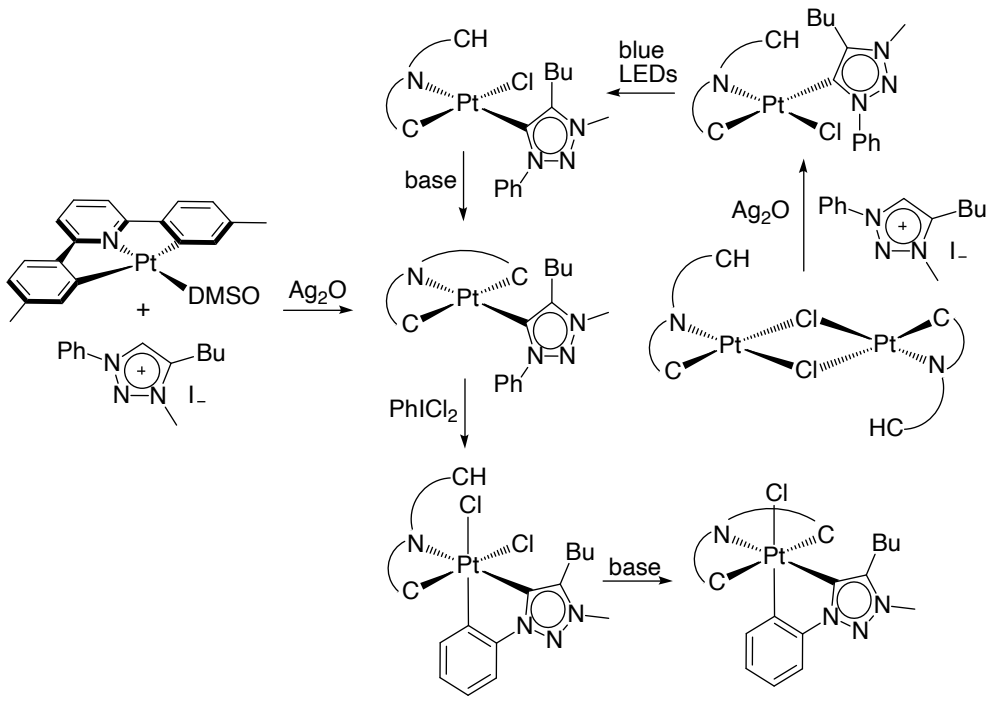

Scheme 1.8: *Synthesis of [Pt(CNC)(CC*)Cl].*

[Pt(*CNC*)(trz)Cl] showed weak room-temperature emission with a quantum yield of 0.0032. The unfavourable *trans* arrangement of the cyclometallated carbon atoms of the *CNC* ligand could be leading to less efficient SOC and therefore a higher k_{nr} value. This observation is in agreement with the lower quantum yields of the *mer*- compared to the *fac*-isomers of tris-bidentate Pt^{IV} complexes.

1.4 Applications of Pt^{IV} complexes

1.4.1 Chemosensing

One of the early studies on organometallic Pt^{IV} complexes by Swager and co-workers explored the oxidative addition reaction to bis-cyclometallated Pt^{II} complexes for chemosensing of cyanogen halides (X–CN).[40] X–CN are highly toxic blood agents and their detection is of high importance. Upon exposure of the Pt^{II} complexes (in solution or dispersed in poly(methyl methacrylate) (PMMA) films) to cyanogen halides, the formation of Pt^{IV} compounds was observed, shifting the emission to higher energies (Figure 1.10). A blue shift of the signal upon sensing provides a dark-field turn-on phosphorescence with negligible background signal.

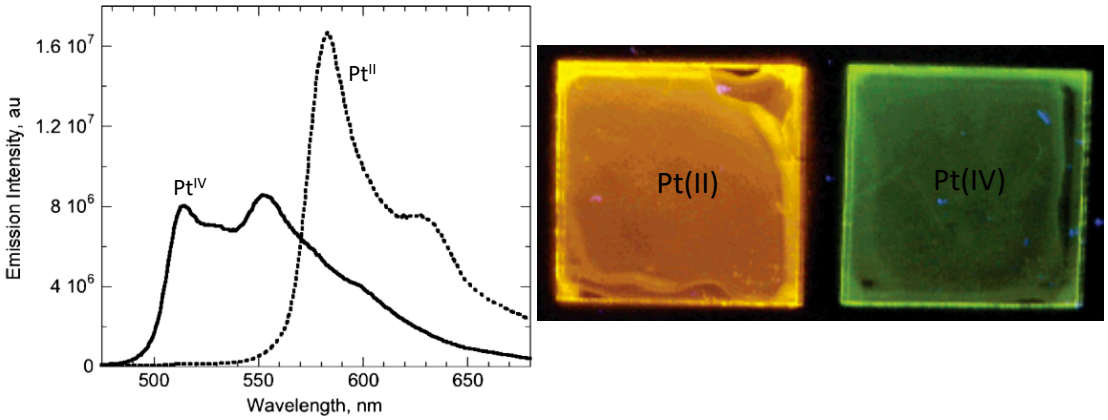

Figure 1.10: *left: PMMA film emission spectra of Pt(thpy)$_2$ before (dotted) and after exposure (solid) to BrCN vapour for 15 s; right: PMMA films of Pt(thpy)$_2$ under UV light before (left) and after(right) exposure to BrCN for 15 s.*[†]

The complexes used in this study were based on Pt(thpy)$_2$ (Figure 1.11). The homoleptic complexes were synthesised using Pt(SEt$_2$)$_2$Cl$_2$ as a precursor by reacting it with the ligands, which were previously lithiated with *tert*-butyllithium in THF/Et$_2$O. The heteroleptic complex was prepared by cracking the chloro-bridged dimer [Pt(μ-Cl)(ppy)]$_2$ with SEt$_2$, followed by reaction with the lithiated thpy.

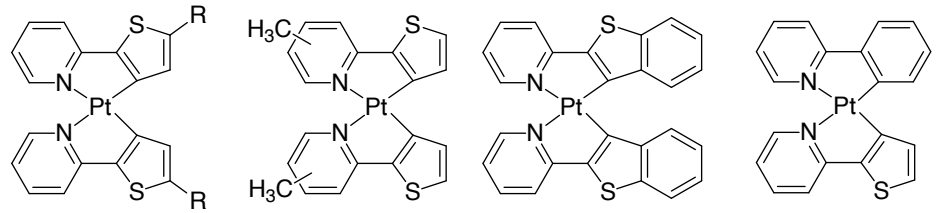

Figure 1.11: *Structures of complexes probed for use as chemosensors for cyanogen halides by Swager and co-workers.*[40]

1.4.2 Photoactivated Chemotherapy (PACT)

The first metal complex used in cancer chemotherapy was cisplatin (*cis*-diammine-dichloroplatinum(II), PtCl$_2$(NH$_3$)$_2$). Its biological activity was first discovered in 1964 when Rosenberg and co-workers were studying the effects of electricity on *E. coli* bacteria.[41] They found that cell division was inhibited by a substance present under the experimental conditions. After a series of experiments, they established that what was causing this biological effect was in fact cisplatin. Pt-based drugs currently account for 50% of the clinically used anticancer chemotherapeutics.[42] However, there

[†]Adapted with permission from Dark-Field Oxidative Addition-Based Chemosensing: New Bis-cyclometalated Pt(II) Complexes and Phosphorescent Detection of Cyanogen Halides, S. W. Thomas, K. Venkatesan, P. Müller, T. M. Swager, *Journal of the American Chemical Society*, 2006, **128**, 51, 16641-16648. Copyright 2006 American Chemical Society.[40]

is a constant urge for the development of new drugs, as the use of the current ones is associated with many challenges, such as the occurrence of severe side effects and resistance.

One proposed strategy to reduce the high toxicity is the activation of the drug specifically at the site of action.

In photodynamic therapy (PDT), a photosensitiser is activated by the use of light, leading to the production of reactive oxygen species (ROS), primarily singlet oxygen ($^1O_2$), that damage cellular components, leading to cell death. However, PDT relies on the presence of dioxygen, which is often limited in hypoxic tumour regions.[43]

In photoactivated chemotherapy (PACT), light is used as a trigger that turns inactive species into cytotoxic ones. Some Pt^{IV} complexes have shown to be potentially suitable for use as pro-drugs in PACT. They offer the advantages of being kinetically inert and more water-soluble than their Pt^{II} analogues. The photoreduction of such complexes can lead to the release of their axial ligands and formation of cytotoxic Pt^{II} species. The released ligands can be biologically active molecules themselves and can trigger a biological response.

A recent example looked at a Pt^{IV} complex with a functionalised terpyridine ligand (Figure 1.12).[44] The use of conjugated ligands leads to a shift of the absorption band to higher wavelengths, which is beneficial for tissue penetration. $[Pt(OCOCH_3)_2Cl(NNN)][CF_3SO_3]$ showed high stability under physiological conditions and in the presence of reducing glutathione. Irradiation with 365 nm light leads to the reduction of the complex with the release of its axial ligands. The complex showed higher cytotoxicity on A2780 cell lines compared to cisplatin.

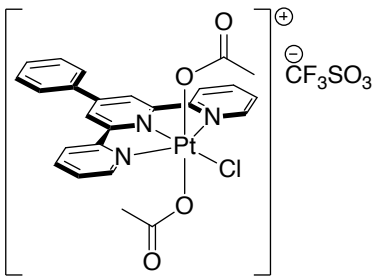

Figure 1.12: *Chemical structure of $[Pt(OCOCH_3)_2Cl(NNN)][CF_3SO_3]$.*

Very recently, de Segura *et al.* prepared rare examples of luminescent cyclometallated Pt^{IV} complexes with potential anticancer applications. The Pt^{IV} complexes in-

corporated two 2-phenylbenzthiazole *NC* ligands, a monodentate pentafluorophenyl ligand and a monodentate pyridine-based ligand (Figure 1.13).

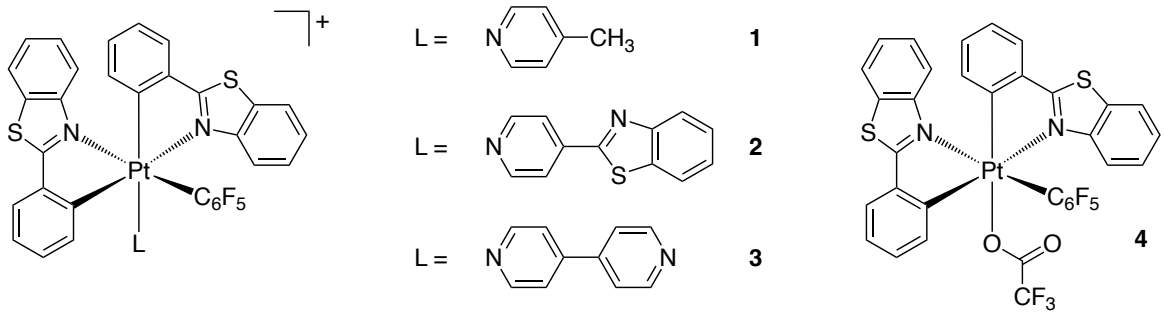

Figure 1.13: *Chemical structure of complexes prepared by de Segura et al.*

All complexes showed emission at room temperature in deoxygenated CH_2Cl_2 with quantum yields of $\approx$ 0.01. Complexes **1**–**3** demonstrated significant cytotoxicity against A549 and HeLa tumor cells, with selective activity compared to non-tumoral cells. The neutral complex **4** was the least cytotoxic, but exhibited increased antiproliferative activity under photoirradiation (15 min), showing potential as a photosensitizer for PDT.

CHAPTER 2

Platinum complexes incorporating tridentate *NCN*-coordinating ligands

Chapter 2: Platinum complexes incorporating tridentate *NCN*-coordinating ligands

2.1 Target compounds

Work by previous PhD students in our group had succeeded in the isolation of a few Pt^{IV} complexes incorporating tridentate cyclometallating ligands based on 1,3-di(2-pyridyl)benzene (dpybH).[45–47] Lisa Murphy developed a method for the oxidation of Pt(dpyb)Cl to Pt(dpyb)Cl_3. Gemma Freeman and Melissa Walden managed to isolate compounds of the type $3+2+1$, which incorporate one tridentate dpyb, one bidentate and one monodentate chloride ligand (Figure 2.1). Three different bidentate ligands were successfully incorporated into the coordination sphere: 2-phenylpyridine (ppy, *NC*), 2,2'-bipyridine (bpy, *NN*) and 2-(3-(4-*tert*-butylphenyl)1H-1,2,4-triazol-5-yl)pyridine) (*NN*$^-$).

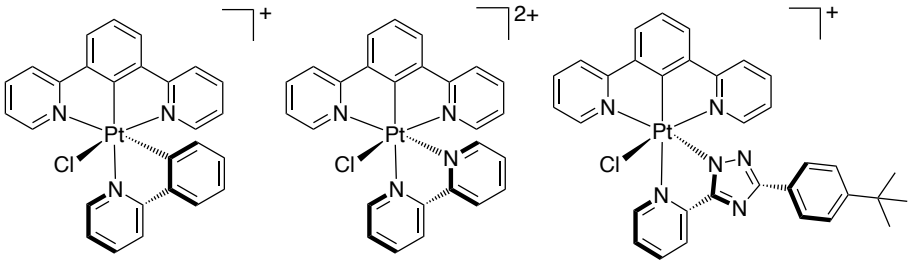

Gemma Freeman Melissa Walden

Figure 2.1: *The Pt^{IV} complexes synthesised by Gemma Freeman and Melissa Walden*

The identity of these complexes was confirmed by X-ray crystallography, but their purification required laborious procedures involving multiple recrystallisations or HPLC. In all cases, the isolated yields were very low.

At the outset of the work described in this thesis we therefore sought to (i) optimise the synthesis and purification of such complexes, (ii) obtain them in amounts sufficient for a more thorough investigation of photophysical and electrochemical properties, and (iii) prepare further examples to allow the effects of modification of the ligand to be probed. We also wished to explore whether bis-tridentate complexes of Pt^{IV} could be prepared that contain at least one *NCN* ligand, together with a second tridentate ligand. Earlier attempts to isolate such complexes had not led to definitive results.

2.2 Synthesis of the proligands

DpybH was used as the archetypal tridentate proligand to prepare Pt(dpyb)Cl as a precursor to the target Pt^{IV} complexes. It was synthesised by Suzuki cross-coupling of benzene-1,3-diboronic acid with 2 equiv. of 2-bromopyridine in a DME/water mixture (1:1), according to an established procedure (Scheme 2.1).[48]

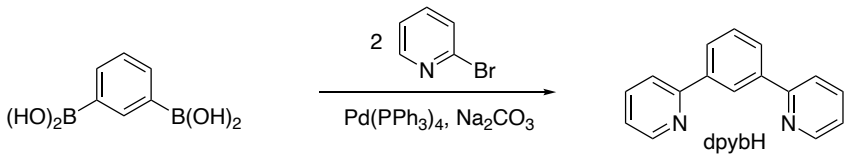

Scheme 2.1: *Synthesis of dpybH proligand*

The synthesis of the tridentate ligands containing two 1,2,4-triazole rings is shown in Scheme 2.2. These ligands had been previously prepared by Melissa Walden, following a procedure adapted from Mydlak *et al.*[49]

The first step involved the reaction of 2,6-pyridinecarbonitrile with an excess of hydrazine monohydrate. The diamidrazone intermediate that formed was further reacted with the appropriate benzoyl chloride. This was followed by a thermal cyclisation step, leading to the formation of the 1,2,4-triazole rings.

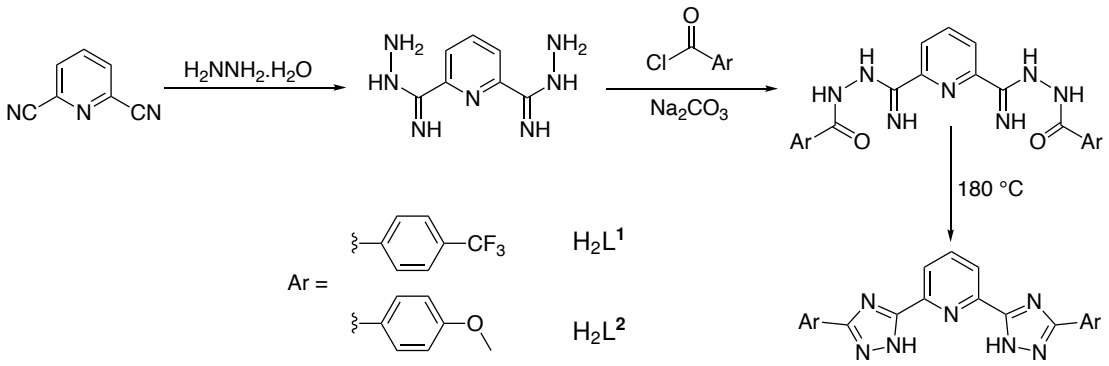

Scheme 2.2: *Synthesis of HNNNH proligands containing two 1,2,4-triazole rings*

2.3 Synthesis of Pt complexes

2.3.1 Synthesis of Pt^{II} complex

Pt(dpyb)Cl was prepared by reaction of dpybH and K_2PtCl_4 in acetic acid (Scheme 2.3).[50]

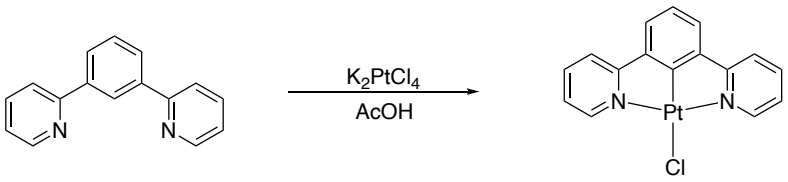

Scheme 2.3: *Synthesis of Pt^{II}(dpyb)Cl*

A crystal structure of Pt(dpyb)Cl had already been obtained (CCDC code: GUDCEN).[50] A single crystal grown in the present work turned out to be a new polymorph, in which the molecules pack in a parallel arrangement, rather than the herringbone packing in the reported structure (Figure 2.2). All crystal structures reported here have been determined by Dr Dmitry Yufit or Dr Toby Blundell at Durham University.

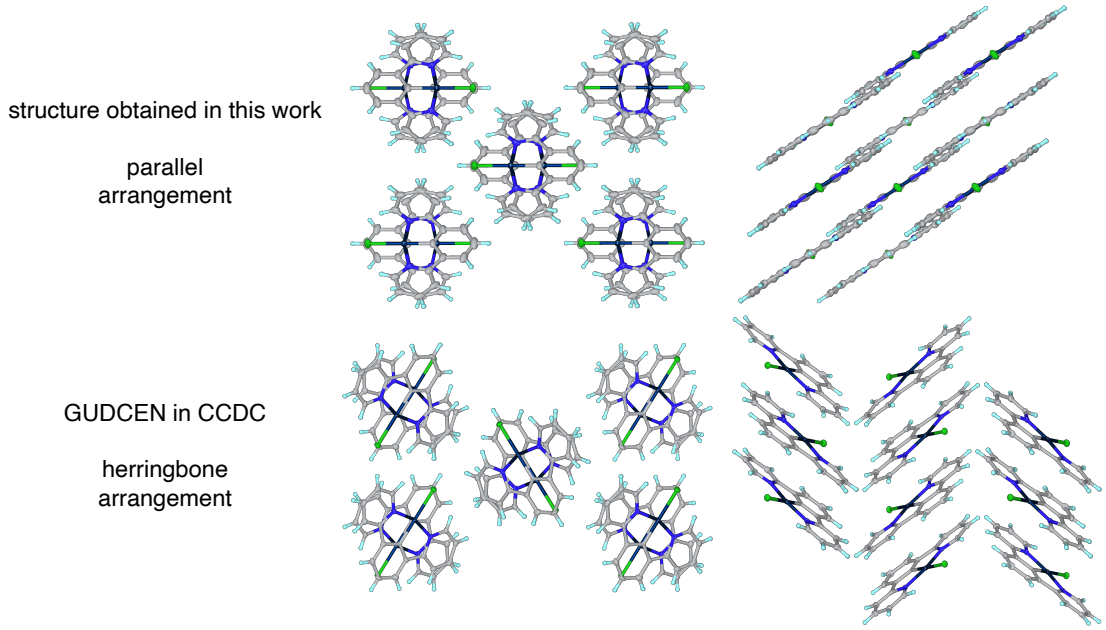

Figure 2.2: *Crystal structures of Pt(dpyb)Cl showing the difference in packing between the structure obtained in this work (top) and the one reported in the literature (GUDCEN, bottom).*

2.3.2 Oxidation of Pt^{II} to Pt^{IV}

Lisa Murphy[47] developed a procedure for the oxidation of Pt(dpyb)Cl to Pt(dpyb)Cl_3 (Scheme 2.4). Chlorine gas, generated by adding concentrated HCl to $KMnO_4$ in a separate flask, is bubbled through a solution of Pt(dpyb)Cl in the minimum volume of chloroform with the partial exclusion of light. While the original procedure suggested maintaining a steady supply of Cl_2 for 30 minutes, it has been found in the present work that 10 minutes is usually sufficient. Longer times are not desirable due to the possibility of ligand chlorination and/or degradation of the complex (see Chapter 3).

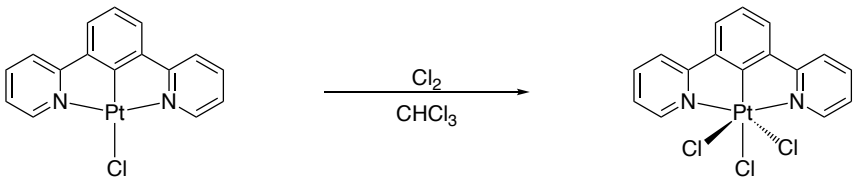

Scheme 2.4: *Oxidation of Pt^{II}(dpyb)Cl to Pt^{IV}(dpyb)Cl_3 using Cl_2.*

2.3.3 Synthesis of 3 + 2 + 1 Pt^{IV} complexes with bidentate ligands incorporating 1,2,4-triazole rings

Four complexes of this type, containing a bidentate pyridyl-triazole ligand, were successfully prepared. The selected ligands are shown in Figure 2.3 (synthesised by Melissa Walden). There are two possible bidentate modes of binding of these ligands to the metal through the N atoms (Figure 2.3). The triazole can bind through deprotonation of the NH (azole-like) or through the neutral N (imine-like).

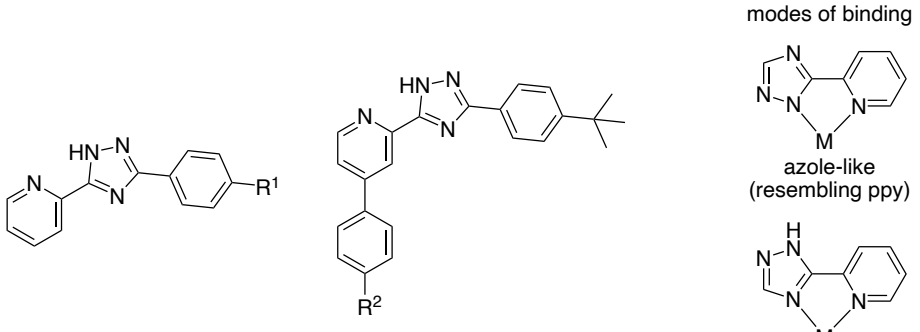

Figure 2.3: *The pyridyl-triazole ligands used (left) and schematic of the possible binding modes of bidentate 1,2,4-triazole ligands*

The first attempt at preparing such a complex was made by reacting Pt(dpyb)Cl_3 with 1 equiv. of HL^3 in boiling ethylene glycol in the presence of AgOTf to facilitate the removal of Cl^-. After work-up, a red crystal suitable for X-ray diffraction was obtained by the slow diffusion of diethyl ether into a DCM solution of the product. It revealed the formation of an unprecedented complex with three *NCN*-coordinated Pt^{II} centres each bound to a single L^3 triazole ligand. One of the N-donors is anionic, whereas the other two are neutral, leading to an overall charge of 2+. Selected bond lengths and bond angles are summarised in Table 2.1. A short Pt–Pt distance of 3.0908(3) Å was found between two of the Pt^{II} centres (Pt1 and Pt2 in Figure 2.4). The Pt(dpyb) units are off-centre with a C–Pt1–Pt2–C torsion angle of 41.6°. The planes defined by the Pt(dpyb) units containing Pt1 and Pt2, respectively, are mutually almost parallel

with an angle of about 6°. Complexes of this type could show potential for excimer formation and NIR emission, due to face-to-face interactions between the two Pt(dpyb) units, which are held in close proximity.[51–53] The ^{1}H NMR spectrum of the isolated crystals was in agreement with the obtained crystal structure. The isolation of this unexpected product – featuring three Pt centres each in oxidation state +2 – shows that the starting Pt^{IV} material must have significant propensity to reduction under the reaction conditions.

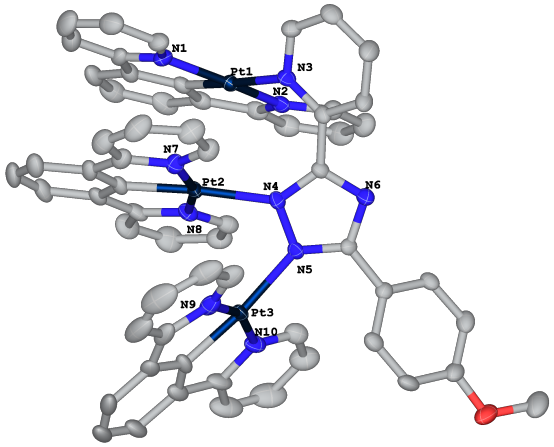

Figure 2.4: *Molecular structure of the cation of* $[\{Pt(dpyb)\}_3L^3]^{2+}$

Table 2.1: *Selected bond lengths (Å) and bond angles (°) of* $\{Pt(dpyb)\}_3L^3$

Bond	Bond Length / Å	Bond Angle	Bond Angle / °
Pt1 – Pt2	3.0908(3)	N2 – Pt1 – N1	160.3(2)
Pt1 – N1	2.054(5)	C7 – Pt1 – N3	176.9(2)
Pt1 – N2	2.042(5)	N7 – Pt2 – N8	160.82(19)
Pt1 – N3	2.153(5)	C27 – Pt2 – N4	175.9(2)
Pt1 – C7	1.916(6)	N9 – Pt3 – N10	160.4(2)
Pt2 – N4	2.127(4)	C47 – Pt3 – N5	173.6(2)
Pt2 – N7	2.036(5)		
Pt2 – N8	2.043(5)		
Pt2 – C27	1.917(5)		
Pt3 – N5	2.130(4)		
Pt3 – N9	2.029(5)		
Pt3 – N10	2.046(5)		
Pt3 – C47	1.922(6)		

In an attempt to mitigate the competitive reduction of the Pt^{IV}, the reaction was subsequently attempted at a lower temperature of 111 °C in toluene. The originally targeted complex was successfully obtained in this way, together with the analogues containing L^4–L^6 (Scheme 2.5). The selection of these conditions was guided by methodology established previously for the preparation of isoelectronic Ir^{III} complexes of the form

Ir(*NCN*)(*NC*)Cl from [Ir(*NCN*)Cl(μ-Cl)]$_2$ precursors.[54,55] The work-up involved isolating the precipitate by centrifugation, followed by washing with toluene, hexane and diethyl ether and extraction into DCM. After solvent removal under reduced pressure, the products were ion-exchanged with KPF_6 and recrystallised from DCM/diethyl ether giving net yields between 27 and 92%.

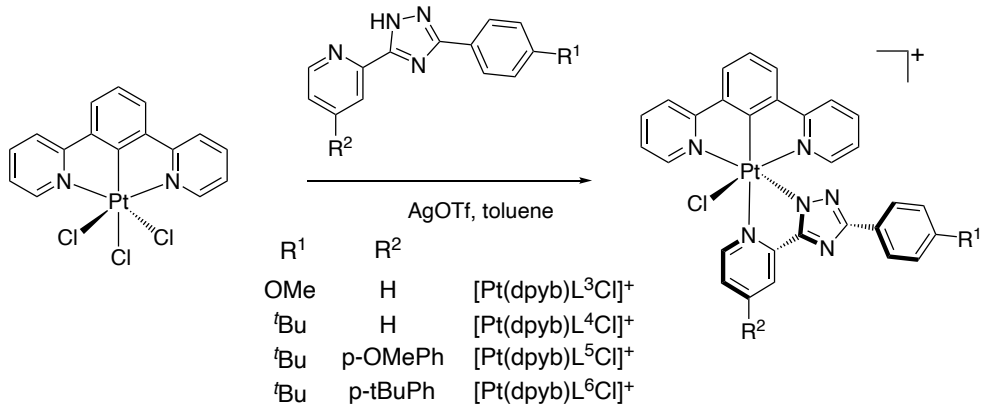

Scheme 2.5: *Synthesis of [Pt(dpyb)L^{3}Cl]$^+$, [Pt(dpyb)L^{4}Cl]$^+$, [Pt(dpyb)L^{5}Cl]$^+$ and [Pt(dpyb)L^{6}Cl]$^+$ from Pt(dpyb)Cl$_3$*

Single crystals of [Pt(dpyb)L^{3}Cl]PF_6 and [Pt(dpyb)L^{6}Cl]PF_6 suitable for X-ray diffraction were obtained by the slow diffusion of diethyl ether into a CH_2Cl_2 solution of each complex (Figure 2.5). [Pt(dpyb)L^{3}Cl]PF_6 co-crystallised with a molecule of DCM and [Pt(dpyb)L^{6}Cl]PF_6 with a molecule of diethyl ether. In both cases, the triazole ring is deprotonated ('azole-like' binding mode in Figure 2.3) and is *trans* to Cl, whereas the pyridine ring is *trans* to the cyclometallated carbon of the dpyb ligand. This arrangement probably arises due to the stronger *trans* effect of the metallated carbon and anionic nitrogen and mirrors what is observed for the aforementioned Ir(*NCN*)(*NC*)Cl complexes, where the pyridine of the *NC* ligand is always found *trans* to the carbon of the *NCN*.

Selected bond lengths and angles for [Pt(dpyb)L^{3}Cl]PF_6 and [Pt(dpyb)L^{6}Cl]PF_6 are summarised in Table 2.2. Both complexes show pseudo-octahedral geometries about the Pt with *trans*-N–Pt–N angles deviating the most from linearity at 161.71° and 161.46°, values quite typical for tridentate ligands binding through the formation of two 5-membered chelate rings. The shortest bond lengths to the Pt are Pt–C at 1.944(3) Å and 1.949(6) Å, and Pt–N_{triaz} at 2.010(2) Å and 1.980(6) Å in the complexes of L^3 and L^6, respectively. The atoms *trans* to these atoms show the longest bonds to the Pt centre, highlighting the weaker bonding of the Cl ligand and the stronger *trans* influence of the cyclometallated C$^-$ and the triazole N$^-$, compared to the pyridyl N.

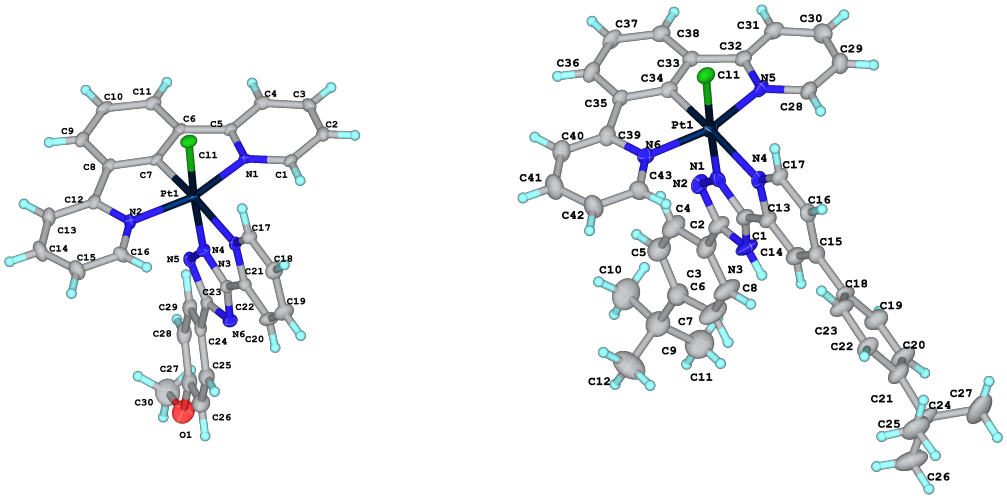

(a) *[Pt(dpyb)L^{3}Cl]$^+$* ***(b)*** *[Pt(dpyb)L^{6}Cl]$^+$*

Figure 2.5: *Molecular structures of [Pt(dpyb)L^{3}Cl]$^+$ and [Pt(dpyb)L^{6}Cl]$^+$ in the crystal.*

Table 2.2: *Selected bond lengths (Å) and bond angles (°) of [Pt(dpyb)L^{3}Cl]PF$_6$ and [Pt(dpyb)L^{6}Cl]PF$_6$*

	[Pt(dpyb)L^{3}Cl]PF$_6$	[Pt(dpyb)L^{6}Cl]PF$_6$
Pt – Cl	2.3057(7)	2.3160(16)
Pt – N_{dpyb_1}	2.041(2)	2.035(5)
Pt – N_{dpyb_2}	2.036(2)	2.040(5)
Pt – N_{py}	2.162(2)	2.186(5)
Pt – N_{triaz}	2.010(2)	1.980(6)
Pt – C	1.944(3)	1.949(6)
N – Pt – N	161.71(10)	161.46(19)
N – Pt – Cl	171.62(7)	174.13(15)
C – Pt – N	174.22(10)	171.2(2)

The aromatic portions of the ^{1}H NMR spectra of [Pt(dpyb)L^{3}Cl]PF$_6$ and the starting Pt^{II}(dpyb)Cl precursor in d_6-acetone are shown in Figure 2.6. The highest peak for the ^{1}H NMR spectrum of [Pt(dpyb)L^{3}Cl]PF$_6$ around 9.6 ppm corresponds to H^7. No satellite peaks for that proton coupling to ^{195}Pt can be seen. All of the dpyb signals are downshifted compared to Pt(dpyb)Cl due to the higher charge, except for the protons *ortho* to nitrogen (H^1 in Figure 2.6). These protons lie above the plane of the pyridyl ring of the triazole ligand and thus experience a shielding ring current effect from it.

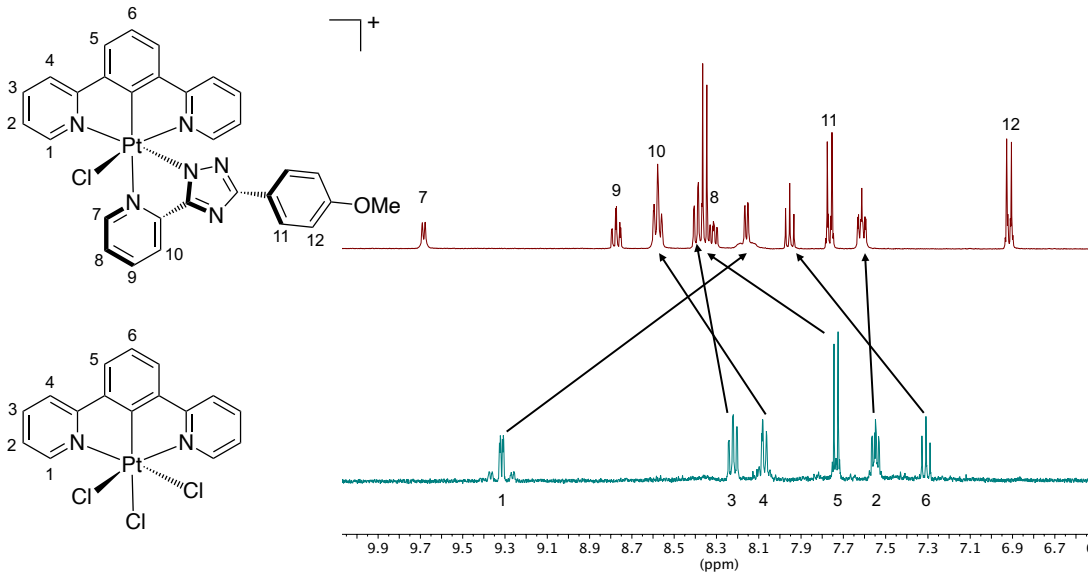

Figure 2.6: *Aromatic region of ^{1}H NMR spectra of [Pt(dpyb)L^{3}Cl]PF_6 and Pt(dpyb)Cl in d_6-acetone at 400 MHz. Most relevant protons are numbered and arrows show the shift for the corresponding protons.*

2.3.4 Synthesis of 3 + 2 + 1 Pt^{IV} complexes with 2-phenylpyridine and 2,2'-bipyridine

$[Pt(dpyb)(ppy)Cl]^{+}$ and $[Pt(dpyb)(bpy)Cl]^{2+}$ (Figure 2.6) had previously been prepared by PhD student Gemma Freeman but only in very small quantities of 1-2 mg, insufficient for their full characterisation. Both complexes were prepared again according to the general procedure described above. The ppy complex required purification by column chromatography on silica with CH_3CN/water/saturated $KNO_{3(aq)}$ as the mobile phase. The pure complex (according to ^{1}H NMR) was obtained in only 11% yield. The bpy complex was obtained in high purity more readily in 88% yield.

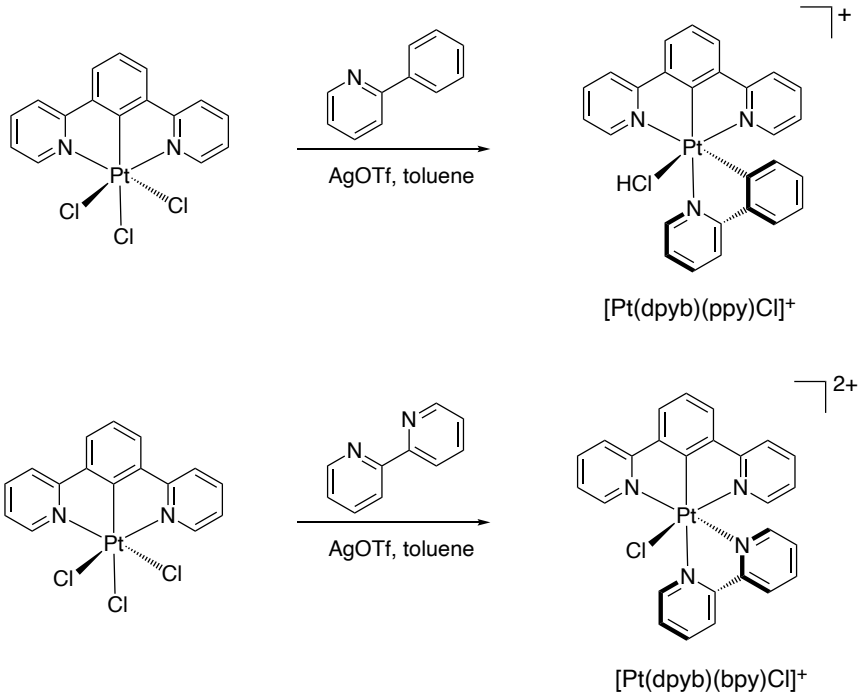

Scheme 2.6: *Synthesis of [Pt(dpyb)(ppy)Cl]$^{+}$ and [Pt(dpyb)(bpy)Cl]$^{2+}$ from Pt(dpyb)Cl$_3$*

2.3.5 Synthesis of bis-tridentate Pt^{IV} complexes

Background to related bis-tridentate organometallic Ir^{III} complexes

Bis-tridentate complexes of Ir^{III}, which is isoelectronic with Pt^{IV}, have been the subject of quite extensive research. Among the various structures studied are [Ir(*NCN*)(*NNN*)]$^{2+}$ (**1**), [Ir(*NCN*)(*NNC*)]$^{+}$ (**2**) and Ir(*NCN*)(*CNC*) (**3**), where the *NCN* ligand is 1,3-di(2-pyridyl)-4,6-dimethylbenzene (dpyx), the *NNN* is 2,2':6',2"-terpyridine, the *NNC* is 6-phenyl-2,2'-bipyridine and the *CNC* is 2,6-diphenylpyridine (Figure 2.7).[9,54] Complexes **1** and **2** were prepared by heating the chloro-bridged dimer [Ir(dpyx)Cl(μ-Cl)]$_2$ with the corresponding *NNN* or *NNC* tridentate ligand in ethylene glycol at 196 °C. AgOTf was used in the case of complex **2** to aid in the abstraction of the chlorides. Complex **3** was synthesised by heating [Ir(dpyx)Cl(μ-Cl)]$_2$ in molten 2,6-diphenylpyridine as the reaction solvent at 74–76 °C.

Complex **1** is only weakly emissive at room temperature in degassed CH_3CN (Φ < 0.01%). Complexes **2** and **3** show room-temperature emission in deaerated CH_3CN with quantum yields of 2.3 and 21%, respectively.

These structures will provide a foundation for the synthesis of Pt^{IV} analogues, as no known examples of bis-tridentate Pt^{IV} complexes currently exist.

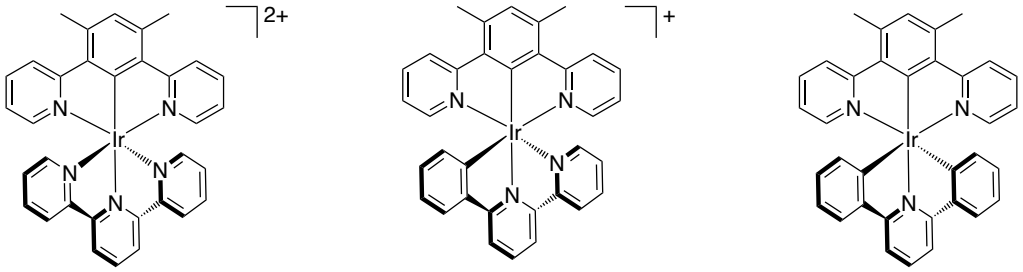

Figure 2.7: *Structures of iridium(III) complexes containing an NCN ligand, reported by Williams and co-workers.*[9,54]

Synthesis of [Pt(dpyb)(*NNN*)]$^{3+}$

The synthesis of [Pt(dpyb)(tpy)]$^{3+}$ (Figure 2.9) was first attempted by heating Pt(dpyb)Cl_3 and tpy in dry refluxing ethylene glycol for 18 h. No AgOTf was used, so that the complex could be obtained with a chloride counterion. It was assumed that the 3+ complex with a chloride counterion would be soluble in an ethylene glycol / water mixture, so water was added and the resulting precipitate removed by centrifugation. The ^{1}H NMR spectrum of the precipitate revealed it to be a mixture of the starting Pt(dpyb)Cl_3 and its reduced version Pt(dpyb)Cl. Meanwhile, the filtrate was added dropwise to saturated $KPF_{6(aq)}$, in order to precipitate the sought-after complex as its hexafluorophosphate salt. Crystallisation of the precipitate led to a crystal suitable for X-ray diffraction (Figure 2.8)

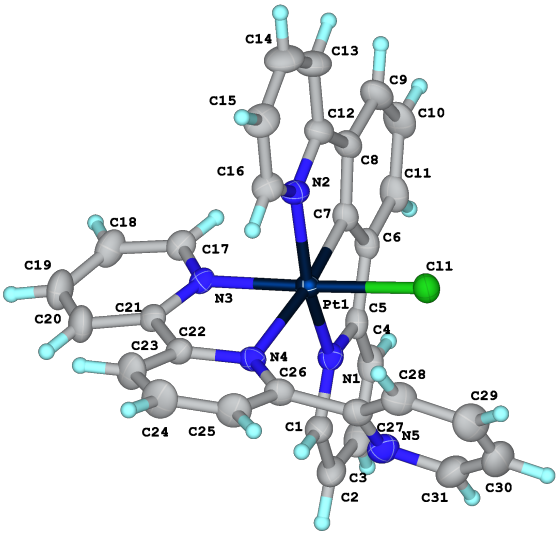

Figure 2.8: *Molecular structure of the cation of [Pt(NCN-dpyb)(NN-tpy)][PF_6]$_2$*

The structure reveals the complex to be one in which the tpy ligand is bound as a bidentate *NN* ligand with the 6th site occupied by a chloride (Figure 2.8). It is unusual for tpy to bind as a bidentate ligand.[56] However, this structure is not consistent with the

^{1}H spectrum of the bulk material in solution, which showed only one environment for the lateral rings of the terpyridine. Apparently, most of the molecules present were indeed the targeted complex, whilst [Pt(*NCN*-dpyb)(*NN*-tpy)Cl]$^{2+}$ may have been only a minor product that happened to crystallise readily. Nevertheless, the desired complex could not be purified any further, so another attempt was made to synthesise it using different conditions. [Pt(dpyb)(tpy)]$^{3+}$ was successfully synthesised according to the general procedure described previously, by heating the starting materials in toluene in the presence of 3 equiv. of AgOTf to aid the abstraction of all three chloride ligands. A related complex with one dpyb ligand and one non-symmetric *NNN* ligand containing a 7-azaindole lateral ring, namely 6-(N-7-azaindolyl)-2,2′-bipyridine (azbpy), was also synthesised (Figure 2.9). To the best of our knowledge, these are the first known examples of bis-tridentate Pt^{IV} complexes.

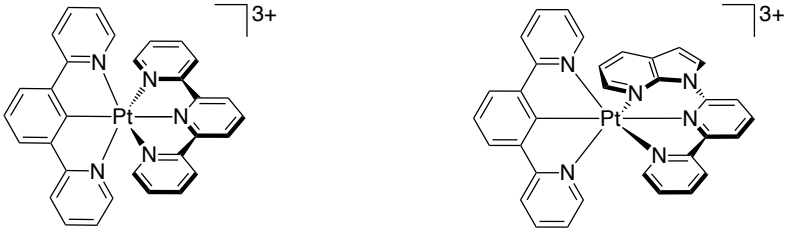

Figure 2.9: *Chemical structures of [Pt(dpyb)(NNN)]$^{3+}$ complexes in crystal*

The ligand azbpy binds with the formation of one 5- and one 6-membered chelating ring, whereas tpy binds with the formation of two 5-membered chelating rings. When bound to a metal, 5,6-chelating ligands similar to azbpy have been found to give bite angles closer to 180°, which results in stronger ligand fields, and which can have a beneficial impact on luminescence quantum yield by attenuating non-radiative decay in d-d states.[57–59] Crystals suitable for X-ray diffraction were obtained for both [Pt(dpyb)(tpy)][PF_6]$_3$ and [Pt(dpyb)(azbpy)][PF_6]$_3$ by the slow diffusion of diethyl ether into an acetone solution of the respective complex.

Selected bond lengths and bond angles are summarised in Table 2.3. Both complexes show pseudo-octahedral geometries about the Pt. The corresponding bond lengths are similar for the two complexes but the N^{az}–Pt–N^{py} angle is indeed closer to being linear, at 171.4° compared to the N^{py}–Pt–N^{py} angle in the tpy complex at 160.1°.

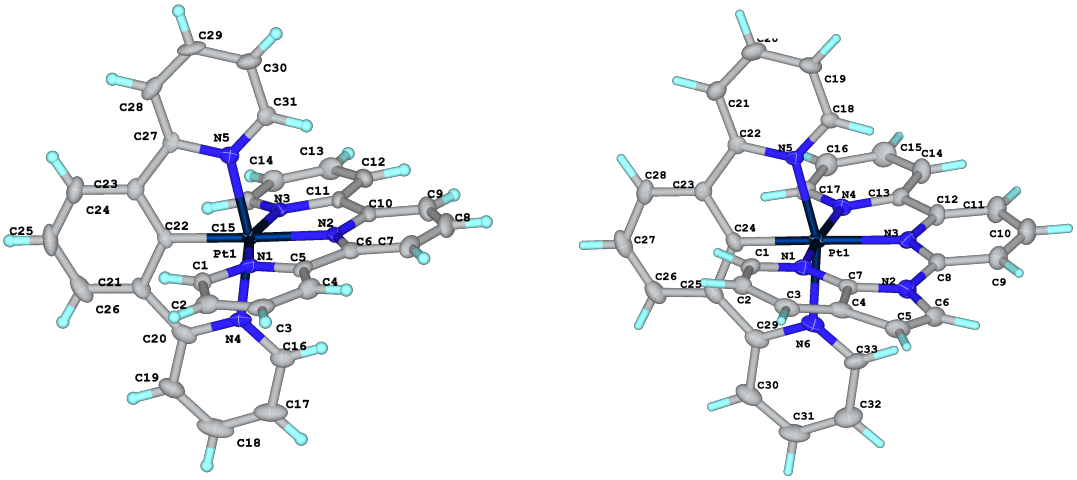

(a) *[Pt(dpyb)(tpy)]$^{3+}$* ***(b)*** *[Pt(dpyb)(azbpy)]$^{3+}$*

Figure 2.10: *Molecular structures of [Pt(dpyb)(tpy)]$^{3+}$ and [Pt(dpyb)(azbpy)]$^{3+}$*

Table 2.3: *Selected bond lengths (Å) and bond angles (°) of [Pt(dpyb)(tpy)][PF_6]$_3$ and [Pt(dpyb)(azbpy)][PF_6]$_3$*

	[Pt(dpyb)(tpy)]$^{3+}$	[Pt(dpyb)(azbpy)]$^{3+}$
Pt – $N^{NNN_{az}}$	–	2.028(7)
Pt – N^{NNN}	2.020(5)	2.098(7)
Pt – $N^{N_{py}NN}$	2.042(5) / 2.038(5)	2.032(7)
Pt – N^{NCN}	2.052(5) / 2.057(6)	2.043(6) /2.055(7)
Pt – C	1.980(5)	1.951(8)
$N^{NNN/NNN_{az}}$ – Pt – $N^{NNN/N_{py}NN}$	160.1(2)	171.4(3)
N^{NCN} – Pt – N^{NCN}	161.0(2)	162.2(3)
C – Pt – N^{NNN}	177.8(2)	173.7(3)

Attempted synthesis of complexes of the type [Pt(dpyb)(*CNC*)]$^{+}$, [Pt(dpyb)(*NCN*)]$^{2+}$ and [Pt(dpyb)(*NNC*)]$^{2+}$

The syntheses of [Pt(*NCN*-dpyb)(*CNC*-dppy)]$^{+}$ (dppyH = 2,6-diphenylpyridine), [Pt(*NCN*-dpyb)$_2$]$^{2+}$ and [Pt(*NCN*-dpyb)(*NCN*-F_2-dpyb)]$^{2+}$ were attempted by reacting Pt(dpyb)Cl_3 with the corresponding ligand in the presence of AgOTf in either ethylene glycol or toluene (Scheme 2.7). All of the reactions yielded mixtures of products, most of which could not be identified. In each case, some reduction to Pt^{II} was also observed, with either Pt(dpyb)Cl or [Pt(dpyb)(CH_3CN)]$^{+}$, being observed by NMR and mass spectrometry. In some instances, they were even formed in sufficient amounts that they could be isolated.

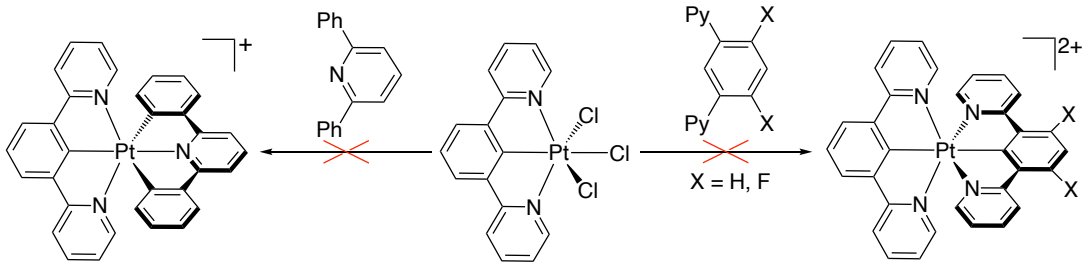

Scheme 2.7: *Attempted synthesis of [Pt(dpyb)(dppy)]$^{+}$, [Pt(dpyb)$_2$]$^{2+}$ and [Pt(dpyb)(F$_2$-dpyb)]$^{2+}$*

The attempted synthesis of [Pt(*NCN*-dpyb)(*NNC*-phbpy)]$^{2+}$ following the same procedure was also not successful (Scheme 2.8). Two recrystallisations from hot ethanol led to the isolation of a compound of which a single crystal suitable for X-ray diffraction was obtained. It revealed the formation of a Pt^{II}(dpyb) complex in which the 4th coordination site is occupied by phbpyH, bound monodentate through the lateral pyridine ring (Figure 2.11). An attempt was made to re-oxidise this complex back to Pt^{IV} using the oxidising agent PhICl$_2$, but rather than obtaining the desired complex, the outcome was the formation of mainly Pt(dpyb)Cl$_3$.

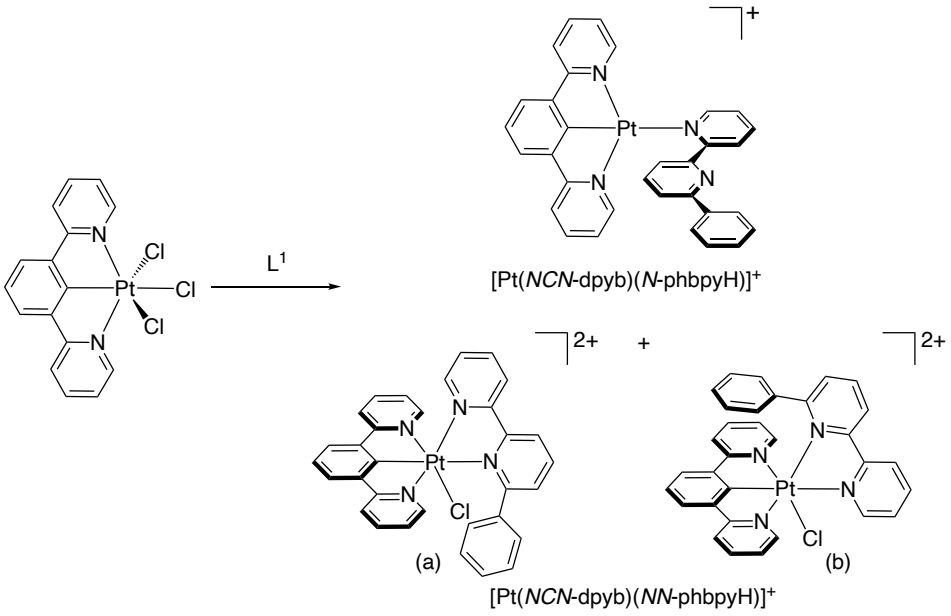

Scheme 2.8: *Attempted synthesis of [Pt(dpyb)(phbpy)]$^{2+}$, leading either to a Pt^{II} complex or to two mutually isomeric Pt^{IV} complexes of the 3 + 2 + 1 type.*

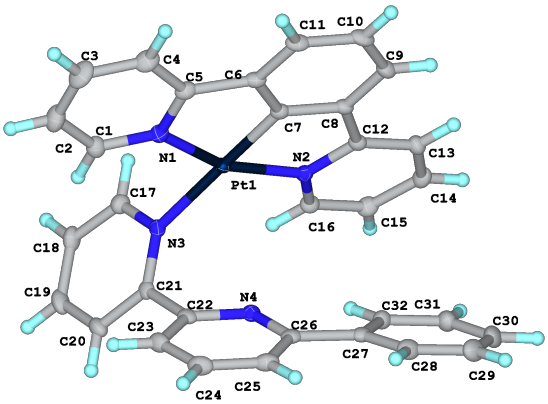

Figure 2.11: *Molecular structure of [Pt(NCN-dpyb)(N-phbpyH)]$^{+}$ in the crystal*

Another attempt at the same reaction yielded a mixture of two isomers of a 3 + 2 + 1 complex, in which the phbpy binds as a bidentate ligand through the two pyridine rings, with no cyclometallation of the phenyl ring (Scheme 2.8). Single crystals suitable for X-ray diffraction were obtained for both products by the slow diffusion of diethyl ether into a DCM solution of the complex (Figure 2.12). In isomer (a) the phenyl ring of the dpyb ligand is *trans* to the central pyridine of the phbpy ligand, whereas for (b) the phenyl ring of the dpyb ligand is *trans* to the terminal pyridine ring of the phbpy ligand. Although these two isomers were initially isolated independently, scrambling occurred in acetone-d_6 solution at ambient temperature over the course of a few days, evidenced by ^{1}H NMR.

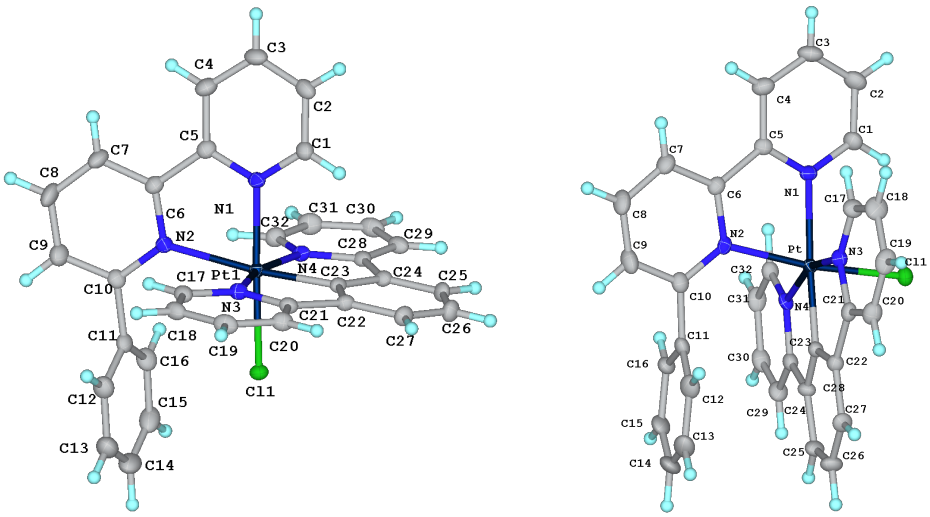

Figure 2.12: *Molecular structures of the two isomers of [Pt(dpyb)(HL^{7})Cl]$^{2+}$ in the crystal.*

Attempted synthesis of Pt^{IV} complexes with tridentate ligands containing two 1,2,4-triazole rings

Melissa Walden attempted to synthesise $[Pt(dpyb)(L^2)]^+$ (Scheme 2.9), but unequivocal evidence for its formation was not obtained.

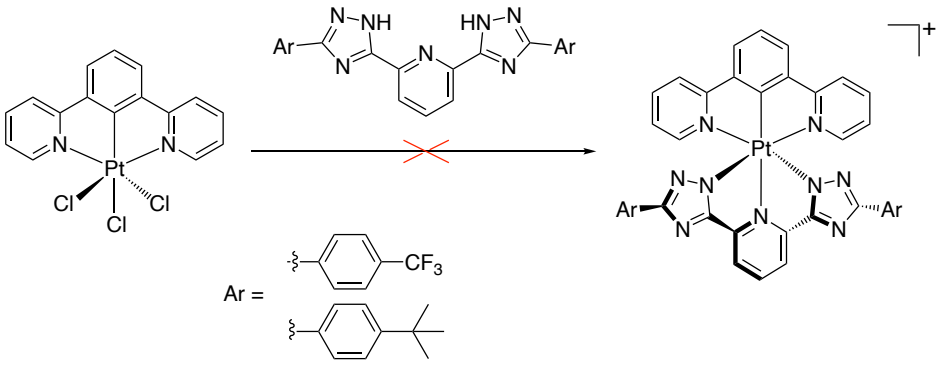

Scheme 2.9: *Synthesis of [Pt(dpyb)(tBu/CF_3-triazole)]$^+$*

Several further attempts were made during the present work, as summarised in Table 2.4. Base was used in some instances to facilitate the deprotonation of the azoles. All of the procedures gave a peak in the ASAP mass spectrum at the expected *m/z* value of 925 (L^1) or 901 (L^2) for the molecular ion, except for the use of toluene with no AgOTf. A variety of purification techniques were used in attempts to isolate the products, including recrystallisation from different solvents and column chromatography with different mobile phases. However, the isolation of a pure product was not achieved from any of the reactions.

Table 2.4: *Different conditions probed for the synthesis of [Pt(dpyb)(tBu/CF_3-triazole)]$^+$*

solvent	AgOTf	base	microwave	T / °C	time
ethylene glycol	✓	✗	✗	200	72 h
ethylene glycol	✓	✗	✗	200	2 h
ethylene glycol	✗	✗	✗	200	5 h
ethylene glycol	✓	✗	✗	175	24 h
ethylene glycol	✗	Et_3N	✗	175	24 h
ethylene glycol	✓	✗	✓	150	30 min
ethylene glycol	✓	K_2CO_3	✓	130	20 min
ethylene glycol	✓	NaOMe	✓	130	20 min
ethylene glycol	✓	Et_3N	✓	130	20 min
toluene	✗	✗	✗	111	24 h
toluene	✓	✗	✗	125	24 h
DCE	✓	✗	✓	120	30 min
DCE	✓	K_2CO_3	✓	130	30 min

2.3.6 Photophysical properties

The absorption spectra of the complexes in CH_3CN solution at room temperature are shown in Figure 2.13 (data also summarised in Table 2.5). Each complex displays intense bands at high energy < 300 nm, which can be ascribed to π– π^* transitions within the ligands. [Pt(dpyb)L^{5}Cl]PF_6 and [Pt(dpyb)L^{6}Cl]PF_6 show higher molar absorptivity in the low energy region, compared to [Pt(dpyb)L^{3}Cl]PF_6 and [Pt(dpyb)L^{4}Cl]PF_6, reflecting the presence of the additional aromatic ring.

For complexes [Pt(dpyb)(bpy)Cl][PF_6]$_2$ and [Pt(dpyb)(tpy)][PF_6]$_3$ the lowest-energy unoccupied orbitals are more likely located on the pyridine rings of the more electron-deficient tpy or bpy ligands than on the *NCN*. The bands appearing at 340 and 357 nm in [Pt(dpyb)(tpy)][PF_6]$_3$ have obvious counterparts in [Pt(tpy)Cl_3]$^+$ (340 and 356 nm)[60] and are therefore concluded to arise from transitions involving the tpy ligand as the acceptor. Similarly, [Pt(dpyb)(bpy)Cl][PF_6]$_2$ shows intense bands at 320 (appearing as a shoulder) and 309 nm, comparable to the tris-bidentate complex, [Pt(ppy)$_2$(bpy)]$^+$, reported by Bernhard and co-workers (332sh, 316 nm), and thus likely involving bpy as the acceptor.[31]

None of the complexes were luminescent at room temperature in acetonitrile solution or at 77K in butyronitrile. Although some weak emission was observed in some samples, it closely resembled the emission profile of the Pt^{II} precursors, and was almost certainly due to a light-activated reduction back to Pt^{II} on the timescale of the measurement, or to the presence of small amounts of impurities from the outset.

Table 2.5: *UV-vis absorption data for [Pt(dpyb)L$^{3–6}$Cl]PF_6, [Pt(dpyb)(ppy)Cl]PF_6, [Pt(dpyb)(bpy)Cl][PF_6]$_2$ and [Pt(dpyb)(tpy)][PF_6]$_3$ in CH_3CN at 298 K.*

complex	absorption λ_{max}/nm (ε/M^{-1}cm^{-1})
[Pt(dpyb)L^{3}Cl]PF_6	266 (44700), 279sh (38900), 322 (15200), 340sh (13500)
[Pt(dpyb)L^{4}Cl]PF_6	260 (35500), 279sh (25300), 323 (16200), 341sh (10900)
[Pt(dpyb)L^{5}Cl]PF_6	259 (47100), 279sh (37700), 326 (42400)
[Pt(dpyb)L^{6}Cl]PF_6	257 (42800), 280 (41900), 301 (37800)
[Pt(dpyb)(ppy)Cl]PF_6	256 (13360), 265 (12700), 285 (11800), 308 (11300), 319 (10900), 332sh (7820), 348 (5820)
[Pt(dpyb)(bpy)Cl][PF_6]$_2$	268 (15800), 280 (18000), 309 (24500), 320sh (26200)
[Pt(dpyb)(tpy)][PF_6]$_3$	273sh (24500), 281 (27400), 294 (22500), 325 (20800), 339sh (15200), 357 (13000)

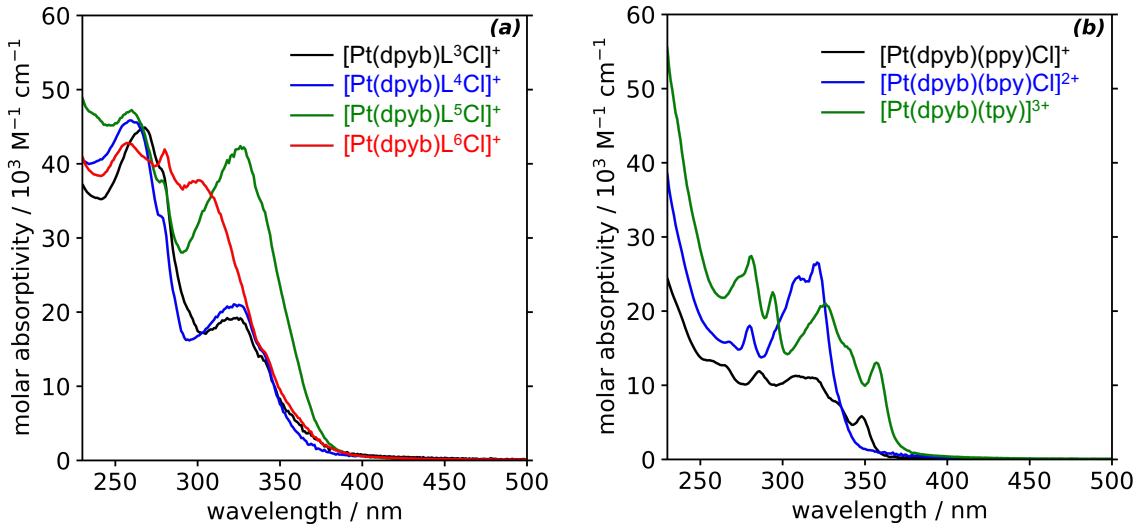

Figure 2.13: *UV-vis absorption spectrum of [Pt(dpyb)L$^{3-6}$Cl]PF$_6$, [Pt(dpyb)(ppy)Cl]PF$_6$, [Pt(dpyb)(bpy)Cl][PF$_6$]$_2$ and [Pt(dpyb)(tpy)][PF$_6$]$_3$ in CH$_3$CN at 298 K.*

2.3.7 Electrochemistry

The redox properties of the complexes were investigated in acetonitrile in the presence of 0.1M NBu_4PF_6 as supporting electrolyte. The cyclic voltammograms for complexes [Pt(dpyb)L$^{3-6}$Cl]PF$_6$ are shown in Figure 2.14 and those of [Pt(dpyb)(ppy)Cl]PF$_6$, [Pt(dpyb)(bpy)Cl][PF$_6$]$_2$ and [Pt(dpyb)(tpy)][PF$_6$]$_3$ in Figure 2.15. E^0 values are also collated in Table 2.6. For each complex, an irreversible reduction peak between –0.22 and –1.48 V vs Fc^+ | Fc is observed, corresponding to reduction of the Pt(IV) to Pt(II), as seen for other Pt(IV) complexes.[31] The potential required for the reduction of the Pt(IV) centre decreases with the increase in overall charge of the cations – least negative for the 3+ terpyridine-containing complex cation and most negative for the singly charged complex cation [Pt(dpyb)(ppy)Cl]$^+$.

One further reversible reduction was observed at lower reduction potentials for all complexes apart from [Pt(dpyb)(ppy)Cl]PF$_6$, probably associated with the reduction of the bpy and tpy ligands. For complex [Pt(dpyb)(bpy)Cl][PF$_6$]$_2$, there is a small reversible reduction at –1.96V vs Fc^+ | Fc.

Oxidation peaks were only observed for complexes [Pt(dpyb)L$^{3-6}$Cl]PF$_6$ in the range investigated, likely thanks to the presence of the electron-rich 1,2,4-triazole ring. The complex with the more electron-donating *p*-OMe-phenyl-substituted triazole ring exhibits the lowest oxidation potential of 1.19V vs Fc^+ | Fc. The highest occupied molecular orbital (HOMO) is likely located

on the triazole-containing ligands $L^{3–6}$ and therefore the oxidation potential of the complex is affected by the change in substituent on that ligand.

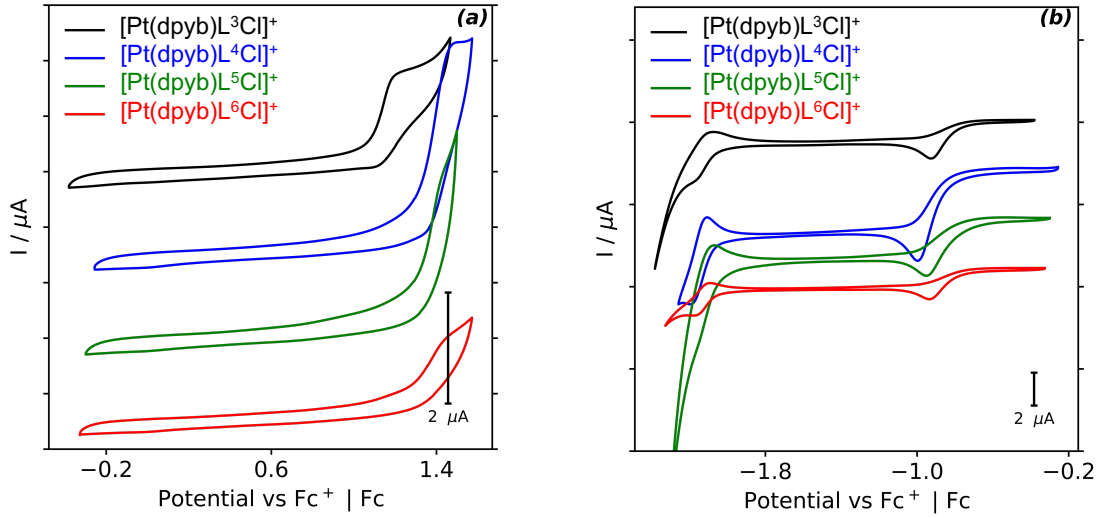

Figure 2.14: *Cyclic voltammograms of [Pt(dpyb)L$^{3–6}$Cl]PF$_6$ recorded in 0.1 M NBu$_4$PF$_6$/CH$_3$CN, scan rate = 50 mV s^{-1}.*

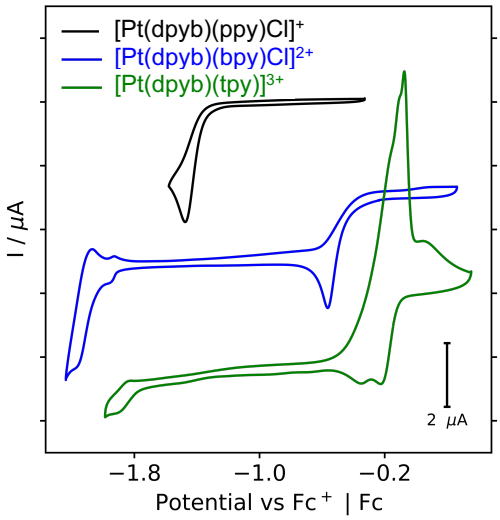

Figure 2.15: *Cyclic voltammograms of [Pt(dpyb)(ppy)Cl]PF$_6$, [Pt(dpyb)(bpy)Cl][PF$_6$]$_2$ and [Pt(dpyb)(tpy)][PF$_6$]$_3$ recorded in 0.1 M NBu$_4$PF$_6$/CH$_3$CN, scan rate = 50 mV s^{-1}.*

Table 2.6: *Electrochemical data for [Pt(dpyb)L$^{3-6}$Cl]PF_6, [Pt(dpyb)(ppy)Cl]PF_6, [Pt(dpyb)(bpy)Cl][PF_6]$_2$ and [Pt(dpyb)(tpy)][PF_6]$_3$ in CH_3CN solution with 0.1M NBu_4PF_6*

complex	E^{ox}_{pa} / V[a]	E^{red}_{pc} / V[c]
[Pt(dpyb)L^{3}Cl]PF_6	1.19	–0.93[d], –2.17
[Pt(dpyb)L^{4}Cl]PF_6	1.48	–1.00[d], –2.20
[Pt(dpyb)L^{5}Cl]PF_6	1.43	–0.95[d], –2.17
[Pt(dpyb)L^{6}Cl]PF_6	1.44	–0.94[d], –2.16
[Pt(dpyb)(ppy)Cl]PF_6	–[c]	–1.48[d]
[Pt(dpyb)(bpy)Cl][PF_6]$_2$	–[c]	–0.56[d], –1.96, –2.16
[Pt(dpyb)(tpy)][PF_6]$_3$	–[c]	–0.22[d], –0.35, –1.89

[a]E_{pa} refers to the anodic peak potential for the irreversible oxidation waves. [b]E_{pc} refers to the cathodic peak potential for the reduction waves. [c]Oxidation outside of the accessible window. [d]Irreversible reduction.

2.4 Chapter summary

The Pt^{IV} complex Pt(dpyb)Cl_3 was synthesised by oxidizing Pt^{II}(dpyb)Cl with chlorine. From this complex, several 3 + 2 + 1 type complexes were prepared, each featuring a tridentate dpyb ligand, one bidentate ligand, and a monodentate chloride ligand. The bidentate ligands used in these complexes included pyridyl-triazole ligands *NN*$^-$, 2,2'-bipyridine *NN*, and 2-phenylpyridine *NC*. Additionally, two bis-tridentate complexes were synthesised, incorporating a dpyb *NCN* ligand and an *NNN*-type ligand, marking the first examples of bis-tridentate Pt^{IV} complexes.

The photophysical properties of all of the complexes were investigated. The absorption spectra of the complexes in CH_3CN solution at room temperature show intense high-energy bands (< 300 nm) attributed to π– π^* transitions in the ligands, with lower-energy bands extending to 400 nm likely involving some metal participation. None of the complexes displayed detectable luminescence at room temperature in acetonitrile or at 77K in butyronitrile.

The redox properties of the complexes were examined in acetonitrile with 0.1M NBu_4PF_6 as the supporting electrolyte. Each complex exhibits an irreversible reduction peak between –0.22 and –1.48 V vs Fc^+ | Fc, corresponding to the Pt(IV) to Pt(II) reduction. The reduction potential becomes less negative with increasing cation charge. Oxidation peaks were observed only for [Pt(dpyb)L$^{3-6}$Cl]PF_6, with the complex featuring an electron-rich triazole ring showing the lowest oxidation potential of 1.19V vs Fc^+ | Fc.

CHAPTER 3

Platinum complexes incorporating tridentate *NNC* ligands

Chapter 3: Platinum complexes incorporating tridentate *NNC* ligands

3.1 Target compounds

Building on the work from Chapter 2, we expanded our research to the synthesis of Pt^{IV} compounds featuring tridentate *NNC* ligands, in contrast to the previously examined *NCN* ligands. By employing differently substituted phenylboronic acids, we can easily modify the cyclometallating ring of the *NNC* ligand. Our investigation will include the synthesis of various Pt^{IV} complexes of the $3+2+1$ type, as well as bis-tridentate complexes, followed by an exploration of their electrochemical and photophysical properties.

3.2 Synthesis of the proligands

Seven *NNC* (HL^{7}–HL^{13}) and four *NC* (3-OMe-ppy, 4-OMe-ppy, 2,4-F_2-ppy and 4-CF_3-ppy) proligands were synthesised by Suzuki and Stille cross-coupling reactions according to standard procedures (Scheme 3.1).[48,61] The reactions were performed in degassed solvent under an atmosphere of nitrogen using $Pd(PPh_3)_4$ or $Pd(PPh_3)_2Cl_2$ as the catalyst.

6-Bromo-2,2′-bipyridine was synthesised by Stille coupling of 2,6-dibromopyridine and 2-(tributylstannyl)pyridine. A Suzuki cross-coupling of the product with 1 mol equiv. of the appropriate *meta*- or *para*-substituted phenylboronic acid in DME/water (1:1) gave $HL^{7–11}$. The synthesis of 8-(6-phenylpyridin-2-yl)quinoline (HL^{13}) was achieved by two consecutive Suzuki cross-coupling reactions, the first between 2,6-dibromopyridine and 8-quinolinyl boronic acid, and the second between the resulting 2-bromo-5-(8-quinolinyl)pyridine and phenylboronic acid. HL^{12} was prepared by a Stille cross-coupling of 6-bromo-2,2′-bipyridine with 2-(tributyltin)thiophene. While Suzuki cross-coupling reactions are typically preferred over Stille cross-coupling reactions due to the toxic nature of organotin compounds, heteroaryl boronic acids are unstable. Therefore, a Stille cross-coupling reaction was used in this case.[62,63]

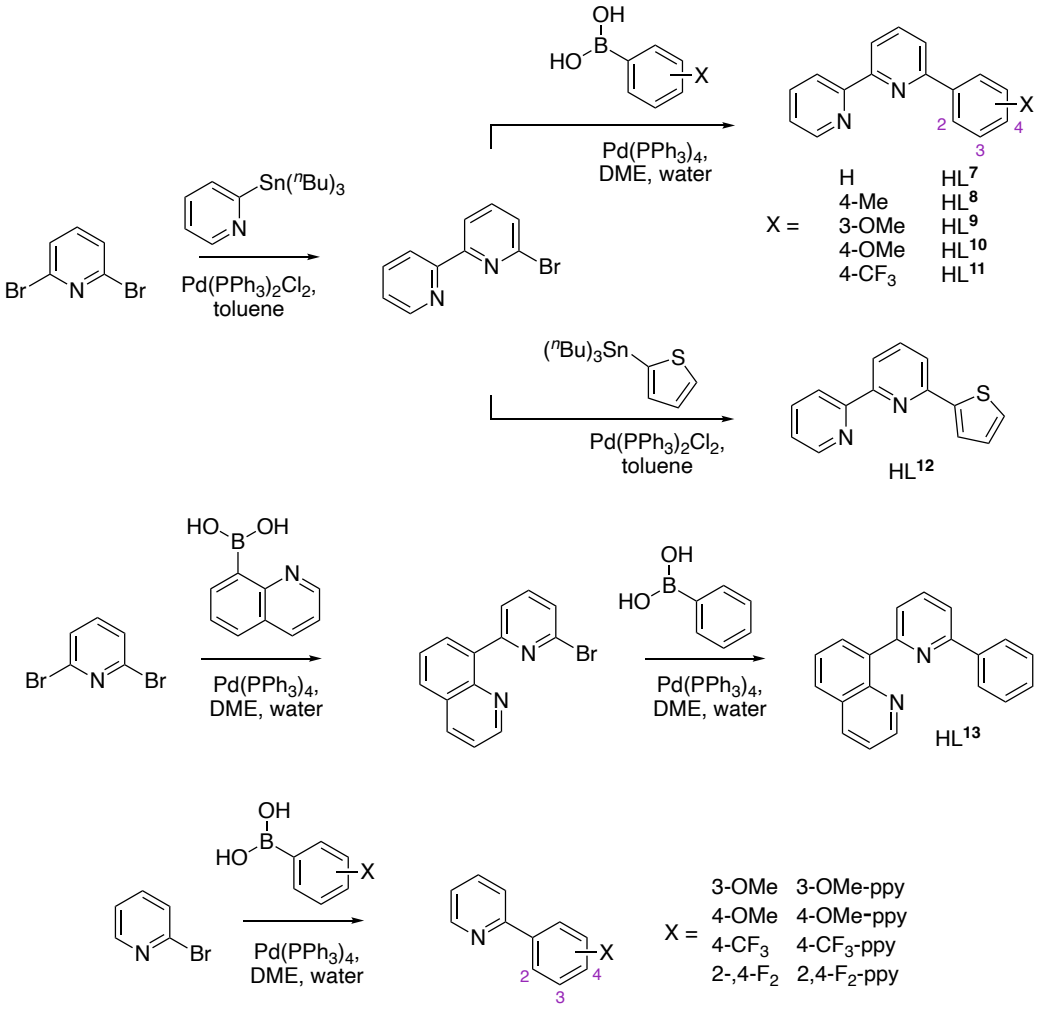

Scheme 3.1: *Synthesis of NNC and NC proligands.*

The *NC* proligands 2-(3-methoxyphenyl)pyridine (3-OMe-ppy), 2-(4-methoxyphenyl)pyridine (4-OMe-ppy) and 2-(2,4-difluorophenyl)pyridine (2,4-F_2-ppy) were prepared by Suzuki cross-coupling reactions with 2-bromopyridine and the corresponding substituted phenylboronic acid through conventional heating in DME/water. 2-[4-(Trifluoromethyl)phenyl]pyridine (4-CF_3-ppy) was synthesised by a microwave-assisted method, in which DME was used as the solvent and $Pd(PPh_3)_4$ as the catalyst.[64] The reaction was heated at 120 °C for 1h. The products were isolated in yields between 66 and 95%.

The proligand HL^{13} binds with the formation of one 5- and one 6-membered chelating ring, whereas the rest of the *NNC* ligands form complexes with two 5-membered chelating rings. Similarly to the ligand azbpy from Chapter 2, HL^{13} may provide bite angles that are close to 180°, which could result in stronger ligand fields and therefore have beneficial luminescence effects.

3.3 Synthesis of Pt^{II} complexes

Two methods were used for the synthesis of PtL^7Cl (Scheme 3.2). The more commonly used method for the preparation of Pt(*NNC*)Cl complexes involves the addition of a degassed aqueous solution of K_2PtCl_4 to a solution of the ligand in degassed CH_3CN and subsequent reflux of the mixture for 24 h.[65] An alternative procedure used acetic acid as the solvent, as in the preparation of Pt(dpyb)Cl in Chapter 2, and we found it to give higher yields of PtL^7Cl and in higher purity (according to the ^1H NMR spectrum). This route was therefore also used for the preparation of all of the other Pt^{II}(*NNC*)Cl complexes (Scheme 3.2).

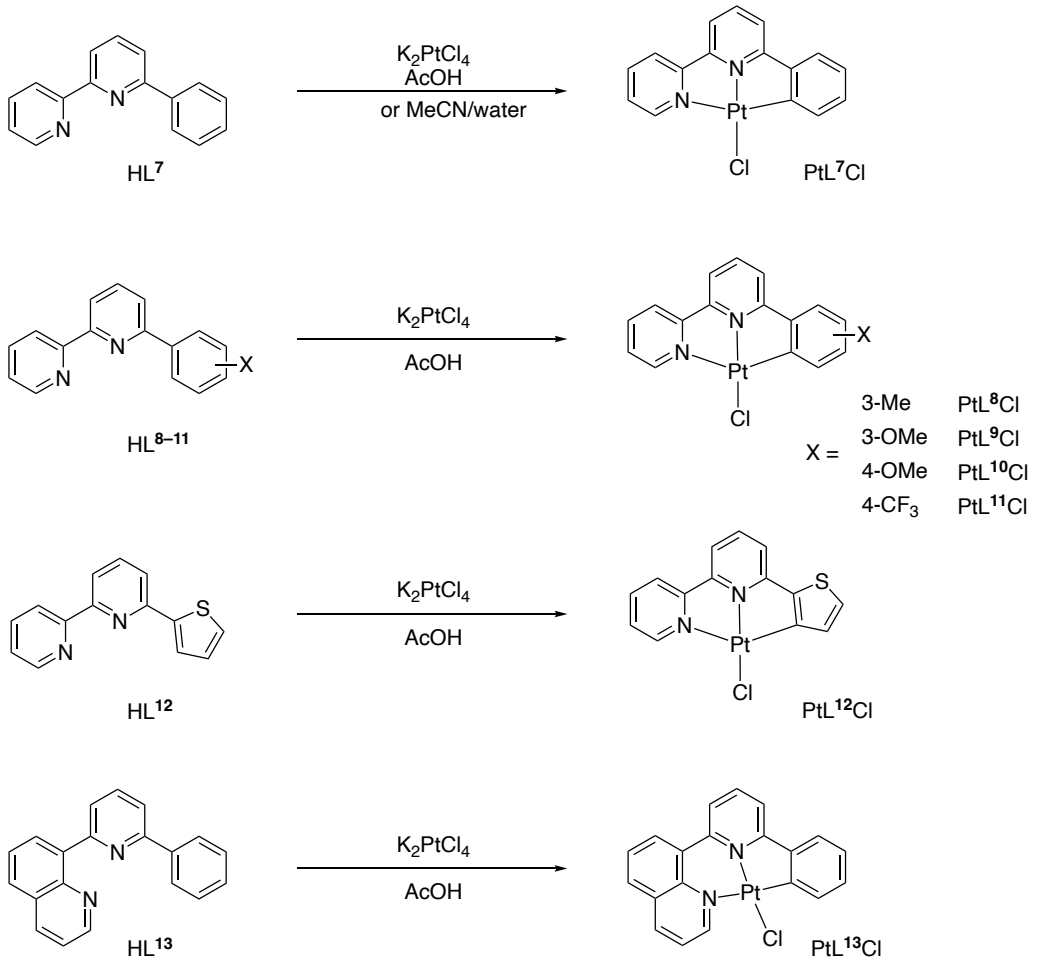

Scheme 3.2: *Synthesis of Pt^{II} complexes.*

Crystals of complexes PtL^9Cl and $PtL^{13}Cl$ were obtained that were suitable for X-ray diffraction by the slow evaporation of a DMSO solution of the respective complex (Figure 3.1). Selected bond lengths and bond angles are summarised in Table 3.2. As anticipated for $PtL^{13}Cl$, which contains one 5- and one 6-membered chelate, the C–Pt–N angle is larger at 173.3(3)°, compared to 161.79(7)°for PtL^9Cl (with two 5-membered chelates).

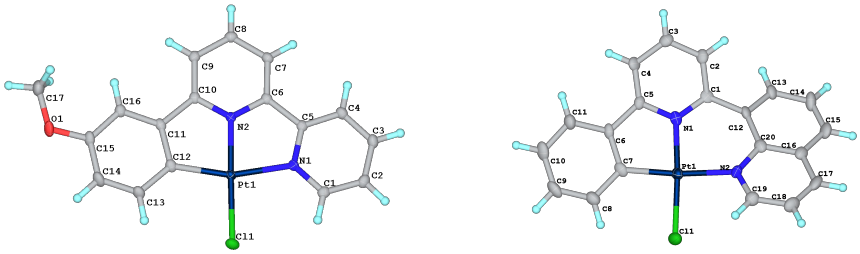

Figure 3.1: *Molecular structures of complexes PtL[9]Cl and PtL[13]Cl.*

Table 3.1: *Selected bond lengths (Å) and bond angles (°) of PtL[9]Cl and PtL[13]Cl.*

	PtL[9]Cl	PtL[13]Cl
Pt – Cl	2.3157(5)	2.300(2)
Pt – N1	2.1067(15)	1.988(6)
Pt – N2	1.9476(15)	2.112(6)
Pt – C	1.9937(19)	1.995(8)
C – Pt – N	161.79(7)	173.3(3)
N – Pt – Cl	178.58(5)	174.3(2)

3.4 Synthesis of Pt^{IV} complexes

3.4.1 Oxidation of Pt^{II} to Pt^{IV}

The complexes PtL[7]Cl, PtL[8]Cl, PtL[11]Cl and PtL[13]Cl were oxidised using chlorine gas, following the same procedure as for the oxidation of Pt(*NCN*)Cl complexes in Chapter 2 (Scheme 3.3). PtL[7]Cl_3 and PtL[13]Cl_3 were isolated in high purity in this way. The corresponding reaction of PtL[8]Cl did lead to the formation of PtL[8]Cl_3, but the ^{1}H NMR spectrum showed the product to be accompanied by a small proportion of a second, related complex. X-ray diffraction analysis of a crystal of PtL[8]Cl_3 subsequently showed that it had co-crystallised with a complex (which we shall refer to as PtL[8Cl]Cl_3) incorporating a chlorine atom in the metalated phenyl ring, at the position *para* to the C–Pt bond. Meanwhile, the attempted oxidation of PtL[9]Cl to PtL[9]Cl_3 by the same procedure gave uniquely the ring-chlorinated product PtL[9Cl]Cl_3 (Scheme 3.3). Metallation of the phenyl ring has been found to activate the CH *para* to the metal in some Ir^{III} bis-tridentate complexes containing *NNC* or *NCN* ligands. For example, treatment of a complex of the type [Ir(*NCN*)(*NNC*)]$^+$ with N-bromosuccinimide (NBS) in CH_3CN at room temperature results in the selective electrophilic bromination of the aryl ring of the *NNC* ligand in that position.[9]

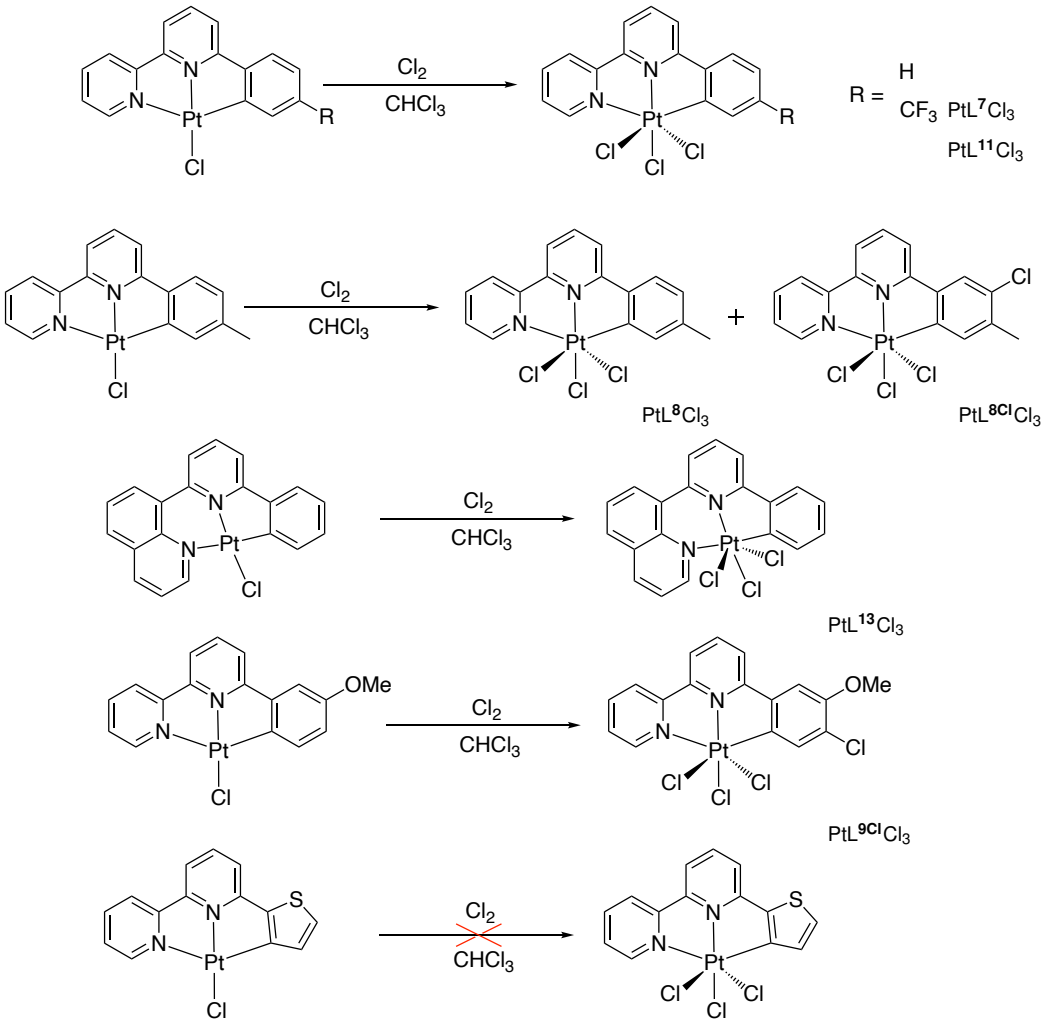

Scheme 3.3: *Oxidation of the Pt^{II} complexes with Cl_2 to generate $Pt^{IV}L^nCl_3$ complexes.*

In an attempt to suppress this competitive halogenation, a different reagent was investigated, namely $PhICl_2$. This compound is a milder oxidant than Cl_2 itself and has been used successfully by others for the oxidation of Pt^{II} to Pt^{IV} compounds, as discussed in Chapter 1.[66] Equimolar amounts of $PtL^{9}Cl$ and $PhICl_2$ were dissolved in the minimum volume of $CHCl_3$ and the mixture was stirred overnight with the partial exclusion of light (Scheme 3.4). This reaction resulted in the successful isolation of the target $PtL^{9}Cl_3$. $PtL^{12}Cl$ and $PtL^{10}Cl$ were also oxidised to $PtL^{12}Cl_3$ and $PtL^{10}Cl_3$ according to this method. While the oxidation of $PtL^{12}Cl$ proceeded cleanly, that of $PtL^{10}Cl$ resulted in the formation of two main products – the target $PtL^{10}Cl_3$, as well as a chlorinated product $Pt^{10Cl}Cl_3$. The two products were separated by column chromatography on silica with hexane / ethyl acetate.

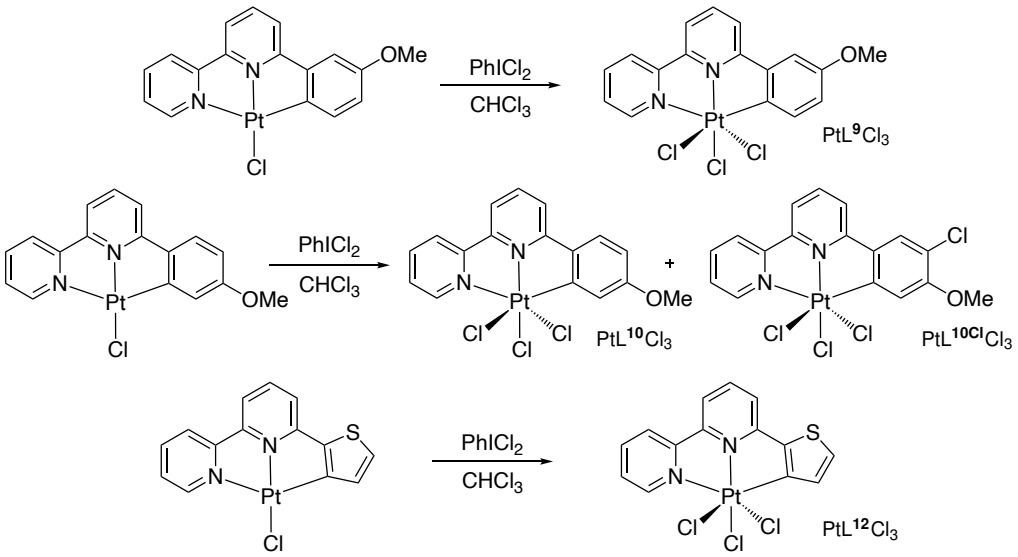

Scheme 3.4: *Oxidation of the Pt^{II} complexes with $PhICl_2$.*

It is possible that the electron-donating methoxy substituent further activates the metallated ring to such an extent that even the milder $PhICl_2$ reagent gives some ring oxidation. However, as some $PtL^{10Cl}Cl$ was also isolated, it is possible that the competitive ring chlorination actually occurs prior to oxidation of Pt. The formation of the Pt^{II} complex $PtL^{10Cl}Cl$ as a by-product of the reaction was suggested by both ^1H NMR and X-ray crystallography (Figure 3.2).

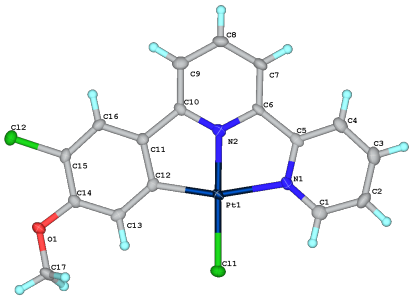

	$Pt^{10Cl}Cl$
Pt – Cl	2.3168(15)
Pt – N1	2.118(5)
Pt – N2	1.948(5)
Pt – C	1.998(6)
C – Pt – N	161.9(2)
N – Pt – Cl	176.40(15)

Figure 3.2: *Molecular structure of complex $Pt^{10Cl}Cl$ (left). Selected bond lengths (Å) and bond angles (°) of $Pt^{10Cl}Cl$ (right).*

The ^{1}H NMR spectra of PtL^{7}Cl and PtL^{7}Cl$_3$ in d$_6$-DMSO are shown in Figure 3.3. A deshielding of all the protons is seen upon oxidation, resulting in a downfield shift of the signals in the ^{1}H NMR spectrum. The J-coupling constants ^{195}Pt-^{1}H^{1} and ^{195}Pt-^{1}H^{2} of the Pt^{IV} complex are both smaller than those in the Pt^{II} parent (e.g., $^{3}J_{^{195}\text{Pt-}^{1}\text{H}^{2}}$ $\approx$ 27 Hz for Pt^{IV}; $^{3}J_{^{195}\text{Pt-}^{1}\text{H}^{2}}$ $\approx$ 43 Hz for Pt^{II}). Both of these effects are consistent with trends reported in the oxidation of Pt^{II} to Pt^{IV} in other complexes, as noted in the introduction. A reduction in the magnitude of coupling constants to ^{195}Pt can be rationalised in terms of the lower s-contribution in the d^{2}sp^{3}-hybridized Pt^{IV} relative to the dsp^{2} Pt^{II} centre.[67,68]

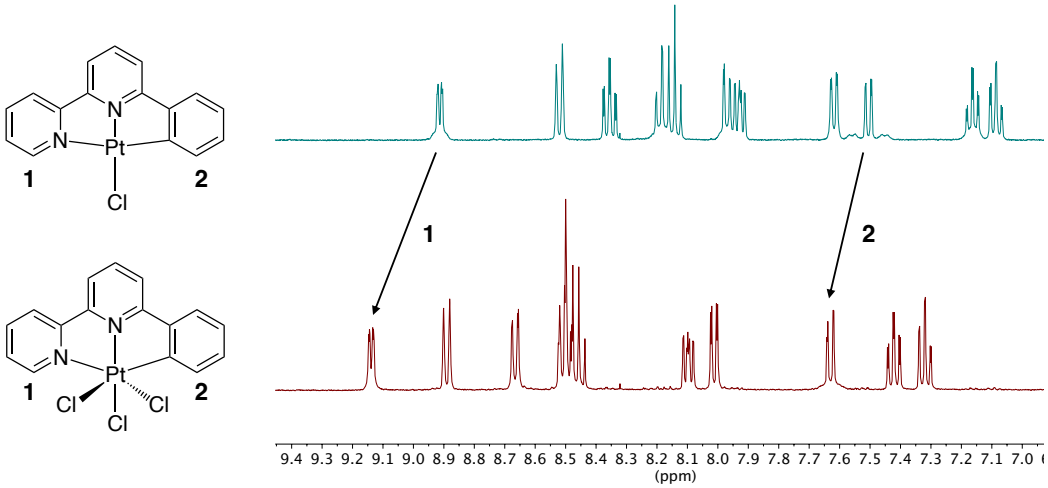

Figure 3.3: *^{1}H NMR spectra of PtL^{7}Cl and PtL^{7}Cl$_3$ in d$_6$-DMSO at 400 MHz. The protons most diagnostic of oxidation are numbered and the arrows highlight the shift upon oxidation*

Crystals suitable for X-ray diffraction of all of the Pt^{IV}Cl$_3$ complexes, apart from PtL^{10}Cl$_3$, were obtained by the slow evaporation of a DMSO solution of the respective complex (Figure 3.4). The crystal structures of the complexes confirmed the +4 oxidation state (neutral molecules with three chloride and one C^{-} ligands attached to the metal centre) and pseudo-octahedral geometries about the metal. Selected bond lengths and bond angles are summarised in Table 3.2.

The *trans*-bond angles Cl–Pt–Cl and N–Pt–Cl are close to linear, whereas N–Pt–C are mostly between 160.86° to 162.03°. The only exception is PtL^{13}Cl$_3$, for which it is closer to linear at 172.49°, reflecting the combination of 5- and 6-membered chelates as discussed earlier.

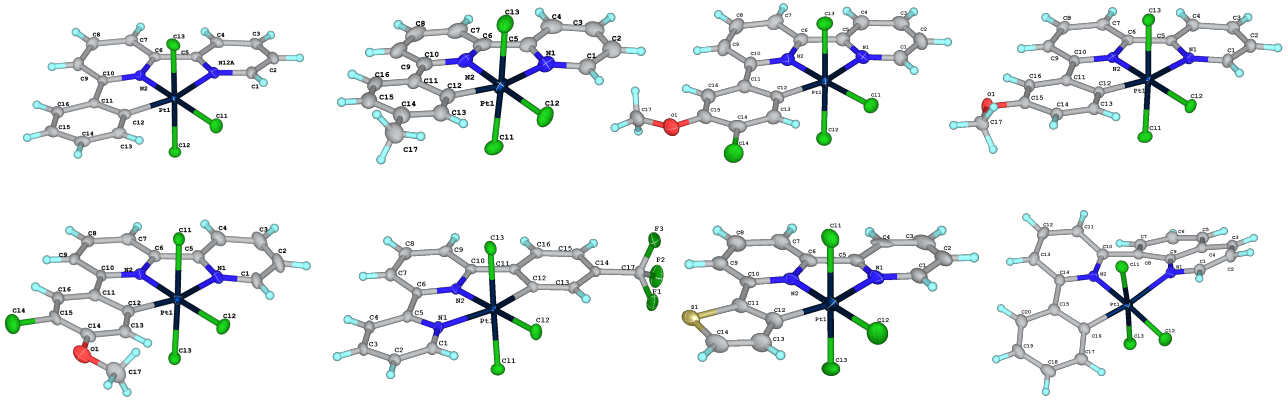

Figure 3.4: *Molecular structures of $Pt^{IV}Cl_3$ complexes.*

Table 3.2: *Selected bond lengths (Å) and bond angles (°) of $Pt^{IV}Cl_3$ complexes.*

	L^7	L^8	L^9	L^{9Cl}	L^{10Cl}	L^{11}	L^{12}	L^{13}
Pt – Cl1	2.3112(5)	2.325(2)	2.3250(6)	2.3146(11)	2.3262(9)	2.3196(8)	2.3218(11)	2.3223(6)
Pt – Cl2	2.3279(5)	2.305(2)	2.3175(6)	2.3034(12)	2.3141(9)	2.3012(8)	2.3108(14)	2.3057(6)
Pt – Cl3	2.3135(5)	2.320(2)	2.3137(6)	2.3228(12)	2.3214(9)	2.3144(8)	2.3200(13)	2.3185(6)
Pt – N1	2.1323(17)	2.167(7)	2.137(2)	2.158(4)	2.143(3)	2.164(3)	2.136(3)	2.168(2)
Pt – N2	1.9747(16)	1.975(6)	1.9649(19)	1.975(4)	1.975(3)	1.975(3)	1.977(4)	2.0101(19)
Pt – C	2.0543(19)	2.013(8)	2.004(2)	2.011(4)	2.007(3)	1.998(3)	2.013(4)	2.000(2)
Cl – Pt – Cl	179.278(18)	177.40(8)	174.68(2)	178.44(4)	178.69(3)	178.09(3)	178.53(5)	176.39(2)
C – Pt – N	161.30(7)	161.9(3)	162.92(9)	160.86(18)	162.03(13)	161.37(11)	160.88(18)	172.49(9)
N – Pt – Cl	177.52(5)	177.1(2)	179.36(6)	177.50(12)	178.29(9)	178.06(8)	179.23(10)	177.47(6)

3.4.2 Synthesis of 3 + 2 + 1 Pt^{IV} complexes with bidentate ligands incorporating 1,2,4-triazole rings

Three complexes of the form [Pt(*NNC-L*^{7})(*NN*)Cl]$^{+}$ were synthesised, where *NN* represents one of the 1,2,4-triazole ring-containing ligands L^{3}, L^{4} or L^{5} from Chapter 2 (Scheme 3.5). Informed by the method developed in Chapter 2 for *NCN* complexes, they were prepared by heating $PtL^{7}Cl_3$ with HL^{3} and 2 equiv. of AgOTf in toluene at 125 °C overnight with the exclusion of light. $[PtL^{7}L^{3}Cl]PF_6$ and $[PtL^{7}L^{5}Cl]PF_6$ required purification by column chromatography on silica with CH_3CN/water/saturated $KNO_{3(aq)}$ as the mobile phase.

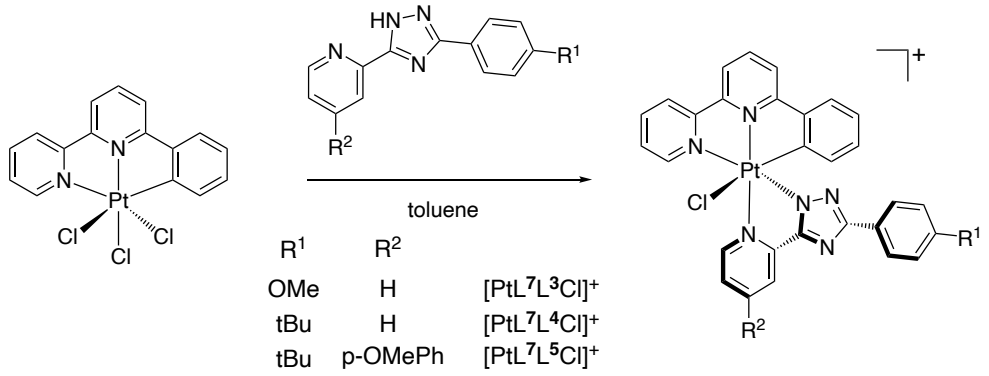

R^1	R^2	
OMe	H	$[PtL^{7}L^{3}Cl]^{+}$
tBu	H	$[PtL^{7}L^{4}Cl]^{+}$
tBu	p-OMePh	$[PtL^{7}L^{5}Cl]^{+}$

Scheme 3.5: *Chemical structures of $[PtL^{7}L^{3}Cl]PF_6$, $[PtL^{7}L^{4}Cl]PF_6$ and $[PtL^{7}L^{5}Cl]PF_6$*

The ^{1}H NMR spectra of $[PtL^{7}L^{3}Cl]PF_6$ and $[PtL^{7}L^{5}Cl]PF_6$ are shown in Figure 3.5. The most deshielded proton is the one closest to the pyridyl nitrogen of the triazole ligand. The electron-donating OMe group leads to an upfield shift of H^{3} (arrow 3). For these complexes, the most shielded proton is the one next to the cyclometallated carbon. Interestingly, while ^{195}Pt coupling to the proton *ortho* to the pyridyl ring of the triazole ligand could not be seen for the complexes with a tridentate *NCN* dpyb ligand (Chapter 2, Figure 2.6), very pronounced satellites are observed for the complexes with the tridentate *NNC* ligand L^{7} ($^{3}J_{^{195}Pt\text{-}^{1}H} \approx 26$ Hz for protons 1 and $^{3}J_{^{195}Pt\text{-}^{1}H} \approx 25$ Hz for protons 2).

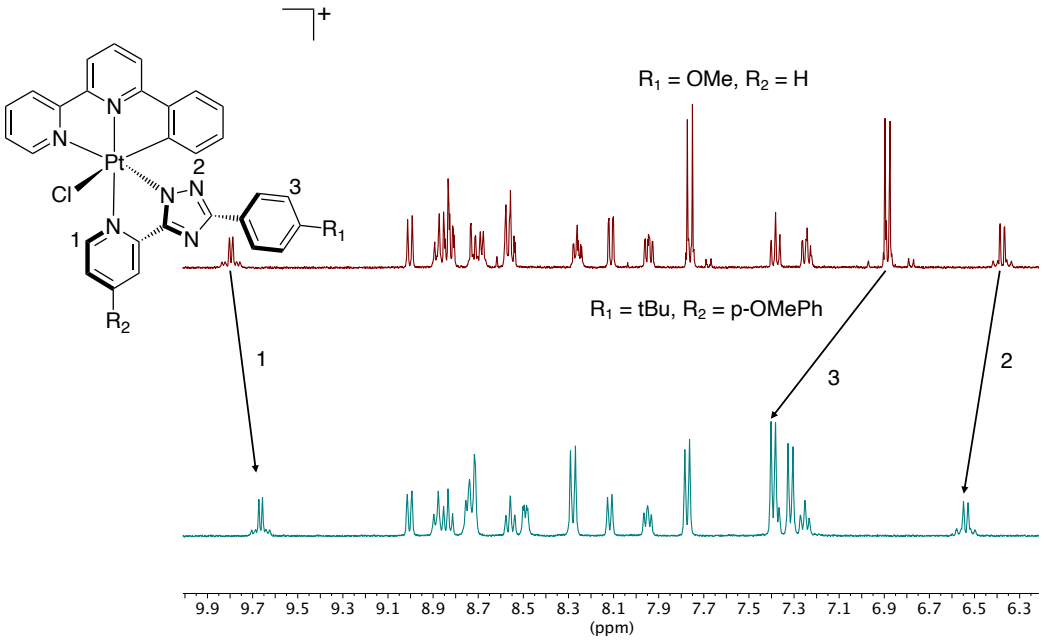

Figure 3.5: *Aromatic region of ^{1}H NMR spectra of $[PtL^{7}L^{3}Cl]PF_6$ and $[PtL^{7}L^{5}Cl]PF_6$ in d_6-acetone. Most relevant protons are numbered and arrows show the shift upon change of R_1 and R_2.*

3.4.3 Synthesis of 3 + 2 + 1 Pt^{IV} complexes with 2,2'-bipyridine and of bis-tridentate complexes with 2,2';6',2''-terpyridine

$[PtL^{7}(bpy)Cl]^{2+}$ and $[PtL^{7}(tpy)]^{3+}$ were both successfully synthesised according to the general procedure described previously, but using 3 equiv. of AgOTf in the case of $[PtL^{7}(tpy)]^{3+}$ to aid the abstraction of all three chloride ligands.

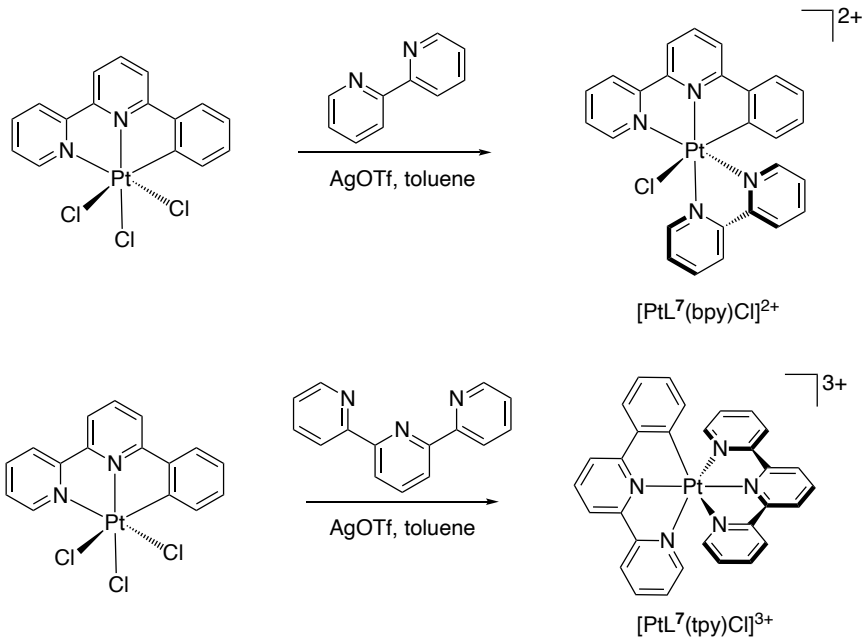

Figure 3.6: *Chemical structures of $[PtL^{7}(bpy)Cl]^{2+}$ and $[PtL^{7}(tpy)]^{3+}$ complexes.*

A single crystal of $[PtL^7(bpy)Cl][PF_6]_2$ suitable for X-ray diffraction was obtained by the slow diffusion of diethyl ether into an acetone solution of the complex (Figure 3.7). The complex co-crystallised with a molecule of acetone per complex.

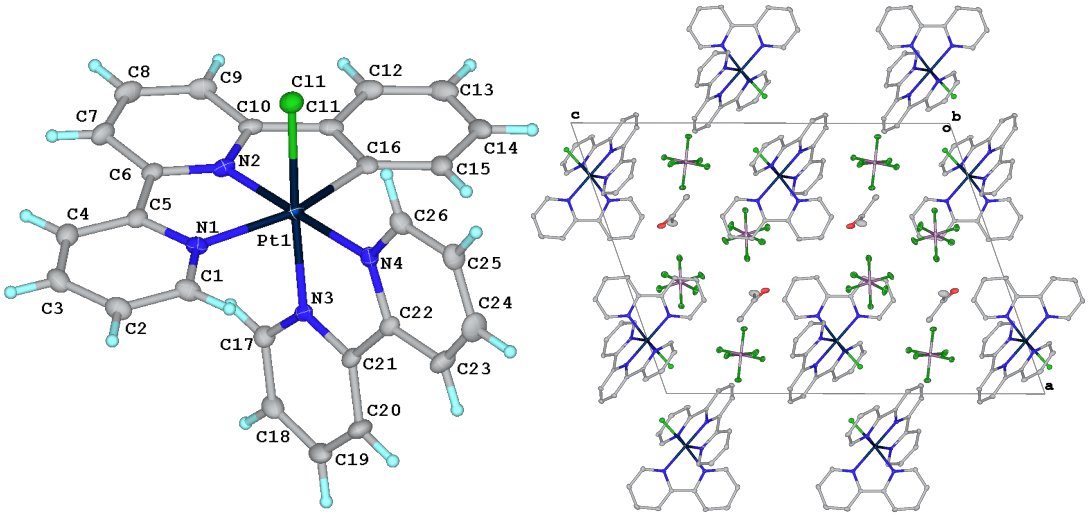

Figure 3.7: *Molecular structure of cation and crystal packing of* $[PtL^7(bpy)Cl][PF_6]_2$

Selected bond lengths and bond angles are summarised in Table 3.3. The complex shows pseudo-octahedral geometry about the metal. The Pt–N bond to the nitrogen of the central pyridine of the phbpy ligand is the shortest bond to Pt at 1.985(4) Å, consistent with what is observed across the series of $Pt^{IV}(NNC)Cl_3$ complexes.

Table 3.3: *Selected bond lengths (Å) and bond angles (°) of* $[PtL^7(bpy)Cl][PF_6]_2$

Bond	Bond Length / Å	Bond Angle	Bond Angle / °
Pt – Cl	2.2861(12)	N – Pt – N	178.65(16)
Pt – N1	2.109(4)	N – Pt – Cl	174.91(11)
Pt – N2	1.985(4)	C – Pt – N	160.79(16)
Pt – N3	2.037(4)		
Pt – N4	2.034(3)		
Pt – C	2.091(4)		

A crystal suitable for X-ray diffraction was also obtained for $[PtL^{7}(tpy)][OTf]_3$ by the slow diffusion of diethyl ether into an CH_3CN solution of the complex. However, the structure has generic disorder, arising from the similarity of terpyridine and phenylbipyridine ligands, and it could not serve as definitive proof of identity. The disorder in the crystal of the bis-tridentate complex motivated the synthesis of a modified complex with an added substituent on one of the ligands in the hope of overcoming the disorder by making the ligands 'more different'. An *in-situ* bromination reaction was first attempted as a potentially easy way to access a modified complex (Scheme 3.6). As mentioned before, some bis-tridentate Ir^{III} complexes with *NNC* ligands have been found to undergo bromination at the position para to the metallated carbon under very mild conditions when reacted with NBS.[9,69] $[PtL^{7}(tpy)][PF_6]_3$ and NBS were dissolved in CD_3CN. The deuterated solvent was used in order to allow the reaction to be monitored conveniently by ^1H NMR. Unfortunately, no reaction was observed upon stirring for 24 hours, nor after adding an excess of NBS and heating for a further 24 hours, or heating in a microwave for 30 minutes. Evidently, the high positive charge on the Pt^{IV} complex, compared to Ir^{III} systems, deactivates the metallated ring to electrophilic bromination.

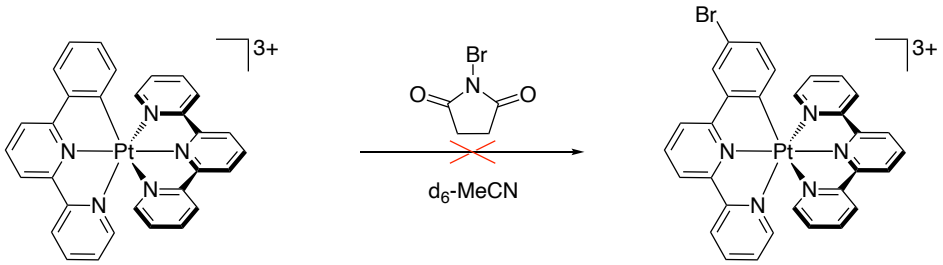

Scheme 3.6: *Attempted in situ-bromination of $[PtL^{7}(tpy)][PF_6]_3$*

We therefore prepared the tolylbipyridine analogue of $[PtL^{7}(tpy)][PF_6]_3$, as it would contain a tolyl rather than a phenyl group, thus rendering the *NNC* and *NNN* ligand 'more different' from one another in the crystal. The reaction of $PtL^{8}Cl_3$ with tpy according to the general procedure afforded the complex $[PtL^{8}(tpy)][PF_6]_3$ (Scheme 3.7).

A single crystal suitable for X-ray diffraction was obtained by the slow evaporation of an acetone solution of the complex (Figure 3.8). Along with the *NCN* systems reported in Figure 2.9, we believe it to be the first structurally characterised example of any Pt^{IV} complex in which the metal ion is bound by two tridentate ligands.

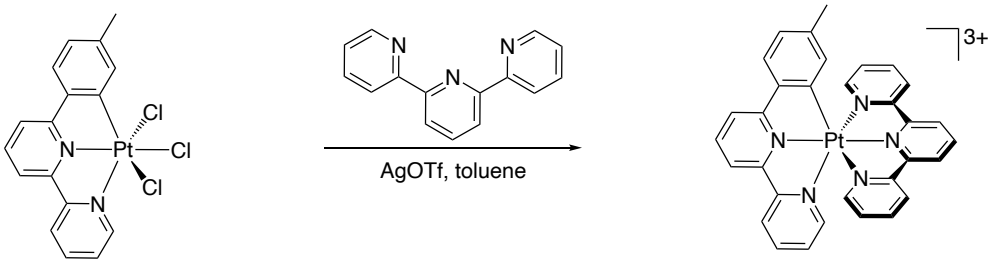

Scheme 3.7: *Chemical structure of [PtL^{8}(tpy)][PF$_6$]$_3$*

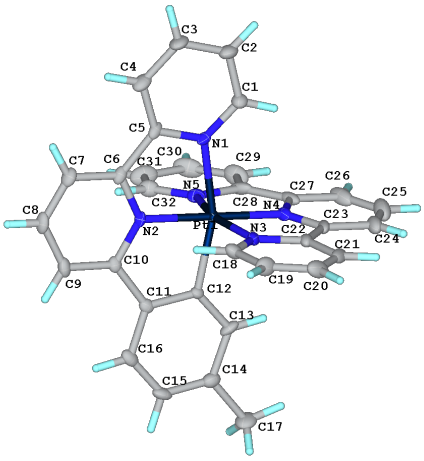

	[PtL^{8}(tpy)][PF$_6$]$_3$
Pt – N1	2.148(7)
Pt – N2	1.995(8)
Pt – C	2.043(9)
Pt – N3	2.054(9)
Pt – N4	1.958(8)
Pt – N5	2.043(9)
C – Pt – N1	160.5(3)
N2 – Pt – N4	179.1(4)
N3 – Pt – N5	161.7(3)

Figure 3.8: *Molecular structure of the cation of [PtL^{8}(tpy)][PF$_6$]$_3$ with selected bond lengths (Å) and bond angles (°) tabulated.*

3.4.4 Synthesis of Pt^{IV} complexes containing an *NNC* ligand and a second cyclometallating ligand

Synthesis of 3 + 2 + 1 Pt^{IV} complexes

Five 3 + 2 + 1 Pt^{IV} complexes with an *NNC* tridentate, an *NC* bidentate and one monodentate chloride ligand were prepared by reacting a Pt(*NNC*)Cl$_3$ complex with an *NC*H proligand in toluene in the presence of AgOTf (Figure 3.9). The complexes were isolated in low yields between 4% and 14%.

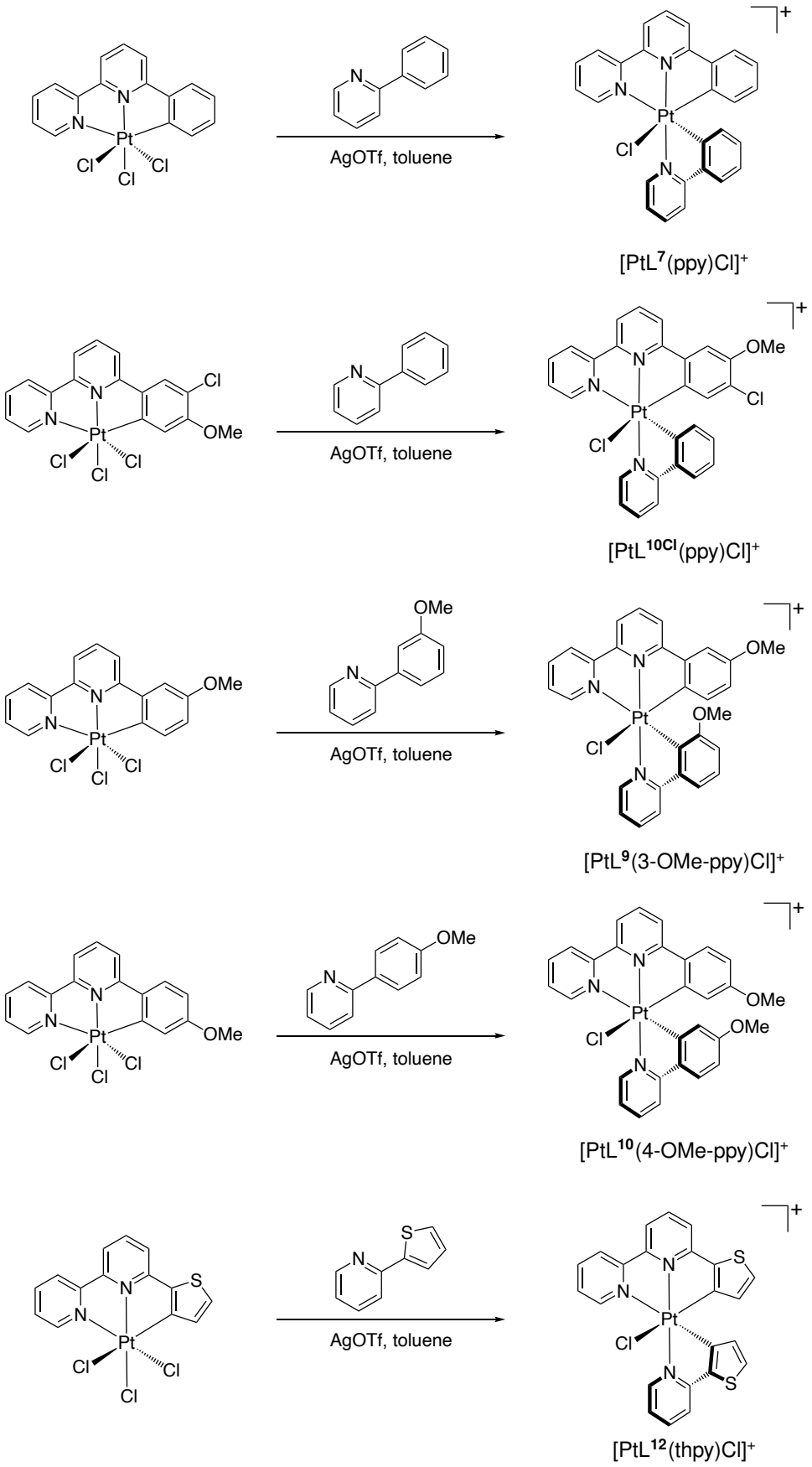

Figure 3.9: *Synthesis of complexes [PtL^{7}(ppy)Cl]$^{+}$, [PtL^{10Cl}(ppy)Cl]$^{+}$, [PtL^{9}(3-OMe-ppy)Cl]$^{+}$, [PtL^{10}(4-OMe-ppy)Cl]$^{+}$ and [PtL^{12}(thpy)Cl]$^{+}$.*

[Pt^{7}(ppy)Cl]PF_6 and [Pt^{10Cl}(ppy)Cl]PF_6 were purified by gradient column chromatography on silica with CH_3CN / water / saturated aqueous KNO_3 as the mobile phase. [PtL^{9}(3-OMe-ppy)Cl]PF_6 was purified by gradient reverse phase column chromatography on C18 silica with water / CH_3CN as the mobile phase. The purification of [PtL^{10}(4-OMe-ppy)Cl]PF_6 involved multiple fractional precipitations from DCM / diethyl ether. The attempted synthesis of [PtL^{12}(thpy)Cl]$^+$ upon reaction of PtL$^{12}Cl_3$ with 2-thienylpyridine (thpyH) under the same conditions did lead to a pure sample of the desired product, confirmed by X-ray crystallography, but it proved to be unstable in solution, probably through dissociation of the chloride ligand (further discussed later).

Single crystals suitable for X-ray diffraction were obtained for all the complexes (Figure 3.10). They crystallise in centrosymmetric space groups ($P2_1/c$ for [PtL^{7}(ppy)Cl]OTf and $P\bar{1}$ for the others) and the crystals thus comprise a racemic mixture of the two enantiomers of each complex.

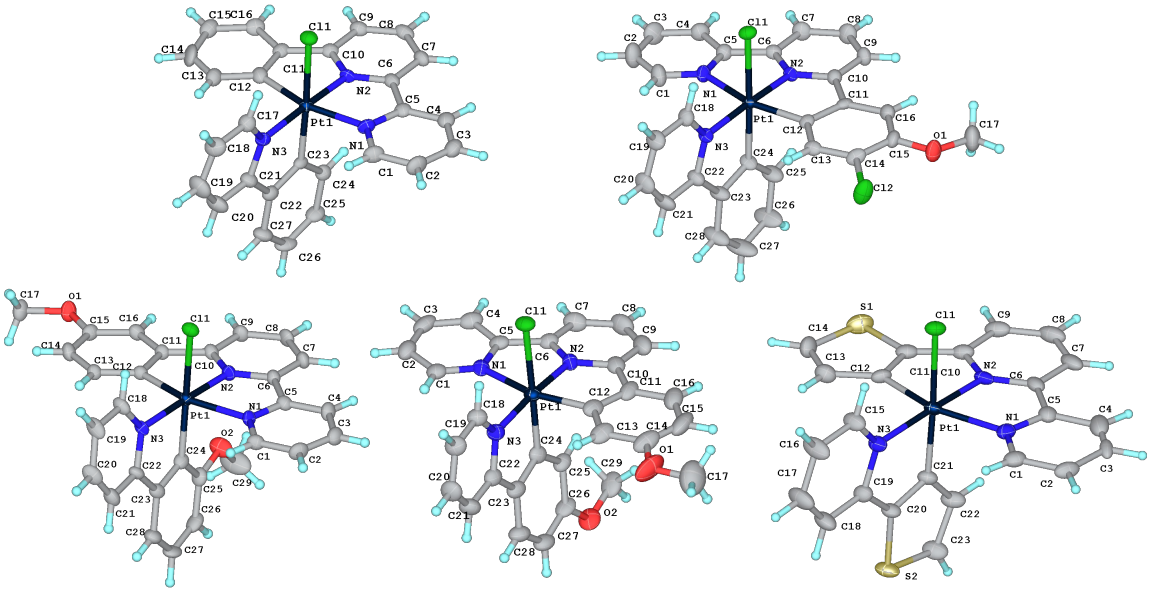

Figure 3.10: *Molecular structures of [PtL^{7}(ppy)Cl]$^+$, [Pt^{10Cl}(ppy)Cl]$^+$, [PtL^{9}(3-OMe-ppy)Cl]$^+$, [PtL^{10}(4-OMe-ppy)Cl]$^+$ and [PtL^{12}(thpy)Cl]$^+$.*

Each structure shows the expected pseudo-octahedral geometry around the Pt^{IV} centre, with the plane of the bidentate *NC* ligand perpendicular to that of the tridentate *NNC* ligand, and with the coordination number of 6 being completed by the monodentate chloride. In each case, the conclusions from ^{1}H NMR as to the orientation of the *NC* ligand are confirmed: the pyridyl ring of the *NC* ligand is bound *trans* to the pyridyl

Table 3.4: *Selected Bond Lengths (Å) and Angles (deg) for [Pt(NNC)(NC)Cl]⁺ Complexes*

	[PtL^{7}(ppy)Cl]$^{+a}$	[Pt^{10Cl}(ppy)Cl]$^{+b}$	[PtL^{9}(3-OMe-ppy)Cl]$^{+a}$	[PtL^{10}(4-OMe-ppy)Cl]$^{+b}$	[PtL^{12}(thpy)Cl]$^{+b}$
Pt–C^{NNC}	2.089(5)/2.067(4)	1.996(6)	2.027(6)	2.018(4)	2.021(7)
Pt–N1$^{\underline{N}NC}$ (lateral)	2.067(4)/2.089(5)	2.141(5)	2.154(5)	2.134(4)	2.124(6)
Pt–N2$^{N\underline{N}C}$ (central)	1.972(4)	1.962(5)	1.983(5)	1.965(4)	1.981(6)
Pt–C^{NC}	2.013(4)	2.031(6)	2.035(6)	2.015(4)	2.014(7)
Pt–N^{NC}	2.037(4)	2.035(5)	2.046(4)	2.046(4)	2.048(6)
Pt–Cl	2.417(1)	2.4232(13)	2.4199(14)	2.427(1)	2.4121(17)
N1$^{\underline{N}NC}$–Pt–C^{NNC}	160.70(18)	161.7(2)	161.0(2)	161.20(17)	159.6(3)
N2$^{N\underline{N}C}$–Pt–C^{NNC}	80.40(16)/80.34(17)	82.1(2)	82.2(2)	81.89(16)	81.0(3)
N2$^{N\underline{N}C}$–Pt–N1$^{\underline{N}NC}$	80.34(17)/80.40(16)	79.65(19)	78.81(19)	79.33(15)	78.6(3)
N2$^{N\underline{N}C}$–Pt–N^{NC}	176.44(15)	174.77(19)	178.0(2)	176.49(15)	174.7(2)
N1$^{\underline{N}NC}$–Pt–Cl	90.46(12)/90.02(12)	86.96(13)	88.12(14)	88.20(11)	89.57(17)
N^{NC}–Pt–C^{NC}	80.84(17)	81.3(2)	80.7(2)	81.28(17)	81.1(3)
N^{NC}–Pt–Cl	96.01(12)	95.46(14)	93.62(14)	95.51(11)	94.26(18)
C^{NC}–Pt–Cl	176.74(13)	176.59(17)	173.01(18)	176.73(14)	175.2(2)

[a] Trifluoromethanesulfonate salt. [b] Hexafluorophosphate salt.

ring of the *NNC* ligand, with the phenyl ring of the *NC* ligand metallated *trans* to the chloride ligand. The preference for this isomer probably arises from the relative *trans* influences of the ligating atoms, namely, $C^- > N > Cl$.[70]

It is worth noting that for $[PtL^9(3\text{-OMe-ppy})Cl]^+$ the bidentate ligand exclusively binds in a mode that is different from that of the tridentate ligand. The OMe group on the phenyl ring of the tridentate ligand is *para* to the Pt centre, whereas that of the bidentate ligand is *ortho* to the Pt centre. This is also evident in the NMR spectra of the complex (Figure 3.11).

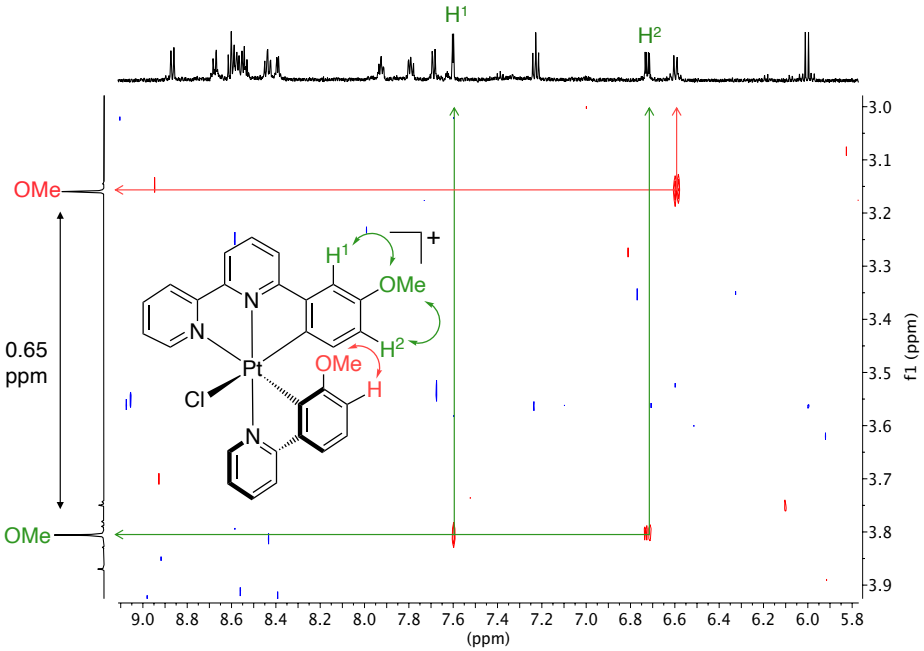

Figure 3.11: *A region of the NOESY NMR spectrum of $[PtL^9(3\text{-OMe-ppy})Cl][PF_6]$, showing the OMe region of the ^1H NMR on the left and the aromatic region along the top. The OMe groups and the protons on the phenyl ring with which the OMe protons are coupling are shown in red for the bidentate and in green for the tridentate ligand. The same colour arrows show the corresponding cross peaks in the NOESY spectrum.*

The ^1H NMR spectrum shows a big difference in the shift of the OMe protons of the tridentate and bidentate ligand at 3.81 ppm and 3.16 ppm, respectively. A much smaller difference in shift is seen for $[PtL^{10}(4\text{-OMe-ppy})Cl]^+$, where they appear at 3.67 ppm and 3.59 ppm, respectively. The upfield shift of the OMe protons on the bidentate ligand is a result of a shielding effect from the ring current of the central aromatic pyridine ring of the tridentate ligand, which is in the plane perpendicular to the ring that the OMe protons are in. The NOESY spectrum also shows two cross-peaks for the OMe protons of the tridentate ligand coupling to the protons on the carbons *meta* to the Pt centre, and only one cross peak in the case of the bidentate

ligand, for the coupling of the OMe protons with the protons on the carbon *para* to the pyridine ring.

The complex [PtL^{12}(thpy)Cl]$^+$ was successfully isolated at first, but new peaks started to appear in its ^{1}H NMR spectrum after one day in acetone-d_6 solution (Figure 3.12). After a few days, all of the original peaks had disappeared and the newly appeared peaks had replaced them. The integrals were still consistent with those that would be expected for the target complex (assignment shown in Figure 3.12). A possible explanation for the change in the spectrum could be that the monodentate Cl ligand is replaced by another species, e.g., by a solvent molecule. The labilisation of the Pt–Cl bond is possibly a result of the high *trans* influence of the cyclometallating carbon of the *NC* ligand. Similar behaviour has been observed for Ir(*NCN*)(*NC*)Cl complexes in a range of solvents, in a process that appears to be accelerated by visible light.[55]

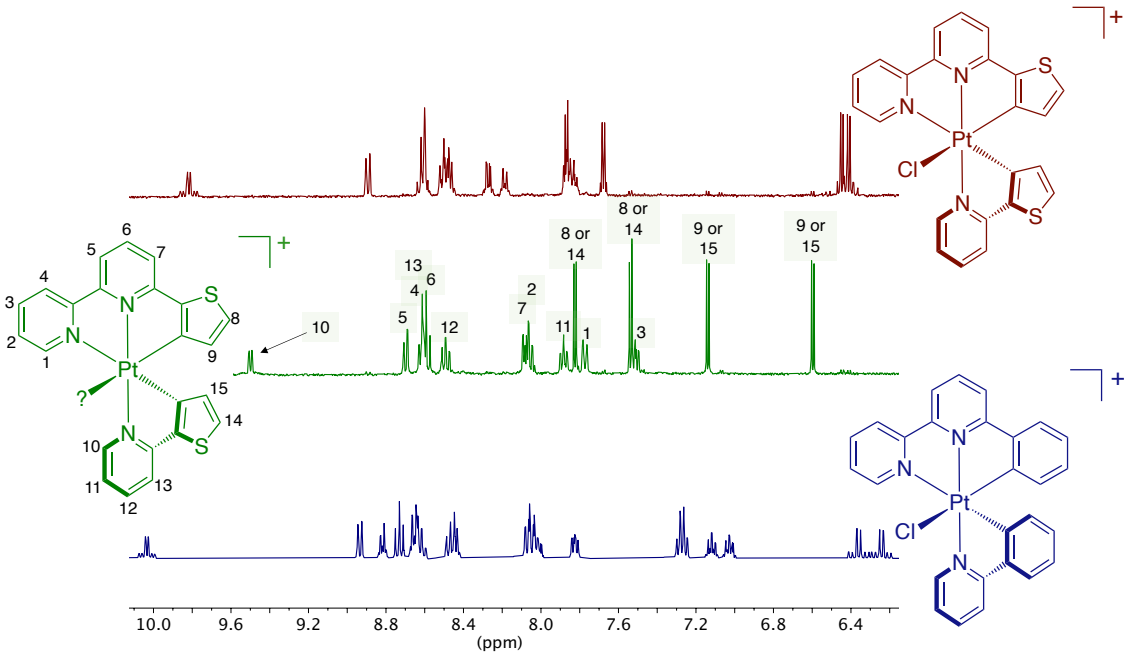

Figure 3.12: *^{1}H NMR spectra of [PtL^{12}(thpy)Cl]$^+$ when initially synthesised (red) and after a few days (green). The ^{1}H NMR spectrum of [PtL^7(ppy)Cl]$^+$ (blue) is also included for comparison.*

The synthesis of $[PtL^{11}(4\text{-}CF_3\text{-}ppy)Cl]^+$ containing one electron-withdrawing CF_3 group on the phenyl rings of each of the two ligands was also attempted (Scheme 3.8). The ^1H NMR and mass spectra indicated some formation of the complex, but it was not possible to isolate a pure sample.

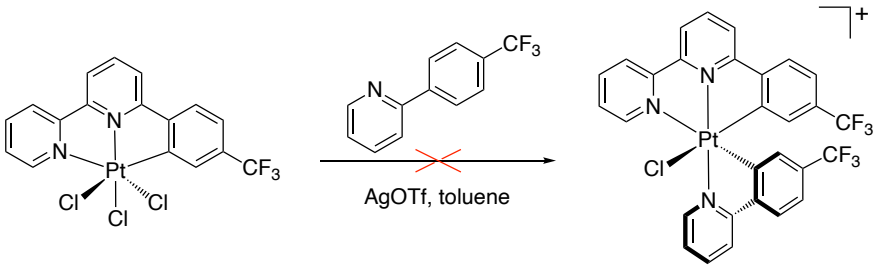

Scheme 3.8: *Attempted synthesis of $[PtL^{11}(4\text{-}CF_3\text{-}ppy)Cl]^+$.*

Synthesis of bis-tridentate Pt^{IV} complexes

The homoleptic complex $[PtL^7{}_2]^{2+}$ containing two *NNC*-coordinated phenylbipyridines was synthesised by reaction of PtL^7Cl_3 with HL^7 in the presence of 3 equiv. AgOTf according to the general procedure (Scheme 3.9). The complex was purified by column chromatography on alumina with CH_3CN/water/saturated $KNO_{3(aq)}$ as the mobile phase, followed by three recrystallisations from acetone / diethyl ether solution. To the best of our knowledge, this is the first example of a bis-cyclometallated bis-tridentate Pt^{IV} complex. The ^1H NMR spectrum of $[PtL^7{}_2]^{2+}$ is shown in Figure 3.9. An upfield shift is observed for the protons next to the lateral pyridyl ring due to shielding from the ring current effect of the central pyridine ring that they lie above. Satellites due to coupling with ^{195}Pt are seen for the protons next to the lateral pyridyl and next to the cyclometallated carbon with $^3J_{^{195}Pt\text{-}^1H} \approx 12$ Hz and $^3J_{^{195}Pt\text{-}^1H} \approx 34$ Hz, respectively. The high-resolution electrospray mass spectrum in Scheme 3.9 shows the isotope pattern corresponding to $[PtL^7{}_2]^{2+}/2$, which closely matches the simulated one (m/z = 328.0712 for $[M]^{2+}/2$; calcd for $[C_{32}H_{20}N_4{}^{194}Pt]^{2+}/2$ = 328.0736).

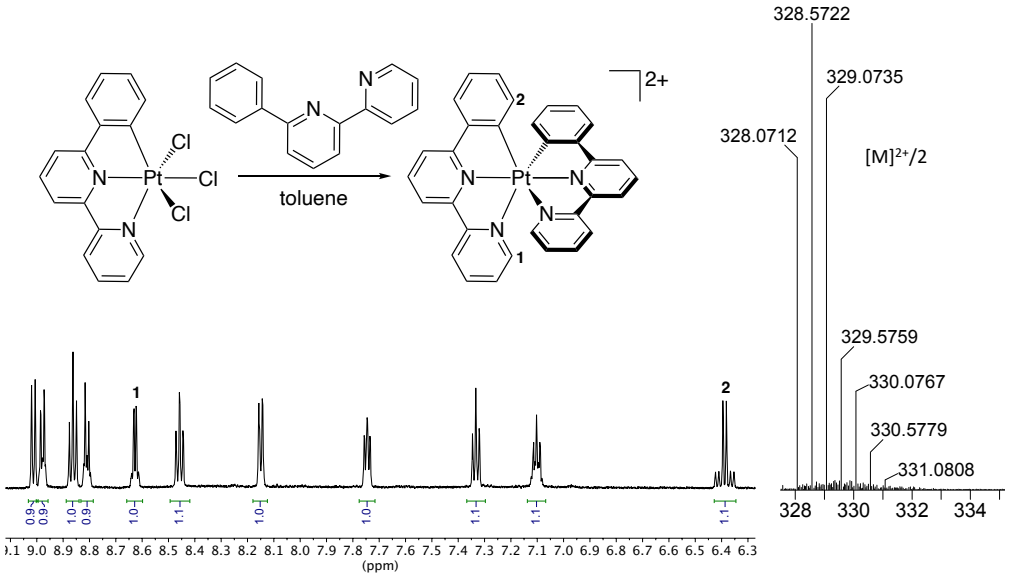

Scheme 3.9: *Synthesis of $[PtL^{7}_{2}]^{2+}$ (top left); the ^{1}H NMR spectrum of $[PtL^{7}_{2}]^{2+}$ in d_6-acetone with numbers showing two diagnostic protons and their corresponding peaks in the spectrum (bottom left); isotope pattern from an accurate mass experiment corresponding to $[PtL^{7}_{2}]^{2+}$/2 (right)*

The synthesis of related hompleptic complexes with other *NNC* ligands was also attempted (Scheme 3.10). There was no indication of the formation of $[PtL^{12}_{2}]^{2+}$ in either the ^{1}H NMR or mass spectrum. In the case of $[PtL^{9}_{2}]^{2+}$, the outcome was somewhat unclear.

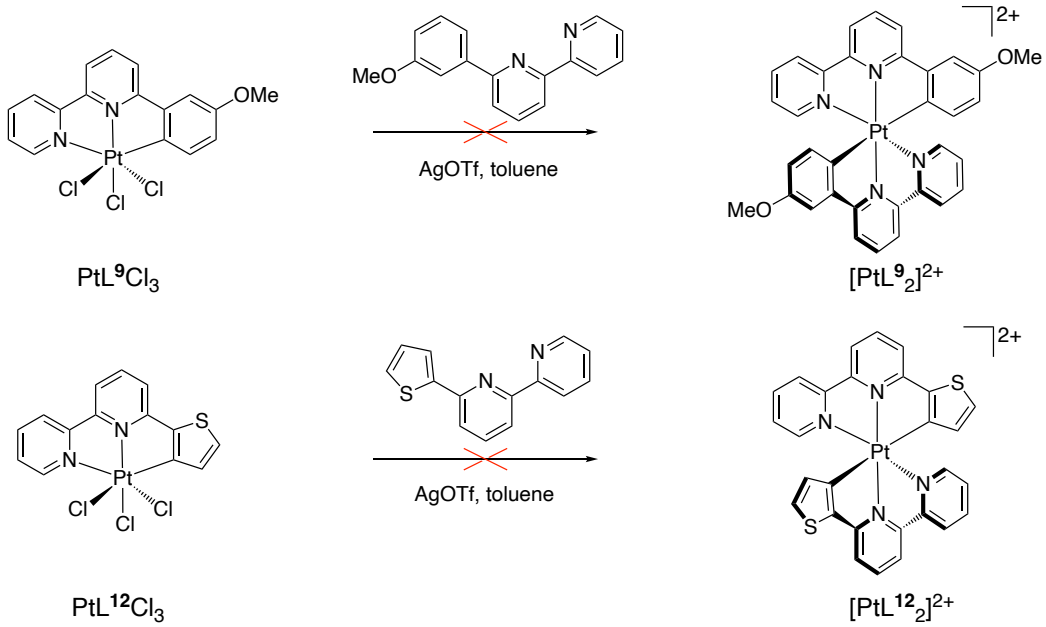

$PtL^{9}Cl_3$ $[PtL^{9}_{2}]^{2+}$

$PtL^{12}Cl_3$ $[PtL^{12}_{2}]^{2+}$

Scheme 3.10: *Attempted synthesis of $[PtL^{9}_{2}]^{2+}$ and $[PtL^{12}_{2}]^{2+}$.*

Figure 3.13 shows the ^{1}H NMR spectrum of the material isolated, together with that of $[PtL^{7}_2]^{2+}$ for comparison. The shifts for the protons do seem to indicate the formation of a compound related to $[PtL^{7}_2]^{2+}$. Nonetheless, the integrals do not add up to the expected number of protons and thus the spectrum suggests the formation of a mixture of related compounds. Two different products could be forming depending on the preference for the second ligand to bind through the carbon that is either *ortho* or *para* to the OMe group (the two modes of binding are shown in Figure 3.13). The ESI$^+$ mass spectrum of $[PtL^{9}_2]^{2+}$ showed a peak at *m/z* 358, which would be expected for either of these isomeric structures, corresponding to $[M]^{2+}/2$. Attempts to isolate a single product by recrystallisation or column chromatography were unsuccessful.

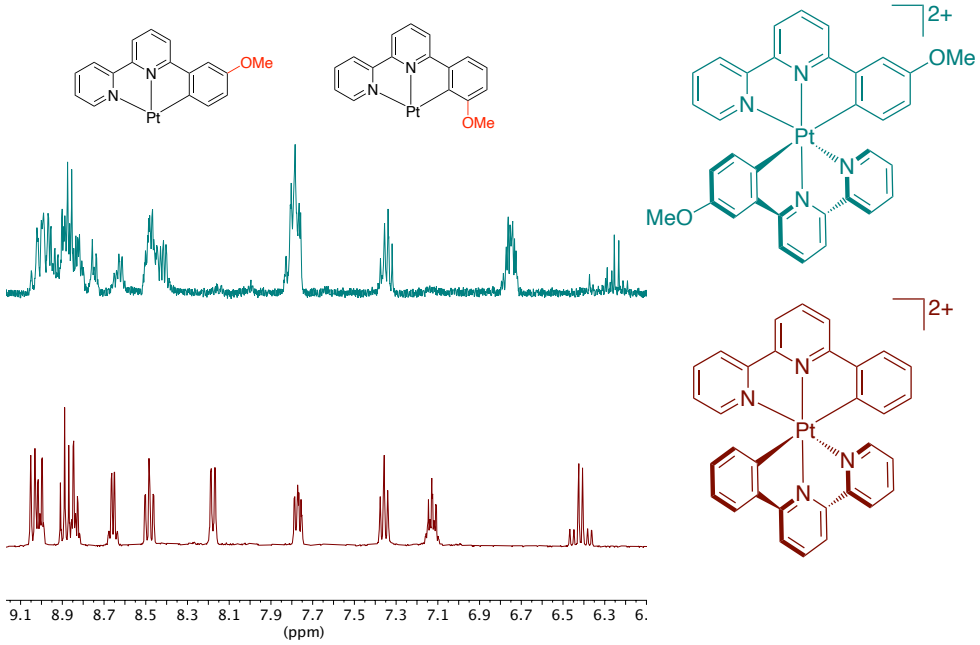

Figure 3.13: *^{1}H NMR spectra of $[PtL^{9}_2]^{2+}$ (green) and of $[PtL^{7}_2]^{2+}$ (red) reproduced from Scheme 3.9 for comparison. The two possible NNC modes of binding of L^{9} are shown at the top of the figure.*

Given the ambidentate nature of the *meta*-methoxy phenylbipyridine derivative, the corresponding *para*-methoxy isomer was targeted instead (Scheme 3.11) together with the *p*-CF_3 analogue. There is only one possible site of metallation in these ligands. The attempt to prepare $[PtL^{10}_2]^{2+}$ resulted in the isolation of a 3 + 2 + 1 type product (confirmed by ^{1}H NMR), for which the central pyridine ring of one of the ligands is *trans* to the terminal pyridine ring of the other ligand, such that the phenyl ring is not in the right position to metallate. It is reminiscent of structure (b) in Figure 2.12 in Chapter 2. In an attempt to force the cyclometallation to occur, Na_2CO_3 base was

added to an CH_3CN solution of this product and the mixture was heated to 50 °C for 5 days. Purification by multiple fractional precipitations led to the isolation of a small amount (< 1 mg) of the target bis-tridentate product. Efforts were made to prepare more of this complex, but proved unsuccessful. Meanwhile, $[PtL^{11}{}_2]^{2+}$ could not be isolated.

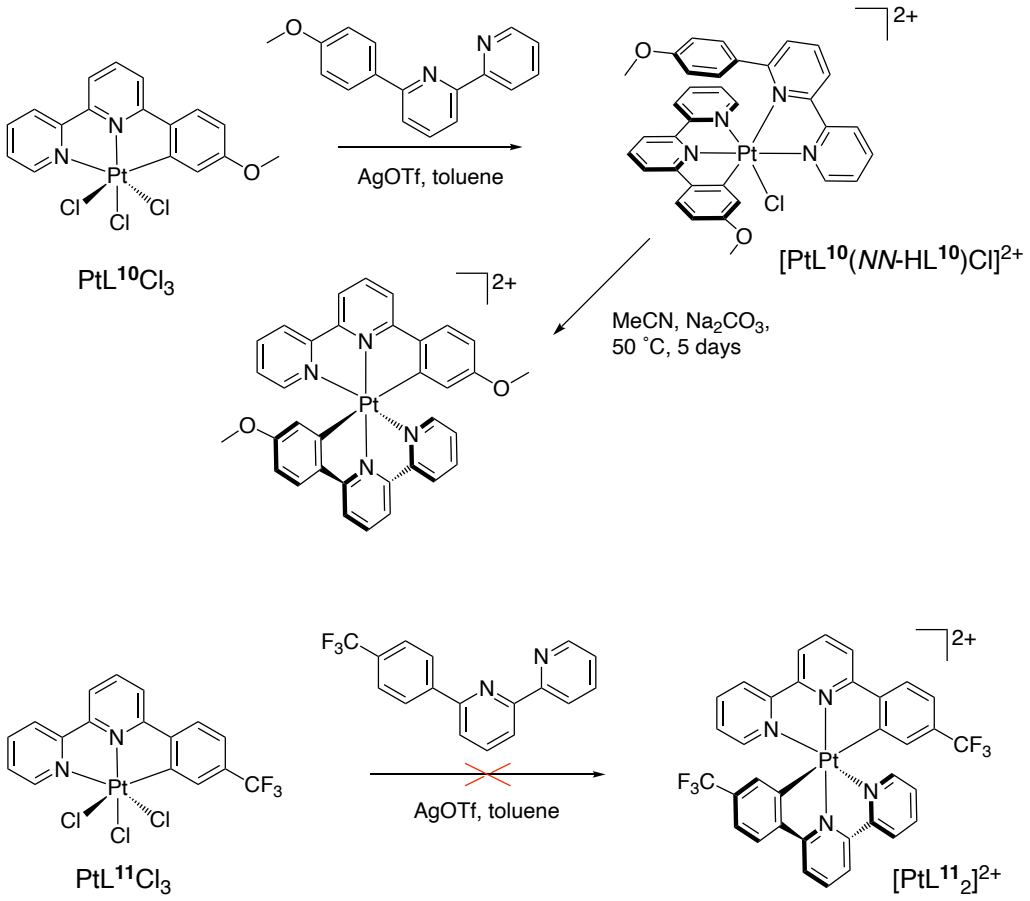

$PtL^{10}Cl_3$ $[PtL^{10}(NN\text{-}HL^{10})Cl]^{2+}$ $PtL^{11}Cl_3$ $[PtL^{11}{}_2]^{2+}$

Scheme 3.11: *Synthesis of* $[PtL^{10}{}_2]^{2+}$ *and* $[PtL^{11}{}_2]^{2+}$.

3.4.5 Photophysical properties

Pt^{II} complexes

While a variety of Pt(*NNC*)Cl complexes have been investigated in the literature, there has been no systematic study of the influence of substituents in the aryl ring on the photophysical properties, nor have luminescence data for most of the *NNC* Pt^{II} complexes, used as precursors here, been reported. Their UV-visible absorption spectra are shown in Figure 3.14 with data summarised in Table 3.5. Each complex displays intense bands at high energy < 300 nm, which can be ascribed to π–π* transitions within the ligands. Weaker bands stretching into the visible region can be attributed to $d_{Pt}|\pi_{\underline{NNC}} \rightarrow \pi^*_{\underline{NNC}}$ transitions (MLCT/LLCT).[71] All complexes, apart from PtL^9Cl and

PtL^{13}Cl, exhibit similar spectra, with the most significant low-energy band appearing around 435 nm. PtL^{9}Cl shows a distinct band at about 400 nm, unlike the broader band around 370 nm seen in the other complexes. Complex PtL^{13}Cl shows a broad band at 353 nm and a tail extending to 460 nm.

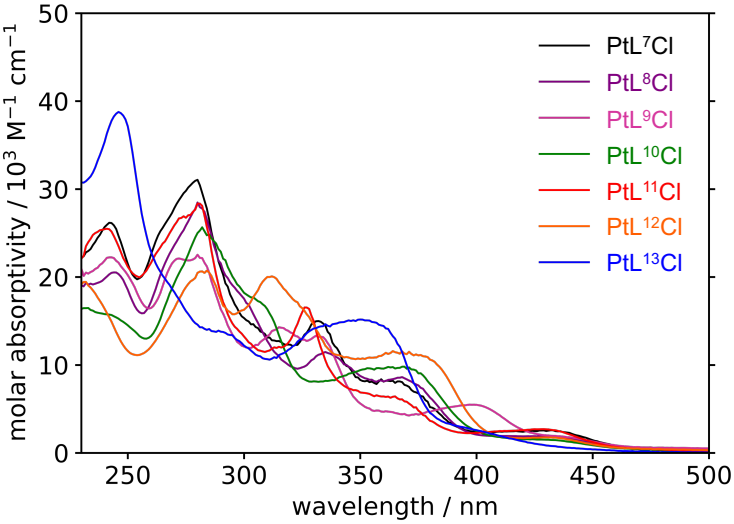

Figure 3.14: *UV-vis absorption spectra for PtL$^{7–13}$Cl in CH_2Cl_2 at 298 K.*

Table 3.5: *UV-vis absorption data for PtL$^{7–13}$Cl in CH_2Cl_2 at 298 K.*

complex	absorption λ_{max}/nm (ε/M^{-1}cm^{-1})
PtL^{7}Cl	242 (26000), 279 (31000), 332 (15000), 365 (7900), 433 (2600)
PtL^{8}Cl	245 (21000), 281 (28000), 334 (11000), 370 (8500), 433 (1900)
PtL^{9}Cl	243 (22000), 273 (22000), 280 (22000), 316 (14200), 333 (13000), 398 (5500), 441 (1800)
PtL^{10}Cl	240 (16000), 284 (25000), 307 (17000), 365 (9600), 433 (1500)
PtL^{11}Cl	240 (25000), 273 (27000), 281 (28000), 327 (17000), 367 (6100), 430 (2700)
PtL^{12}Cl	232 (19000), 284 (21000), 311 (20000), 370 (11000), 433 (1700)
PtL^{13}Cl	246 (38800), 294 (13400), 332 (14300), 353 (15100)

All the Pt^{II} complexes are luminescent in deoxygenated solution at room temperature. The photoluminescence spectra vary more than the absorption spectra with different aryl substituents (Figure 3.15, Table 3.6). At 77 K, all complexes display a vibrationally well-resolved spectrum with three visible vibrational components, and the 0,0 component the most intense. The λ(0,0) emission red-shifts slightly with the addition of a methyl group in the 4 position (from PtL^{7}Cl to PtL^{8}Cl), more with a methoxy group in the same position (PtL^{10}Cl), and even more when the methoxy group is *para* to the Pt–C bond (PtL^{9}Cl). This trend aligns with the common interpretation of the emissive state being of $^3[d_{Pt}|\pi_{Ar} \rightarrow \pi^*_{NN}]$ character, where the HOMO is mostly delocalised

over the metal and aryl ring of the *NNC* ligand (π_{Ar}), and the LUMO is primarily associated with the diimine part of the ligand (π^*_{NN}). Electron-rich substituents in the aryl ring (e.g., MeO versus Me) are therefore expected to reduce the HOMO–LUMO gap, resulting in more red-shifted emission. An electron-donating substituent *para* to the metal-carbon bond is more effective at increasing the electron density at the metal than one positioned *meta*, due to the conjugation pathway. The more electron-rich nature of thienyl compared to phenyl rings similarly explains why PtL^{12}Cl is significantly red-shifted compared to PtL^{7}Cl. The blue-shift observed from PtL^{7}Cl to PtL^{11}Cl is due to the electron-withdrawing CF_3 group stabilising the HOMO. The slight red-shift seen from PtL^{7}Cl to PtL^{13}Cl can be attributed to the enhanced conjugation resulting from substituting a pyridine ring with a quinoline.

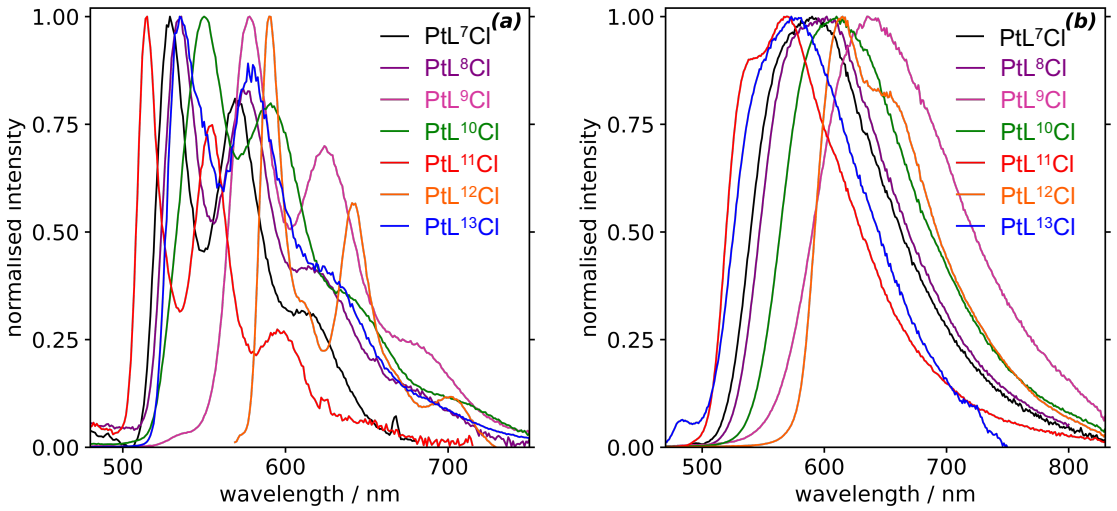

Figure 3.15: *Emission spectra of complexes PtL$^{7–13}$Cl in (a) diethyl ether / isopentane / ethanol (2:2:1 v/v) at 77 K (b) deoxygenated CH_2Cl_2 at 298 K.*

At room temperature in solution, the spectra become broader with just a little vibrational structure remaining only for PtL^{11}Cl and PtL^{12}Cl (Figure 3.15b). The order of emission λ_{max} is the same as at 77 K, except λ_{max} for PtL^{9}Cl is slightly red-shifted beyond that of PtL^{12}Cl, and those of PtL^{7}Cl and PtL^{8}Cl are more red-shifted than that of PtL^{13}Cl. The rigidochromic effect (the difference between λ_{max} at 77 K and room temperature) is more pronounced for the phenyl complexes PtL$^{7–11}$Cl and PtL^{13}Cl than those for the thienyl complex PtL^{12}Cl and quinoline complex PtL^{13}Cl. This likely reflects the greater LLCT versus MLCT character of the emissive state in the outliers PtL^{12}Cl and PtL^{13}Cl. This has been observed in related *NC*-coordinated thienylpyridine complexes of Pt^{II} and Ir^{III}.[72] The quantum yields of complexes PtL$^{7–12}$Cl are around a few percent and the lifetimes are a few hundred nanoseconds, typical of

phosphorescence from Pt(*NNC*)Cl systems (Table 3.6). Out of these complexes, the most red-shifted, PtL^{9}Cl, has the lowest quantum yield and shortest lifetime, consistent with the increased non-radiative decay expected for lower-energy excited states among structurally similar complexes.[73–75] The thienyl complex, PtL^{12}Cl displays a longer lifetime despite its low-energy emission, consistent with an emissive state of lower metal character resulting in less efficient spin-orbit coupling to facilitate the formally forbidden phosphorescence transition.[76] PtL^{13}Cl shows a 10-fold lower quantum and a longer lifetime of 8.5 µs, probably again reflecting a lower metal participation in the excited state.

Table 3.6: *Photophysical data for PtL$^{7–13}$Cl in deoxygenated CH_2Cl_2 at 298 K and in diethyl ether/isopentane/ethanol (2:2:1 v/v) at 77 K. Values in parentheses refer to air-equilibrated solutions.*

	emission at 298 K			emission at 77 K	
complex	λ_{em}/nm	Φ_{lum}/%	τ/ ns	λ_{em}/nm	τ/ µs
PtL^{7}Cl	590	1.7	270 [180]	529, 571, 611	16
PtL^{8}Cl	599	2.7	470 [240]	535, 576, 616, 683	13
PtL^{9}Cl	640	1.2	250 [150]	578, 624, 679	10
PtL^{10}Cl	610	2.6	830 [300]	551, 590, 640, 706	11
PtL^{11}Cl	538sh, 570	4.3	440 [300]	515, 554, 597	23
PtL^{12}Cl	614, 651	3.6	1300 [300]	590, 610sh, 642, 702	14
PtL^{13}Cl	576	0.2	8500 [300]	535, 580, 630	36

$Pt^{IV}Cl_3$ complexes

The absorption spectra of complexes PtL$^{n}Cl_3$ have been recorded in CH_2Cl_2 solution at room temperature (Figure 3.16 and Table 3.9). The most notable difference between the spectra of the Pt^{II}Cl and $Pt^{IV}Cl_3$ complexes is the absence in the Pt^{IV} compounds of the lowest-energy band around 430 nm that was present prior to oxidation, consistent with the visually much paler colour of the Pt^{IV} material. The change can readily be interpreted in terms of the change in the oxidation state at the metal, which will serve to lower the energy of the metal-centred orbitals in the $^{1}[d_{Pt}|\pi_{Ar} \rightarrow \pi^{*}_{NN}]$ transitions, thus increasing the absorption energy. A second difference is the rather lower molar absorptivities of the Pt^{IV} complex with fewer sharply defined bands.

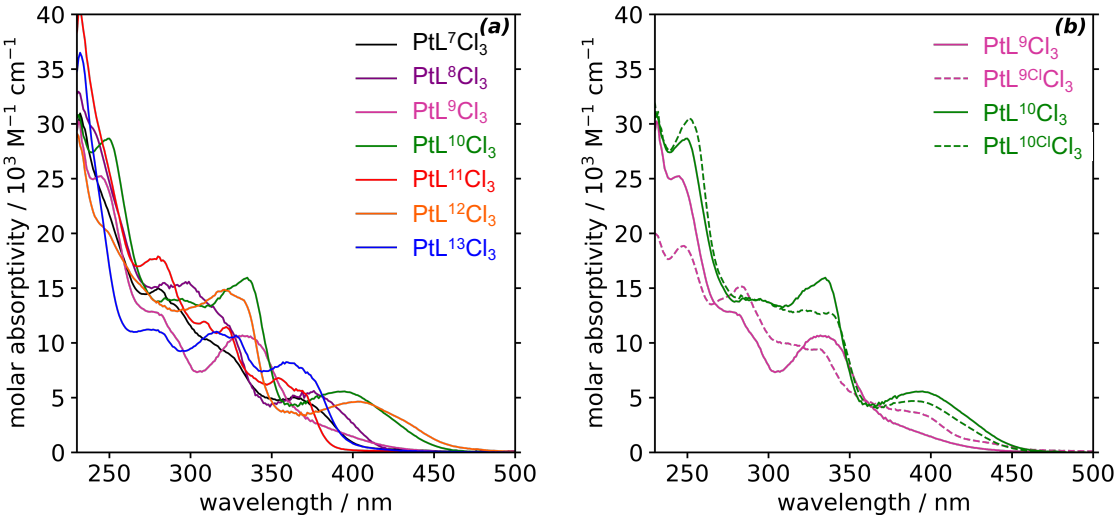

Figure 3.16: *UV-vis absorption spectra for (a) $PtL^{7-13}Cl_3$ (b) phenyl-chlorinated products $PtL^{9Cl}Cl$, $PtL^{10Cl}Cl$, with the nonchlorinated analogues ($PtL^{9}Cl$, $PtL^{10}Cl$) reproduced for comparison, in CH_2Cl_2 at 298 K.*

There is rather more variation in the spectra according to the substituents or identity of the aromatic ring than there was in the absorption of the Pt^{II} complexes, but some trends remain that were evident from the emission spectra of the Pt^{II} complexes. For example, there is a blue shift in the lowest-energy absorption band on introduction of the electron-withdrawing CF_3 substituent in $PtL^{11}Cl_3$ and, conversely, a red-shift arising from the methyl substituent in $PtL^{8}Cl_3$. For the methoxy-substituted complex $PtL^{10}Cl_3$ and thienyl derivative $PtL^{12}Cl_3$, the band is red-shifted further to λ_{max} around 400 nm and extending well into the visible region, tailing to $\lambda > 450$ nm. Such a trend suggests that the underlying transitions again feature significant $\pi_{Ar} \rightarrow \pi^*_{NN}$ character, and thus have an energy influenced heavily by the substituents in the aryl ring, or whether it is thienyl versus phenyl. Interestingly, the *para*-to-Pt methoxy complex $PtL^{9}Cl_3$ does not show a clear-cut band around 400 nm, although it does feature a very long tail in this region extending to about 450 nm. Moreover, the phenyl-chlorinated analogue of this compound, $PtL^{9Cl}Cl_3$, shows a band in this region, as evident from Figure 3.16b which compares the spectra of the two chlorinated products with their parents. It seems likely that such a band is present, therefore, also in $PtL^{9}Cl_3$ but that its intensity is suppressed relative to the other complexes.

None of the $PtL^{n}Cl_3$ complexes displays any detectable photoluminescence in solution at room temperature. In some samples at 77 K, there was evidence of some weak emission, but the spectral profile was found to closely resemble that of the Pt^{II}

precursors. Given that we noted some competitive reduction of the PtL^nCl_3 materials back to PtL^nCl, some emission from Pt^{II} contaminants is not unexpected.

Table 3.7: *UV-vis absorption data for $PtL^{7–13}Cl$ in CH_2Cl_2 at 298 K.*

complex	absorption λ_{max}/nm (ε/$M^{-1}cm^{-1}$)
PtL^7Cl_3	281 (14900), 324sh (8970), 367 (4870)
PtL^8Cl_3	295 (15400), 322sh (11800), 374 (5500)
PtL^9Cl_3	244 (25200), 276 (12900), 333 (10600), 390sh (1950)
$PtL^{9Cl}Cl_3$	248 (18900), 284 (15100), 330sh (9390), 388sh (3690), 437sh (840)
$PtL^{10}Cl_3$	248 (28500), 292 (13900), 334 (15900), 394 (5570)
$PtL^{10Cl}Cl_3$	251 (30200), 292 (13900), 322 (12600), 336 (12700), 389 (4690)
$PtL^{11}Cl_3$	271 (17200), 310 (11800), 323 (11400), 355 (6760), 371 (5340)
$PtL^{12}Cl_3$	247sh (20400), 321 (14900), 333sh (13900), 403 (4640)
$PtL^{13}Cl_3$	232 (36500), 278 (11200), 316 (11000), 328sh (10700), 365 (7970)

Pt^{IV} complexes featuring *NN*, *NN*⁻ and *NNN* ligands

The absorption spectra of the complexes in MeCN solution at room temperature are shown in Figure 3.17 (data also summarised in Table 3.8). Each complex displays intense bands at high energy < 300 nm, which can be ascribed to π–π* transitions within the ligands. The lowest-energy unoccupied orbitals are likely located on the pyridine rings of the most conjugated tpy and phbpy ligands. The transitions at 368 nm (for all complexes containing L^7) and 379 nm (appearing as a shoulder in the tolbpy-containing $[PtL^8(tpy)][PF_6]_3$) are also observed for the parent PtL^7Cl_3 and PtL^8Cl_3 (Figure 3.16), respectively. Similarly, the bands appearing at 348 and 364 nm in $[PtL^7(tpy)][PF_6]_3$ and $[PtL^8(tpy)][PF_6]_3$ have counterparts in $[Pt(tpy)Cl_3]^+$ (340 and 356 nm) and are therefore probably associated with transitions involving the *NNN* ligand as the acceptor.[60] $[PtL^7L^5Cl]PF_6$ shows higher molar absorptivity in the low energy region, compared to $[PtL^7L^3Cl]PF_6$ and $[PtL^7L^4Cl]PF_6$, reflecting the increase in conjugation with the addition of an extra aromatic ring. None of the complexes were found to be luminescent at room temperature in acetonitrile solution or at 77 K in butyronitrile. Similarly to the $Pt^{IV}Cl_3$, in those samples where some emission was observed, it so closely resembled the profile of the emission of the Pt^{II} precursors, that it was almost certainly due to some reduction back to Pt^{II} on the timescale of the measurement or the presence of small amounts of impurities.

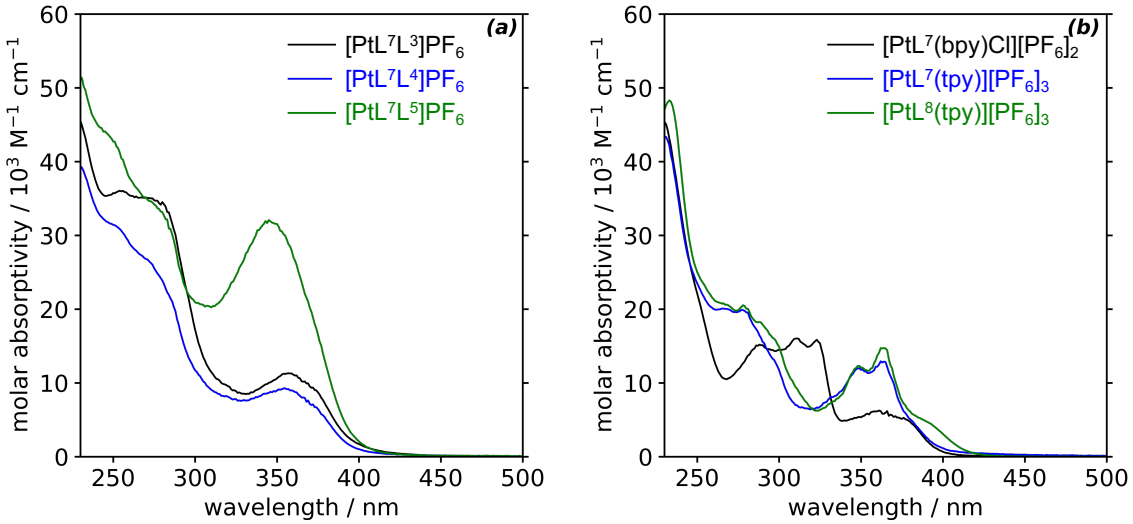

Figure 3.17: *UV-vis absorption spectra for (a) $[PtL^7L^{3–5}Cl]PF_6$ and (b) $[PtL^7(bpy)Cl][PF_6]_2$, $[PtL^7(tpy)][PF_6]_3$ and $[PtL^8(tpy)][PF_6]_3$ in CH_3CN at 298 K.*

Table 3.8: *UV-vis absorption data for $[PtL^7L^{3–5}Cl]PF_6$, $[PtL^7(bpy)Cl][PF_6]_2$, $[PtL^7(tpy)][PF_6]_3$ and $[PtL^8(tpy)][PF_6]_3$ in CH_3CN at 298 K.*

complex	absorption λ_{max}/nm (ε/$M^{-1}cm^{-1}$)
$[PtL^7L^3Cl]PF_6$	288 (14900), 310 (15700), 323 (15400), 368 (5550)
$[PtL^7L^4Cl]PF_6$	268 (19700), 278 (19700), 348 (11700), 364 (12400)
$[PtL^7L^5Cl]PF_6$	233 (47900), 268 (20300), 278 (20300), 289sh (18200), 348 (12100), 364 (14500), 390sh (3940)
$[PtL^7(bpy)Cl][PF_6]_2$	255 (35700), 276 (34600), 358 (10900), 373sh (8840)
$[PtL^7(tpy)][PF_6]_3$	254 (30600), 278sh (24600), 358 (8920), 373sh (6620)
$[PtL^8(tpy)][PF_6]_3$	249 (43100), 279sh (32600), 347 (31700)

Pt^{IV} complexes featuring two cyclometallated ligands

The absorption spectra of the four complexes of type $[Pt(NNC)(NC)Cl]^+$ and the bis-tridentate $[Pt(NNC)_2]^{2+}$, namely $[PtL^7(ppy)Cl]^+$, $[Pt^{10Cl}(ppy)Cl]^+$, $[PtL^9(3\text{-OMe-ppy})Cl]^+$, $[PtL^{10}(4\text{-OMe-ppy})Cl]^+$ and $[PtL^7{}_2]^{2+}$, are shown in Figure 3.18, with numerical data in Table 3.10. Figure 3.18a compares the absorption spectrum of the unsubstituted $[PtL^7(ppy)Cl]^+$ and $[PtL^7{}_2]^{2+}$ with that of their precursor PtL^7Cl_3. The spectra are similar. The main difference between $[PtL^7(ppy)Cl]^+$ and PtL^7Cl_3 is the higher molar absorptivity of $[PtL^7(ppy)Cl]^+$ across most of the shorter-wavelength range < 350 nm, which can readily be attributed to the presence of the additional aromatic rings and transitions associated with them. It is notable, on the other hand, that there is barely any difference between the spectra in the region of the lowest-energy band (i.e., λ > 350 nm). This observation is consistent with the notion that the unoccupied orbitals

of lowest energy in this complex would be expected to be the π* of the bipyridine moiety of the *NNC* ligand. The extended conjugation over the two *ortho*-linked pyridine rings will lead to the lowest-energy charge-transfer transitions being those involving the *NNC* ligand as the acceptor, as opposed to the *NC* ligand. The fact that there is essentially no shift in this lowest-energy band relative to $PtL^{7}Cl_3$ then implies that the energy of filled orbitals involved in the transition is relatively unchanged, pointing towards a predominantly $\pi_{\underline{NNC}} \rightarrow \pi^*_{\underline{NNC}}$ character to the transition. Similar observations are made for the other three [Pt(*NNC*)(*NC*)Cl]$^+$ complexes upon comparing them with their precursors. For $[PtL^{7}{}_2]^{2+}$, the replacement of the monodentate chloride ligand of complex $[PtL^{7}(ppy)Cl]^+$ by a pyridine ring has little effect on the excited state energy. Indeed, the main difference in the absorption spectra between the two complexes is the higher molar absorptivities across the wavelength range, reflecting the presence of the second tridentate ligand with its more extended conjugation.

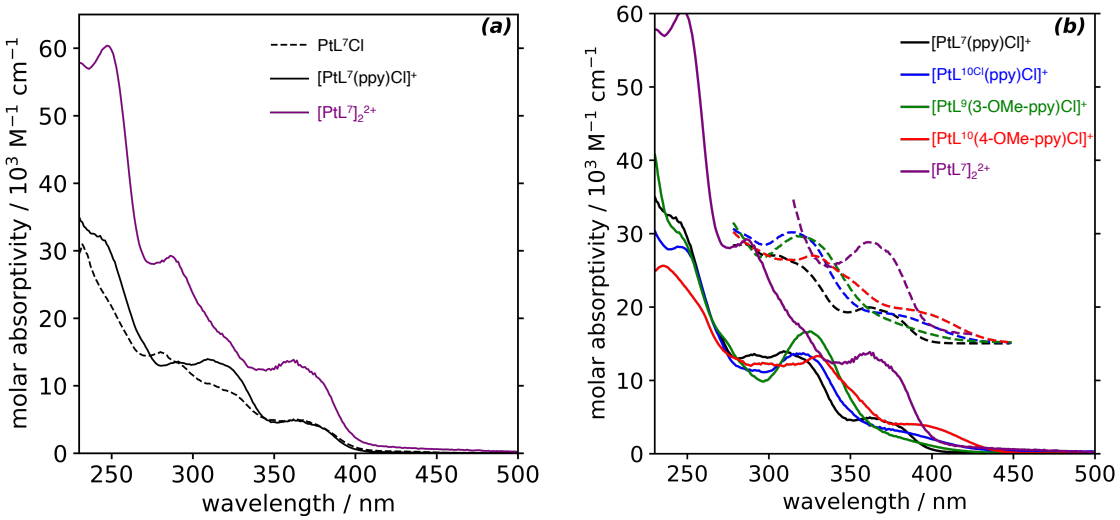

Figure 3.18: *UV-vis absorption spectra of (a) $PtL^{7}Cl$, $[PtL^{7}(ppy)Cl]^+$ and $[PtL^{7}{}_2]^{2+}$, and of (b) $[PtL^{7}(ppy)Cl]^+$, $[Pt^{10Cl}(ppy)Cl]^+$, $[PtL^{9}(3\text{-}OMe\text{-}ppy)Cl]^+$, $[PtL^{10}(4\text{-}OMe\text{-}ppy)Cl]^+$ and $[PtL^{7}{}_2]^{2+}$ (with offset photoluminescence excitation spectra as dashed lines) in CH_3CN at 298 K.*

The variation in the absorption spectra according to the substituent in the aryl ring (Figure 3.18) shows that there is a red-shift in the lowest-energy band for $[PtL^{10}(4\text{-}OMe\text{-}ppy)Cl]^+$ and $[Pt^{10Cl}(ppy)Cl]^+$, and a long-wavelength tail in $[PtL^{9}(3\text{-}OMe\text{-}ppy)Cl]^+$, just as there was in the $PtL^{n}Cl_3$ precursors. The trend is consistent with an increase in electron density on the aryl ring in the $\pi_{\underline{NNC}} \rightarrow \pi^*_{\underline{NNC}}$ transition upon introduction of a methoxy substituent.

Table 3.9: *UV-vis absorption data for [PtL^{7}(ppy)Cl]$^{+}$, [Pt^{10Cl}(ppy)Cl]$^{+}$, [PtL^{9}(3-OMe-ppy)Cl]$^{+}$, [PtL^{10}(4-OMe-ppy)Cl]$^{+}$ and [PtL$^{7}_{2}$]$^{2+}$ in CH_3CN at 298 K.*

complex	absorption λ_{max}/nm (ε/M^{-1}cm^{-1})
[PtL^{7}(ppy)Cl]$^{+}$	242sh (32100), 290 (13400), 310 (13900), 364 (4850), 378sh (3960)
[Pt^{10Cl}(ppy)Cl]$^{+}$	247 (28100), 319 (13700), 383 (2980), 464sh (360)
[PtL^{9}(3-OMe-ppy)Cl]$^{+}$	246sh (29800), 324 (16500), 386sh (1850)
[PtL^{10}(4-OMe-ppy)Cl]$^{+}$	298 (12300), 330 (13300), 392 (3950)
[PtL$^{7}_{2}$]$^{2+}$	248 (60400), 287 (29200), 319 (17300), 362 (13900), 378sh (11000)

All five complexes are found to be luminescent in deoxygenated solution at room temperature (Figure 3.19 and Table 3.10), and their luminescence excitation spectra closely match the absorption spectra (Figure 3.18b). [PtL^{7}(ppy)Cl]$^{+}$ displays a somewhat structured spectrum, with a vibrational progression of around 1300 cm^{-1}, typical of coupling to aromatic C=C vibrations, and with the (0,1) band apparently the vibrational component of highest intensity. There is a large blue shift in the emission spectrum relative to that of the Pt^{II} precursor, mirroring the trend already observed in absorption. The luminescence quantum yield under these conditions is 4% and the temporal decay of the emission follows mono-exponential kinetics with a lifetime of 42 μs. The emission is severely quenched in the presence of oxygen, as might be expected for such a long-lived excited state: air-equilibrated solutions show only a very weak signal. The long lifetime is consistent with the emission being phosphorescence from the triplet state, but the value is two orders of magnitude longer than that of PtL^{7}Cl. Making the approximation that the emitting state is formed with unit efficiency (a reasonable approximation given the close match of the excitation and absorption spectra), the radiative rate constant, k_r, is estimated to be around 940 s^{-1} (Table 3.10). This value is small compared not only with efficient organometallic emitters like Ir(ppy)$_3$ and Pt(dpyb)Cl but also with the Pt(*NNC*)Cl precursor complexes (for which k_r is around 10^4–10^5 s^{-1}), suggesting that spin-orbit coupling pathways are much less efficient in the Pt^{IV} complex. Such a conclusion is consistent with an excited state of predominantly $^3[\pi_{\mathrm{NN\underline{C}}} \rightarrow \pi^*_{\mathrm{\underline{NN}C}}]$ character, with relatively little metal character, in line with the conclusions about the lowest-energy singlet states from absorption spectroscopy above.

This interpretation is supported by the data at 77 K. Firstly, the lifetime at this temperature is increased to a very long value of 280 µs (compared to 16 µs for PtL^7Cl). Secondly, the emission spectrum – which now displays very well-resolved vibrational structure – is only marginally blue-shifted compared to the room temperature spectrum, whereas PtL^7Cl displays a large blue-shift of around 2000 cm^{-1} on cooling. Large rigidochromic effects are more typical of complexes with excited states of MLCT character than those where the excited state is more ligand-localised.

The bis-bidentate complex $[PtL^7{}_2]^{2+}$ displays absorption and emission spectra that are very similar in profile to those of $[PtL^7(ppy)Cl]^+$. Given that the lowest-energy singlet and triplet excited states in the latter were concluded to be largely localised on the tridentate ligand, the similarity in the spectral profiles is probably to be anticipated. In emission, there is just a very small red shift in the λ_{max} values of the homoleptic complex (a few nm only) and slightly more intense tail to long wavelengths. The quantum yield and lifetime are a little reduced, but otherwise, the optical properties are very similar.

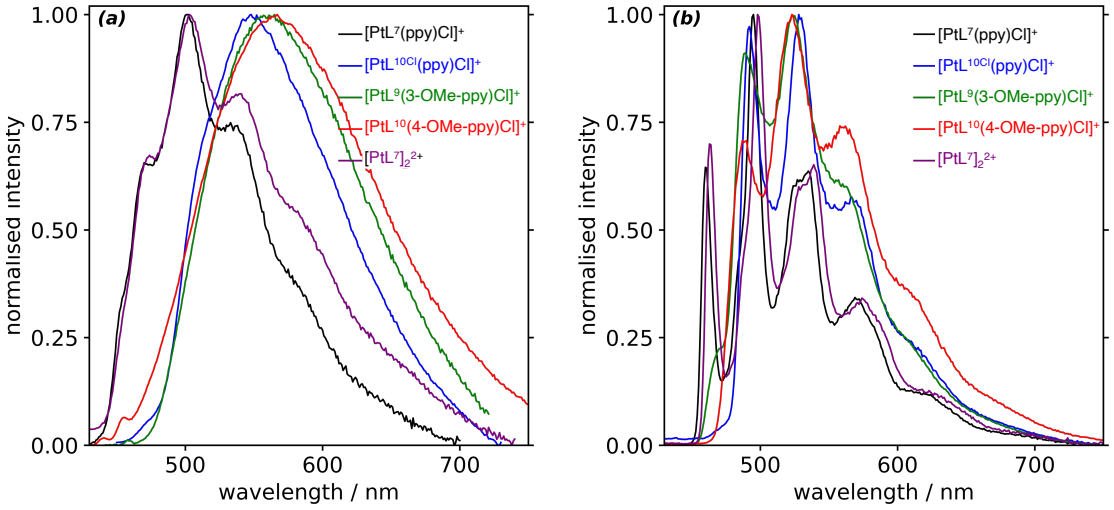

Figure 3.19: *Emission spectra of complexes $[PtL^7(ppy)Cl]^+$, $[Pt^{10Cl}(ppy)Cl]^+$, $[PtL^9(3\text{-}OMe\text{-}ppy)Cl]^+$, $[PtL^{10}(4\text{-}OMe\text{-}ppy)Cl]^+$ and $[PtL^7{}_2]^{2+}$ in (a) butyronitrile at 77 K and (b) deoxygenated CH_3CN at 298 K.*

3.4.6 Electrochemistry

The redox properties of complexes $[PtL^7L^{3\text{–}5}Cl]PF_6$, $[PtL^7(bpy)Cl][PF_6]_2$, $[PtL^7(tpy)][PF_6]_3$ and $[PtL^8(tpy)][PF_6]_3$ were investigated in 0.1 M acetonitrile solution of NBu_4PF_6. The cyclic voltammograms of the pyridyltriazole-containing complexes in Figure 3.21 and those of the bypiridyl and terpyridyl complexes are shown in Figure 3.20. The

Table 3.10: *Photophysical data for complexes [PtL^{7}(ppy)Cl]$^{+}$, [Pt^{10Cl}(ppy)Cl]$^{+}$, [PtL^{9}(3-OMe-ppy)Cl]$^{+}$, [PtL^{10}(4-OMe-ppy)Cl]$^{+}$ and [PtL$^{7}_{2}$]$^{2+}$*

	emission at 298 K[a]					emission at 77 K[b]	
complex	λ_{em}/nm	Φ_{lum}/%	τ^{c}/µs	k_r/ $10^3 s^{-1}$	k_{nr}/ $10^3 s^{-1}$	λ_{em}/nm	τ/µs
[PtL^{7}(ppy)Cl]$^{+}$	472, 501, 534	4.0	42 [–[d]]	0.94	23	461, 496, 527sh, 536, 571, 619	280
[Pt^{10Cl}(ppy)Cl]$^{+}$	548	1.5	5.0 [0.7]	3.0	200	493, 530, 569, 623	180
[PtL^{9}(3-OMe-ppy)Cl]$^{+}$	559	0.40	0.77 [0.39]	6.0	1300	490, 526, 561, 616	120
[PtL^{10}(4-OMe-ppy)Cl]$^{+}$	565	0.90	7.7 [0.52]	1.2	130	487, 522, 562, 607	240
[PtL$^{7}_{2}$]$^{2+}$	474, 503, 539, 586sh	1.0	30 [–[d]]	0.33	33	465, 499, 530sh, 540, 577, 633	250

[a] in CH_3CN [b] in butyronitrile [c] in deoxygenated solution; corresponding values in parenthesis refer to air-equilibrated solutions [d] Quenching by oxygen led to an emission intensity that was too low to reliably determine a lifetime in air-equilibrated solution.

results are also summarised in Table 2. For each complex, an irreversible reduction peak between –0.65 and –1.06 V vs Fc^+ | Fc is observed, corresponding to reduction of the Pt^{IV} to Pt^{II}, as seen for other Pt^{IV} complexes.[31] The potential required for the reduction of the Pt^{IV} centre decreases with the increase in overall charge of the cations – least negative for the 3+ terpyridine-containing complex cations and most negative for the singly charged pyridyltriazole-containing complex cations. One or two further reductions were observed at lower reduction potentials, possibly associated with the reduction of the phbpy, bpy and tpy ligands. Oxidation peaks were only observed for the pyridyltriazole ligand-containing complexes, likely due to the presence of the electron-rich 1,2,4-triazole ring. The complex with the more electron-donating *p*-OMe-phenyl-substituted triazole ring exhibits the lowest oxidation potential of 1.23 V vs Fc^+ | Fc. The highest occupied molecular orbital (HOMO) is likely located on the pyridyltriazole ligand and therefore the oxidation potential of the complex is affected by the change in substituent on that ligand.

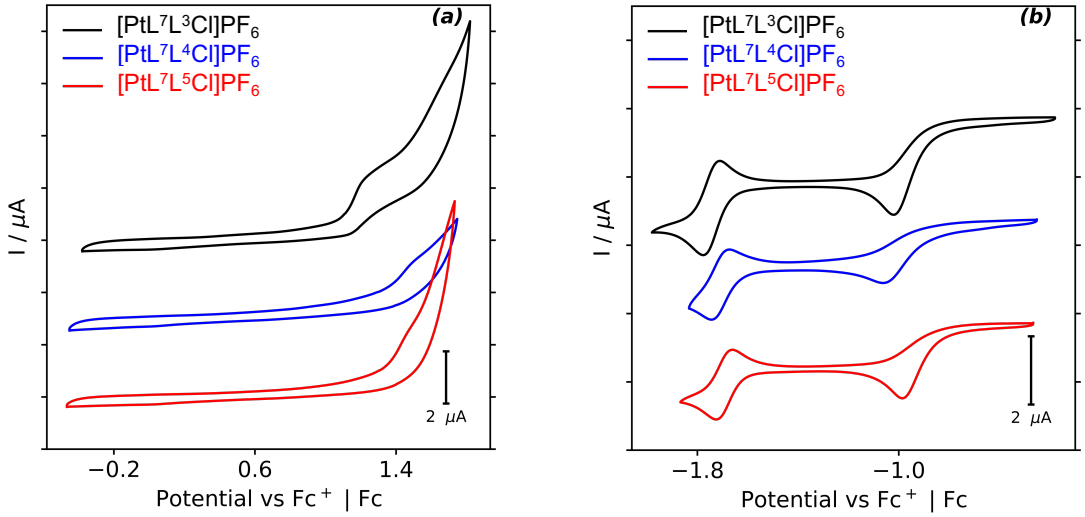

Figure 3.20: *Cyclic voltammograms of* $[PtL^7L^{3–5}Cl]PF_6$ *recorded in 0.1 M* NBu_4PF_6/CH_3CN*, scan rate = 50 mV* s^{-1}*.*

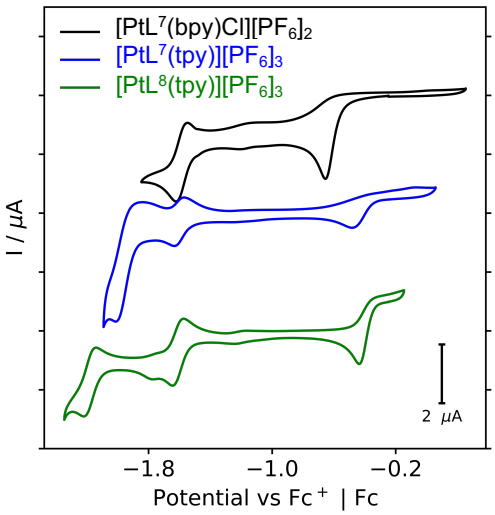

Figure 3.21: *Cyclic voltammograms of [PtL⁷(bpy)Cl][PF₆]₂, [PtL⁷(tpy)][PF₆]₃ and [PtL⁸(tpy)][PF₆]₃ recorded in 0.1 M NBu₄PF₆/CH₃CN, scan rate = 50 mV s⁻¹.*

Table 3.11: *Electrochemical data for [PtL⁷L³⁻⁶Cl]PF₆, [PtL⁷(ppy)Cl]PF₆, [PtL⁷(bpy)Cl][PF₆]₂ and [PtL⁷(tpy)][PF₆]₃ in CH₃CN solution in the presence of 0.1M NBu₄PF₆*

complex	E_{pa}^{ox} / V[a]	E_{pc}^{red} / V[b]
$[PtL^7L^3Cl]PF_6$	1.23	–1.01[d], –1.78
$[PtL^7L^4Cl]PF_6$	1.50	–1.06[d], –1.75
$[PtL^7L^5Cl]PF_6$	1.46	–0.97[d], –1.73
$[PtL^7(bpy)Cl][PF_6]_2$	–[c]	–0.65[d], –1.62
$[PtL^7(tpy)][PF_6]_3$	–[c]	–0.48[d], –1.63, –2.01
$[PtL^8(tpy)][PF_6]_3$	–[c]	–0.44[d], –1.65, –1.78, –2.22

[a]E_{pa} refers to the anodic peak potential for the irreversible oxidation waves. [b]E_{pc} refers to the cathodic peak potential for the reduction waves. [c]Oxidation outside of the accessible window. [d]Irreversible reduction.

3.5 Chapter summary

Several Pt^{IV}(*NNC*)Cl_3 complexes were synthesised by oxidising their Pt^{II}(*NNC*)Cl precursors using chlorine or $PhICl_2$. Reactions with bidentate ligands yielded 3 + 2 + 1 type complexes, each featuring a tridentate *NNC* ligand, one bidentate ligand, and a monodentate chloride ligand. The bidentate ligands used included pyridyl-triazole *NN*⁻, 2,2'-bipyridine *NN*, and various phenyl-substituted 2-phenylpyridines *NC*. Additionally, bis-tridentate complexes incorporating both an *NNC* ligand and an *NNN*-type ligand were synthesised. Notably, the first examples of bis-cyclometallated Pt^{IV} complexes of the form $[Pt(NNC)_2]^{2+}$ were also prepared.

The photophysical properties of all of the complexes were investigated. Only the bis-cyclometallated complexes were found to be emissive at room temperature in deoxygenated acetonitrile and at 77 K in butyronitrile. Phosphorescence quantum yields between 0.4 and 4% were observed. Some control over the emission energy is achieved through simple modification of the aryl ring.

CHAPTER 4

Platinum complexes with *ortho*-phenyl-appended tridentate *NNC* ligands

Chapter 4: Platinum complexes with *ortho*-phenyl-appended tridentate *NNC* ligands

4.1 Aims and objectives

The platination reaction of 6,6'-diphenyl-2,2'-bipyridine presents an intriguing opportunity to explore the coordination chemistry of platinum with tetradentate ligands. Specifically, this reaction could lead to the formation of a Pt(*CNNC*) complex, where the ligand binds to the platinum center in a tetradentate *CNNC* mode. A detailed discussion of platinum complexes incorporating various tetradentate ligands is provided in Chapter 6.

However, in practice, when 6,6'-diphenyl-2,2'-bipyridine is reacted with K_2PtCl_4 in acetic acid, it has emerged from the work described here that the ligand seems to prefer to coordinate in a tridentate *CNN* mode. This coordination involves the nitrogen atoms of the bipyridine moiety and one carbon atom from one of the phenyl rings, resulting in cyclometallation. Notably, no second cyclometallation occurs at the other phenyl ring, so it merely serves as a substituent on the pyridine ring. The structure of 6,6'-diphenyl-2,2'-bipyridine, along with its potential binding modes to platinum, is depicted in Figure 4.1.

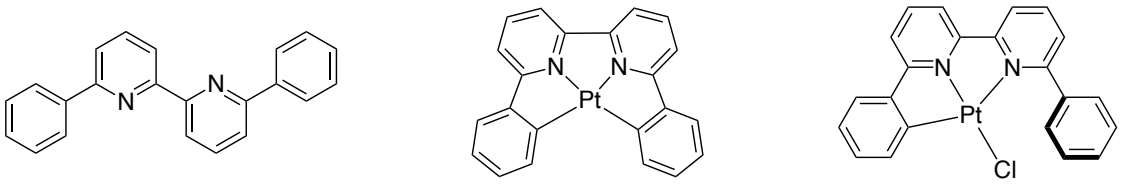

6,6'-diphenyl-2,2'-bipyridine tetradentate CNNC binding mode tridentate CNN binding mode

Figure 4.1: *The structure of 6,6'-diphenyl-2,2'-bipyridine and its potential binding modes to Pt*

This chapter will focus on the preparation of Pt^{IV} complexes with such *ortho*-phenyl-appended tridentate *NNC* ligands and their photophysical properties.

4.2 Synthesis of the proligands

Initially, 6,6'-diphenyl-2,2'-bipyridine and its bis 4-*tert*-butylphenyl version were inadvertently obtained as homocoupled products from reactions intended for synthesising ligands for dinuclear complexes (see Chapter 5). We subsequently decided that fur-

ther investigation of these ligands would be of merit and thus the ligands were deliberately synthesised. The first step in the strategy involved a Suzuki cross-coupling between 2,6-dibromopyridine and the relevant phenylboronic acid. This was followed by a Stille cross-coupling reaction between 2-bromo-6-phenylpyridine or 2-bromo-6-(4-(*tert*-butyl)phenyl)pyridine and their corresponding stannyl analogues (Scheme 4.1). The stannyl reactants were prepared by lithiating and subsequently stannylating their brominated counterparts.

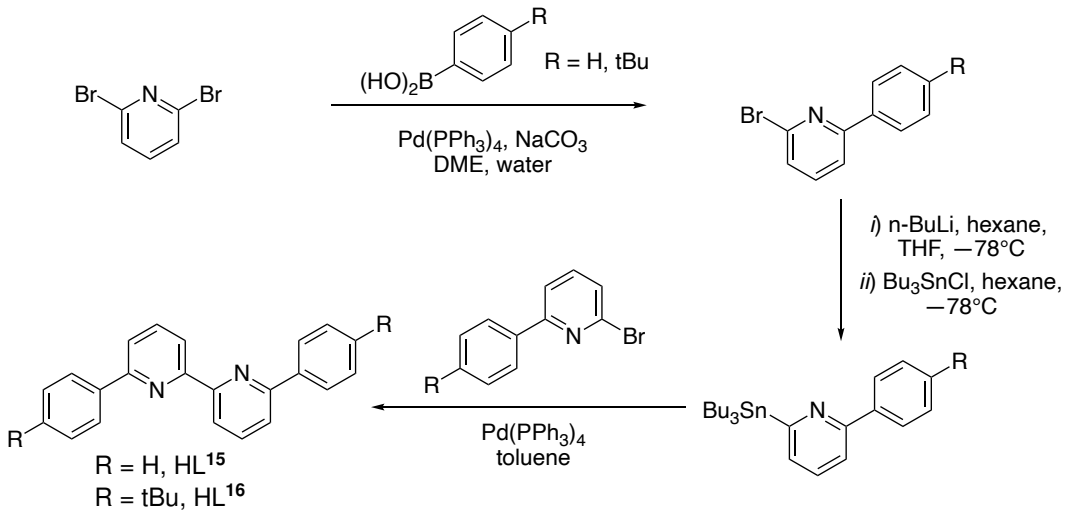

Scheme 4.1: *Synthesis of proligands HL[15] and HL[16]*

4.3 Preparation of the complexes

Complexation reactions were carried out by reacting the ligands HL[15] and HL[16] with K_2PtCl_4 in acetic acid (Scheme 4.2). Despite the potential of these ligands to bind Pt^{II} in a tetradentate *CNNC* mode, similarly to the *NCCN* ligands of Chapter 6, only tridentate *NNC* Pt^{II} complexes with an ancillary Cl ligand were isolated in each instance. The additional phenyl ring remains unbound, simply acting as a substituent on the lateral pyridine ring. The Pt^{II} complexes were subsequently oxidised with $PhICl_2$ to give the trichloro Pt^{IV} complexes $PtL^{15}Cl_3$ and $PtL^{16}Cl_3$.

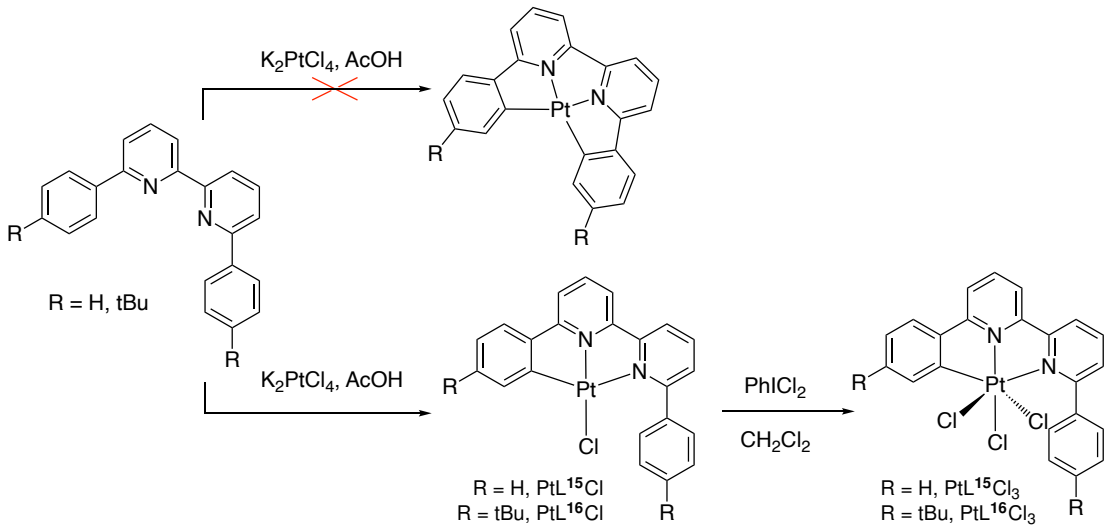

Scheme 4.2: *Synthesis of complexes PtL[15]Cl and PtL[16]Cl*

$PtL^{15}Cl_3$ and $PtL^{16}Cl_3$ were reacted with 2-phenylpyridine in toluene at reflux, in an attempt to obtain 3 + 2 + 1 complexes analogous to those of Chapter 3. The removal of the chloride ions was aided by the use of silver triflate. The precipitated products from the reaction mixture were isolated, washed, and then anion exchanged with aqueous KPF_6 to obtain the hexafluorophosphate salts $[PtL^{15}(ppy)Cl]PF_6$ and $[PtL^{16}(ppy)Cl]PF_6$. In both cases, NMR data showed that the *NC* ligand binds with the pyridine ring *trans* to the central pyridine ring of the *NNC* ligand and the phenyl ring *trans* to the ancillary chloride ligand. The proton next to the coordinating nitrogen atom of the *NC* ligand experiences significant deshielding, which aligns with its closeness to the Pt–Cl bond. The binding mode was later also confirmed by X-ray crystallography (*vide infra*).

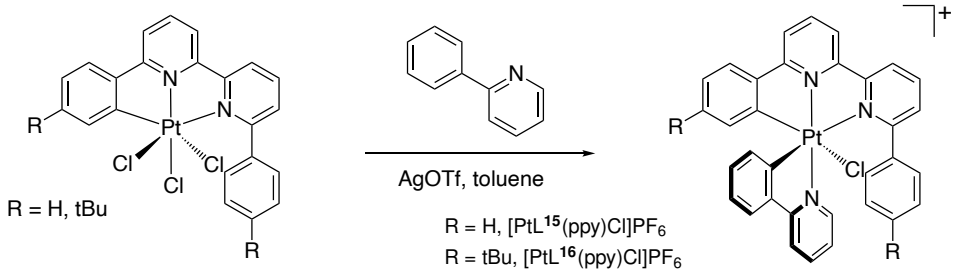

Scheme 4.3: *Synthesis of complexes [PtL[15](ppy)Cl]PF_6 and [PtL[16](ppy)Cl]PF_6*

The ^{1}H NMR spectra of the complexes at room temperature in d_6-acetone show very broad signals for the protons on the non-cyclometallated phenyl rings *ortho* and *meta* to the carbon connected to the pyridine ring (Figure 4.2). This could be explained by hindrance to the rotation of that phenyl ring on the NMR timescale caused by its

proximity to the pyridine ring of the *NC* ligand. Similar behaviour has been observed for tris-bidentate Ir^{III} complexes $[Ir(NC)_2(NN)]^+$ with a phenyl substituent *ortho* to one of the coordinating N or cyclometallating C atoms and its origin was confirmed by variable temperature (VT) NMR.[77] The close-lying non-cyclometallated phenyl ring also exerts a shielding effect on the pyridine ring of the *NC* ligand. For example, the proton next to the coordinating nitrogen shifts upfield by 0.55 ppm for $[PtL^{15}(ppy)Cl]PF_6$ and by 0.67 ppm for $[PtL^{15}(ppy)Cl]PF_6$, compared to those of complex $[PtL^{7}(ppy)Cl]PF_6$ in d_6-acetone at 599 MHz.

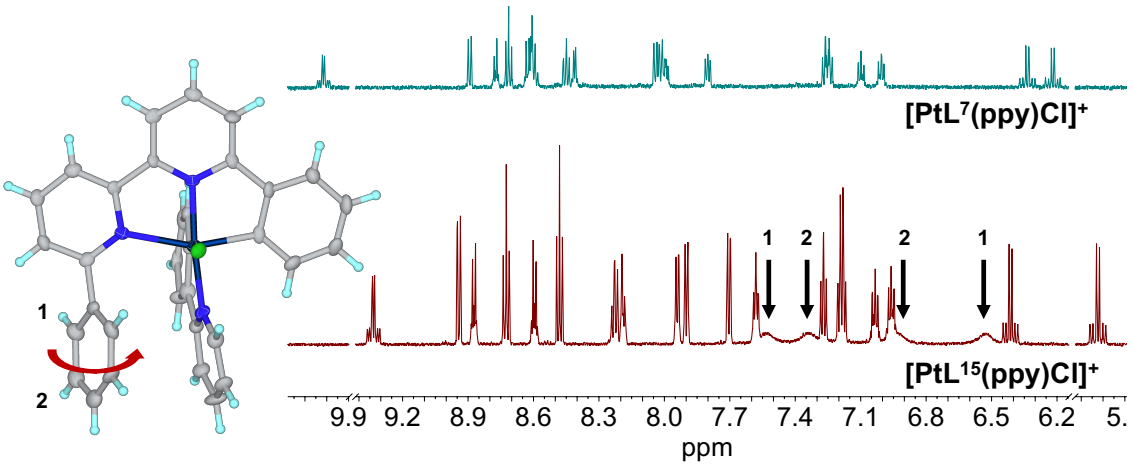

Figure 4.2: *Aromatic region of the ^{1}H NMR spectra of $[PtL^{7}(ppy)Cl]PF_6$ (top) and $[PtL^{15}(ppy)Cl]PF_6$ (bottom) in d_6-acetone at 599 MHz. The molecular structure of $[PtL^{15}(ppy)Cl]^+$ is shown on the left with a red arrow showing the rotating phenyl ring and numbered protons. Black arrows indicate the broad signals corresponding to the numbered protons.*

Crystals suitable for X-ray diffraction of the final complexes $[PtL^{15}(ppy)Cl]PF_6$ and $[PtL^{16}(ppy)Cl]PF_6$ were obtained (Figure 4.3). Selected bond lengths and bond angles are summarised in Table 4.1. Both structures show *pseudo*-octahedral geometry around the Pt^{IV} centre, with the plane of the bidentate *NC* ligand perpendicular to that of the tridentate *NNC* ligand. The non-cyclometallated ring lies *pseudo*-parallel to the pyridine ring of the *NC* ligand with interplane distances of 3.540 and 3.593 Å for $[PtL^{15}(ppy)Cl]PF_6$ and $[PtL^{16}(ppy)Cl]PF_6$, respectively.

Table 4.1: *Selected bond lengths (Å) and bond and interplane angles (°) for [PtL[15](ppy)Cl]PF_6 and [PtL[16](ppy)Cl]PF_6.*

	[PtL[15](ppy)Cl]PF_6	[PtL[16](ppy)Cl]PF_6
Pt – C^{NNC}	2.002(8)	1.998(8)
Pt – $N^{\underline{N}NC}$	2.001(7)	1.995(7)
Pt – $N^{\underline{N}NC}$	2.234(8)	2.201(8)
Pt – C^{NC}	2.017(9)	2.029(8)
Pt – N^{NC}	2.036(8)	2.047(8)
Pt – Cl	2.438(2)	2.394(2)
interplane distance	3.540	3.593
$N^{\underline{N}NC}$–Pt–N^{NC}	174.6(3)	173.8(3)
$N^{\underline{N}NC}$–Pt–C^{NNC}	159.4(3)	160.3(3)
C^{NC}–Pt–Cl	175.8(3)	177.1(3)
interplane angle	13.916	16.941

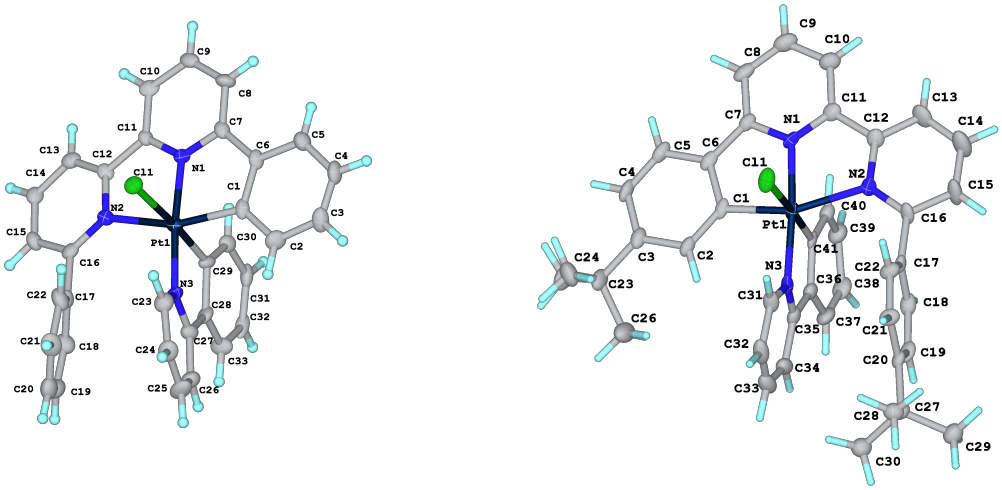

Figure 4.3: *Molecular structures of [PtL[15](ppy)Cl]PF_6 and [PtL[16](ppy)Cl]PF_6 in crystals.*

4.4 Photophysical properties

4.4.1 Absorption

The absorption spectra of all of the complexes are shown in Figures 4.4 and 4.5, with numerical data in Table 4.2. The intense transitions at high energy (< 300 nm) can be attributed to $\pi - \pi^*$ transitions within the ligands. The main contrast between the spectra of the Pt^{II} and Pt^{IV} complexes is the blue shift of the lowest energy band in the Pt^{IV} complexes, which aligns with the decrease in the energy of the d-orbitals, associated with increasing oxidation state. A slight red shift of the lowest energy band is seen in the absorption spectra of all complexes containing a *tert*-butyl group, compared to their non-substituted analogues. The complexes of the type [PtL^n(ppy)Cl]PF_6 show

absorption profiles closely resembling those of the PtL^nCl_3 precursors, which is consistent with the lowest unoccupied orbitals being located on the tridentate ligand. The presence of an extra phenyl ring in $[PtL^{15}(ppy)Cl]PF_6$ and $[PtL^{16}(ppy)Cl]PF_6$ leads to higher molar absorptivities across the entire wavelength range compared to the parent, unsubstituted $[PtL^{7}(ppy)Cl]PF_6$.

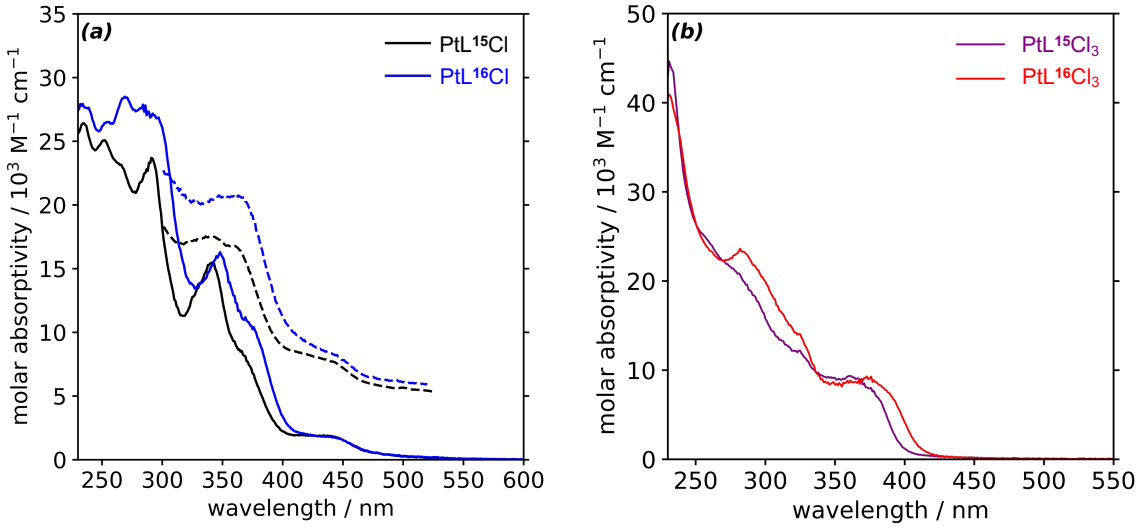

Figure 4.4: *UV-vis absorption spectra of (a) $PtL^{15}Cl$ and $PtL^{16}Cl$ (with offset photoluminescence excitation spectra (dashed)) and (b) $PtL^{15}Cl_3$ and $PtL^{16}Cl_3$ in CH_2Cl_2 solution at 298 K.*

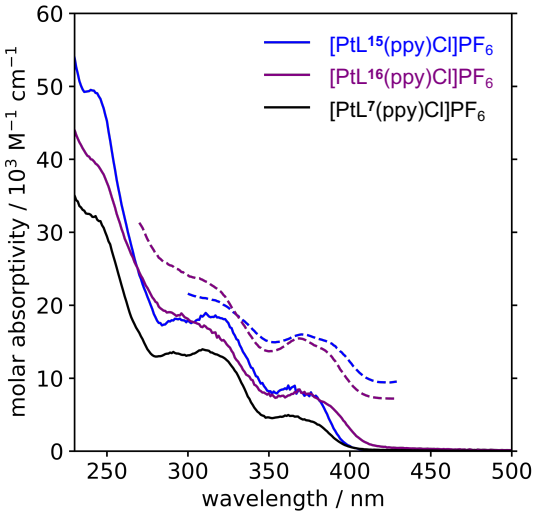

Figure 4.5: *UV-vis absorption spectra of $[PtL^{15}(ppy)Cl]PF_6$ and $[PtL^{16}(ppy)Cl]PF_6$ (with offset photoluminescence excitation spectra (dashed)) in CH_3CN solution at 298 K. The absorption spectrum of $[PtL^{7}(ppy)Cl]PF_6$ is also shown for comparison (black line).*

Table 4.2: *UV-vis absorption data for $PtL^{15}Cl$, $PtL^{16}Cl$, $PtL^{15}Cl_3$ and $PtL^{16}Cl_3$ in CH_2Cl_2 and for $[PtL^{15}(ppy)Cl]PF_6$ and $[PtL^{16}(ppy)Cl]PF_6$ in CH_3CN at 298 K.*

complex	absorption λ_{max}/nm (ε/$M^{-1}cm^{-1}$)
$PtL^{15}Cl$	235 (26400), 252 (25100), 265sh (23100), 291 (23700), 341 (15500), 370sh (7440), 442 (1830)
$PtL^{16}Cl$	235 (27700), 254 (26500), 270 (28400), 289 (27300), 348 (16300), 376sh (10400), 444 (1730)
$PtL^{15}Cl_3$	232 (44100), 260sh (24300), 283sh (20300), 325 (12200), 362 (9300), 379sh (7250)
$PtL^{16}Cl_3$	233 (40200), 283 (23300), 326sh (13700), 361sh (8840), 377 (8680)
$[PtL^{15}(ppy)Cl]PF_6$	242 (49400), 293 (18100), 317 (18600), 364 (8730), 378 (7490)
$[PtL^{16}(ppy)Cl]PF_6$	244sh (39200), 310(17200), 371(7990), 387sh (6300)

4.4.2 Emission

The Pt^{II} complexes are weakly emissive in deoxygenated dichloromethane solution at room temperature and in a glass of diethyl ether/isopentane/ethanol (2:2:1 v/v) at 77 K. Their excitation spectra closely match the absorption spectra (Figure 4.4). No emission was detected for the trichloro Pt^{IV} complexes $PtL^{15}Cl_3$ and $PtL^{16}Cl_3$. $[PtL^{15}(ppy)Cl]PF_6$ and $[PtL^{16}(ppy)Cl]PF_6$ are both emissive in deoxygenated CH_3CN solution at room temperature and in a glass of butyronitrile at 77 K, with their excitation spectra closely matching their absorption spectra Figures 4.5. The emission spectra of all of the complexes are shown in Figures 4.6 and 4.7, with numerical data in Table 4.3.

The Pt^{II} complexes show weak emission at room temperature with photoluminescence quantum yields of 0.1 and 0.2% for the non-substituted and the *tert*-butyl-substituted complex, respectively. The luminescence lifetimes are around 20 ns for both. The quantum yields and lifetimes are around 10–fold lower than those of the unsubstituted $PtL^{7}Cl$. This effect could be attributed to a large increase in the non-radiative decay due to libration of the phenyl ring, which is in close proximity to the ancillary chloride ligand. The emission spectrum of $PtL^{16}Cl$ at 77 K is slightly red-shifted compared to that of $PtL^{15}Cl$, consistent with the presence of the slightly electron-donating *tert*-butyl substituent on the phenyl ring. No significant shift is observed at room temperature. Some vibrational structure is evident only at 77 K for both compounds.

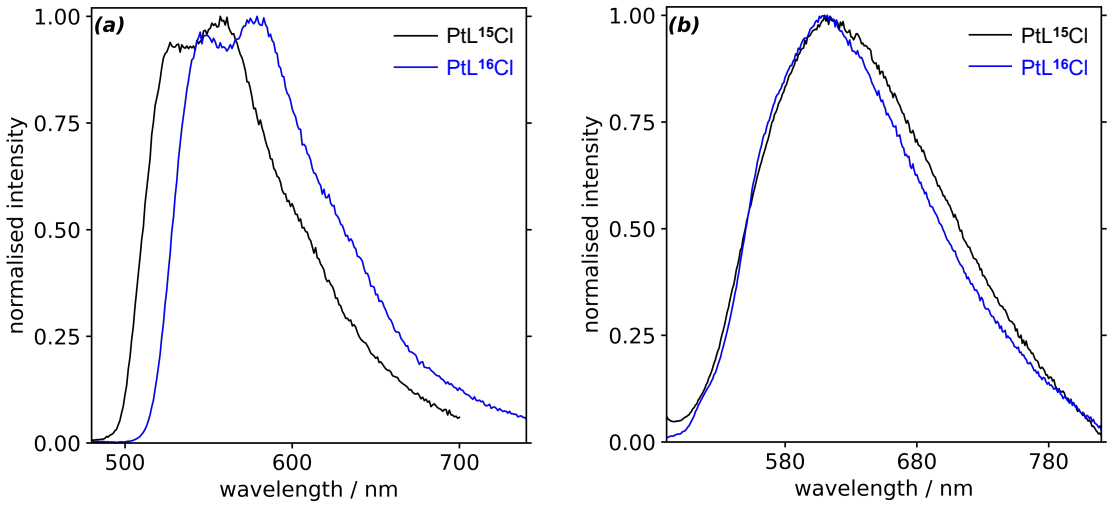

Figure 4.6: *Emission spectra of Pt^{II} complexes in (a) diethyl ether/isopentane/ethanol (2:2:1 v/v) at 77 K (b) deoxygenated CH_2Cl_2 at 298 K.*

Complexes $[PtL^{15}(ppy)Cl]PF_6$ and $[PtL^{16}(ppy)Cl]PF_6$ show structured emission at 77 K with the (0,1) band the component of highest intensity. Some structure is still retained at room temperature. The variation in the emission spectra according to the substituent in the aryl ring shows that there is a small red-shift (10 nm) for $[PtL^{16}(ppy)Cl]PF_6$. The emission of $[PtL^{15}(ppy)Cl]PF_6$ is in turn slightly red-shifted relative to that of $[PtL^{7}(ppy)Cl]PF_6$. The photoluminescence quantum yields of the phenyl-substituted complexes are comparable to that of $[PtL^{7}(ppy)Cl]PF_6$ ($\approx$ 4%) (see Chapter 3). The lifetimes are slightly longer at 55 and 64 µs for the phenyl and the *p*-^{t}Bu-phenyl substituted complexes, compared to 42 µs for $[PtL^{7}(ppy)Cl]PF_6$. The emission is significantly quenched in air-equilibrated solutions.

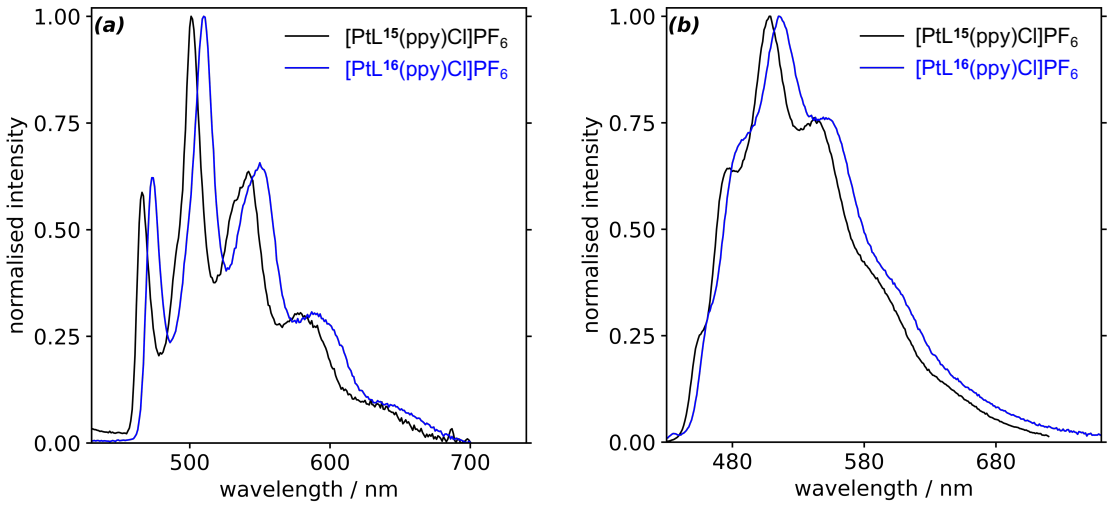

Figure 4.7: *Emission spectra of complexes $[PtL^{15}(ppy)Cl]PF_6$ and $[PtL^{16}(ppy)Cl]PF_6$ in (a) butyronitrile at 77 K (b) deoxygenated CH_3CN at 298 K.*

Given the retention of the solution-state photophysical properties upon phenyl substitution *ortho* to the coordinating nitrogen of the lateral pyridine ring, we became intrigued by the possibility of exploring whether the close proximity of the phenyl substituent and the pyridine ring on the *NC* ligand might impact the solid-state photophysical properties of the complexes. Figure 4.8 shows the non-cyclometallated phenyl ring and the pyridine ring of the *NC* ligand of complex [PtL^{15}(ppy)Cl]PF$_6$ highlighted in pink. The distance between the planes of those two rings is 3.54 Å.

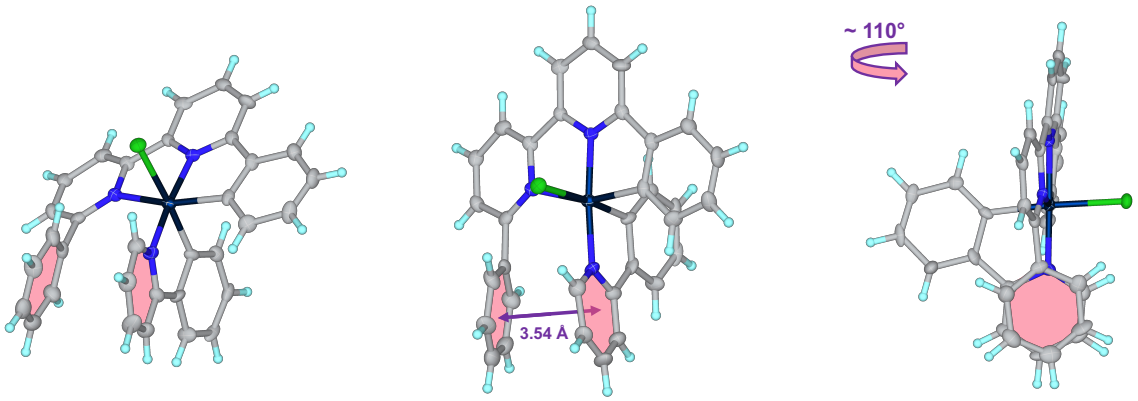

Figure 4.8: *Molecular structure of [PtL^{15}(ppy)Cl]PF$_6$, showing the close proximity of the non-cyclometallated phenyl ring of the tridentate ligand and the pyridine ring of the bidentate ligand.*

Poly(methyl methacrylate) (PMMA) films of three different complex concentrations (0.1%, 1%, and 10% by weight), along with neat films of [PtL^{7}(ppy)Cl]PF$_6$, [PtL^{15}(ppy)Cl]PF$_6$, and [PtL^{16}(ppy)Cl]PF$_6$, were prepared using the drop cast method on sapphire substrates. The absorption and emission spectra of all of the PMMA and neat films are shown in Figures 4.9 and 4.10, respectively, with data summarised in Table 4.4.

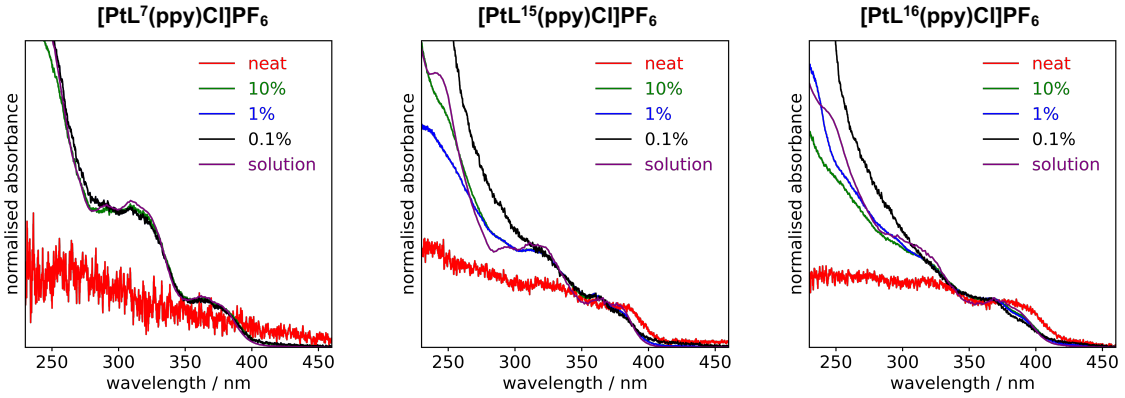

Figure 4.9: *UV-vis absorption spectra of 0.1, 1 and 10 wt % doped PMMA and neat films of complexes [PtL^{7}(ppy)Cl]PF$_6$, [PtL^{15}(ppy)Cl]PF$_6$ and [PtL^{16}(ppy)Cl]PF$_6$.*

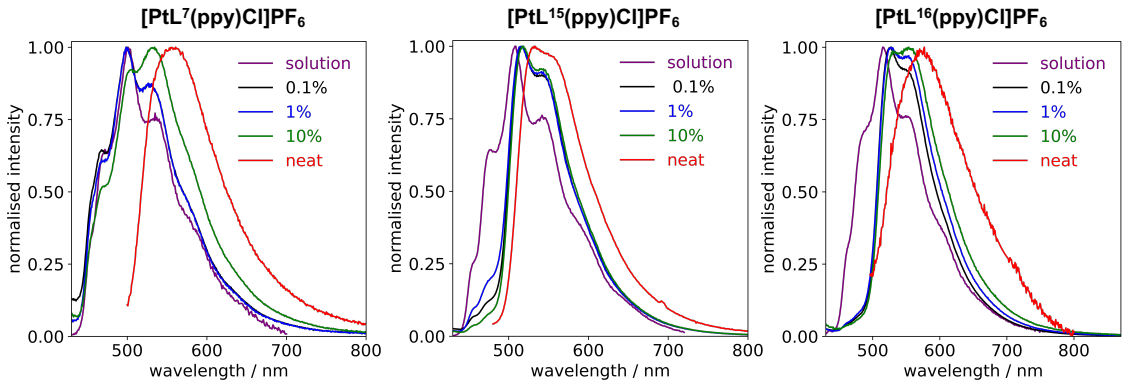

Figure 4.10: *Emission spectra of 0.1, 1 and 10 wt % doped PMMA and neat films of complexes [PtL^{7}(ppy)Cl]PF$_6$, [PtL^{15}(ppy)Cl]PF$_6$ and [PtL^{16}(ppy)Cl]PF$_6$*

The quantum yields of each doping concentration of the complexes [PtL^{15}(ppy)Cl]-PF$_6$ and [PtL^{16}(ppy)Cl]PF$_6$ in PMMA consistently surpass those of [PtL^{7}(ppy)Cl]PF$_6$ (up to more than 3-fold), suggesting that the $\pi - \pi$ interactions may have a beneficial influence on the emission intensity. The highest quantum yield is exhibited by the 1 wt % PMMA film of [PtL^{15}(ppy)Cl]PF$_6$ at 33%. Lifetimes are around 15 µs for all PMMA films. A detailed examination of each PMMA film of [PtL^{15}(ppy)Cl]PF$_6$ and [PtL^{16}(ppy)Cl]PF$_6$ reveals variations in the emission profile depending on the excitation wavelength (Figures 4.11 and 4.12). For example, the emission spectrum of the 1% PMMA film of [PtL^{15}(ppy)Cl]PF$_6$ at λ_{ex} = 380 nm closely resembles that of the solution (Figure 4.11). However, when excited at 350 nm, the solution-like emission band appears diminished and a different band (λ_{max} = 515, 545 nm) becomes more prominent. A further decrease in the band resembling the solution emission is observed at 365 nm excitation. Monitoring the emission at 460 nm (solution-like emission band) yields an excitation spectrum whose profile matches that of the solution absorption, with a broad band at 378 nm. In contrast, monitoring the emission at 540 nm produces a spectrum with λ_{max} = 343, 360 nm.

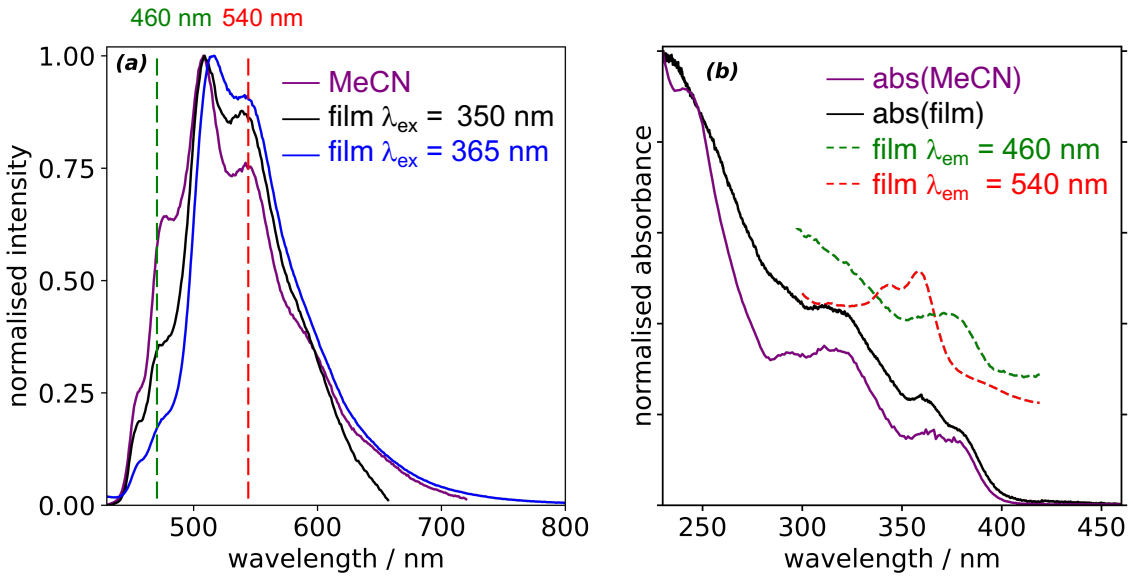

Figure 4.11: *(a) Emission spectrum of [PtL[15](ppy)Cl]PF_6 in deaerated CH_3CN solution and in 1 wt % PMMA film at λ_{ex} = 350 nm and 365 nm. (b) UV-vis spectrum of [PtL[15](ppy)Cl]PF_6 in solution and 1% PMMA film (with offset photoluminescence excitation spectra (dashed) at λ_{em} = 460 (green) and 540 nm (red)).*

Identical behaviour is observed for the films of complex [PtL[16](ppy)Cl]PF_6. For instance, the 10 wt % PMMA film of this complex shows diminution of the intensity of the band around 470 nm with decreasing the excitation wavelength from 385 nm to 365 nm (Figure 4.12). Monitoring the emission intensity at 470 nm produces an excitation spectrum that closely resembles the solution absorption spectrum, whereas monitoring the emission at 540 nm yields an excitation spectrum with λ_{max} = 347, 364 nm. These results suggest that, for these two complexes, there might be an additional emissive state involved in the solid-state emission, possibly involving interactions between the phenyl substituent and pyridine ligand of the *NC* ligand.

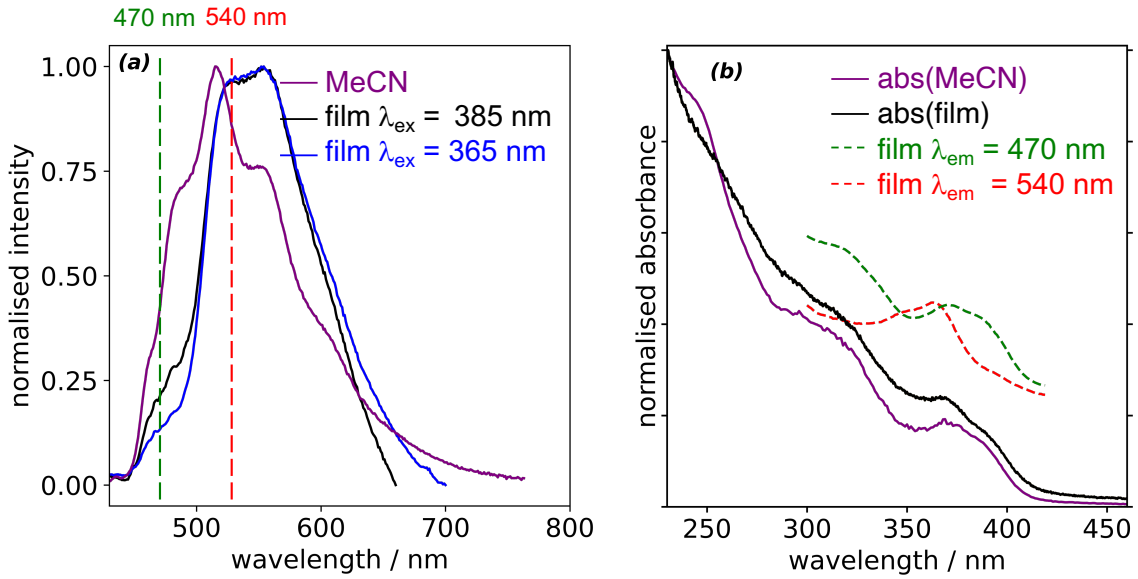

Figure 4.12: *(a) Emission spectrum of [PtL^{16}(ppy)Cl]PF$_6$ in deaerated CH$_3$CN solution and in 10 wt % PMMA film at λ_{ex} = 385 nm and 365 nm. (b) UV-vis spectrum of [PtL^{16}(ppy)Cl]PF$_6$ in solution and 1% PMMA film (with offset photoluminescence excitation spectra (dashed) at λ_{em} = 470 (green) and 540 nm (red)).*

In contrast, while [PtL^7(ppy)Cl]PF$_6$ shows a slight red-shift with increasing wt % in PMMA, there is no variation in the emission profile of each film with excitation wavelength and no dependence of the excitation spectra on λ_{em} (Figure 4.13). For example, no significant change can be seen in the emission spectra of [PtL^7(ppy)Cl]PF$_6$ in CH$_3$CN solution and 1 wt % film in PMMA excited at λ_{ex} = 380 nm and 350 nm (Figure 4.13). In addition, no difference can be observed in the excitation spectra of 1 wt % PMMA film registered at λ_{em} = 470 nm and 530 nm.

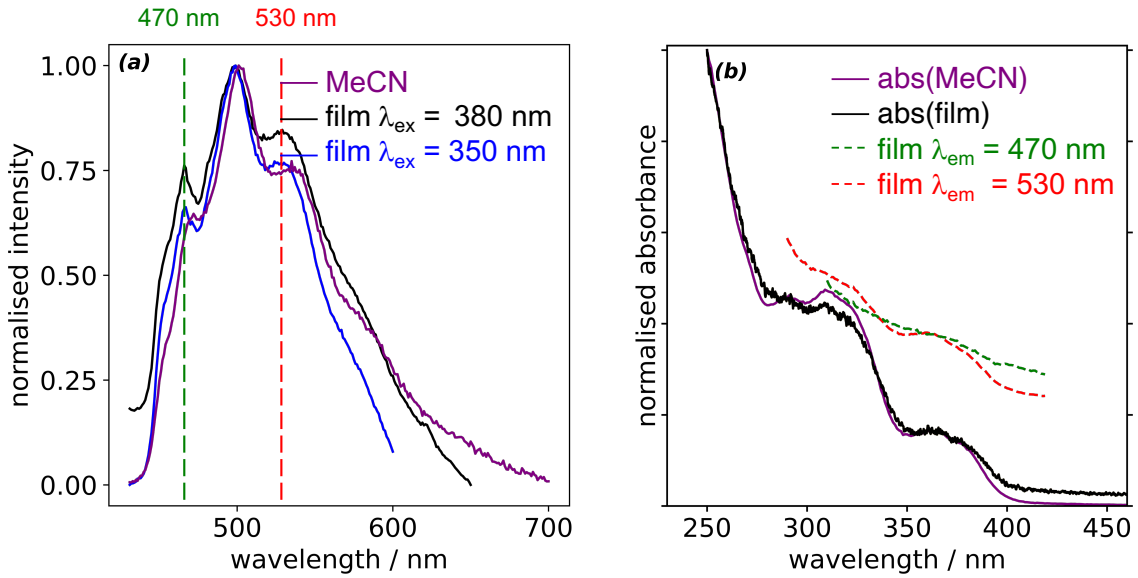

Figure 4.13: *(a) Emission spectrum of [PtL^7(ppy)Cl]PF$_6$ in deaerated CH$_3$CN solution and in 1 wt % PMMA film at λ_{ex} = 380 nm and 350 nm. (b) UV-vis spectrum of [PtL^7(ppy)Cl]PF$_6$ in solution and 1% PMMA film (with offset photoluminescence excitation spectra (dashed) at λ_{em} = 470 (green) and 530 nm (red)).*

To rule out the possibility of a Pt^{II} impurity being involved in the emission, we also prepared PMMA and neat films of the Pt^{II} precursors (Figure 4.14). In each case, the emission maximum is red-shifted (> 0.12 eV) when compared to the corresponding film of the Pt^{IV} analogue. Furthermore, the quantum yields are lower, and the lifetimes are all biexponential and shorter than those for the Pt^{IV} complexes, with one component around 1 µs and the other between 2.5 and 4 µs. These findings affirm that the emission from the Pt^{IV} films is unlikely to originate from any Pt^{II} species.

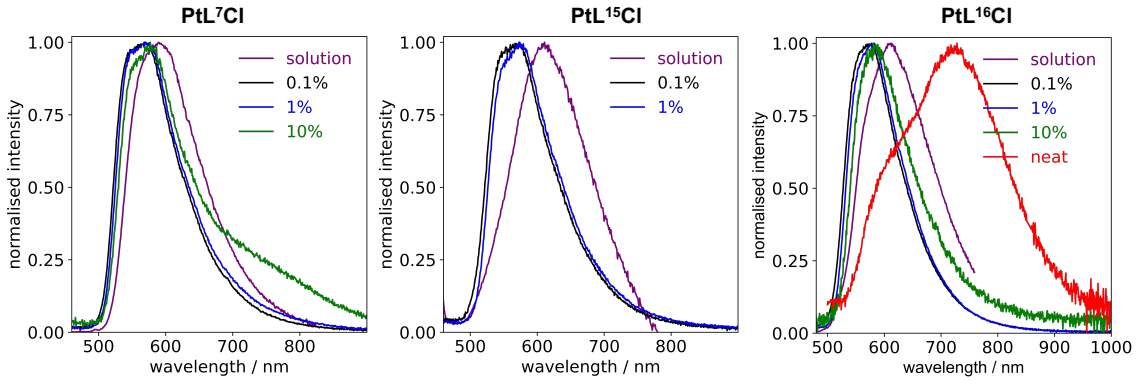

Figure 4.14: *Emission spectra of 0.1%, 1% and 10% PMMA and neat films of complexes PtL^{7}Cl, PtL^{15}Cl and PtL^{16}Cl*

Table 4.3: *Photophysical data for complexes PtL^{7}Cl, PtL^{15}Cl, PtL^{16}Cl, [PtL^{7}(ppy)Cl]PF$_6$, [PtL^{15}(ppy)Cl]PF$_6$ and [PtL^{16}(ppy)Cl]PF$_6$*

	emission at 298 K					emission at 77 K	
complex	λ_{em}/nm	Φ_{lum}/%	τ/µs	k_r/ $10^3 s^{-1}$	k_{nr}/ $10^3 s^{-1}$	λ_{em}/nm	τ/µs
PtL^{7}Cl	590[a]	1.7[a]	0.03[a]	61[a]	3640[a]	529, 571, 611[b]	16[b]
PtL^{15}Cl	617[a]	0.1[a]	0.02[a]	83[a]	55400[a]	530, 557[b]	17[b]
PtL^{16}Cl	610[a]	0.2[a]	0.02[a]	109[a]	49900[a]	548, 579[b]	15[b]
[PtL^{7}(ppy)Cl]$^+$	472, 501, 534[c]	4.0[c]	42[c]	0.94[c]	23[c]	461, 496, 527sh, 536, 571, 619[d]	280[d]
[PtL^{15}(ppy)Cl]$^+$	485, 515, 555[c]	4.3[c]	55[c]	0.78[c]	17[c]	467, 501, 544, 580, 639[d]	350[d]
[PtL^{16}(ppy)Cl]$^+$	475, 508, 545[c]	3.3[c]	64[c]	0.51[c]	15[c]	474, 511, 550, 593, 650[d]	350[d]

[a] in CH_2Cl_2 [b] in diethyl ether/isopentane/ethanol (2:2:1 v/v) [c] in CH_3CN [d] in butyronitrile

Table 4.4: *Photophysical data for complexes PtL^{7}Cl, PtL^{15}Cl, PtL^{16}Cl, [PtL^{7}(ppy)Cl]PF$_6$, [PtL^{15}(ppy)Cl]PF$_6$ and [PtL^{16}(ppy)Cl]PF$_6$ in the solid state at different doping wt % PMMA and in neat films.*

	Φ_{lum}/%				τ/µs		
complex	0.1%	1%	10%	neat	0.1%	1%	10%
PtL^{7}Cl	11	9	3	0.1	1.2, 3.6	1.1, 2.9	0.9, 2.5
PtL^{15}Cl	6	5	2	1	1.1, 3.7	1.5, 4.0	1.0, 3.5
PtL^{16}Cl	9	8	3	1	1.1, 3.9	1.0, 3.6	0.97, 2.5
[PtL^{7}(ppy)Cl]$^+$	7	12	9	1	15	15	14
[PtL^{15}(ppy)Cl]$^+$	24	33	29	4	17	16	14
[PtL^{16}(ppy)Cl]$^+$	25	22	12	0.2	16	17	12

4.5 DFT

Density functional theory (DFT) and time-dependent density functional theory (TD-DFT) calculations with Tamm-Dancoff approximation (TDA) were performed at the level of theory including spin-orbit coupling (SOC) and zeroth-order regular approximation (ZORA). Geometry optimisations in the ground state were performed using B3LYP/ def2-TZVP.

The HOMO of the Pt^{IV} complexes at the S_0 geometry is located mainly on the Pt centre and the cyclometallated phenyl rings of the bidentate and tridentate ligands in the case of $[PtL^{7}(ppy)Cl]PF_6$ and $[PtL^{15}(ppy)Cl]PF_6$, and only on that of the tridentate ligand in the case of $[PtL^{16}(ppy)Cl]PF_6$. The LUMO is located on the pyridine rings of the tridentate ligand for all complexes. Molecular orbital plots of some of the frontier orbitals of the complexes are shown in Figure 4.15.

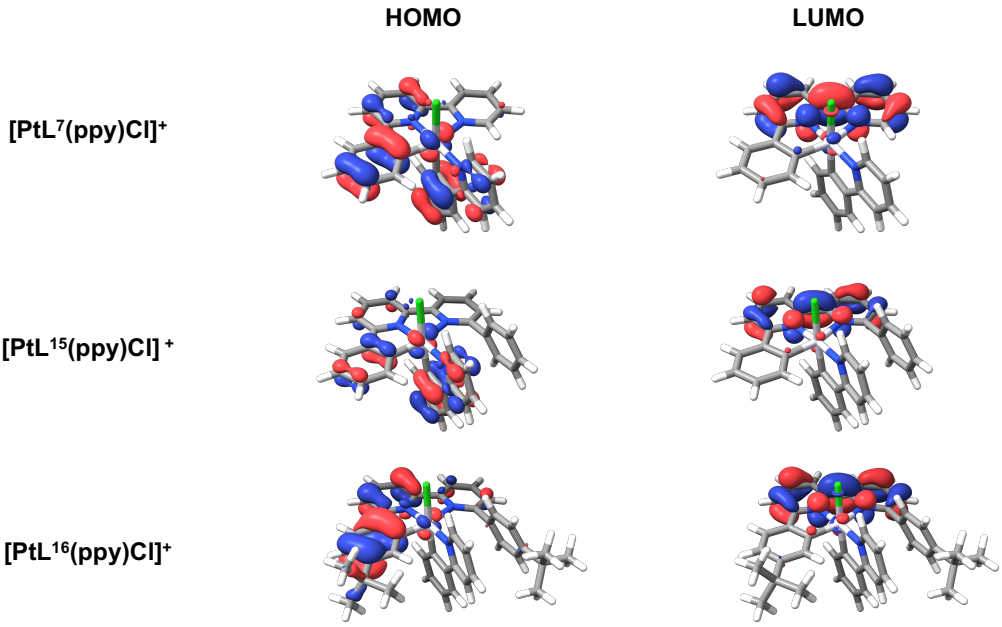

Figure 4.15: *Frontier orbital plots for $PtL^{7}Cl$, $PtL^{15}Cl$ and $PtL^{16}Cl$ at the S_0 geometry.*

Figure 4.16 presents the molecular orbital (MO) energy level diagrams for the ground state of complexes $[PtL^{15}(ppy)Cl]PF_6$ and $[PtL^{16}(ppy)Cl]PF_6$. The HOMO of complex $[PtL^{16}(ppy)Cl]PF_6$ is 0.18 eV higher in energy than that of $[PtL^{15}(ppy)Cl]PF_6$ due to slight electron donation from the ^{t}Bu to the cyclometallated phenyl ring onto which the HOMO is located. This results in a smaller energy gap for the former complex, which aligns with the slight red shift in the absorption and emission spectra.

For complexes [PtL^{15}(ppy)Cl]PF$_6$ and [PtL^{16}(ppy)Cl]PF$_6$, HOMO–1 and HOMO–2 are partially located on the non-cyclometallated phenyl ring of the tridentate ligand, as well as on the *NC* ligand (Figure 4.16). This indicates that these parts of the ligands may play a role in some of the excited states responsible for emission.

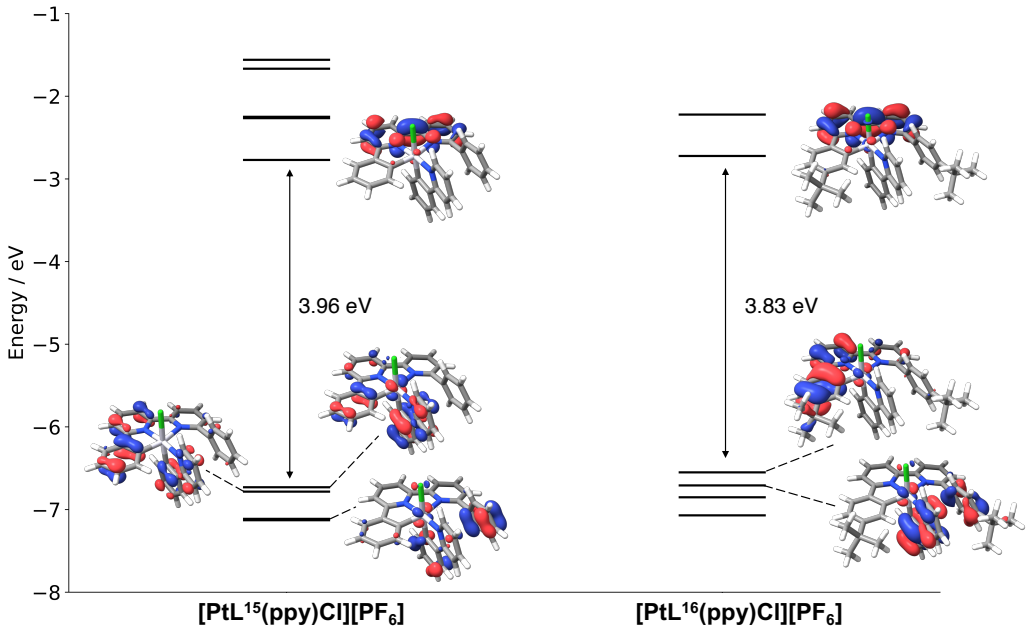

Figure 4.16: *Molecular orbital diagrams showing selected orbitals of complexes PtL^{15}Cl and PtL^{16}Cl, and their energies.*

4.6 Chapter summary

Two new complexes of the type [Pt(*NNC*)(*NC*)Cl]$^+$, incorporating a phenyl substituent at the 6-position of the lateral pyridine ring, were synthesised. The photophysical properties of these complexes in solution were compared to those of the 'parent' unsubstituted [PtL^7(ppy)Cl]PF$_6$. The comparison indicated minimal differences, with both sets of complexes exhibiting quantum yields of $\approx$ 4% and long lifetimes in the range of tens of microseconds. X-ray crystallography showed that, in each case, the phenyl substituent of the *NNC* ligand lies *pseudo*-parallel to the pyridine ring of the *NC* ligand, a feature that we hypothesised could influence the solid-state emission properties of these complexes.

To test this, PMMA films were prepared at three different concentrations (0.1%, 1%, and 10% by weight) as well as neat films of both complexes and [PtL^7(ppy)Cl]PF$_6$. The quantum yields of the two new complexes in PMMA consistently surpassed those of [PtL^7(ppy)Cl]PF$_6$, with increases of up to more than threefold. These results confirm the significant impact of the $\pi - \pi$ interaction on the solid-state photophysical properties of the complexes and will be explored in the future in LEECs.

CHAPTER 5

Dinuclear platinum complexes featuring tridentate ligands

Chapter 5: Dinuclear platinum complexes featuring tridentate ligands

5.1 Introduction

Dinuclear metal complexes can show very distinct photophysical properties, compared to their mononuclear analogues. In the case of coordinatively saturated complexes of d^6 ions like Ir^{III}, the incorporation of a second metal ion can have a beneficial effect on quantum yields, especially for red and NIR emitters.[78–82]

Kozhevnikov, Williams and co-workers reported an Ir complex incorporating a pyrimidine-bridged ditopic ligand (L^1) with two tridentate *NCN* coordinating sites (Figure 5.1).[83] The coordination sphere around each metal centre was completed by a bidentate *NC* tolylpyridine ligand and a monodentate chloride. The *NC* ligand binds with the pyridine nitrogen atom *trans* to the cyclometallated carbon on the tridentate ligand. Three different structural isomers were formed in the reaction and their separation was achieved by column chromatography. The *meso* form occurs when the two chlorides are positioned on the same side of the bis-chelate ligand plane, while the *rac* pair of enantiomers arises when the chloride ligands are on opposite sides of this plane.

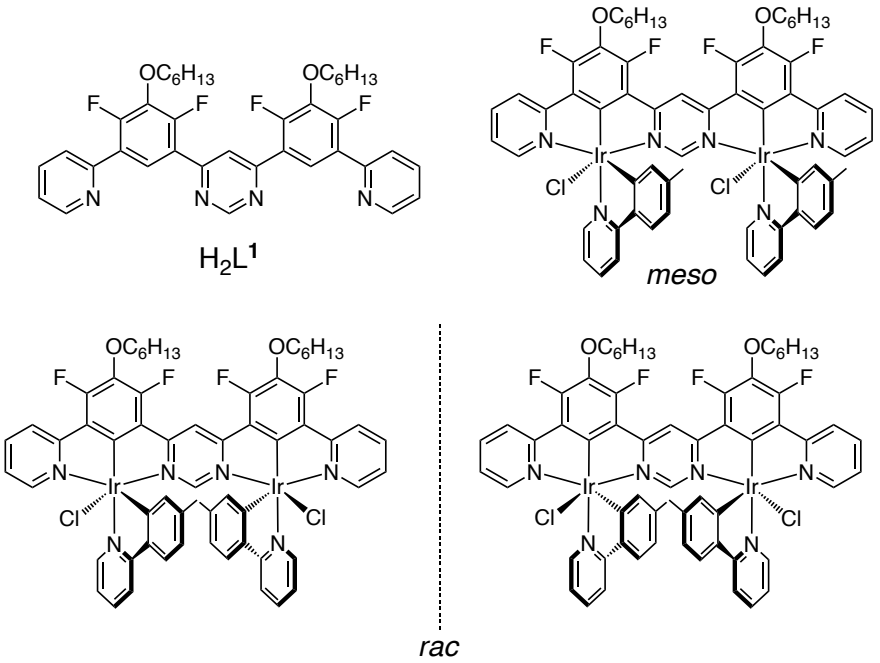

Figure 5.1: *The pyrimidine-bridged ditopic ligand (H_2L^1) and its Ir^{III} complexes reported by Kozhevnikov, Williams and co-workers.*[83]

The photophysical properties of these complexes were investigated and compared to those of their mononuclear analogue (Figure 5.2). The *meso* and *rac* isomers show almost identical photophysical properties to each other. The introduction of a second Ir ion leads to a red shift in the absorption spectrum. This effect was thought to occur due to a stabilisation of the pyrimidine-based π^* orbital. Similarly, a red shift is seen in the emission spectra of the dinuclear complexes compared to that of their mononuclear counterpart, albeit not as large as that seen in the absorption. A red shift in the emission is typically accompanied by a decrease in the quantum yield due to faster non-radiative decay (k_{nr}) and (often) slower radiative decay (k_r). However, in this instance, the dinuclear complexes show an enhanced quantum yield compared with the mononuclear analogue.

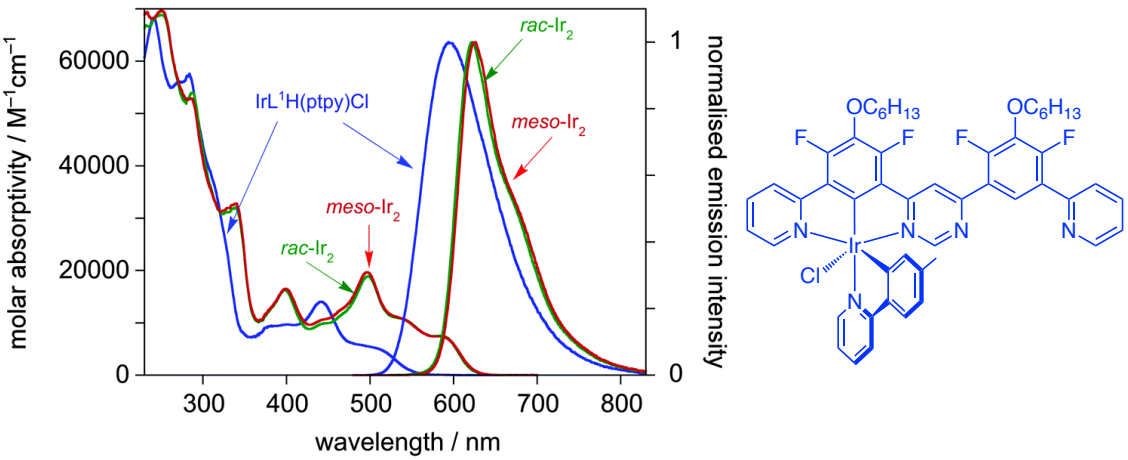

Figure 5.2: *Absorption and photoluminescence spectra of the mononuclear (blue lines) and the rac and meso forms of the dinuclear complex (green and red lines respectively), reported by Kozhevnikov, Williams and co-workers, in solution in CH_2Cl_2 at 298 K. Adapted from ref. 83 with permission from The Royal Society of Chemistry.*

Estimates of the radiative and non-radiative rate constants revealed that while the latter is indeed somewhat increased, the addition of the second metal ion leads to a > 4-fold increase in k_r. The larger red shift in the absorption compared to the emission indicates that the S_1–T_1 energy gap (ΔE_{S-T}) is reduced in the dinuclear complexes. The smaller energy gap could allow for more efficient mixing between these states, leading to more efficient SOC pathways and therefore higher k_r. A review on multinuclear Pt complexes by Williams and co-workers further discusses the potential reasons for such an increase.[78] Dinuclear complexes of this type typically show higher extinction coefficients (as seen in this case), suggesting increased oscillator strengths of the spin-allowed transitions. The allowedness of the phosphorescent transition will

increase with an increase in the oscillator strength of the *singlet* transitions to which the triplet state couples, resulting in higher k_r.

Shafikov *et al.* prepared another complex featuring the aforementioned bis-chelate ligand (**1**) and one with a monotopic *NCN* analogue of the ditopic ligand **1m**, wherein the pyrimidine ring is substituted by pyridine, for comparison (Figure 5.3, left).[84] The coordination sphere was completed by two or one tridentate CNC ligands, respectively. Puttock *et al.* reported a series of Ir^{III} complexes incorporating Schiff-base ONN-NNO bis-chelate ligands (**2**, Figure 5.3, right).[85] The complexes were compared to both their mononuclear counterparts **2'**, where only one Ir was bound to the bis-chelate ligand, as well as to mononuclear complexes with a monotopic analogue of the bis-chelate ligand with a pyridine ring replacing the pyridine **2m**. The coordination sphere around each Ir ion is completed by a tridentate *NCN* ligand.

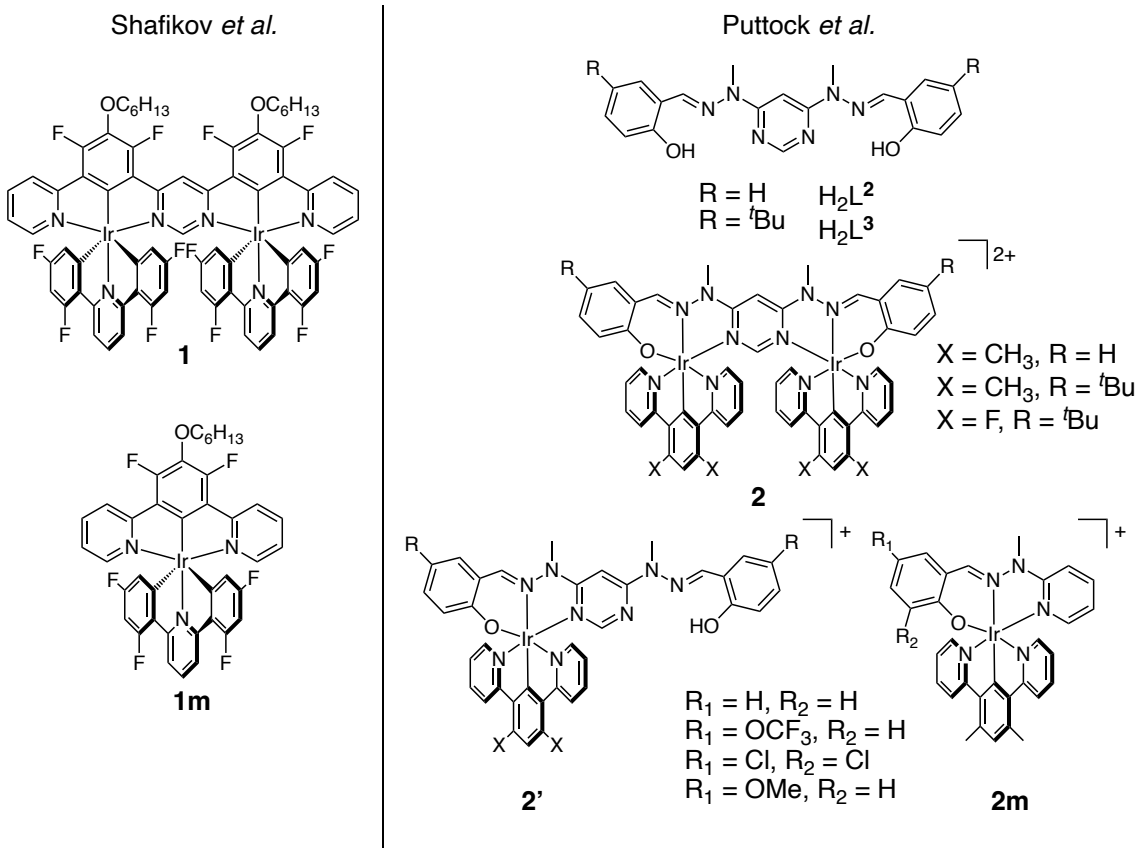

Figure 5.3: *Ir^{III} complexes reported by Shafikov et al.[84] (left) and Puttock et al.[85] (right)*

While complex **1** shows a large red shift in the emission wavelength compared to its mononuclear counterpart **1m** (e.g. from 537 to 642 nm in toluene at 300 K), the class of complexes **2** emit at wavelengths comparable to those of their mononuclear analogues **2'** and **2m**. All of the complexes exhibit a significant increase in luminescence quantum yields compared to their mononuclear counterparts, seemingly attributable to an enhancement in the radiative rate constant.

Similar beneficial effects of a second metal centre can also be observed for platinum. For square planar complexes of Pt^{II}, a rigid linker can hold the two metal centres in close proximity, aiding intramolecular face-to-face interactions. Such a strategy has been widely employed in the search for efficient NIR emitters.[51–53,86,87] However, there are also examples of dinuclear Pt^{II} complexes where the two metal-containing units are rigidly held apart, employing ligands similar to ones described above for Ir^{III}.

The reactions of the aforementioned bis-chelate ligands $H_2L^{\mathbf{1–3}}$ with potassium tetrachloroplatinate in an attempt to obtain dinuclear Pt^{II} complexes were reportedly challenging due to the formation of highly insoluble mono-platinated intermediates, that failed to react further, probably due to their poor solubility.[88,89]

The introduction of two *tert*-butyl groups into the positions *para* to the N of the pyridine rings of the pyrimidine-bridged *NCN-NCN* ligand ($H_2L^{\mathbf{1}}$) led to its successful complexation and thus to the formation of a dinuclear Pt^{II} complex with a chloride ancillary ligand (**3**, Figure 5.4).[88] The corresponding mononuclear complex **3m** with a tridentate ligand was also prepared for comparison. Similar observations to the Ir^{III} examples were noted, including a red shift in absorption and emission spectra, and higher molar absorptivities for the dinuclear complex compared to its mononuclear counterpart. However, the luminescence quantum yield for the former was found to be lower in this case, which was attributed to a much higher k_{nr}, probably due to the influences of the energy gap law, given the low energy emission ($\lambda_{em} \approx 620$ nm). ΔE_{S-T} in the dinuclear complex was found to be sufficiently small that the complex shows thermally activated delayed fluorescence (TADF). While no excimer emission was observed in solution at room temperature, excimer emission centred at $\lambda_{em} = 810$ nm predominates in polystyrene films at concentrations $\geq$ 1% w/w and in neat film. An NIR-emitting OLED device incorporating the complex was fabricated with $EQE_{max} = 0.51\%$ ($\lambda_{EL} = 805$ nm).

A follow-up publication looked at the influence of chloro-to-iodo ancillary ligand exchange on the photophysical properties displayed by the dinuclear complex.[90] The iodo dinuclear complex **4** has around a 3-fold larger k_r, compared to its chloro analogue **3**, attributed to a smaller ΔE_{S-T}, and leading to improved TADF.

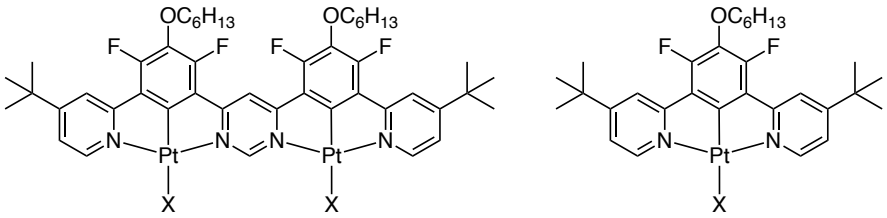

Figure 5.4: *Dinuclear and mononuclear Pt^{II} complexes reported by Pander et al.*[88]

5.2 Aims and objectives

Despite the above interesting properties displayed by Ir^{III} and Pt^{II} complexes, there appear to be no reports of dinuclear Pt^{IV} complexes featuring such ditopic extended conjugated aromatic ligands. Building upon our findings regarding Pt^{IV} complexes incorporating *NNC* ligands discussed Chapters 3 and 4, we were intrigued by the prospect of synthesising analogous dinuclear systems. The synthesis of ditopic bis-tridentate pyrimidine-bridged *CNN-NNC*-coordinating ligands will be described in this chapter, together with an investigation into their complexation to Pt in the +2 and +4 oxidation states.

5.3 Synthesis of the proligands

The ligands H_2L**17–19** were identified as suitable targets and synthesised as shown in Scheme 5.1. The requisite intermediate, 2-phenyl-6-(tributylstannyl)pyridine, was synthesised in two different ways. In the first method, 2-bromo-6-phenylpyridine was prepared by a Suzuki cross-coupling between 2,6-dibromopyridine and phenylboronic acid and subsequently lithiated with ^{n}BuLi. The second one involved the direct lithiation of 2-phenylpyridine with ^{n}BuLi in the presence of 2-dimethylaminoethanol. In both cases, the lithiated phenylpyridine intermediate was reacted with tributyltin chloride to yield 2-phenyl-6-(tributylstannyl)pyridine.

The Stille cross-coupling reaction to 4,6-dichloropyrimidine was first attempted using the Pd^{II} catalyst $Pd(PPh_3)_2Cl_2$. None of the desired pyrimidine-bridged product

was detected by mass spectrometry and the main product isolated was the homo-coupled 6,6'-diphenyl-2,2'-bipyridine. Changing the catalyst to $Pd^0(PPh_3)_4$ gave 4,6-bis(6-phenylpyridin-2-yl)pyrimidine successfully.

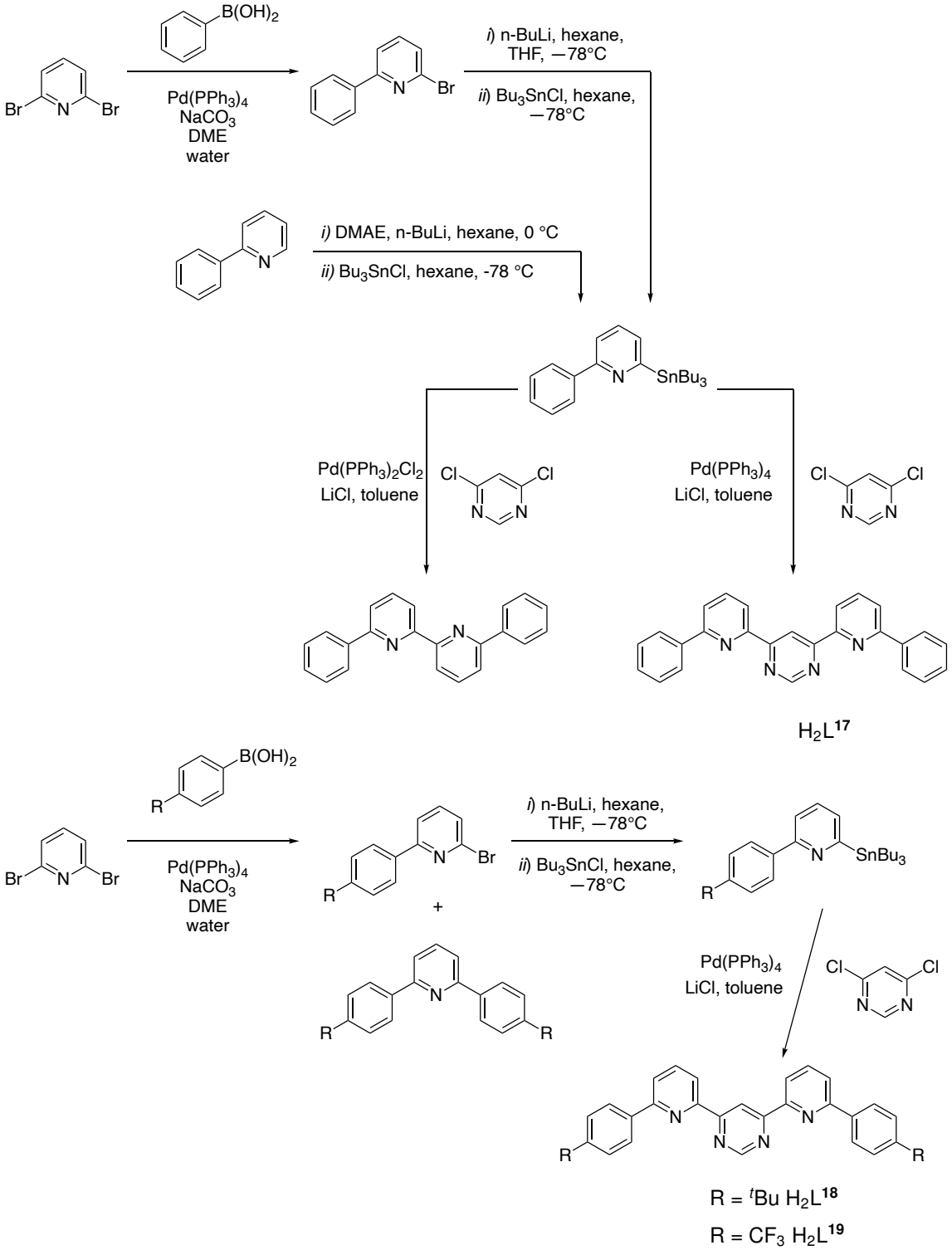

Scheme 5.1: *Synthesis of proligands H_2L^{17}, H_2L^{18} and H_2L^{19}*

Two derivatives of the ligand with a *tert*-butyl (H_2L^{18}) or CF_3 (H_2L^{19}) substituent on each phenyl ring *para* to the pyridine ring were also prepared. In those instances, the first step involved a Suzuki cross-coupling between 2,6-dibromopyridine and the

relevant *p*-substituted phenylboronic acid, identical to the first method described for the synthesis of the unsubstituted ligand. This step resulted in the formation of a 1:1 mixture of the target monocoupled product and a dicoupled *p*-phenyl disubstituted 2,6-diphenylpyridine in both cases, which required separation by reverse phase column chromatography. The monocoupled product was then lithiated, stannylated and reacted with 4,6-dichloropyrimidine to give the disubstituted bis-chelate product, as before.

5.4 Preparation of the complexes

The complexation reactions of H_2L^{17} with K_2PtCl_4 in acetic acid resulted in the exclusive formation of the mononuclear Pt^{II} complex (Scheme 5.2). The incorporation of the second metal ion was attempted by using acetonitrile / water as the solvent and / or by increasing the number of equivalents of K_2PtCl_4 but these efforts were unsuccessful. Assuming that the poor solubility of the mononuclear complex was preventing further reaction, we decided to prepare the *tert*-butyl- and CF_3-substituted derivatives with the aim to enhance the solubility of the ligand and the resulting mononuclear complex. However, the complexation reaction of H_2L^{18} also resulted solely in the formation of the mononuclear complex, whereas that of H_2L^{19} yielded a mixture of other products whose ^1H NMR did not indicate the formation of either a mono- or dinuclear complex. $HL^{18}PtCl$ was isolated as a red solid after filtration through a plug of silica with CH_2Cl_2.

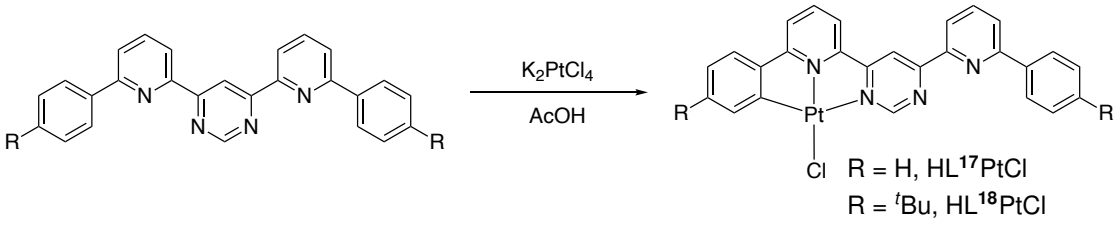

Scheme 5.2: *Synthesis of mononuclear complexes $HL^{17}PtCl$ and $HL^{18}PtCl$*

Crystals suitable for X-ray diffraction of the mononuclear complex $HL^{17}PtCl$ were obtained from the slow evaporation of a CH_2Cl_2 solution (Figure 5.5).

Since our attempts to incorporate the second metal were unsuccessful, we proceeded with the oxidation of the mononuclear complexes with $PhICl_2$ (Figure 5.3). The resulting $HL^{17}Pt^{IV}Cl_3$ and $HL^{18}Pt^{IV}Cl_3$ complexes were isolated as yellow solids.

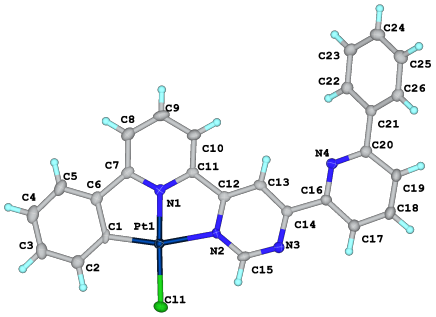

Pt – C	1.992(5)
Pt – $N^{pyridine}$	2.119(4)
Pt – $N^{pyrimidine}$	1.954(4)
Pt – Cl	2.3020(13)
C – Pt – $N^{pyrimidine}$	162.01(19)
$N^{pyridine}$ – Pt – Cl	177.45(12)

Figure 5.5: *Molecular structure of the $HL^{18}PtCl$ in the crystal (left) with selected bond lengths (Å) and bond angles (°) (right).*

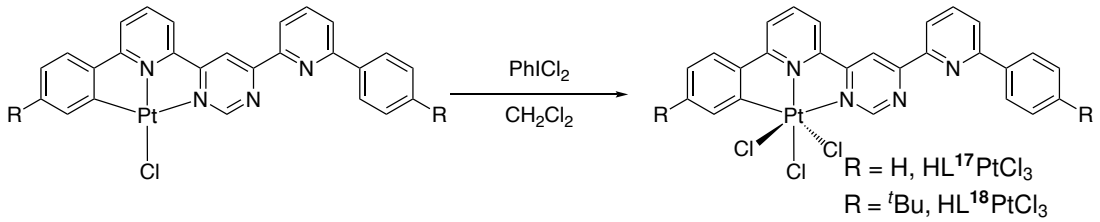

Scheme 5.3: *Synthesis of mononuclear complexes $HL^{17}PtCl_3$ and $HL^{18}PtCl_3$.*

The ^{1}H NMR spectra of the Pt^{IV} complexes show the expected deshielding of all of the protons on the rings bound to Pt upon oxidation (see Chapter 3). The aromatic regions of the ^{1}H NMR spectra of $HL^{17}PtCl$ and $HL^{17}PtCl_3$ are shown in Figure 5.6.

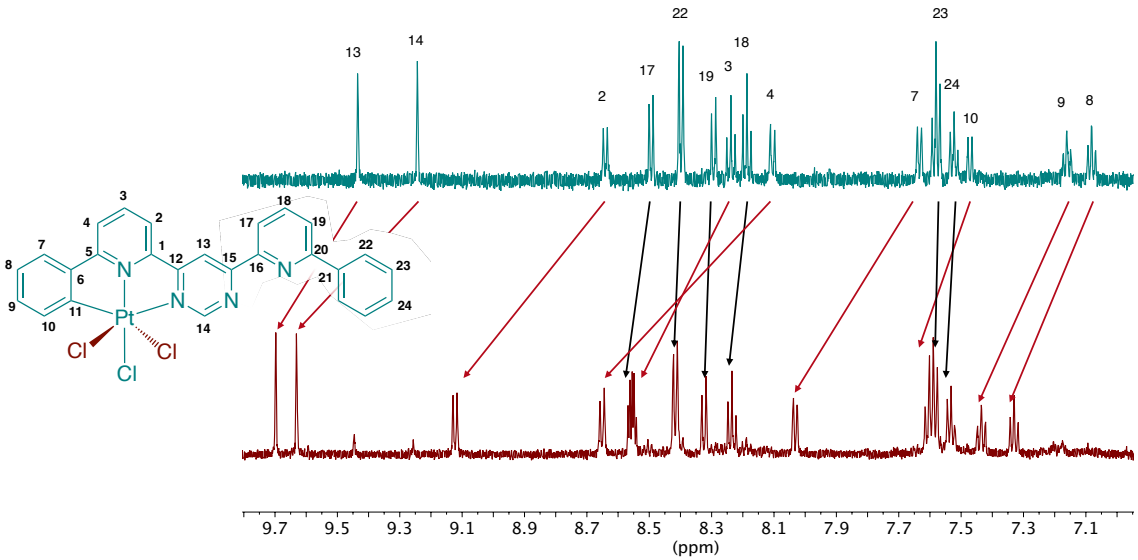

Figure 5.6: *The aromatic regions of the ^{1}H NMR spectra of $HL^{17}PtCl$ and $HL^{17}PtCl_3$ in d_6-DMSO at 599 MHz. All protons are numbered and arrows show the shift upon oxidation. Red and black arrows refer to resonances on the platinated and uncomplexed units, respectively.*

We speculated whether the mononuclear Pt^{IV} complexes might be able to be platinated at the uncoordinated *NNC* unit more readily than the Pt^{II} analogues, and so they were treated with K_2PtCl_4 in acetic acid (Scheme 5.4).

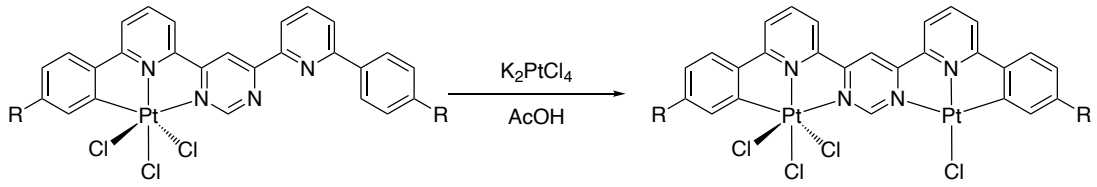

Scheme 5.4: *Synthesis of dinuclear complexes* $L^{17}(Pt^{II}Cl)(Pt^{IV}Cl_3)$ *and* $L^{18}(Pt^{II}Cl)(Pt^{IV}Cl_3)$

In each case, the product was washed with water, methanol and diethyl ether, extracted into CH_2Cl_2, filtrated through a silica plug and the solvent removed under reduced pressure to yield a brown solid. Figure 5.7 shows the aromatic regions of the ^{1}H NMR spectra of $HL^{17}PtCl_3$ and the product of the second complexation reaction. The ^{1}H NMR spectrum of the product reveals a shift in some peaks compared to the starting material, suggesting that a different species had formed. There are two pairs of protons on the phenyl ring of the starting material (labelled 22 and 23), each with an integration of 2 in the ^{1}H NMR spectrum. The ^{1}H NMR spectrum of the product of the reaction shows 16 different environments, each with an integration of 1, which would be expected for a dinuclear complex with one Pt centre in a 4+ oxidation state and one Pt centre in a 2+ oxidation state. The full assignment of the ^{1}H NMR spectrum of this complex was not achieved due to degradation on the timescale of the 2D NMR experiments. Although the analogous product of the same reaction with *tert*-butyl-substituted $HL^{18}PtCl_3$ was not isolated successfully, we proceeded with subsequent steps.

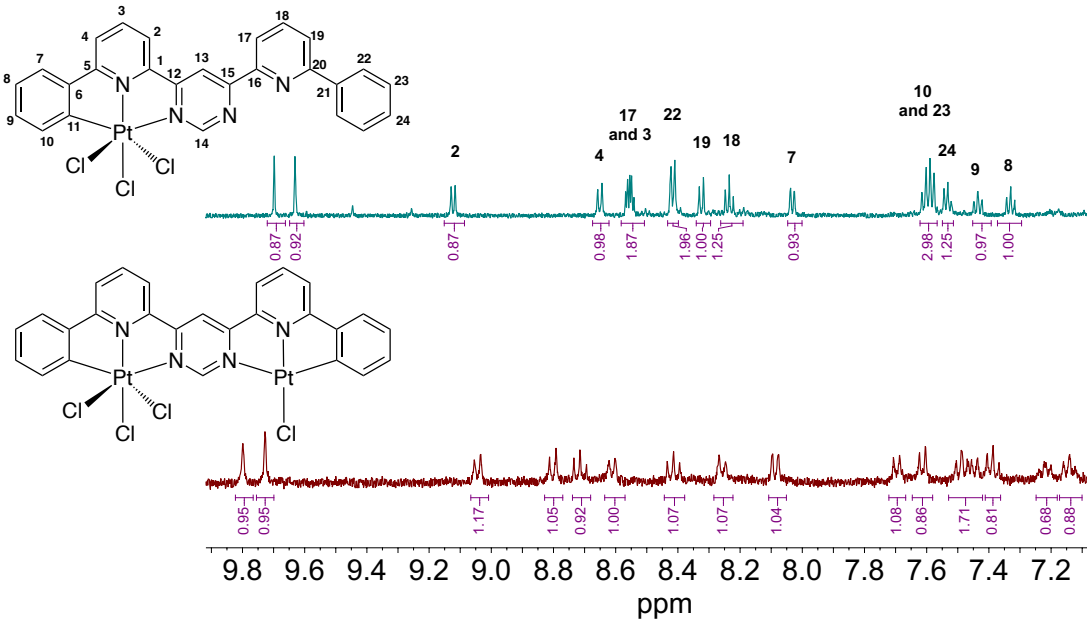

Figure 5.7: *The aromatic regions of the ^{1}H NMR spectra of $HL^{17}PtCl_3$ and $L^{17}(Pt^{II}Cl)(Pt^{IV}Cl_3)$*

The next step involved the oxidation of the Pt^{II} / Pt^{IV} complexes to obtain the dinuclear Pt^{IV} complexes (Scheme 5.5).

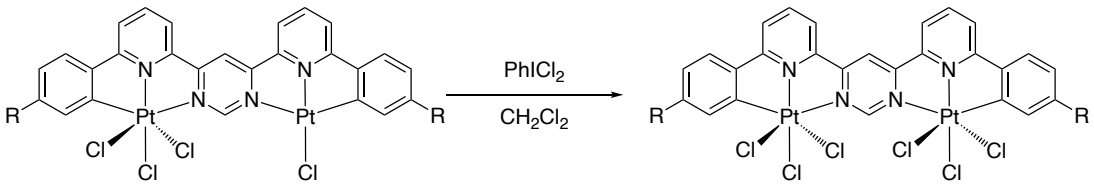

R = H, $L^{17}(Pt^{IV}Cl_3)_2$
R = ^{t}Bu, $L^{18}(Pt^{IV}Cl_3)_2$

Scheme 5.5: *Synthesis of dinuclear complexes $L^{17}(Pt^{IV}Cl_3)_2$ and $L^{18}(Pt^{IV}Cl_3)_2$*

The ^{1}H NMR spectra of the products of those reactions indicated the formation of the target complexes for both L^{17} and L^{18}, showing a reduction in the number of distinct environments due to the formation of the C_{2v} symmetric Pt^{IV} / Pt^{IV} complexes. Figure 5.6 shows the ^{1}H NMR spectrum of complex $L^{18}(Pt^{IV}Cl_3)_2$ with numbers indicating peaks and their corresponding protons on the structure.

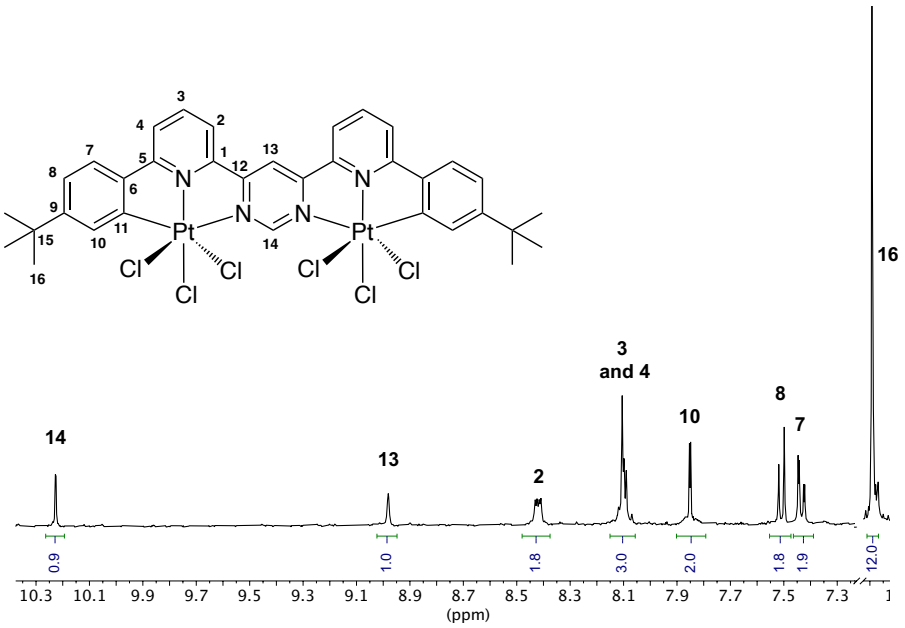

Figure 5.8: *The ^{1}H NMR spectrum of $(Pt^{IV}Cl_3)_2L^{18}$ and its assignments.*

Multiple attempts were made at the reaction of the dinuclear Pt^{IV} / Pt^{IV} complexes with 2-phenylpyridine to form dinuclear analogues of the complexes discussed in Chapters 3 and 4. Assuming that the 2-phenylpyridine binds with the pyridine nitrogen *trans* to the pyridine of the *NNC* unit, as seen in the previous chapters for the mononuclear Pt^{IV} complexes of this type, different isomers could potentially form depending on whether the chloride ligands are on one (*meso*) or opposite sides of the bis-chelate ligand plane (*rac*). The latter will comprise of a racemic mixture of enantiomers.

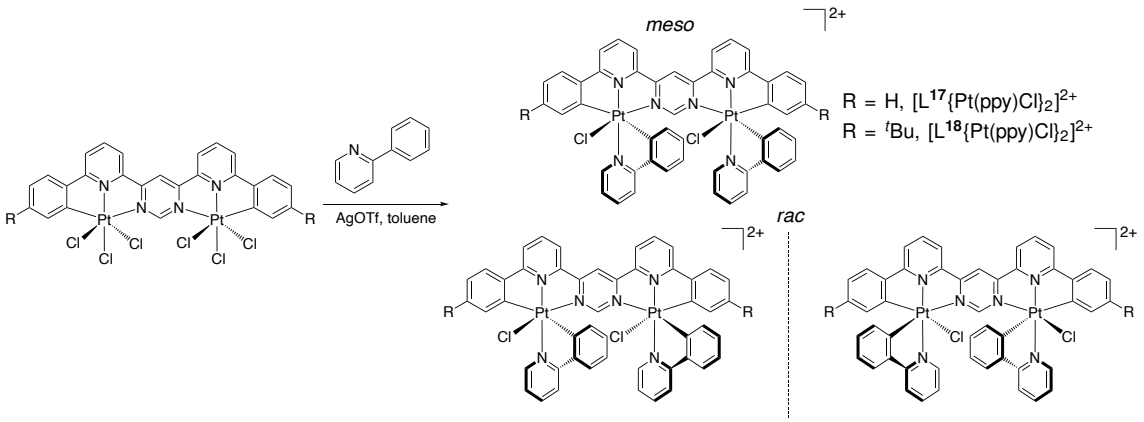

Scheme 5.6: *Synthesis of $[L^{17}\{Pt(ppy)Cl\}_2]^{2+}$ and $[L^{18}\{Pt(ppy)Cl\}_2]^{2+}$, showing potential meso and rac isomers.*

Small amounts of a solid, whose ^{1}H NMR spectrum was consistent with that expected for the target complex, were isolated for L^{18} after multiple recrystallisations and reverse-phase column chromatography. Figure 5.9 shows the ^{1}H NMR spectra of $[L^{18}\{Pt(ppy)Cl\}_2]^{2+}$ and of $[PtL^{7}(ppy)Cl]^{+}$ for comparison. The most deshielded signal (10.03 ppm, labelled **2** in Figure 5.9) in the ^{1}H NMR spectrum of $[PtL^{7}(ppy)Cl]^{+}$ corresponds to the proton *ortho* to the nitrogen of the pyridine ring of the *NC* ligand. Satellites due to coupling to ^{195}Pt can be observed with $^{3}J_{^{195}Pt\text{-}^{1}H} \approx 25$ Hz. The most deshielded signal in the ^{1}H NMR spectrum of $[L^{18}\{Pt(ppy)Cl\}_2]^{2+}$ can be seen at 10.11 ppm, also showing satellites with $^{3}J_{^{195}Pt\text{-}^{1}H} \approx 25$ Hz. Similarly, the most shielded signals at 6.36 ppm and 6.24 ppm in the ^{1}H NMR spectrum of $[PtL^{7}(ppy)Cl]^{+}$ show satellites due to coupling to Pt with $^{3}J_{^{195}Pt\text{-}^{1}H} \approx 33$ Hz each, and correspond to the protons *ortho* to the cyclometallated carbon atoms on the phenyl rings of the *NC* (**3**) and *NNC* (**1**) ligands, respectively. Likewise, the peaks at 6.42 ppm and 6.05 ppm in the ^{1}H NMR spectrum of $[L^{18}\{Pt(ppy)Cl\}_2]^{2+}$ also show satellites with $^{3}J_{^{195}Pt\text{-}^{1}H} \approx 33$ and 35 Hz and likely correspond to the protons *ortho* to the cyclometallated carbon atoms on the phenyl rings of the *NC* and bis-chelate ligands, respectively. $[L^{18}\{Pt(ppy)Cl\}_2]^{2+}$ was purified by reverse phase HPLC to give very small amounts of product which were used for the photophysical studies. Notably, the ^{1}H NMR suggested the formation of a single species, but the assignment to a structural isomer (*meso* or *rac*, discussed above) was not achieved.

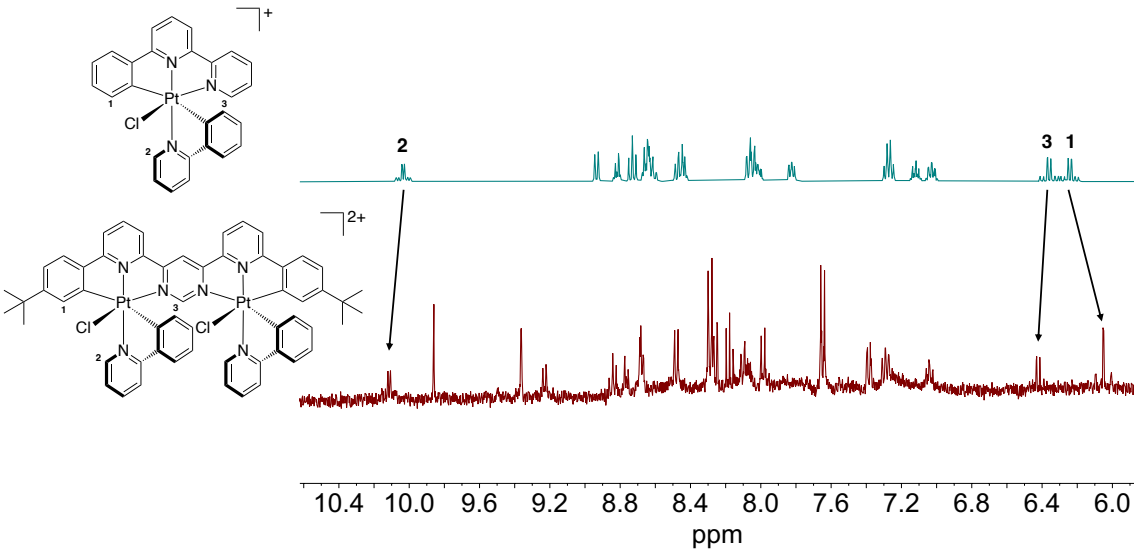

Figure 5.9: *The ^{1}H NMR spectra of $[PtL^{7}(ppy)Cl]^{+}$ and $[L^{18}\{Pt(ppy)Cl\}_2]^{2+}$ in d_6-acetone at 400 MHz with numbers indicating peaks and their corresponding protons. Only the meso isomer of complex $[L^{18}\{Pt(ppy)Cl\}_2]^{2+}$ is shown.*

5.5 Photophysical properties

5.5.1 Absorption

The absorption spectra of complexes $HL^{17\text{-}18}PtCl$ and $HL^{17\text{-}18}PtCl_3$ are shown in Figure 5.10. The intense transitions at high energy (< 300 nm) can be ascribed to $\pi - \pi^*$ transitions within the ligands. The main contrast between the spectra of the Pt^{II} and Pt^{IV} complexes is the blue shift of the lowest energy band in the Pt^{IV} complexes, which aligns with the decrease in the energy of the d-orbitals, associated with increasing oxidation state, as discussed in the previous chapters. The lowest energy band of the Pt^{II} complexes extends all the way up to 600 nm.

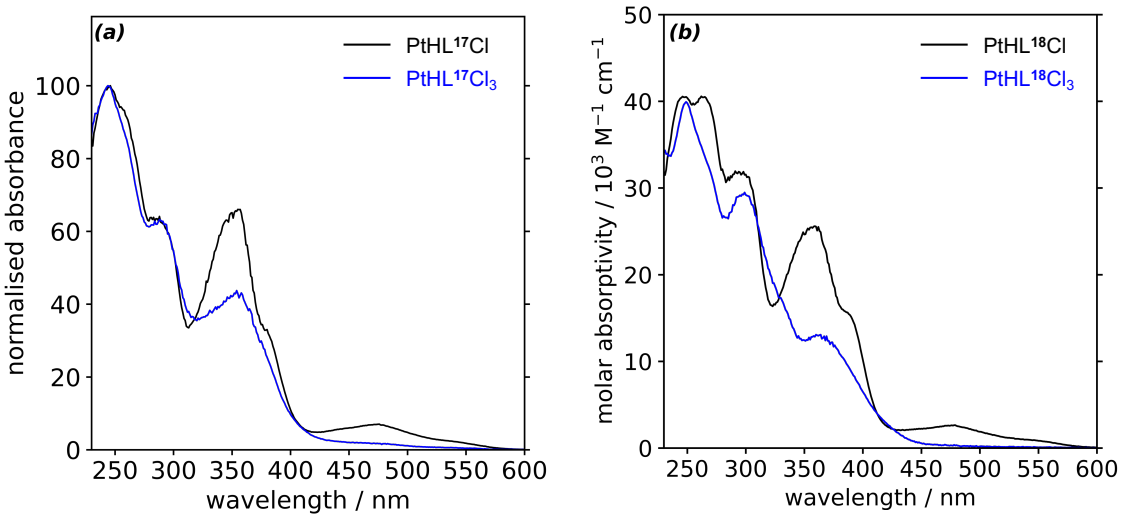

Figure 5.10: *UV-vis absorption spectra of (a) $HL^{17}PtCl$ and $HL^{17}PtCl_3$, and (b) $HL^{18}PtCl$ and $HL^{18}PtCl_3$ in CH_2Cl_2 at 298 K.*

The absorption profile of complex $[L^{18}\{Pt(ppy)Cl\}_2]^{2+}$ resembles that of its mononuclear Pt^{IV} precursor $HL^{18}PtCl_3$ (Figure 5.11). Note that molar absorptivity data for complex $[L^{18}\{Pt(ppy)Cl\}_2]^{2+}$ were not collected due to the limited amount of product obtained.

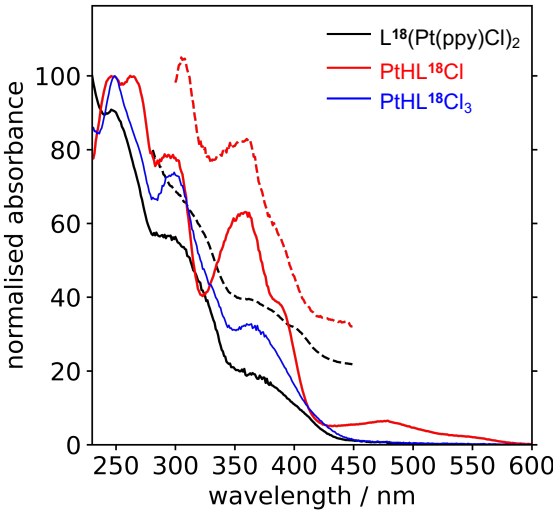

Figure 5.11: *UV-vis absorption spectrum of $[L^{18}\{Pt(ppy)Cl\}_2]^{2+}$ (with offset photoluminescence excitation spectrum (dashed)) in deoxygenated CH_3CN at 298 K with the spectra of $HL^{18}PtCl$ and $HL^{18}PtCl_3$ in CH_2Cl_2 at 298 K reproduced for comparison.*

Table 5.1: *UV-vis absorption data for $HL^{18}PtCl$ and $HL^{18}PtCl_3$ in CH_2Cl_2 at 298 K.*

complex	absorption λ_{max}/nm (ε/$M^{-1}cm^{-1}$)
$HL^{18}PtCl$	246 (40500), 264 (40500), 296 (31500), 357 (25400), 390sh (15200), 479 (2600), 555 (760)
$HL^{18}PtCl_3$	248 (39800), 299 (29500), 366 (12700)

5.5.2 Emission

$HL^{18}PtCl$ is weakly emissive in deoxygenated dichloromethane solution at room temperature and in a glass of diethyl ether/isopentane/ethanol (2:2:1 v/v) at 77 K (Figure 5.12, Table 5.2). The profile of its excitation spectrum matches that of its absorption. $HL^{18}PtCl$ shows broad emission with a quantum yield of 0.2% at room temperature in deoxygenated CH_2Cl_2. At 77 K, its emission is more structured with the 0,0 component being of the highest intensity.

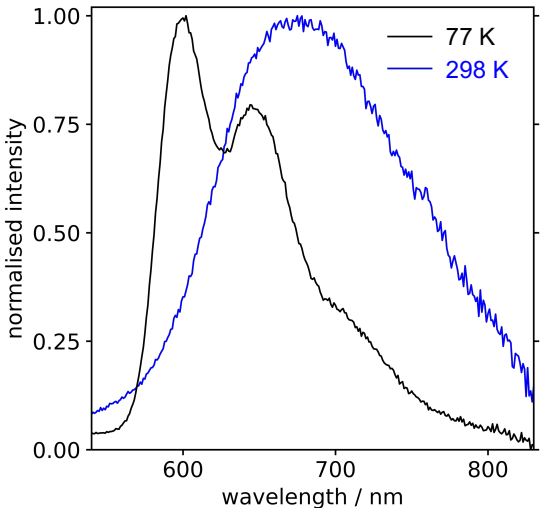

Figure 5.12: *Emission spectra of $HL^{18}PtCl$ in a glass of diethyl ether/isopentane/ethanol (2:2:1 v/v) at 77 K (black) and in deoxygenated CH_2Cl_2 at 298 K (blue).*

$[L^{18}\{Pt(ppy)Cl\}_2][PF_6]_2$ is emissive in deoxygenated CH_3CN solution at room temperature and in a glass of butyronitrile at 77 K. Its excitation spectrum closely matches that of its absorption spectrum (Figure 5.11). Its emission spectra are shown in Figure 5.13, with numerical data in Table 5.2. The data for $[PtL^7(ppy)Cl]PF_6$ are included for comparison. The emission of $[L^{18}\{Pt(ppy)Cl\}_2][PF_6]_2$ is red shifted compared to that of $[PtL^7(ppy)Cl]PF_6$. The radiative rate constant (k_r) was estimated to be 1200 s^{-1} for $[L^{18}Pt(ppy)Cl_2][PF_6]_2$, which is close to the value of 940 s^{-1} for $[PtL^7(ppy)Cl]PF_6$. However, a large increase in k_{nr} results in an overall shorter lifetime and lower luminescence quantum yield.

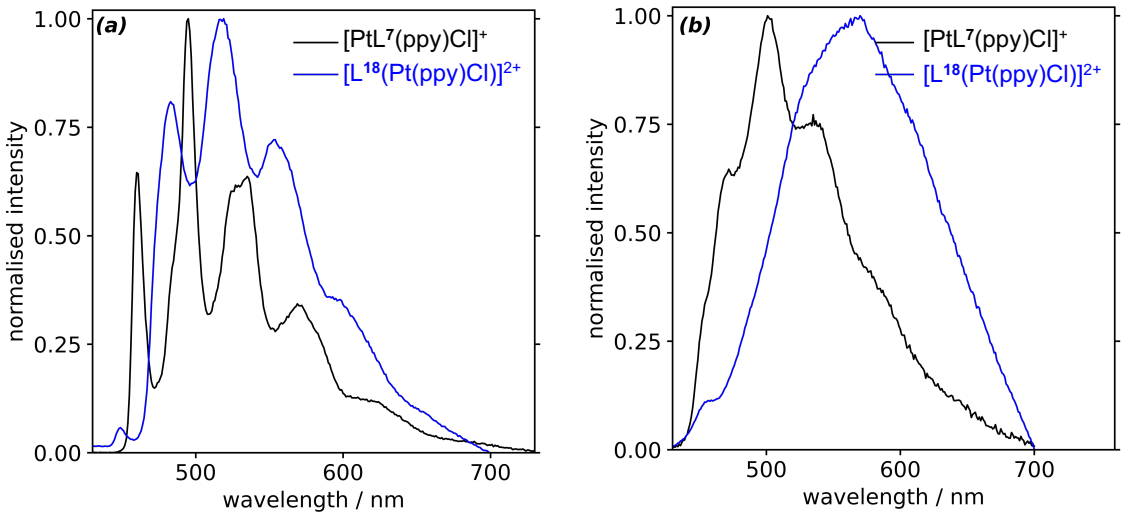

Figure 5.13: *Emission spectra of $[PtL^7(ppy)Cl]^+$ and $[L^{18}\{Pt(ppy)Cl\}_2]^{2+}$ in (a) butyronitrile at 77 K (b) deoxygenated CH_3CN at 298 K.*

Table 5.2: *Photophysical data for complexes HL[18]PtCl, [PtL[7](ppy)Cl]$^+$ and [L[18]{Pt(ppy)Cl}$_2$]$^{2+}$*

complex	emission at 298 K					emission at 77 K	
	λ_{em}/nm	Φ_{lum}/%	τ/µs	k_r/ 10^3s^{-1}	k_{nr}/ 10^3s^{-1}	λ_{em}/nm	τ/µs
HL[18]PtCl	675[a]	0.2[a]	0.03[a]	87[a]	49900[a]	600, 647, 720[b]	12[b]
[PtL[7](ppy)Cl]$^+$	472, 501, 534 [c]	4.0[c]	42[c]	0.94[c]	23[c]	461, 496, 527sh, 536, 571, 619[d]	280[d]
[L[18]{Pt(ppy)Cl}$_2$]$^{2+}$	565[c]	1.6[c]	13[c]	1.2[c]	75[c]	484, 519, 553, 598, 660[d]	150[d]

[a]in CH_2Cl_2 [b]in diethyl ether/isopentane/ethanol (2:2:1 v/v) [c]in CH_3CN [d]in butyronitrile

5.6 Chapter summary

Three ditopic bis-tridentate pyrimidine-bridged *CNN-NNC* ligands were prepared. The complexation reaction of the unsubstituted H_2L^{17} and *t*-Bu substituted H_2L^{18} resulted in the formation of a mononuclear Pt^{II} complex, whereas that of the CF_3-substituted H_2L^{19} gave no evidence of either a mono- or dinuclear complex, but to some other unidentified products. The direct addition of a second Pt^{II} ion to the mononuclear Pt^{II} complexes was not achieved. However, oxidation to Pt^{IV} and the subsequent reaction of the mononuclear Pt^{II} compounds with K_2PtCl_4 led to the formation of dinuclear Pt^{II} / Pt^{IV} complexes. The oxidation of the resulting complexes yielded the dinuclear Pt^{IV} complexes $L^{17}(PtCl_3)_2$ and $L^{18}(PtCl_3)_2$. The reaction of $L^{18}(PtCl_3)_2$ with 2-phenylpyridine resulted in the isolation of trace amounts of [L[18]{Pt(ppy)Cl}$_2$]$^{2+}$, which was used for the photophysical studies.

The photophysical properties of [L[18]{Pt(ppy)Cl}$_2$][PF_6]$_2$ were compared to those of [PtL[7](ppy)Cl]PF_6. As discussed for the examples in the chapter introduction, while [L[18]Pt(ppy)Cl$_2$][PF_6]$_2$ exhibits a red-shifted emission relative to [PtL[7](ppy)Cl]PF_6, the k_r values remain closely comparable. [L[18]{Pt(ppy)Cl}$_2$][PF_6]$_2$ shows a luminescence quantum yield of 1.6% and a lifetime of 13 µs.

CHAPTER 6

Tetradentate *NCCN* ligands

Chapter 6: Tetradentate *NCCN* ligands

6.1 Introduction

The inherent flexibility of Pt^{II} complexes featuring bidentate and, to a lesser extent, tridentate ligands may often lead to out-of-plane geometric distortion in the excited state relative to the ground state, which promotes non-radiative decay pathways. The use of more rigid *tetradentate* ligands offers a potential strategy to mitigate this problem.

Tetradentate ligand design in the literature has mostly employed the use of a spacer atom (N, O or C) to join together two bidentate *NC*-, *NN*- or *CC*-coordinating units. Huo and co-workers made several different types of Pt^{II} complexes incorporating an aniline N-spacer between the two bidentate units in the ligand (Figure 6.1).[91,92] They feature *CNNC*, *NCCN*, or *CCNN* coordinating units. All of the complexes are luminescent with the *CNNC*-type complexes showing the highest quantum yields of $\approx$ 75% in deoxygenated 2-methyltetrahydrofuran solution at room temperature.

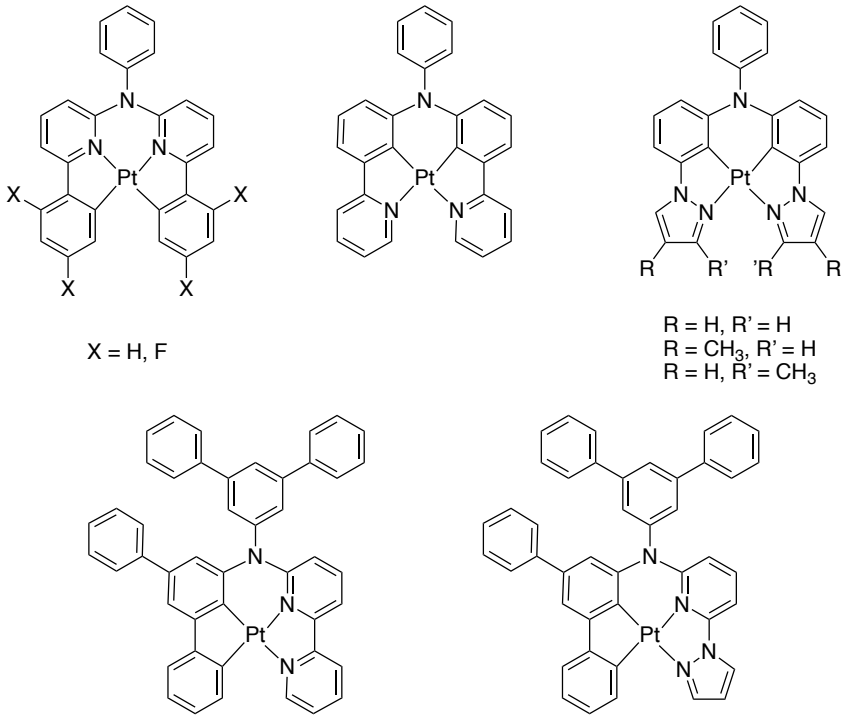

Figure 6.1: *Pt^{II} complexes of tetradentate ligands reported by Huo and co-workers.*[91]

The Pt(*CNNC*) series was later expanded by Solomatina *et al.* who examined the effect of different substituents on the phenyl ring, as well as the effect of replacing one or both phenyl rings by a thiophene or a benzothiophene ring.[93] Their chemical structures and a summary of the photophysical properties in deaerated THF solution at room temperature are shown in Figure 6.2. The replacement of the phenyl rings by a sulfur-containing heterocycle leads to a red-shift in the emission maxima, accompanied by a decrease in the quantum yields.

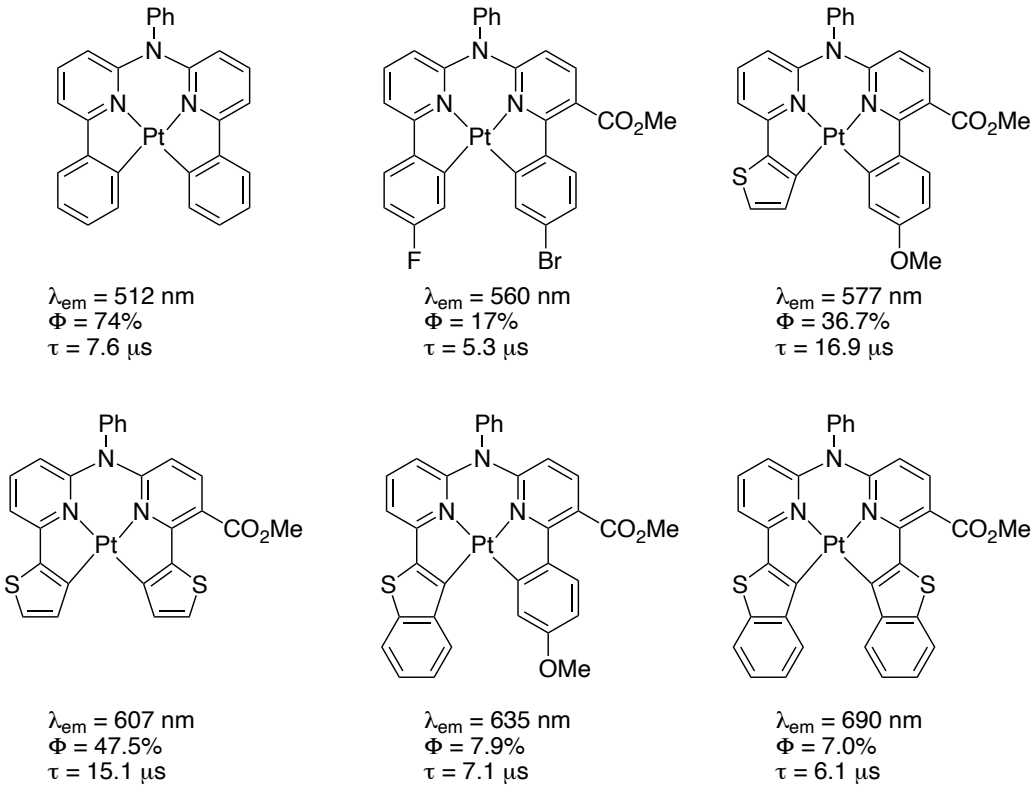

Figure 6.2: *Pt(CNNC) complexes with their corresponding room-temperature emission band maxima (λ_{em}), quantum yields (Φ) and lifetimes (τ). Top left complex was reported by Vezzu et al.[91] and the rest by Solomatina et al.[93]*

Similarly, Yang and co-workers[94,95] looked at derivatives of the *NCCN*-type complexes with an N-spacer by replacing the pyridine rings with isoquinoline, δ-carboline or quinolone moieties. All of the complexes were incorporated into devices showing red to NIR emission and high external quantum efficiencies (up to 31.8%).

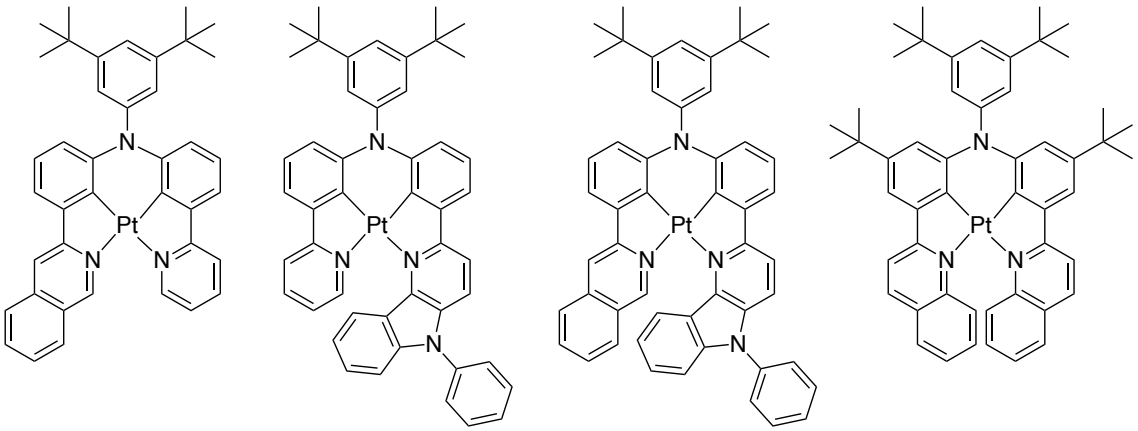

Figure 6.3: *Complexes featuring tetradentate NCCN ligands and their corresponding electroluminescence peak (λ_{EL}) and external quantum efficiencies (EQE).*[94,95]

Pt^{II} complexes with a tetradentate *CNNC* ligand linked by a carbon spacer atom were prepared by Feng *et al.* (Figure 6.4).[96] The complexes were functionalised with norbornene and co-polymerised with a bis(carbazolyl)benzene-based co-monomer. The resulting co-polymers showed almost identical photophysical properties to the discrete complexes, exhibiting bright green luminescence.

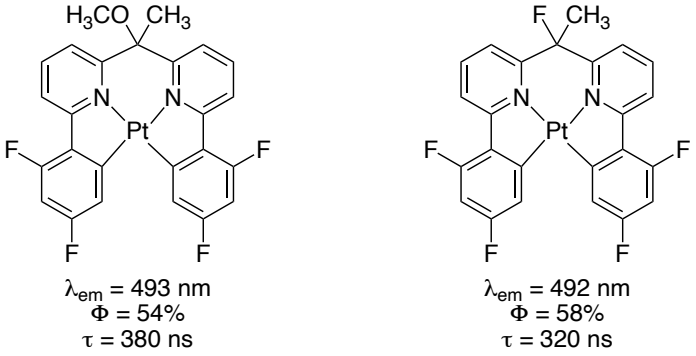

Figure 6.4: *Complexes featuring tetradentate ligands in which two NC units are connected by a carbon linker, along with their corresponding emission band maxima (λ_{max}), luminescence quantum yields (Φ) and lifetimes (τ) in degassed CH_2Cl_2 at room temperature.*[96]

Liao *et al.*[97] reported $N^{-}NNN^{-}$ Pt^{II} complexes with a carbon spacer atom (Figure 6.5). The ligand structures incorporate a spiro-fluorene or acridine unit linked to two bidentate 2-pyridyl triazole or pyrazole moieties. The complexes show very high quantum yields of up to 88% in CH_2Cl_2 solution at room temperature.

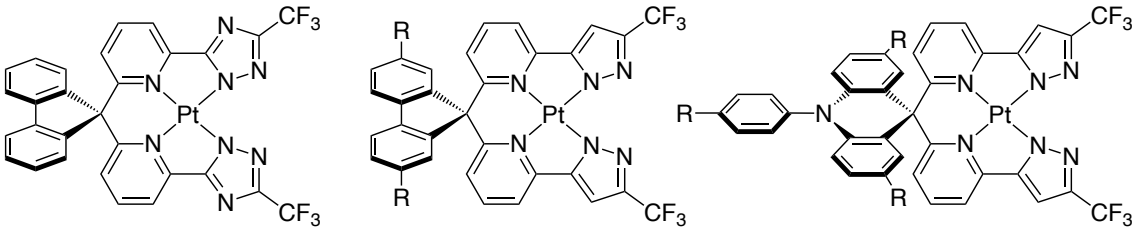

Figure 6.5: *Complexes featuring tetradentate ligands in which two NN⁻ units are connected by a carbon linker, along with their corresponding luminescence quantum yields (Φ).*[97]

Jian Li and co-workers looked at the Pt^{II} complexes of a number of *NCCN*-ligands with an O-spacer atom bridging two different or two of the same *NC* moieties, e.g., methyl-2-phenylimidazole, 3,5-dimethyl-1-phenylpyrazole, phenoxyl pyridine, carbazolyl pyridine and phenyl methyl-imidazole.[98–101] The complexes showed high quantum yields in PMMA films and were incorporated into devices with EQE values of up to 24.8%.

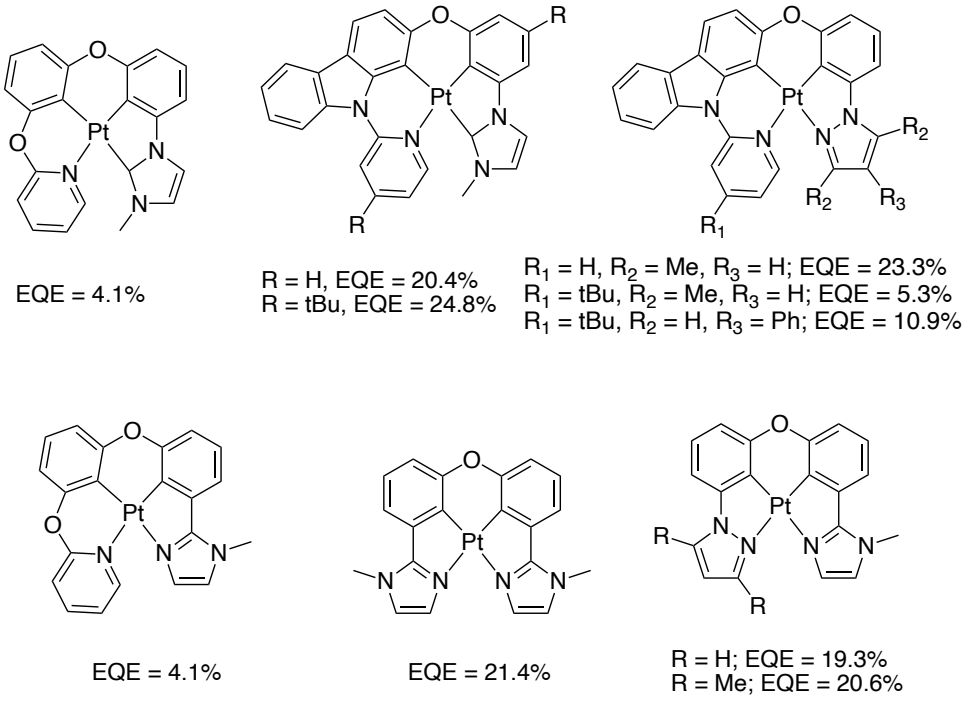

Figure 6.6: *Chemical structures of tetradentate complexes, along with their corresponding external quantum efficiencies (EQE).*[98–101]

Figure 6.7 a)–c) shows the EL spectra of three monochromatic devices employing three different *NCCN* complexes.[101] The testing of different structures for OLEDs led to the fabrication of a Pt-based RGB white OLED, incorporating three different emissive layers, each employing one of the three *NCCN* complexes, with peak EQE of 21.0%.

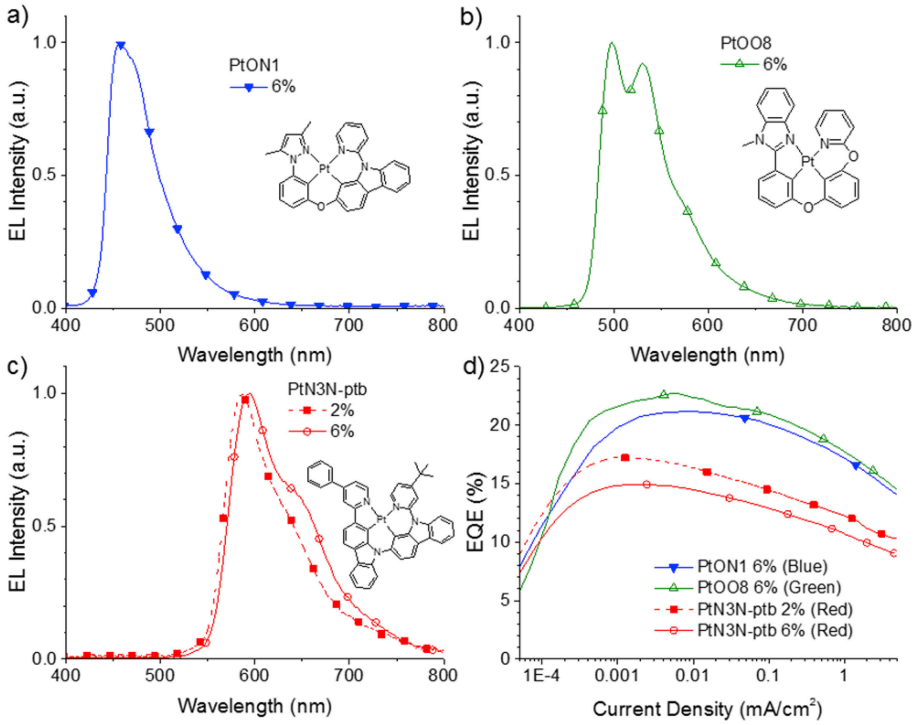

Figure 6.7: *a)–c) EL spectra as a function of wavelength and d) plots of EQE vs. current density of monochromatic devices using each individual emitter. Inset figures are the molecular structures of the emitters used.*†

More recently, Soto *et al.*[102] reported a Pt^{II} *NCCN* complex, incorporating two phenylpyridine units bridged by an oxygen atom. The initial attempt at the synthesis resulted in the formation of a mixture of three species, which were identified as the Pt^{II}, Pt^{III} and Pt^{IV} complexes, with the Pt^{III} complex featuring two Pt^{III} centres bridged by a short Pt–Pt bond (2.74 Å). Subsequently, they performed the reaction again under more rigorously deoxygenated conditions, leading to the exclusive formation of the Pt^{II} complex. Alternatively, the Pt^{IV} complex could be synthesised directly in 43% yield by carrying out the reaction in air. The Pt^{IV} complex could also be reduced back to Pt^{II} by heating in CH_2Cl_2 under N_2 in the presence of activated Zn^0. The selective formation of the Pt^{III} complex could be achieved from the Pt^{II} complex using *N*-chlorosuccinimide (NCS) in CH_2Cl_2 (Figure 6.8a). All of the signals for the ^1H NMR spectrum of the Pt^{IV} complex are slightly downfield shifted compared to those of the Pt^{II} complex. In contrast, those of the Pt^{III} complex are upfield shifted with respect to both the Pt^{II} and Pt^{IV} complexes, as a result of the π–π stacking between the aromatic rings (Figure 6.8b).

†Reprinted from *Org. Electron.*, **37**, G. E. Norby, C. D. Park, B. OBrien, G. Li, L. Huang and J. Li, Efficient white OLEDs employing red, green, and blue tetradentate platinum phosphorescent emitters, 163-168, Copyright 2016, with permission from Elsevier.

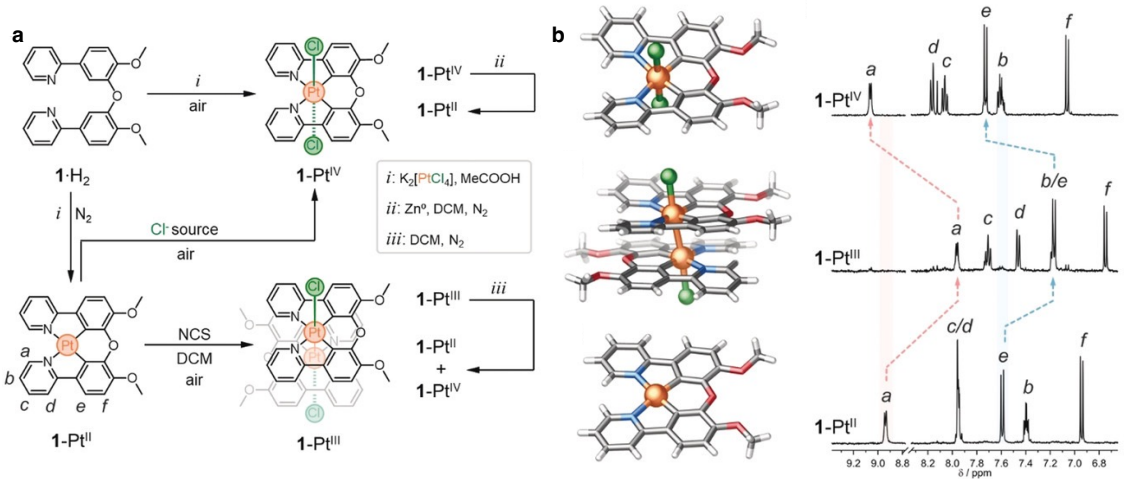

Figure 6.8: *a) Scheme for the syntheses of Pt^{II}, Pt^{III} and Pt^{IV} complexes reported by Soto et al. b) molecular structures of the complexes and the aromatic portion of their corresponding ^1H NMR spectra. Reprinted with permission, copyright Wiley.*[102]

Only the Pt^{II} complex showed photoluminescence. In the solid state, exposure of the CH_2Cl_2 solvate of the complex to MeOH liquid or vapour transforms the orange powder into a yellow powder, which is also accompanied by a shift in the solid state emission from red to light-orange. This transformation occurs reversibly. In DMSO solution, the complex emits green light (λ_{max} = 515 nm). The gradual addition of water to the DMSO solution leads to the slow appearance of a broad excimer band, which almost fully dominates the spectrum at the limiting water content of 90%.

The researchers built on this work by coupling the tetradentate *NCCN* complex to a crown ether (Scheme 6.1).[103] Diphenyl ether was sequentially ortholithiated, borylated and then hydroxylated in a one-pot reaction to yield 2,2-dihydroxydiphenyl ether. The product was then brominated with *N*-bromosuccinimide to give 2,2-oxybis(4-bromophenol). The dibrominated [1.5]dibenzo-18-crown-6 ether was formed by its reaction with tetraethylene glycol ditosylate, which was followed by borylation of the brominated product and a Suzuki-Miyaura coupling with 2-bromopyridine to yield the target ligand.

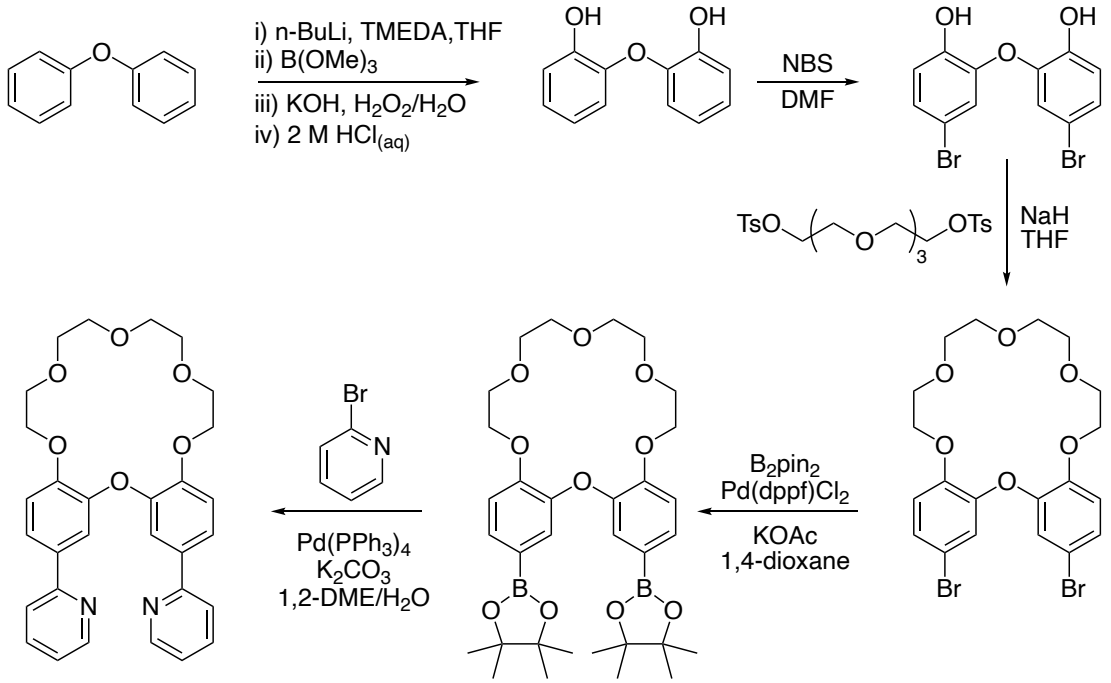

Scheme 6.1: *Scheme for the synthesis of the crown ether-containing ligand.*

The binding of the resulting Pt^{II} complex towards the alkali metal ions Li^+–Cs^+ and Ca^{2+} was tested by ^1H NMR and the affinity constants estimated by spectrophotometric titrations in CH_3CN. Binding of Ca^{2+} results in a shift in the ^1H NMR spectrum, particularly affecting some of the glycolic protons of the crown ether (0.57 ppm shift). Ca^{2+} exhibits the highest affinity constant $K_a = (2.74 \pm 0.24) \times 10^5\ M^{-1}$. The addition of Ca^{2+} to a solution of the complex in CH_3CN results in a 12 nm blue shift in emission and an increase in quantum yield, possibly due to decreased non-radiative decay through rigidification.

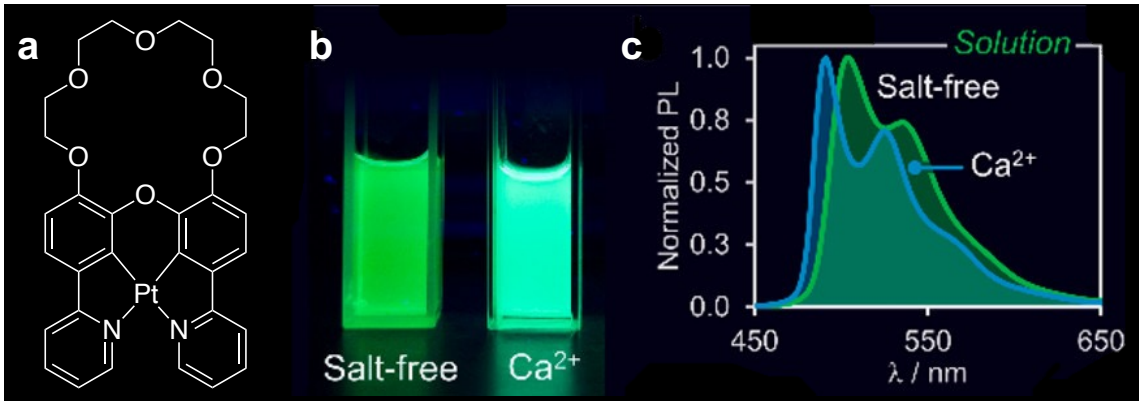

Figure 6.9: *(a) Structure of Pt^{II} complex. (b) Photograph of solutions of the complex in the absence (left) and presence (right) of $Ca(OTf)_2$ in CH_3CN and (c) their corresponding emission spectra.*[†]

[†]Adapted with permission from Multiresponsive Cyclometalated Crown Ether Bearing a Platinum(II) Metal Center, M. A. Soto, V. Carta, M. T. Cano, R. J. Andrews, B. O. Patrick and M. J. MacLachlan, *Inorg. Chem.*, 2022, **61**, 2999-3006. Copyright 2022, American Chemical Society.[103]

The Pt^{II} complex can be oxidised with NCS, forming a 'flytrap' Pt^{III} dimer, containing two crown ether units (Figure 6.10).[104] The crown ether moieties can rotate with respect to one another by rotation around the Pt–Pt bond. Spectroscopic titrations with different ions showed high affinities towards larger cations, e.g. Cs^+ K_a = (1.2 $\pm$ 0.1) $\times$ 10^5 M^{-1}.

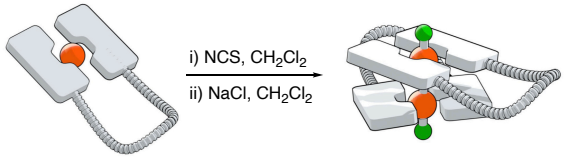

Figure 6.10: *Cartoon representation of the oxidation of the Pt^{II} crown ether-containing complex of Figure 6.9 with NCS, to produce a Pt^{III} dimer. Reprinted with permission, copyright Wiley.*[104]

The formation of the Pt^{III} complex can also be brought about by photoirradiation of the Pt^{II} complex with blue or white light for 70 h. Further prolonged irradiation (7 days) was found to result in the complete oxidation to the mononuclear Pt^{IV} complex, which can then be reduced back to Pt^{II} using Zn^0, as described earlier for the parent system of Figure 6.8.

6.2 Aims and objectives

Previously in the group, Rebecca Salthouse inadvertently isolated a crystal of a Pt^{IV} complex with an *NCCN* ligand incorporating two phenylpyridine units directly coupled together without any bridging atom (Figure 6.11). Unlike the aforementioned ligands which form two 5-membered chelate rings and one 6-membered upon coordination to Pt^{II}, the Salthouse complex has three 5-membered chelate rings. The direct isolation of the oxidised form of the complex, with none of the Pt^{II} observed, hinted that the smaller cavity might favour the smaller Pt^{IV} ion, potentially driving the rapid oxidation of the Pt^{II} form to the Pt^{IV}.

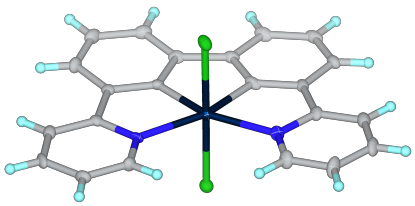

Figure 6.11: *Molecular structure of the Pt^{IV}(NCCN) complex in the crystal, isolated by Rebecca Salthouse.*

This result sparked our interest in this and structurally similar ligands. We decided to deliberately pursue the synthesis of this complex and to explore variations, such as

extending one or two of the side chelate rings by substituting the pyridine ring with an 8-substituted quinoline moiety to form “lateral” 6-membered chelates, rather than by incorporating a spacing atom in the middle chelate ring (Figure 6.12). This contrasts with the examples of Section 6.1, where the 6-membered chelate is the “central” ring. It has been shown that tridentate ligands which contain an 8-substituted quinoline, forming a 6-membered chelate ring, can sometimes offer the metal ion more suitable bite angles (closer to 180°), leading to stronger ligand fields.[57,105] This may have a beneficial effect on the photophysical properties of the complexes, but we were also particularly interested in understanding how these ligand modifications may impact the propensity of the resulting complexes to oxidation.

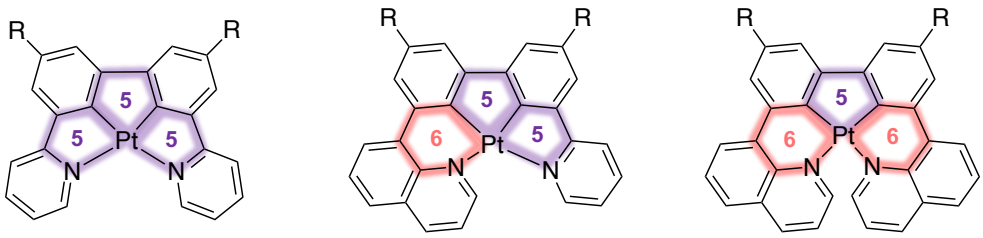

Figure 6.12: *Pt^{II} complexes featuring tetradentate NCCN ligands incorporating 5- and 6-membered chelate rings.*

6.3 Synthesis of the proligands

None of the proligands explored in this work had been reported before. They were prepared using Suzuki, Miyaura and Stille cross-coupling reactions (Scheme 6.2).

2-Bromopyridine was reacted with (3-bromophenyl)boronic acid through a Suzuki cross-coupling reaction, as previously described.[75,106] Subsequently, H_2L^{20} was derived by subjecting the resulting 2-(3-bromophenyl)pyridine to another Suzuki reaction with its pinacolato ester counterpart. The latter was synthesised through a Miyaura cross-coupling of 2-(3-bromophenyl)pyridine and bispinacolato diboron.

The Stille cross-coupling reaction of 2-(tributylstannyl)pyridine with 1,3-dibromo-5-(*tert*-butyl)benzene yielded 2-(3-bromo-5-(*tert*-butyl)phenyl)pyridine, and its corresponding pinacolato ester was obtained through the Miyaura borylation. Subsequently, H_2L^{21} was synthesised akin to H_2L^{20} via a Suzuki cross-coupling reaction, involving the bromo and pinacolato ester phenylpyridine components.

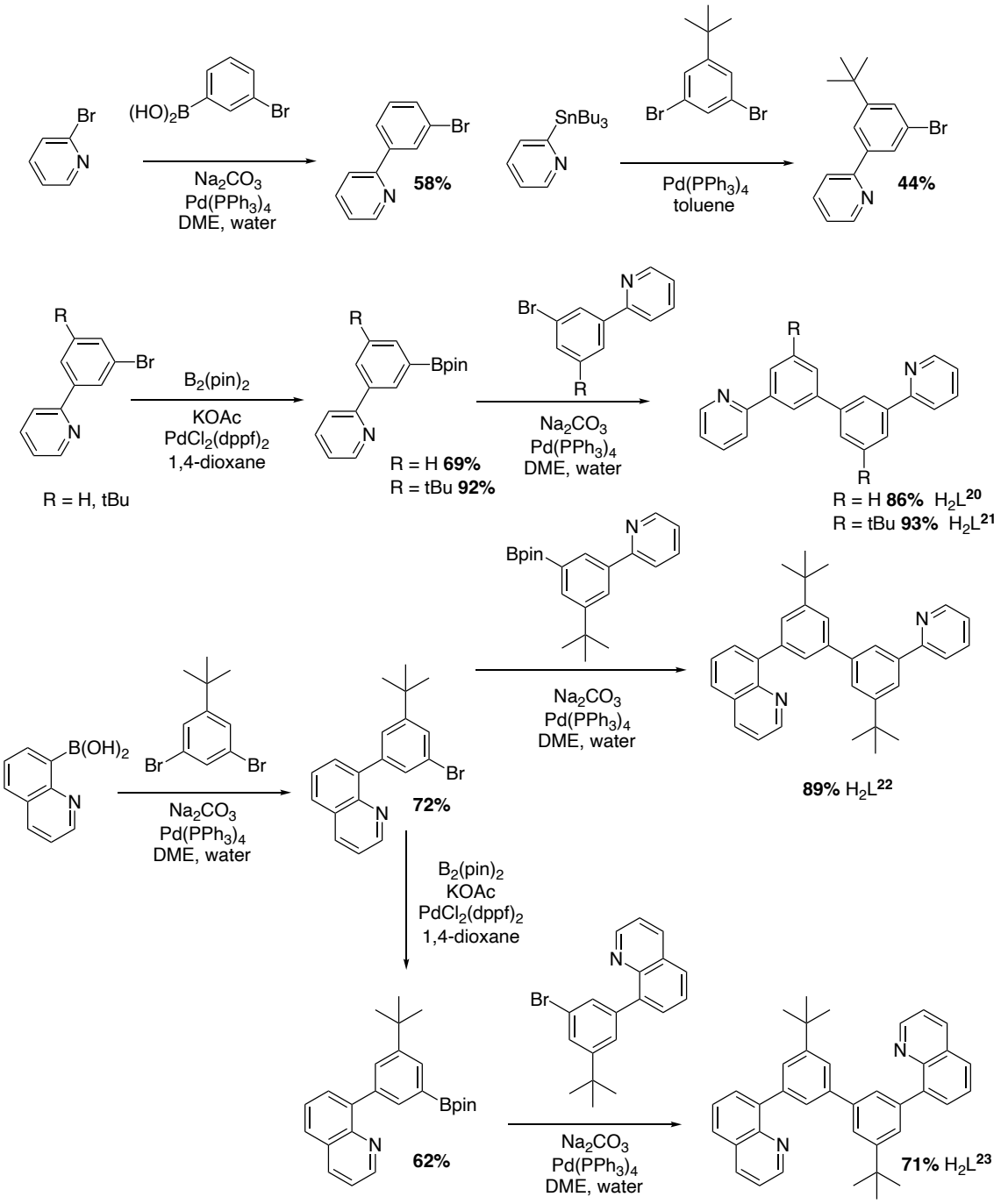

Scheme 6.2: *Synthesis of proligands* $H_2L^{20\text{-}23}$

The proligands containing a quinoline moiety were prepared by starting with a Suzuki cross-coupling reaction between 8-quinolinylboronic acid and 1,3-dibromo-5-(*tert*-butyl)benzene. The assymmetric H_2L^{22} was then synthesised by reacting the resulting precursor with the pinacolato ester of 2-(3-bromo-5-(*tert*-butyl)phenyl)pyridine through another Suzuki reaction, whereas the symmetric H_2L^{23} was obtained by reacting the former with its own pinacolato ester analogue.

6.4 Preparation of the complexes

The complexation of the ligands was achieved by reaction with K_2PtCl_4 in degassed acetic acid at reflux temperature for 72 h. For H_2L^{20} it led to the formation of a yellow solid, which had such poor solubility that it could not be characterised. The *tert*-butyl derivatives were prepared in the hope of augmenting the solubility of the products of complexation. The outcome of the reaction of H_2L^{21} will be discussed later. Both H_2L^{22} and H_2L^{23} yielded mixtures of Pt^{II} and Pt^{IV} complexes (Scheme 6.3), despite the rigorously degassed reaction conditions. The Pt^{II} complexes were found to be readily oxidised to their Pt^{IV} analogues in solution, so their purification proved difficult. On the other hand, the Pt^{IV} compounds were successfully obtained as yellow solids after purification by column chromatography for $PtL^{22}Cl_2$, or recrystallisation from DCM/hexane for $PtL^{23}Cl_2$.

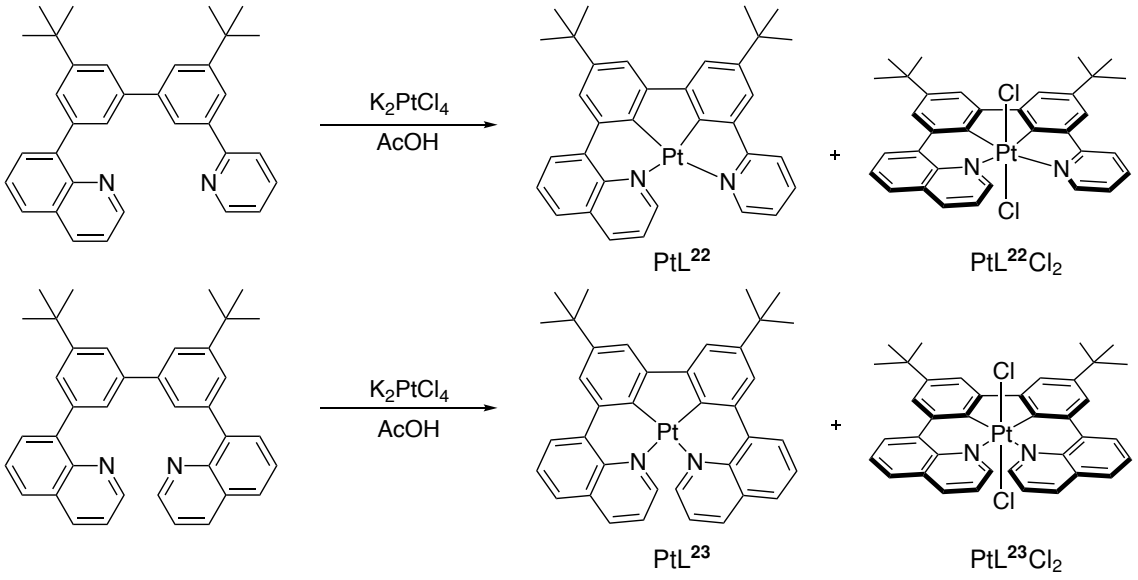

Scheme 6.3: *Synthesis of Pt complexes of* $L^{22\text{-}23}$

The synthesis of the Pt^{II} complexes was achieved by starting with the Pt^{IV} materials using the method described by Soto *et al.*[107] The Pt^{IV} complex was dissolved in DCM and activated zinc was added to the solution. The mixture was degassed by three freeze-pump-thaw cycles and heated at reflux temperature for 5 days after which it was worked up and the products purified as described in the experimental chapter (Chapter 8).

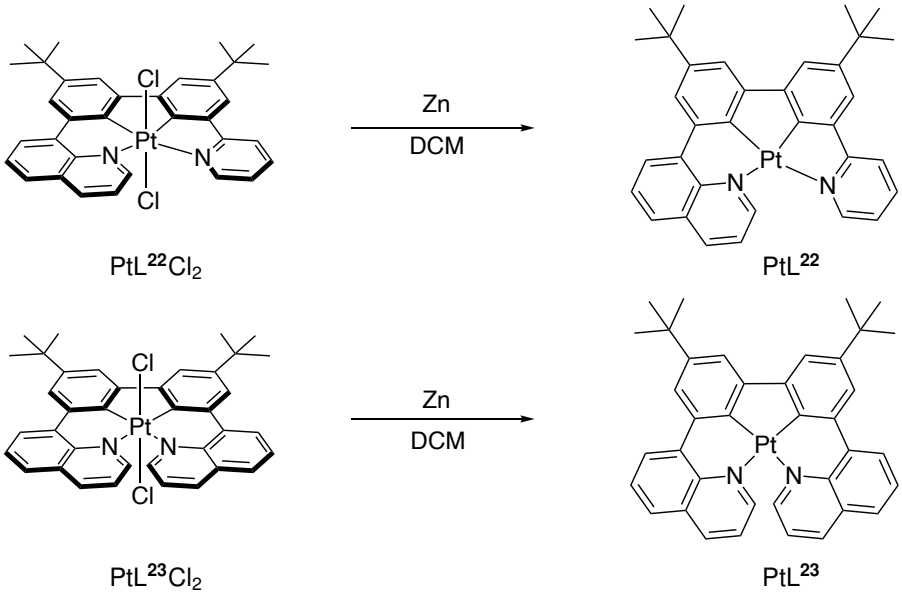

$PtL^{22}Cl_2$ PtL^{22}

$PtL^{23}Cl_2$ PtL^{23}

Scheme 6.4: *The reduction of Pt^{III} and Pt^{IV} complexes to their Pt^{II} analogues using activated zinc.*

For H_2L^{22}, the usual shielding of all protons in going from the Pt^{IV} to the Pt^{II} complex is observed in their ^1H NMR spectra (Figure 6.13). However, the ^1H NMR spectrum of the product of the complexation reaction of H_2L^{21} showed significantly upfield shifted protons compared to those of PtL^{22}. Considering the shared phenylpyridine motif between H_2L^{21} and H_2L^{22} it would be expected that the protons on those rings of the complexes would have similar shifts. This anomalous upfield shift could be explained if the product were of a dinuclear Pt^{III} complex, rather than a Pt^{II} or Pt^{IV} complex (Scheme 6.5). The resulting $\pi - \pi$ stacking between the ligands will lead to the upfield shift, as observed by Soto *et al.*[107] The formation of such Pt^{III} species was subsequently confirmed by X-ray crystallography (Figure 6.16).

Apart from the Pt^{III} complex reported by Soto *et al.*, discussed in the chapter introduction, Pt^{III} examples in the literature commonly involve two or four bridging ligands, necessitating the close proximity of two Pt units.[108–111] In the former case the rest of the coordination sphere around each Pt ion is completed by one bidentate ligand. In some of those instances, the Pt centres are already close together in the Pt^{II} precursor and their oxidation results in the formation of a Pt^{III} complex.

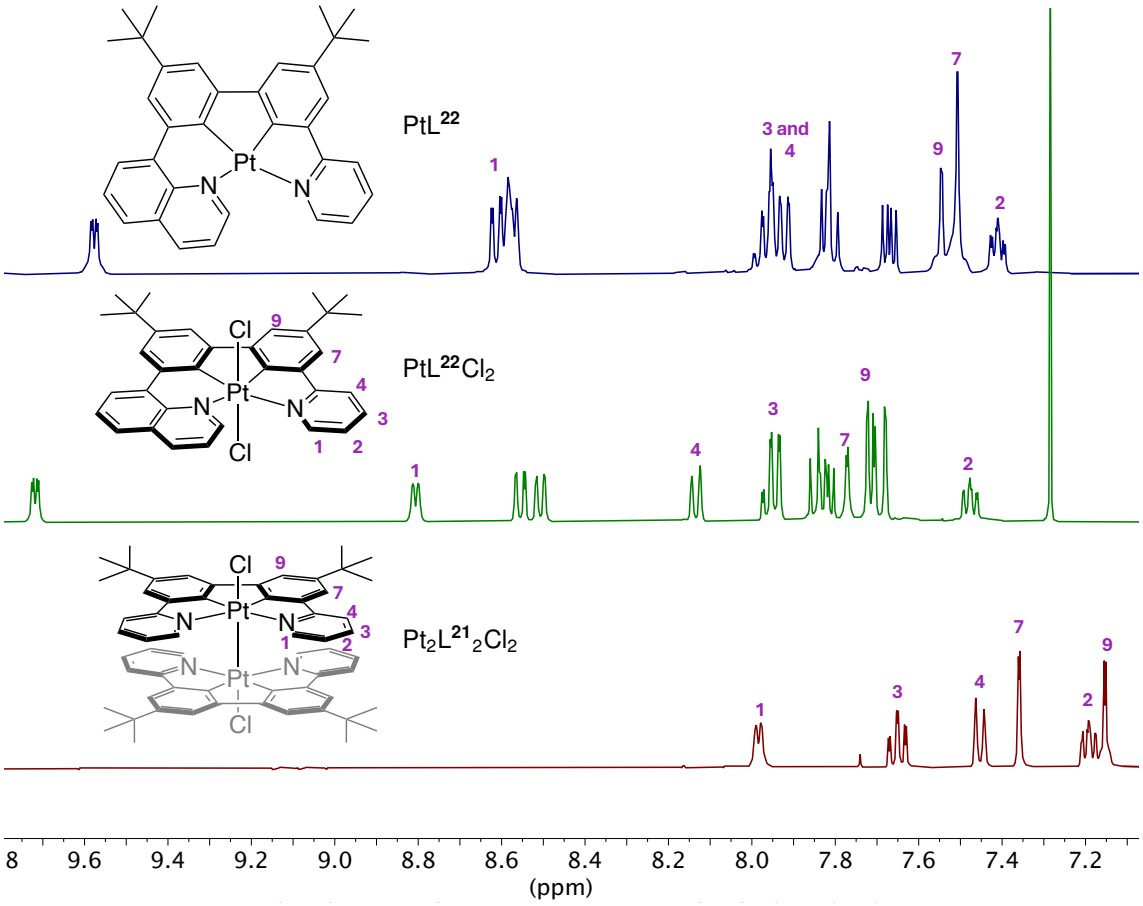

Figure 6.13: *^{1}H NMR spectra of complexes $PtL^{22}Cl$, $PtL^{22}Cl_2$ and $Pt_2L^{21}{}_2Cl_2$ in CD_2Cl_2 at 400 MHz*

The reduction of the Pt^{III} complex $Pt_2L^{21}{}_2Cl_2$ with activated zinc was attempted by following the same procedure as for the reduction of the Pt^{IV} complexes (Scheme 6.5). In this instance, though, no heating was required. Upon degassing the mixture, an immediate darkening of the colour of the supernatant was observed. The mixture was left to stir for an hour and then filtered through celite, and the solvent removed to yield the pure dark-red Pt^{II} complex.

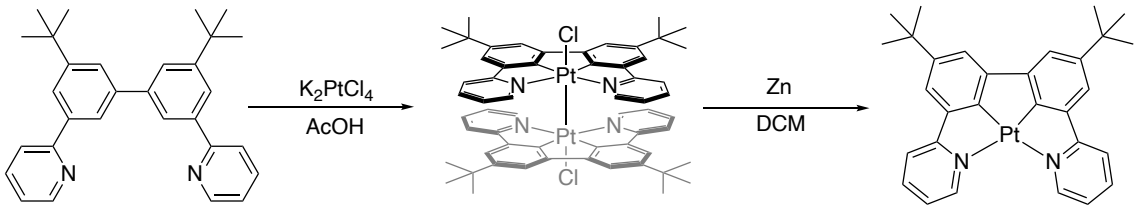

Scheme 6.5: *The synthesis of $Pt_2L^{21}{}_2Cl_2$ and its reduction to PtL^{21}.*

The synthesis of the Pt^{IV} complex of ligand H_2L^{21} was attempted by oxidising both PtL^{21} and $Pt_2L^{21}{}_2Cl_2$ with $PhICl_2$. For $Pt_2L^{21}{}_2Cl_2$ there was no indication of any product formation, whereas for PtL^{21} the oxidation led to mixtures of the Pt^{III} and Pt^{IV} complex (evident in the ^{1}H NMR spectrum). However, their separation was not achieved.

Crystals suitable for X-ray diffraction of all of the synthesised Pt^{II} and Pt^{IV} complexes were also obtained (Figures 6.14, 6.16 and 6.15). Selected bond lengths and bond angles are summarised in Table 6.1.

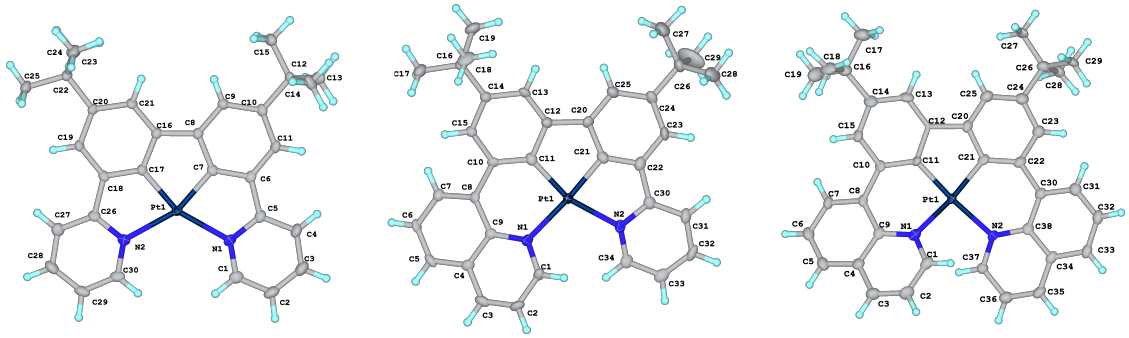

Figure 6.14: *Molecular structures of Pt^{II} complexes PtL^{21}, PtL^{22} and PtL^{23}.*

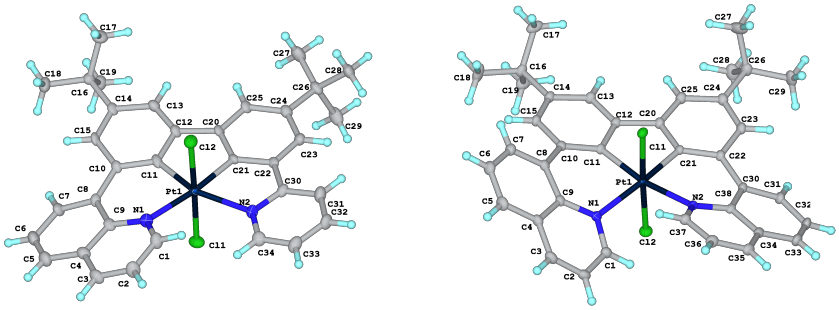

Figure 6.15: *Molecular structures of Pt^{IV} complexes $PtL^{22}Cl_2$ and $PtL^{23}Cl_2$.*

All of the Pt^{II} complexes show pseudo-square planar geometries around the Pt ion and the Pt^{III} and Pt^{IV} complexes show pseudo-octahedral geometries. $C^{\text{trans to py}}$–Pt–N^{py} angles of around 160° for all complexes were far from the ideal 180°. Deviation from the optimal bite angle was likewise noted in the N^{quin}–Pt–$C^{\text{trans to quin}}$ angles (ranging between 169–174°), attributed to out-of-plane distortion stemming from the steric bulk of the pyridine/quinoline units on either side as they approach each other. The interplanar angles within the complexes are listed in Table 6.1. The quinoline-containing complexes are chiral owing to the helical wrapping of the ligand around the metal ion. PtL^{22}, $PtL^{23}Cl_2$ and PtL^{23} all crystallise in the centrosymmetric space group $P\bar{1}$ and the crystals thus comprise a racemic mixture of the two enantiomers of each complex. In contrast, $PtL^{22}Cl_2$ crystallises in the non-centrosymmetric $P2_12_12_1$ space group, so the crystal comprises of a single enantiomer.

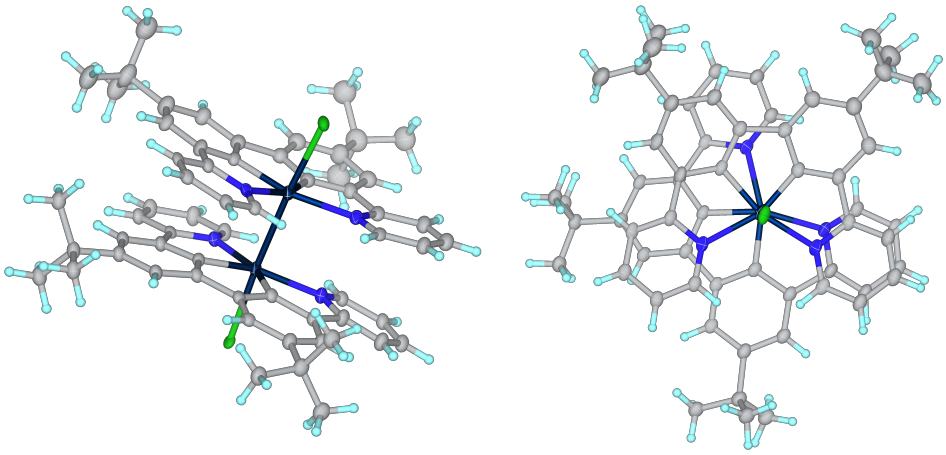

Figure 6.16: *Molecular structure of Pt^{III} complex $Pt_2L^{21}{}_2Cl_2$.*

The Pt^{III} complex has a Pt–Pt bond length of 2.6688(13) Å. The nearest distance between the planes, defined by the two PtL^{21} units, is 3.306(5) Å. The close proximity of the units suggests strong π– π interactions, accounting for the shielding effect seen in the ^1H NMR spectrum. Reduction to Pt^{II} leads to a slight shortening of all Pt–N and Pt–C bonds, possibly due to the loss of coordination sites. The same observation can be made about the reduction of $PtL^{22}Cl_2$ and $PtL^{23}Cl_2$ to their Pt^{II} analogues.

Table 6.1: *Selected bond lengths (Å) and bond and interplane angles (°) for PtL^{21}, PtL^{22} and PtL^{23} (top), and $Pt_2L^{21}{}_2Cl_2$, $PtL^{22}Cl_2$ and $PtL^{23}Cl_2$ (bottom). The planes defined by the phenyl, pyridine and quinoline units of the ligand are abbreviated as ph, py, quin, respectively.*

	PtL^{21}	PtL^{22}	PtL^{23}
Pt – $C^{trans\ to\ py}$	1.935(3) / 1.927(3)	1.964(7)	–
Pt – N^{py}	2.177(2) / 2.178(2)	2.161(6)	–
Pt – N^{quin}	–	2.105(6)	2.089(9) / 2.138(8)
Pt – $C^{trans\ to\ quin}$	–	1.942(7)	1.965(9) / 1.960(10)
$C^{trans\ to\ py}$ – Pt – N^{py}	159.85(10) / 159.66(10)	161.2(2)	–
N^{quin} – Pt – $C^{trans\ to\ quin}$	–	173.4(3)	171.2(4) / 170.6(3)
interplane angle between ph and ph	4.539	8.413	6.506
interplane angle between ph and py	2.132 / 5.166	14.009	–
interplane angle between ph and quin	–	26.746	26.096 / 26.272

	$Pt_2L^{21}{}_2Cl_2$	$PtL^{22}Cl_2$	$PtL^{23}Cl_2$
Pt – $C^{trans\ to\ py}$	1.96(2) / 1.95(3)	1.990(8)	–
Pt – N^{py}	2.21(2) / 2.18(2)	2.282(7)	–
Pt – N^{quin}	–	2.166(7)	2.1785(15) / 2.1692(15)
Pt – $C^{trans\ to\ quin}$	–	1.964(7)	1.9936(17) / 1.9893(17)
Pt – Cl	2.452(6) / 2.480(6)	2.3089(19) / 2.3176(19)	2.3071(4) / 2.3285(4)
Pt – Pt	2.6688(13)	–	–
$C^{trans\ to\ py}$ – Pt – N^{py}	161.5(9) / 159.9(9)	159.9(3)	–
N^{quin} – Pt – $C^{trans\ to\ quin}$	–	173.8(3)	170.25(6) / 169.16(6)
Cl – Pt – Cl	–	177.05(8)	177.198(16)
Cl – Pt – Pt	175.83(16) / 176.11(16)	–	–
interplane angle between ph and ph	9.067 / 10.074	5.529	8.847
interplane angle between ph and py	11.997 / 5.488 / 3.088 / 10.527	8.929	–
interplane angle between ph and quin	–	18.911	23.586 / 23.308

6.5 Photophysical properties

6.5.1 Absorption

The absorption spectra of all of the complexes are shown in Figure 6.17, with numerical data in Table 6.2. The intense transitions at high energy (< 300 nm) can be ascribed to $\pi - \pi^*$ transitions within the ligands. Notably, the spectra of the Pt^{III} and Pt^{IV} complexes contrast with those of the Pt^{II} complexes by the apparent absence of the lowest energy band, consistent with the decrease in the energy of the d-orbitals with increasing oxidation state. Furthermore, the Pt^{III} complex exhibits higher molar absorptivities across the entire wavelength range compared to the other complexes. This can obviously be attributed to the presence of two, rather than one, conjugated Pt(*NCCN*) units per molecule.

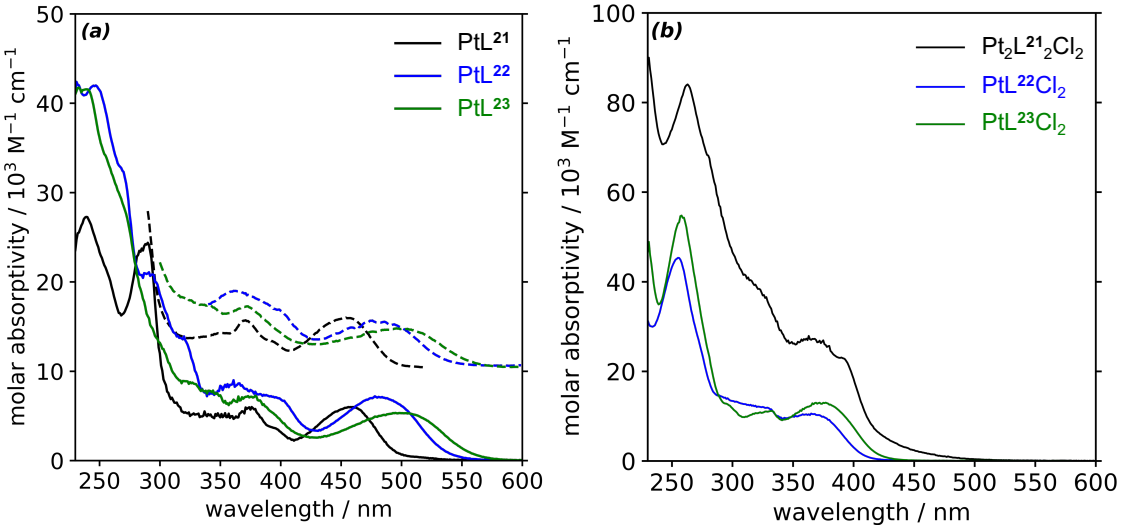

Figure 6.17: *UV-vis absorption spectra of (a) $PtL^{21\text{-}23}$ (with offset photoluminescence excitation spectra as dashed lines) and (b) $Pt_2L^{21}{}_2Cl_2$, $PtL^{22}Cl_2$ and $PtL^{23}Cl_2$ in CH_2Cl_2 solution at 298 K.*

A red shift in the lowest energy band of the Pt^{II} complexes is evident in the following order: λ_{max} PtL^{21} < PtL^{22} < PtL^{23}. This shift can be attributed to the replacement of one or two of the pyridine rings with the quinoline moiety with more extended conjugation. Similarly, the lowest energy band of $PtL^{23}Cl_2$ is slightly red-shifted compared to that of $PtL^{22}Cl_2$.

The lowest energy band of the Pt^{II} complexes red shifts from PtL^{21} to PtL^{22}, and again from PtL^{22}, PtL^{23}, as the pyridine ring is replaced by first one, and then two, more conjugated quinoline moieties. The same trend is observed for $Pt^{IV}L^{23}Cl_2$ compared to $Pt^{IV}L^{22}Cl_2$.

Table 6.2: *UV-vis absorption data for PtL^{21}, PtL^{22}, PtL^{23}, $Pt_2L^{21}{}_2Cl_2$, $PtL^{22}Cl_2$ and $PtL^{23}Cl_2$ in CH_2Cl_2 at 298 K.*

complex	absorption λ_{max}/nm (ε/$M^{-1}cm^{-1}$)
PtL^{21}	239 (27300), 284sh (23400), 290 (24400), 357 (5700), 385sh (3640), 458 (6000)
PtL^{22}	231 (24400), 248 (41900), 269sh (32500), 291 (21100), 322 (13200), 361 (9000), 401 (6750), 484 (7120)
PtL^{23}	233 (41700), 241 (41500), 324 (8590), 345 (7490), 376 (7150), 501 (5310)
$Pt_2L^{21}{}_2Cl_2$	231 (90000), 263 (84000), 324sh (37600), 371 (26500), 393sh (22700)
$PtL^{22}Cl_2$	255 (45300), 297 (13900), 329 (11900), 368 (10500)
$PtL^{23}Cl_2$	258 (54800), 297sh (12500), 331 (11100), 375 (13000)

6.5.2 Emission

All three Pt^{II} complexes are emissive in deoxygenated dichloromethane solution at room temperature and in a glass of diethyl ether/isopentane/ethanol (2:2:1 v/v) at 77 K. Their excitation spectra closely match the absorption spectra (Figure 6.17). The Pt^{IV} complexes are only emissive at 77 K, whereas no emission was detected for the Pt^{III} complex at that temperature. The emission spectra of all of the complexes are shown in Figures 6.18 and 6.19, with numerical data in Table 6.3.

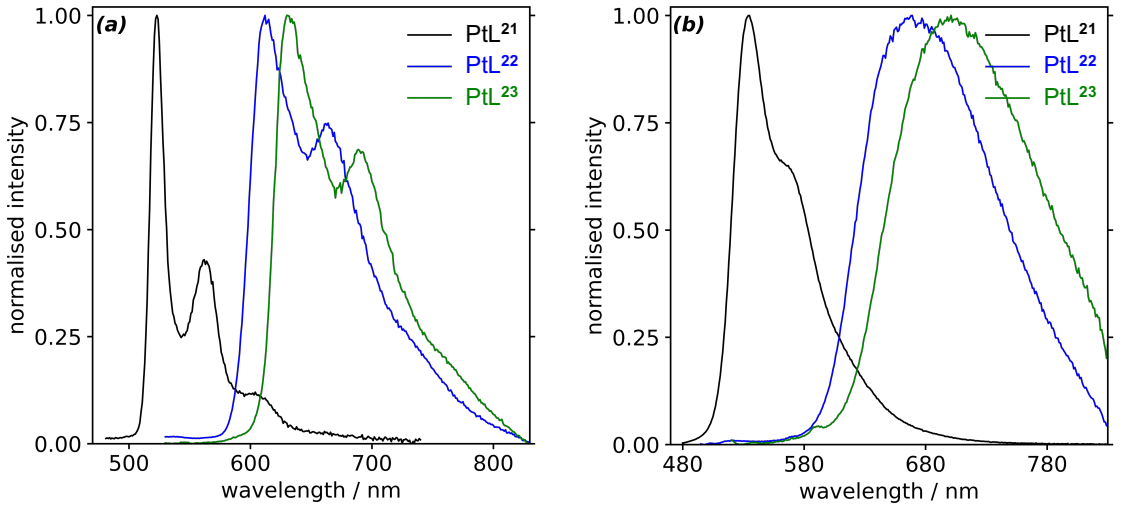

Figure 6.18: *Emission spectra of Pt^{II} complexes in (a) diethyl ether/isopentane/ethanol (2:2:1 v/v) at 77 K (b) deoxygenated CH_2Cl_2 at 298 K.*

The room-temperature emission spectrum of PtL^{21} displays some structure, whereas those of PtL^{22} and PtL^{23} are broad and structureless. The emission of PtL^{22} is significantly red-shifted ($\approx$ 140 nm) compared to that of PtL^{21}, due to the replacement of

one of the pyridine rings by a more conjugated quinoline ring. Further substitution of the second pyridine ring by a quinoline ring in PtL^{23} results in a further – albeit smaller – red shift of 30 nm. The red shift is accompanied by a significant decrease in the photoluminescence quantum yield dropping from 67% to 2.2% to 0.4% for PtL^{21}, PtL^{22} and PtL^{23}, respectively. The lifetimes follow the same trend, decreasing from 3.5 µs to 2.5 µs to 650 ns. This partly reflects the substantial increase in the non-radiative decay rate (see k_{nr} values in Table 3), which may result from the less rigid nature of the quinoline-containing complexes. However, it is also clear that the radiative rate constants decrease. As the ligand becomes more conjugated, the filled ligand orbitals rise in energy, resulting in less efficient mixing with the metal orbitals, leading to lower k_r. The out-of-plane distortion and the longer Pt–C bonds of the 8-substituted quinoline-containing complexes are also likely to lead to a smaller metal participation in the excited state and may therefore further reduce k_r.

At 77 K, a red-shift is also observed in the emission spectra of the Pt^{II} complexes, following the same order from PtL^{21} to PtL^{22} to PtL^{23}. The spectra are all vibrationally well-resolved with PtL^{21} being the most structured, as typically seen for bluer emitters. The 0,0 component is the most intense in each case.

Figure 6.19 compares the emission spectra of $PtL^{22}Cl_2$ and $PtL^{23}Cl_2$ at 77 K with those of their Pt^{II} analogues. The emission of the Pt^{IV} complexes is blue-shifted compared to that of the Pt^{II} complexes and the 0,1 component is the most intense in both cases. Furthermore, the lifetimes of the Pt^{IV} complexes are considerably longer, around 300 µs, compared to 13 µs for the Pt^{II} complexes.

The blue shift in the emission is consistent with an increase in the energy gap, resulting from a decrease in the energy of the metal d-orbitals in the higher oxidation state Pt^{IV} complexes, thereby lowering the energy of the HOMO. Poorer mixing between the lower energy d-orbitals and the ligand orbitals also results in a lower k_r and therefore a longer lifetime. These results are in line with all of our previous work, described in the previous chapter, comparing the photophysical properties of Pt^{II} and Pt^{IV} complexes.

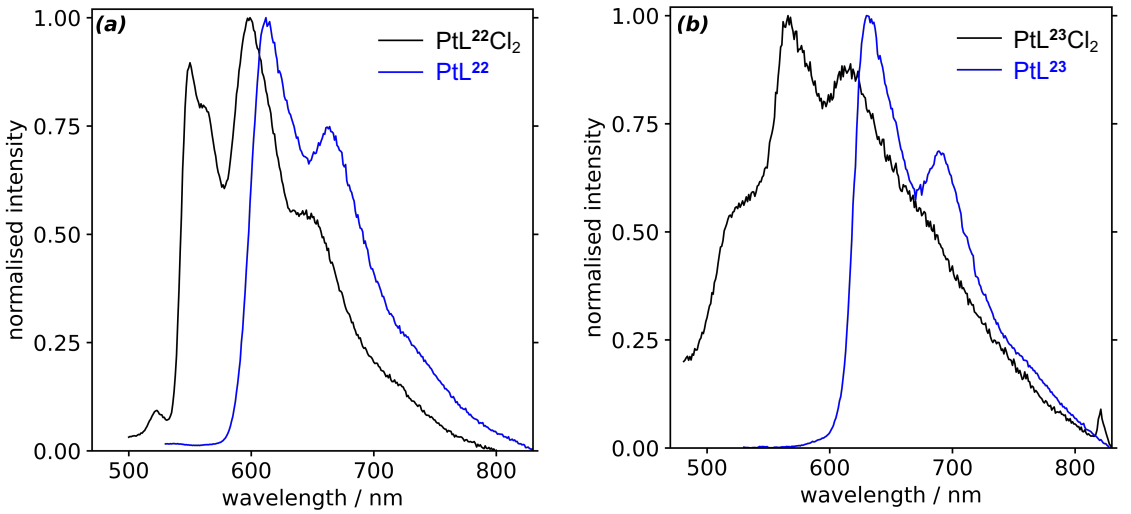

Figure 6.19: *Emission spectra of (a) $PtL^{22}Cl_2$ and PtL^{22}, and (b) $PtL^{23}Cl_2$ and PtL^{23} at 77 K in diethyl ether/isopentane/ethanol (2:2:1 v/v).*

Table 6.3: *Photophysical data for complexes PtL^{21}, PtL^{22}, PtL^{23}, $PtL^{22}Cl_2$ and $PtL^{23}Cl_2$ in deoxygenated CH_2Cl_2 at 298 K and in diethyl ether/isopentane/ethanol (2:2:1 v/v) at 77 K. Values in parentheses refer to air-equilibrated solutions.*

	emission at 298 K					emission at 77 K	
complex	λ_{em}/nm	Φ_{lum}/%	τ/µs	k_r/ $10^3\,s^{-1}$	k_{nr}/ $10^3\,s^{-1}$	λ_{em}/nm	τ/µs
PtL^{21}	534, 570	67 [2.0]	3.5 [0.1]	190	93	523, 564, 607	11
PtL^{22}	670	2.2 [0.4]	2.5 [–]	8.6	390	616, 667	13
PtL^{23}	700	0.4 [–]	0.65 [–]	5.7	1530	525, 577, 635, 688	13
$PtL^{22}Cl_2$	–	–	–	–	–	525, 551, 564sh, 600, 655	270
$PtL^{23}Cl_2$	–	–	–	–	–	521, 565, 616	300

6.6 DFT calculations

Density functional theory (DFT) and time-dependent density functional theory (TD-DFT) calculations with Tamm-Dancoff approximation (TDA) were performed on the complexes. Geometry optimisations in the ground state were performed using B3LYP/ def2-TZVP.

The HOMO of the Pt^{II} complexes at the S_0 geometry is located on the phenyl rings of the ligand and the Pt centre, and the LUMO is located on the pyridine ring for complex PtL^{21} and on the quinoline ring/rings for complexes PtL^{22} and PtL^{23}. Molecular orbital plots for the HOMO and LUMO of PtL^{21} are shown in Figure 6.20. TD-DFT calcula-

tions reveal that the lowest singlet transitions for the Pt^{II} complexes involve the HOMO and LUMO orbitals (> 95% contribution in all cases) and have oscillator strengths > 0.16.

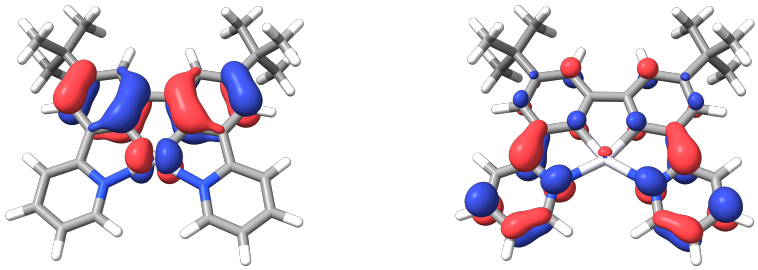

Figure 6.20: *Frontier orbital plots for PtL^{21} at the S_0 geometry.*

Figure 6.21 presents the molecular orbital (MO) energy level diagrams for the ground state of complexes PtL^{22}, PtL^{23}, $PtL^{22}Cl_2$, and $PtL^{23}Cl_2$. For the Pt^{IV} complex $PtL^{22}Cl_2$, the lowest singlet transition primarily involves contributions from the HOMO and the LUMO+1 orbitals (78%). Here, the HOMO is situated on the phenyl rings of the ligand, while the LUMO+1 is along the Pt–Cl bonds. Similarly, the $S_0 \rightarrow S_1$ transition for $PtL^{23}Cl_2$ is characterised by contributions from the HOMO $\rightarrow$ LUMO and HOMO $\rightarrow$ LUMO+2 transitions (40% / 50%). In this case, the HOMO is also located on the phenyl rings of the ligand, the LUMO is situated on the quinoline rings of the ligand, and the LUMO+2 is oriented along the Pt–Cl bonds. Such states have previously been suggested to serve as a pathway for nonradiative deactivation.[31,33,34] Notably, the HOMO of each Pt^{IV} complex is approximately 0.7 eV lower than that of the analogous Pt^{II} complex, reflecting the increase in oxidation state and consequent lowering of the metal d-orbitals. A consequence of this is less efficient mixing between the ligand and the metal d-orbitals, leading to a lower k_r and hence longer lifetimes and lower quantum yields, as noted in section 6.5. It also accounts for the lack of emission of the Pt^{IV} complexes at room temperature, where the rate constants of non-radiative processes evidently greatly exceed those of radiative decay. The larger energy gaps in the Pt^{IV} complexes are also consistent with the blue shift observed in the absorption and emission spectra.

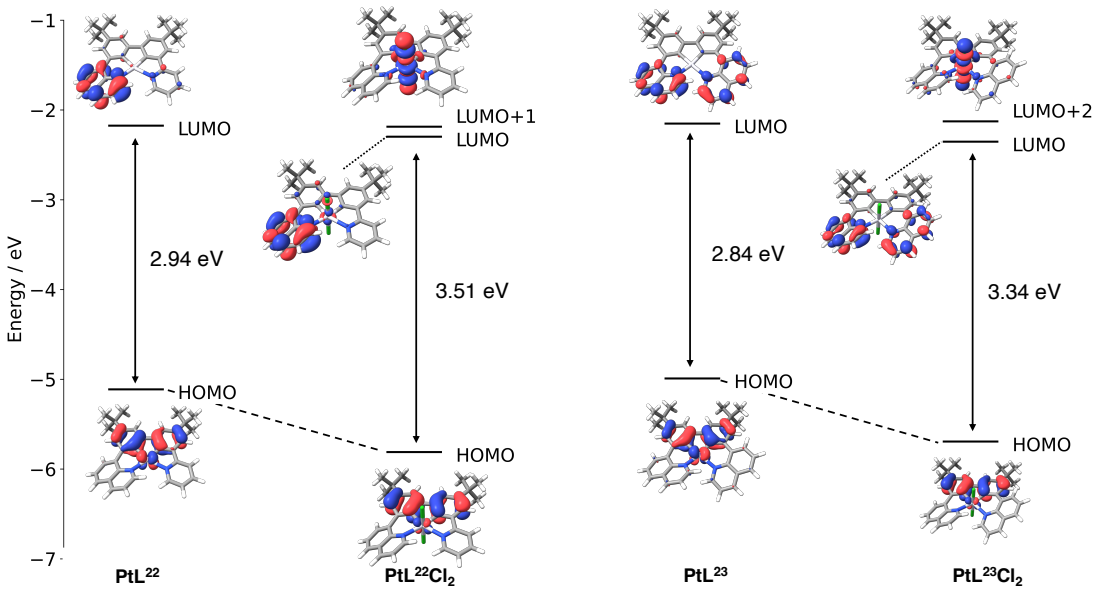

Figure 6.21: *Molecular orbital diagrams showing selected orbitals of complexes PtL^{22}, PtL^{23}, $PtL^{22}Cl_2$ and $PtL^{23}Cl_2$ and their energies.*

6.7 Chapter summary

Four novel tetradentate *NCCN* ligands were synthesised, featuring pyridine or quinoline N-rings and substituted phenyl cyclometallating rings and their platination was attempted. The complexation of the ligand with two unsubstituted pyridine and two 8-substituted quinoline rings led to the formation of a highly insoluble solid, which could not be characterised. The other three ligands initially formed mixtures of Pt complexes in varying oxidation states. The most stable complex of the ligand containing two pyridine and two *tert*-Bu substituted phenyl rings appeared to be the Pt^{III} dimer complex. In contrast, ligands incorporating a quinoline unit seemed to favour the formation of Pt^{IV} complexes. The Pt^{II} complexes of all three ligands were obtained by reducing the corresponding Pt^{III}/Pt^{IV} analogue with activated Zn^0.

The Pt^{IV} complexes are only emissive at 77 K, whereas the Pt^{II} complexes are emissive at both 77 K and in CH_2Cl_2 solution at room temperature. The complex containing two pyridine rings showed the highest quantum yield of 67%.

TD-DFT calculations revealed that the lowest singlet transition for the Pt^{II} complexes at the S_0 geometry is the HOMO $\rightarrow$ LUMO, where the HOMO is localised on the phenyl rings of the ligand and the Pt centre and the LUMO is located on the pyridine or quinoline rings of the ligand (MLCT character). In the case of the Pt^{IV} complexes,

the first singlet transition involves the population of an orbital oriented along the Pt–Cl bonds. Such LMCT states have previously been found to potentially lead to non-radiative deactivation and could therefore explain the lack of emission for these Pt^{IV} complexes.

CHAPTER 7

Conclusions and future work

Chapter 7: Conclusions and future work

The aim of this work was to develop Pt^{IV} complexes incorporating tridentate and tetradentate ligands and to investigate their photophysical properties.

Chapters 2 and 3 detailed the synthesis of Pt^{IV} complexes incorporating *NCN* and *NNC* tridentate ligands. Initially, Pt^{II}(*NCN*)Cl and Pt^{II}(*NNC*)Cl precursors were oxidised using chlorine or $PhICl_2$ to yield the corresponding Pt^{IV}(*NCN/NNC*)Cl_3 species. Subsequent addition of a bidentate or tridentate ligand was carried out by heating in toluene in the presence of AgOTf. The bidentate ligands led to complexes of the type 3 + 2 + 1, which include one tridentate ligand, one bidentate ligand, and a monodentate chloride. Addition of a tridentate ligand gave the first known examples of bis-tridentate Pt^{IV} complexes. The complexes that employed an *NNC* ligand, combined with another cyclometallating ligand (*NC* or *NNC*), were luminescent both at room temperature in degassed acetonitrile and at 77 K in butyronitrile. Their quantum yields ranged between 0.4% and 4%.

Future work could explore the impact of other substituents or different heterocycles on the *NNC* and/or *NC* ligands in an attempt to improve emission efficiencies or tune emission wavelength. Substitution of the monodentate ligand of the 3 + 2 + 1 complexes with, for example, a strong-field acetylide ligand could also be attempted to see what influence it may have on the excited state properties (Figure 7.1).

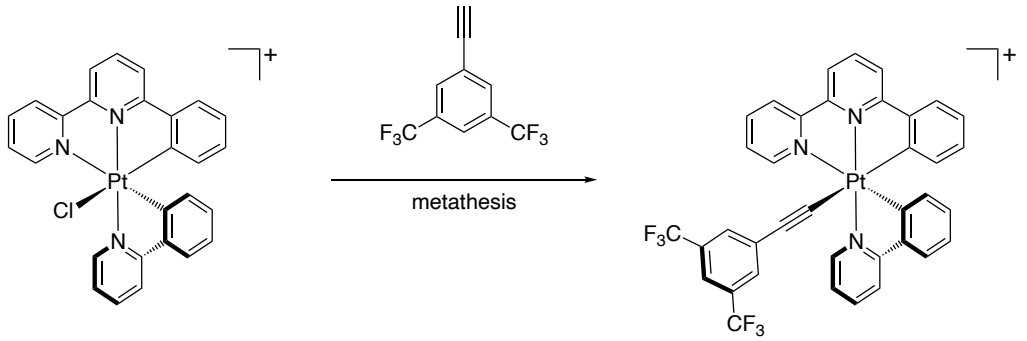

Figure 7.1: *Metathesis of the chloride ligand of [PtL⁷(ppy)Cl]⁺ for 1-ethynyl-3,5-bis(trifluoromethyl)benzene.*

Chapter 4 investigated examples of [Pt(*NNC*)(*NC*)Cl]$^+$ complexes that incorporate a phenyl substituent at the 6-position of the lateral pyridine ring. The solution-state photophysical properties of these substituted complexes were found to be consistent with those of their unsubstituted analogues. However, in PMMA films at concentra-

tions of 0.1%, 1%, and 10% by weight, the quantum yields of the new complexes consistently exceeded those of their unsubstituted counterpart. This enhancement in emission is likely attributed to a $\pi - \pi$ interaction between the phenyl substituent on the *NNC* ligand and the pyridine ring of the *NC* ligand. Future research could focus on incorporating these complexes into light-emitting electrochemical cells (LEECs) to assess their performance in device applications. There are no reported examples of Pt^{IV} complexes in LEECs, in contrast to the innumerable Ir^{III} examples.

Dinuclear complexes featuring bis-tridentate pyrimidine-bridged *CNN-NNC* ligands were explored in Chapter 5. Direct reaction of the ligands with K_2PtCl_4 yielded mononuclear complexes. Oxidation to Pt^{IV} followed by another reaction with K_2PtCl_4 was found to produce dinuclear Pt^{II}/Pt^{IV} complexes, which were further oxidised to form dinuclear Pt^{IV} complexes. A trace amount of a dinuclear complex of the type [*CNN-NNC*{Pt(ppy)Cl}$_2$] was isolated and its photophysical properties investigated and compared to those of the mononuclear [Pt(*NNC*)(*NC*)Cl]$^+$.

These initial efforts have shown some potential for dinuclear Pt^{IV} systems, but further ligand design is required to facilitate ease of access. The addition of more solubilising groups could simplify the complexation reactions, perhaps making the synthesis of these dinuclear complexes more straightforward and efficient. Another promising approach could involve rigidifying the ligand framework, which may enhance the ligand's ability to bind a second platinum centre more effectively.

Chapter 6 focused on synthesising tetradentate *NCCN* ligands, featuring pyridine or quinoline heterocycles and substituted phenyl cyclometallating rings, and their complexation to platinum. The ligands formed mixtures of Pt complexes in various oxidation states. The most stable complex for the ligand containing two pyridine and two *tert*-Bu substituted phenyl rings was identified as a Pt^{III} dimer, while quinoline-containing ligands tended to form Pt^{IV} complexes. Pt^{II} complexes for all three ligands were produced by reducing the corresponding Pt^{III}/Pt^{IV} analogues with activated Zn^0. The Pt^{IV} complexes were only emissive at 77 K, whereas Pt^{II} complexes exhibited emission at both 77 K and in CH_2Cl_2 solution at room temperature, with quantum yields reaching up to 67%.

It would be of interest to explore if light can be used for the $Pt^{IV} \leftrightarrow Pt^{II}$ interconversion, as this could unlock new avenues for applications in photocatalysis or photoactivated chemotherapy. The ability to control the oxidation state of platinum through light exposure could enable targeted activation of the complexes, minimising side effects in therapeutics or enhancing catalytic efficiency in synthetic processes, for example.

CHAPTER 8

Experimental

Chapter 8: Experimental

8.1 Materials and Physical Measurements

Reagents were obtained from commercial sources and used without further purification unless stated otherwise. All solvents used in preparative work were at least Analar grade and water was purified using the Purite$_{STILL}$ plus^{TM} system. Dry solvents were obtained from HPLC grade solvent that had been passed through a Pure Solv 400 solvent purification system and stored over activated 3 or 4 Å molecular sieves. For procedures involving dry solvent, glassware was oven-dried for at least 8 hours prior to use. Reactions requiring an inert atmosphere were carried out using Schlenk-line techniques under an atmosphere of nitrogen.

NMR spectra were recorded on a Bruker Avance-400 (400 MHz ^{1}H and 100 MHz ^{13}C) spectrometer. Two-dimensional NMR (COSY, NOESY, HSQC and HMBC) were acquired by the solution state NMR service at Durham University on Varian VNMRS-600 (600 MHz) or VNMRS-700 (700 MHz) instruments. Chemical shifts (δ) are in ppm, referenced to residual protio-solvent resonances: $CDCl_3$ = 7.26 ppm (^{1}H), 77.2 (^{13}C); DMSO = 2.50 ppm (^{1}H), 39.5 (^{13}C); CH_3CN = 1.93 ppm (^{1}H), 1.3 (^{13}C). Multiplicity is as follows: s (singlet); d (doublet); t (triplet); q (quartet) and m (multiplet). Coupling constants are given in Hertz.

ES-MS data (positive and negative ionisation modes) were obtained on a SQD mass spectrometer interfaced with an Acquity UPLC system with acetonitrile as the carrier solvent. ASAP experiments were performed on Waters Xevo QToF mass spectrometer. Thin-layer chromatography (TLC) was carried out using silica plates (MerckArt 5554) and visualized by UV radiation at 254 and 365 nm.

UV-vis absorption spectra were recorded on a Biotek Instruments UVIKON XS spectrometer operating with LabPower software in matched 1 cm pathlength quartz cuvettes. Emission spectra were acquired on a Jobin Yvon Fluoromax-2 spectrometer equipped with a Hamamatsu R928 photomultiplier tube. All samples were contained within 1 cm pathlength quartz cuvettes modified for connection to a vacuum line. Degassing was achieved by three freezepump thaw cycles whilst connected to the vacuum manifold: final vapour pressure at 77 K was $< 5\times10^{-2}$ mbar. Emis-

sion was recorded at 90° to the excitation source, and spectra were corrected after acquisition for dark count and for the spectral response of the detector. The quantum yields were determined relative to an aqueous solution of $[Ru(bpy)_3]Cl_3$ for which Φ_{lum}= 0.040.[112]

Luminescence lifetimes of the complexes in solution were measured by time-correlated single-photon counting, using a 405 nm pulsed-diode laser as the excitation source. The emission was detected at 90° to the excitation source, after passage through a monochromator, using a Peltier-cooled R928 detector. The longer luminescence lifetimes $\geq$ 10 µs and the lifetimes of all the complexes at 77 K were measured using the same detector operating in multichannel scaling mode following excitation with a microsecond pulsed xenon lamp.

The solid-state samples were prepared via the drop-cast method onto sapphire substrates from CH_3CN solution. For the neat film, this was direct from the stock solution of 1 mg/mL of the complex. The PMMA polymer solution was made up at 100 mg/mL concentration and mixed with the stock solutions of the compounds to create 0.1, 1 and 10 wt % films of the compound by mass in the polymer. These were then also drop-cast onto sapphire substrates. The UV-Vis absorption spectra of the films were measured on a Shimadzu UV-3600 double beam spectrophotometer with a second sapphire substrate as a blank reference. The photoluminescence spectra and quantum yields in films were measured using an integrating sphere in conjunction with an Ocean Optics QePro detector, following excitation at 365 nm with an Ocean Optics LLS-LED.

8.2 Calculations using Density Functional Theory

Density functional theory (DFT) and time-dependent density functional theory (TDDFT) simulations with Tamm-Dancoff approximation (TDA) were performed on the complexes using the ORCA 5.0.3 quantum chemistry software.[113–116] Molecular orbital iso surfaces were visualised using ChimeraX-1.4[117,118] or Avogadro 1.2.0.[119,120] Geometry optimisations of the complexes in the ground state were performed using B3LYP[121,122]/def2-SVP.[123] Triplet excited state (T1) geometries were performed similarly, but also using the BP86[124]/def2-SVP[123] with the RI keyword, and def2-SVP/C[125] and def2/J[126] auxiliary basis sets. Single-point energy calcu-

lations were performed at the B3LYP/def2-SVP level of theory with the aid of the RIJCOSX[127,128] approximation and using CPCM for the solvent CH_3CN or CH_2Cl_2 in all cases. All calculations were performed using very tight geometry and SCF convergence criteria, and using the atom-pairwise dispersion correction with the Becke-Johnson damping scheme (D3BJ).[129,130] Frequency calculations were used to confirm that the respective optimised geometries were energy minima.

8.3 General Procedures

General procedure for Suzuki Cross-Coupling reaction

A mixture of the bromopyridine (1 equiv.), the boronic acid (1 equiv.), Na_2CO_3 (8 equiv.), DME (1 mL per mmol of Na_2CO_3) and water (1 mL per mmol of Na_2CO_3) was degassed by three freeze-pump-thaw cycles. $Pd(PPh_3)_4$ (0.05 equiv.) was added under nitrogen and the mixture heated at reflux temperature for 72 h. After cooling, water was added and the crude product was extracted into DCM. The organic phase was dried over $MgSO_4$, filtered and the solvent was removed under reduced pressure. The crude product was purified by gradient column chromatography on silica with hexane / ethyl acetate.

General procedure for the synthesis of Pt^{II}(NNC)Cl complexes

K_2PtCl_4 (1.14 equiv.) and the *NNC*H proligand (1 equiv.) were dissolved in acetic acid and degassed by three freeze-pump-thaw cycles. The mixture was heated to reflux temperature for 72 h. After cooling down, water was added. The resulting precipitate was isolated, washed successively with water, MeOH and diethyl ether, and extracted into DCM. The solvent was removed under reduced pressure to yield the final product.

General procedures for the synthesis of Pt(NCN)Cl_3 and Pt^{IV}(NNC)Cl_3 complexes

Method 1

Chlorine gas, generated by dropwise addition of HCl to solid $KMnO_4$, was bubbled through a solution of the Pt^{II} complex in $CHCl_3$ for 10 min, with the partial exclusion of light. A pale-coloured precipitate formed and the mixture was left to stir for 1 h. The solvent was removed under reduced pressure.

Method 2

The Pt^{II} complex and $PhICl_2$ were dissolved in $CHCl_3$ and the mixture was left to stir overnight, with the partial exclusion of light. The solvent was removed under reduced pressure and the resulting solid washed with diethyl ether. If further purification was required, the complex was purified by fractional precipitation or by gradient column chromatography on silica with hexane / ethyl acetate as the mobile phase.

General procedure for the synthesis of 3+2+1 Pt^{IV} complexes

A mixture of $Pt^{II}(NNC)Cl_3$ complex (1 equiv.), bidentate ligand (1 equiv.) and AgOTf (2 equiv.) was suspended in dry toluene (3 mL per 0.1 mmol of complex) in a dry Schlenk flask. The mixture was degassed by three freeze-pump-thaw cycles and was heated at 125°C overnight, with the partial exclusion of light. The resulting precipitate was isolated by centrifugation, washed successively with toluene (5 mL), hexane (5 mL) and diethyl ether (5 mL), and extracted into DCM. The solvent was removed under reduced pressure. The crude product was dissolved in acetone and the solution was slowly added dropwise to a saturated aqueous solution of KPF_6 (20 mL). The precipitate was isolated, washed with water (10 mL) and dried. The crude complex was purified by recrystallisation and/or column chromatography.

General procedure for the synthesis of Pt^{IV} 2,2';6',2''-terpyridine complexes

A mixture of $Pt^{II}Cl_3$ complex (1 equiv.), 2,2';6',2''-terpyridine (1 equiv.) and AgOTf (2 equiv.) was suspended in dry toluene (3 mL per 30 mg of complex) in a dry Schlenk flask. The mixture was degassed by three freeze-pump-thaw cycles and was heated at 125°C overnight, with the partial exclusion of light. The resulting precipitate was isolated by centrifugation, washed successively with toluene (5 mL), hexane (5 mL), DCM (5 mL) and diethyl ether (5 mL), and extracted into acetone. The solvent was removed under reduced pressure. The crude product was dissolved in the minimum volume of acetone and the solution was slowly added dropwise to a saturated aqueous solution of KPF_6 (20 mL). The precipitate was isolated, washed with water (10 mL) and dried. The crude complex was purified by recrystallisation.

8.4 Chapter 2 synthesis

8.4.1 Proligands and precursors

1,3-Di(2-pyridyl)benzene (dpybH)

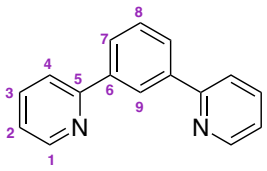

A mixture of benzene-1,3-diboronic acid (1 g, 6.03 mmol), 2-bromopyridine (1.16 mL, 12.06 mmol), DME (50 mL) and water (50 mL) was degassed by three freeze-pump-thaw cycles. $Pd(PPh_3)_4$ (349 mg, 0.3 mmol) was added under nitrogen and the mixture heated at reflux temperature for 72 h. After cooling down, water (10 mL) was added and the crude product was extracted into DCM (3×15 mL). The organic phase was dried over $MgSO_4$, filtered and the solvent was removed under reduced pressure. The crude product was purified by gradient column chromatography from 100% hexane to 60% hexane / 40% ethyl acetate (R_f = 0.2 in EtOAc : hexane = 3 : 7) to yield a colourless oil (1.260 g, 90% yield) ^{1}H NMR (400 MHz, $CDCl_3$) δ_H / ppm 8.77 – 8.71 (m, 1H), 8.67 – 8.63 (m, 1H), 8.12 – 8.05 (m, 1H), 7.90 – 7.84 (m, 1H), 7.83 – 7.77 (m, 1H), 7.66 – 7.58 (m, 1H), 7.31 – 7.25 (m, 1H) ESI$^+$ m/z 232 (100%) $[M + H]^+$ The experimental data obtained are in agreement with literature.[131]

8.4.2 Pt^{II} complexes

Pt(dpyb)Cl

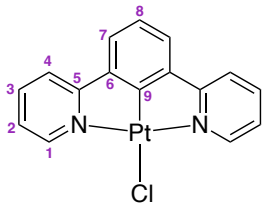

K_2PtCl_4 (306 mg, 0.74 mmol) and dpybH (150 mg, 0.65 mmol) were dissolved in acetic acid (20 mL) and degassed by three freeze-pump-thaw cycles. The mixture was heated to reflux temperature for 72 h. After cooling down, water was added. The resulting precipitate was isolated, washed successively with water (5 mL), MeOH (5 mL) and diethyl ether (5 mL), and extracted into DCM. The solvent was removed under reduced pressure to yield a yellow solid (165 mg, 55% yield). ^{1}H NMR (599 MHz, acetone-d_6) δ_H / ppm 9.40 – 9.33 (m,$^3J_{^{195}Pt-^1H} \approx$ 40 Hz, 1H), 8.01 – 7.91 (m, 2H), 7.75 – 7.67 (m,$^3J_{^{195}Pt-^1H} \approx$ 20 Hz, 2H), 7.52 – 7.41 (m, 2H), 7.35 – 7.29 (m, 2H), 7.27 – 7.22 (m, 1H) ASAP$^+$ *m/z* 467 (100%) $[M - Cl^- + MeCN]^+$ The experimental data obtained are in agreement with literature.[132]

[{Pt(dpyb)}$_3$L^4][PF$_6$]$_2$

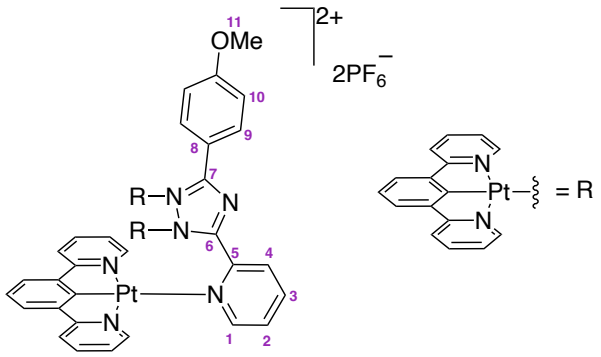

A mixture of Pt(dpyb)Cl$_3$ (28 mg, 0.05 mmol), L^4 (13 mg, 0.05 mmol) and AgOTf (27 mg, 0.10 mmol) was suspended in dry ethylene glycol (3 mL) in a dry Schlenk flask. The mixture was degassed by three freeze-pump-thaw cycles and was heated at reflux temperature overnight, with the partial exclusion of light. The resulting precipitate was removed by centrifugation and the solution was slowly added dropwise to a saturated aqueous solution of KPF$_6$ (20 mL). The precipitate was isolated, washed successively with water (10 mL), methanol (10 mL) and diethyl ether (10 mL). The crude product was recrystallised from DCM/diethyl ether, yielding a red solid (17 mg, 19%) ^{1}H NMR (599 MHz, acetone-d$_6$) δ_H / ppm 9.34 (d, *J* = 5.0 Hz, 1H, H^1), 9.30 (d, *J* = 8.0 Hz, 1H, H^4), 8.90 – 8.86 (m, 2H, H^9), 8.53 – 8.49 (m, 1H, H^3), 8.03 – 7.98 (m, 5H), 7.98 – 7.95 (m, 1H), 7.91 (ddd, *J* = 7.0, 5.5, 1.5 Hz, 1H, H^2), 7.88 – 7.85 (m, 2H), 7.74 (qd, *J* = 7.5, 1.5 Hz, 4H), 7.71 – 7.68 (m, 2H), 7.46 (dd, *J* = 8.0, 1.5 Hz, 2H), 7.35 (d, *J* = 7.5 Hz, 2H), 7.33 (d, *J* = 7.5 Hz, 2H), 7.17 (d, *J* = 7.5 Hz, 2H), 7.15 – 7.09 (m, 3H), 7.09 – 7.03 (m, 2H), 6.97 – 6.94 (m, 2H, H^{10}), 6.85 (ddd, *J* = 7.5, 5.5, 1.5 Hz, 2H), 6.53 (ddd, *J* = 7.5, 5.5, 1.5 Hz, 2H), 3.75 (s, 3H, OCH$_3$ Hs) ^{13}C NMR (151 MHz, acetone-d$_6$) δ_C / ppm 152.7, 130.2, 129.4, 140.2, 140.4, 151.3, 150.4, 126.9, 140.4, 120.8, 140.0, 120.3, 120.1, 124.3, 124.5, 124.2, 124.2, 124.4, 123.8, 114.0, 123.8, 123.5, 54.8 (OMe C)

8.4.3 Pt^{IV} complexes

Pt(dpyb)Cl$_3$

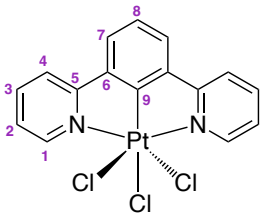

Pt(dpyb)Cl (165 mg, 0.36 mmol) was oxidised according to method 1 outlined above. The product was obtained as a pale yellow solid (182 mg, 100% yield) ^{1}H NMR (400 MHz, DMSO-d$_6$) δ_H / ppm 9.24 (dd, $^{3}J_{^{195}Pt-^{1}H} \approx 27$ Hz, J = 6.0, 1.5 Hz, 2H, H^{1}), 8.50 (dd, J = 8.0, 1.5 Hz, 2H, H^{4}), 8.39 – 8.33 (m, 2H, H^{3}), 8.18 (d, J = 8.0 Hz, 2H, H^{7}), 7.81 (ddd, J = 7.5, 6.0, 1.5 Hz, 2H, H^{2}), 7.62 – 7.54 (m, 1H, H^{8}) ESI^{+} *m/z* 538 (100%) [M – Cl^{-} + MeCN]$^{+}$

3 + 2 + 1 Pt^{IV} complexes

[Pt(dpyb)L^{4}][PF$_6$]

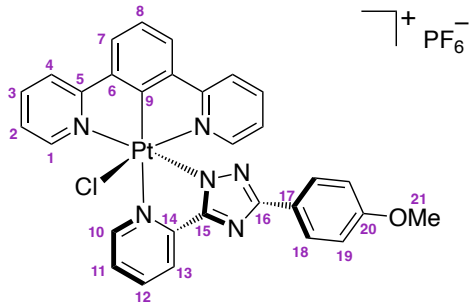

Pt(dpyb)Cl$_3$ (30 mg, 0.06 mmol), L^{4} (14 mg, 0.06 mmol) and AgOTf (29 mg, 0.12 mmol) were reacted according to the general procedure outlined above. The crude product was recrystallised from DCM/diethyl ether, yielding a pale yellow crystalline solid (8 mg, 17%) ^{1}H NMR (599 MHz, acetone-d$_6$) δ_H / ppm 9.69 – 9.64 (m, 1H, H^{10}), 8.77 – 8.71 (m, 1H, H^{12}), 8.58 – 8.52 (m, 3H, H^{4} and H^{13}), 8.38 – 8.34 (m, 2H, H^{3}), 8.32 (d, J = 8.0 Hz, 2H, H^{7}), 8.28 (ddd, J = 8.0, 5.5, 1.5 Hz, 1H, H^{11}), 8.14 – 8.10 (m, $^{3}J_{^{195}Pt-^{1}H} \approx 26$ Hz, 2H, H^{1}), 7.91 – 7.87 (m, 1H, H^{8}), 7.72 – 7.68 (m, 2H, H^{18}), 7.55 (ddd, J = 7.5, 6.0, 1.5 Hz, 2H, H^{2}), 6.88 – 6.83 (m, 2H, H^{19}), 3.75 (s, 3H, H^{21}) ^{13}C NMR (151 MHz, acetone-d$_6$) δ_C / ppm 164.7 (C^{5}), 163.9 (C^{16}), 160.6 (C^{17}), 159.6 (C^{15}), 154.0 (C^{9}), 150.5 (C^{1}), 148.0 (C^{10}), 147.7 (C^{14}), 143.9 (C^{3}), 143.8 (C^{12}), 138.2 (C^{6}), 128.8 (C^{8}), 128.3 (C^{7}), 127.9 (C^{11}), 127.1 (C^{18}), 127.0 (C^{2}), 123.9 (C^{20}), 123.7 (C^{quat}), 123.2 (C^{13}), 113.7 (C^{19}), 54.7 (C^{21}) HRMS (ES^{+}) *m/z* 711.1170 [M – PF$_6$]$^{+}$ calcd for [C$_{30}$H$_{22}$N$_6$OCl^{194}Pt]$^{+}$ 711.1188

[Pt(dpyb)L^5][PF$_6$]

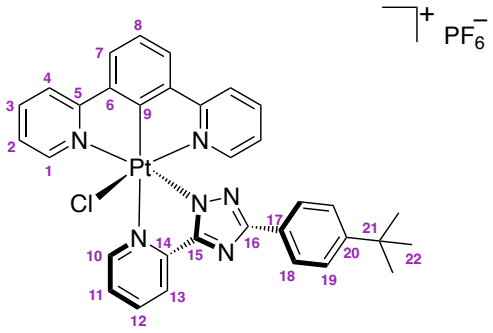

Pt(dpyb)Cl$_3$ (19 mg, 0.04 mmol), L^5 (10 mg, 0.04 mmol) and AgOTf (18 mg, 0.08 mmol) were reacted according to the general procedure outlined above. The crude product was recrystallised from DCM/diethyl ether, yielding a pale yellow crystalline solid (8 mg, 27% yield) ^{1}H NMR (599 MHz, acetone-d$_6$) δ_H / ppm 9.67 (d, *J* = 5.5 Hz, 1H, H^{10}), 8.77 – 8.74 (m, 1H, H^{12}), 8.58 – 8.54 (m, 3H, H^4 and H^{13}), 8.38 – 8.34 (m, 2H, H^3), 8.33 (dd, *J* = 8.0, 1.5 Hz, 2H, H^7), 8.31 – 8.28 (m, 1H, H^{11}), 8.13 (d, *J* = 6.0 Hz, 2H, H^1), 7.92 – 7.88 (m, 1H, H^8), 7.72 – 7.68 (m, 2H, H^{18}), 7.55 (dd, *J* = 7.5, 6.0 Hz, 2H, H^2), 7.35 (dd, *J* = 8.5, 1.5 Hz, 2H, H^{19}), 1.24 (d, *J* = 1.5 Hz, 9H, H^{22}) HRMS (ES$^+$) *m/z* 737.1700 [M – PF$_6$]$^+$ calcd for [C$_{33}$H$_{28}$N$_6$Cl^{194}Pt]$^+$ 737.1691

[Pt(dpyb)L^6][PF$_6$]

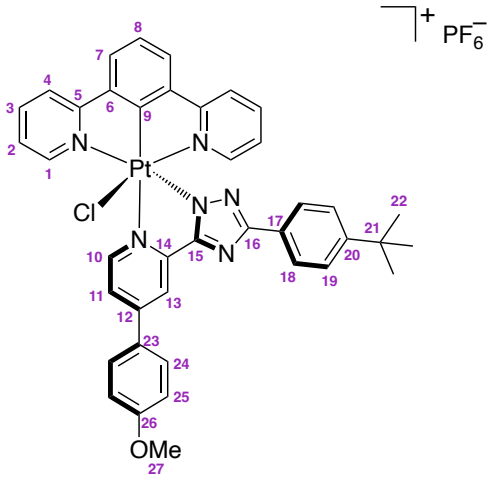

Pt(dpyb)Cl$_3$ (30 mg, 0.06 mmol), L^6 (22 mg, 0.06 mmol) and AgOTf (30 mg, 0.12 mmol) were reacted according to the general procedure outlined above.The crude product was recrystallised from DCM/diethyl ether and washed with chloroform to yield a pale yellow solid (52 mg, 85% yield) ^{1}H NMR (599 MHz, acetone-d$_6$) δ_H / ppm 9.58 (d, *J* = 6.0 Hz, 1H, H^{10}), 8.70 (d, *J* = 2.0 Hz, 1H, H^{13}), 8.59 – 8.54 (m, 2H, H^4), 8.53 (ddd, *J* = 6.0, 2.0, 1.0 Hz, 1H, H^{11}), 8.38 – 8.35 (m, 2H, H^3), 8.33 (dd, *J* = 8.0,

1.0 Hz, 2H, H^7), 8.24 – 8.22 (m, 2H, H^1), 8.22 – 8.19 (m, 2H, H^{24}), 7.92 – 7.88 (m, 1H, H^8), 7.72 (d, *J* = 8.5, 2H, H^{18}), 7.56 (ddd, *J* = 7.5, 6.0, 1.5 Hz, 2H, H^2), 7.36 (d, *J* = 8.5 Hz, 2H, H^{19}), 7.28 (d, *J* = 8.5 Hz, 2H, H^{25}), 3.98 (s, 3H, H^{27}), 1.25 (s, 9H, H^{22}) ^{13}C NMR (151 MHz, acetone-d_6) δ_C / ppm 164.8 (C^5), 162.8 (C^{26}), 154.2 (C^{quat}), 152.1 (C^{20}), 150.5 (C^1), 147.8 (C^{10}), 143.9 (C^3), 138.3 (C^{quat}), 129.4 (C^{24}), 128.7 (C^8), 128.6 (C^{quat}), 128.3 (C^7), 127.2 (C^{23}), 127.0 (C^2), 125.7 (C^{quat}), 125.5 (C^{18}), 125.2 (C^{19}), 123.7 (C^4), 123.7 (C^{11}), 119.0 (C^{13}), 115.2 (C^{25}), 55.2 (C^{27}), 34.3 (C^{21}), 30.5 (C^{22}) HRMS (ES$^+$) *m/z* 843.2083 $[M - PF_6]^+$ calcd for $[C_{40}H_{34}N_6OCl^{194}Pt]^+$ 843.2109

[Pt(dpyb)L^7][PF$_6$]

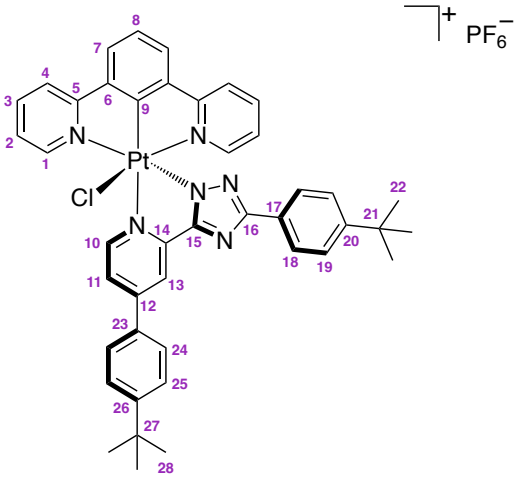

$Pt(dpyb)Cl_3$ (20 mg, 0.04 mmol), L^7 (14 mg, 0.04 mmol) and AgOTf (19 mg, 0.08 mmol) were reacted according to the general procedure outlined above. The crude product was recrystallised from DCM/diethyl ether, yielding a pale yellow crystalline solid (35 mg, 92 % yield) ^{1}H NMR (599 MHz, acetone-d_6) δ_H / ppm 9.64 (d, *J* = 6.0 Hz, 1H, H^{10}), 8.74 (d, *J* = 2.0 Hz, 1H, H^{13}), 8.59 – 8.55 (m, 3H, H^4 and H^{11}), 8.38 – 8.32 (m, 4H, H^3 and H^7), 8.21 (dd, *J* = 6.0, 1.5 Hz, 2H, H^1), 8.17 – 8.12 (m, 2H, H^{24}), 7.92 – 7.88 (m, 1H, H^8), 7.79 (dd, *J* = 8.5, 2.5 Hz, 2H, H^{25}), 7.74 – 7.71 (m, 2H, H^{18}), 7.56 (ddd, *J* = 7.5, 6.0, 1.5 Hz, 2H, H^2), 7.36 (dd, *J* = 8.5, 2.0 Hz, 2H, H^{19}), 1.43 (s, 9H, H^{28}), 1.25 (s, 9H, H^{22}) ^{13}C NMR (151 MHz, acetone-d_6) δ_C / ppm 155.1 (C^{26}), 152.1 (C^{20}), 150.5 (C^1), 148.0 (C^{10}), 143.9 (C^3), 138.3 (C^{quat}), 128.8 (C^8), 128.3 (C^7), 127.5 (C^{24}), 127.0 (C^2), 126.7 (C^{25}), 125.5 (C^{18}), 125.2 (C^{19}), 124.4 (C^{11}), 123.8 (C^4), 119.7 (C^{13}), 34.7 (C^{27}), 34.3 (C^{21}), 30.5 (C^{26} and C^{22}) HRMS (ES$^+$) *m/z* 869.2639 $[M - PF_6]^+$ calcd for $[C_{43}H_{40}N_6Cl^{194}Pt]^+$ 869.2630

[Pt(dpyb)(bpy)][PF_6]

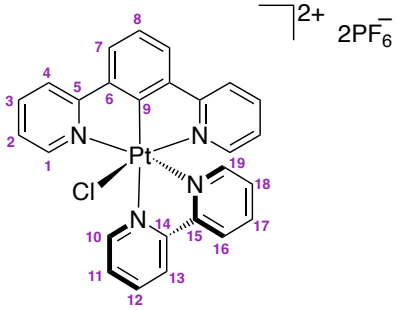

$Pt(dpyb)Cl_3$ (30 mg, 0.06 mmol), 2,2'-bipyridine (9 mg, 0.06 mmol) and AgOTf (29 mg, 0.11 mmol) were reacted according to the general procedure outlined above. The pure product was obtained as a pale yellow solid (45 mg, 88% yield) ^{1}H NMR (599 MHz, acetone-d_6) δ_H / ppm 9.88 – 9.85 (m, 1H, H^{10}), 9.21 (d, J = 8.0 Hz, 1H, H^{13}), 8.99 (d, J = 8.0 Hz, 1H, H^{16}), 8.99 – 8.92 (m, 1H, H^{12}), 8.62 (dd, J = 8.0, 1.5 Hz, 2H, H^4), 8.60 – 8.57 (m, 1H, H^{11}), 8.48 – 8.43 (m, 3H, H^{17} and H^7), 8.44 – 8.38 (m, 2H, H^3), 8.19 – 8.13 (m, 3H, H^{19} and H^1), 8.05 – 7.98 (m, 1H, H^8), 7.76 – 7.72 (m, 1H, H^{18}), 7.57 (ddd, J = 8.0, 6.0, 1.5 Hz, 2H, H^2) ^{13}C NMR (151 MHz, acetone-d_6) δ_C / ppm 151.1 (C^1), 149.8 (C^{19}), 148.6 (C^{10}), 144.6 (C^{17}), 144.5 (C^{12}), 144.4 (C^3), 131.3 (C^{11}), 130.8 (C^{18}), 130.2 (C^8), 129.5 (C^7), 127.5 (C^2), 127.5 (C^{16}), 127.0 (C^{13}), 124.5 (C^4) HRMS (ES^+) *m/z* 308.0427 $[M]^{2+}/2$ calcd for $[C_{26}H_{17}N_4Cl^{194}Pt]^{2+}/2$ 308.0462

[Pt(dpyb)(phpy)][PF_6]

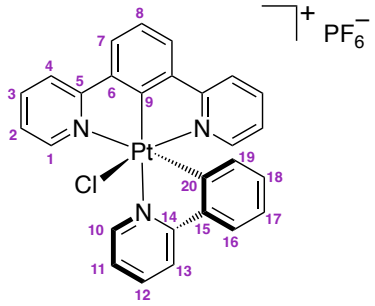

$Pt(dpyb)Cl_3$ (25 mg, 0.05 mmol), 2-phenylpyridine (6.7 µL, 0.05 mmol) and AgOTf (24 mg, 0.09 mmol) were reacted according to the general procedure outlined above. The complex was purified by gradient column chromatography on silica with MeCN, water and saturated aqueous KNO_3 (100 : 0 : 0 to 80 : 19.5 : 0.5) yielding a pale yellow solid (4 mg, 11% yield) ^{1}H NMR (599 MHz, acetone-d_6) δ_H / ppm 9.96 – 9.88 (m, $^3J_{^{195}Pt\text{-}^1H} \approx$ 13 Hz, 1H, H^{10}), 8.66 (d, J = 8.0 Hz, 1H, H^{12}), 8.60 – 8.55 (m, 1H, H^{13}), 8.51 – 8.46 (m, 2H, H^4), 8.30 – 8.24 (m, 3H, H^3 and H^7), 8.11 – 8.06 (m, 2H, H^{11} and H^{16}), 7.98 –

7.89 (m, $^{3}J_{^{195}Pt-^{1}H} \approx 33$ Hz, 2H, H^{1}), 7.84 (dd, J = 8.0, 7.5 Hz, 1H, H^{8}), 7.44 (ddd, J = 7.5, 6.0, 1.5 Hz, 2H, H^{2}), 7.22 – 7.17 (m, 1H, H^{17}), 6.99 – 6.93 (m, 1H, H^{18}), 6.19 (dd, $^{3}J_{^{195}Pt-^{1}H} \approx 38$ Hz, J = 7.9, 1.0 Hz, 1H, H^{19}) ^{13}C NMR (151 MHz, acetone-d_6) δ_C / ppm 150.0 (C^{1}), 148.3 (C^{10}), 142.6 (C^{3}), 142.4 (C^{13}), 132.2 (C^{18}), 129.9 (C^{19}), 127.9 (C^{7}), 127.6 (C^{17}), 127.5 (C^{8}), 126.8 (C^{11}), 126.2 (C^{16}), 126.1 (C^{2}), 123.2 (C^{4}), 122.1 (C^{12}) HRMS (ES$^+$) *m/z* 614.0889 $[M - PF_6]^+$ calcd for $[C_{27}H_{19}N_3Cl^{194}Pt]^+$ 614.0894

Bis-tridentate Pt^{IV} complexes

$[Pt(dpyb)(tpy)][PF_6]_3$

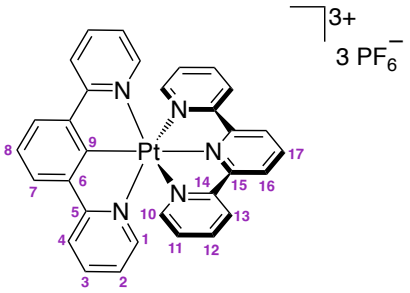

Method 1

$Pt(dpyb)Cl_3$ (19 mg, 0.04 mmol) and 2,2';6',2"-terpyridine (8 mg, 0.04 mmol) were suspended in dry ethylene glycol (3 mL) in a dry Schlenk flask. The mixture was degassed by three freeze-pump-thaw cycles and heated to reflux temperature overnight, with the partial exclusion of light. Water (7 mL) was added and the resulting precipitate was removed by centrifugation. The solution was slowly added dropwise to a saturated aqueous solution of KPF_6 (20 mL). The precipitate was isolated, washed with water (10 mL) and recrystallised from DCM/diethyl ether to yield a pale pink solid (3 mg, 8% yield)

Method 2

$PtL^{7}Cl_3$ (30 mg, 0.06 mmol), 2,2';6',2"-terpyridine (14 mg, 0.06 mmol) and AgOTf (44 mg, 0.17 mmol) were reacted according to the general procedure outlined above. The product was recrystallised from acetone/diethyl ether to yield a pale pink solid (10 mg, 17% yield)

^{1}H NMR (599 MHz, acetone-d_6) δ_H / ppm 9.39 (d, J = 8.5 Hz, 2H, H^{16}), 9.28 (dd, J = 8.5, 8.0 Hz, 1H, H^{17}), 9.07 (dd, J = 8.0, 1.5 Hz, 2H, H^{13}), 8.67 (dd, J = 8.0, 1.5 Hz, 2H, H^{4}), 8.62 – 8.56 (m, 2H, H^{12}), 8.55 (d, J = 8.0 Hz, 2H, H^{7}), 8.39 – 8.33 (m, 2H, H^{3}), 8.27 (dd, J = 6.0, 1.5 Hz, 2H, H^{10}), 8.21 – 8.15 (m, 3H, H^{1} and H^{8}), 7.81 (ddd,

J = 7.5, 6.0, 1.5 Hz, 2H, H^{11}), 7.46 (ddd, J = 8.0, 6.0, 1.5 Hz, 2H, H^{2}) ^{13}C NMR (151 MHz, acetone-d_6) δ_C / ppm 166.1 (C^5), 162.0 (C^9), 158.6 (C^{14}), 154.0 (C^{10}), 151.6 (C^{15}), 151.5 (C^1), 147.0 (C^{17}), 145.6 (C^{12}), 145.1 (C^3), 138.4 (C^6), 131.6 (C^{11}), 131.2 (C^8), 130.1 (C^7), 129.8 (C^{13}), 128.9 (C^{16}), 127.8 (C^2), 125.1 (C^4) HRMS (ES$^+$) *m/z* 219.3802 $[M]^{3+}/3$ calcd for $[C_{31}H_{22}N_5{}^{194}Pt]^{3+}/3$ 219.3834

8.5 Chapter 3 synthesis

8.5.1 Proligands and precursors

6-phenyl-2,2-bipyridine

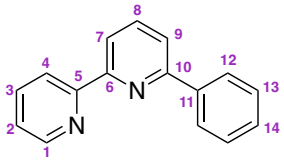

A mixture of 6-bromo-2,2-bipyridine (615 mg, 2.62 mmol), phenylboronic acid (319 mg, 2.62 mmol), Na_2CO_3 (2.218 g, 20.93 mmol), $Pd(PPh_3)_4$ (151 mg, 0.131 mmol), DME (20 mL) and water (20 mL) were reacted according to the general procedure for Suzuki cross-coupling. The product was obtained as an off-white solid (419 mg, 71% yield) (R_f = 0.5 in EtOAc : hexane = 2 : 8) ^{1}H NMR (400 MHz, $CDCl_3$) δ_H / ppm 8.72 (ddd, J = 5.0, 2.0, 1.0 Hz, 1H), 8.70 – 8.65 (m, 1H), 8.40 (dd, J = 8.0, 1.0 Hz, 1H), 8.22 – 8.14 (m, 2H), 7.96 – 7.85 (m, 2H), 7.81 (dd, J = 8.0, 1.0 Hz, 1H), 7.57 – 7.51 (m, 2H), 7.50 – 7.43 (m, 1H), 7.36 (ddd, J = 7.5, 5.0, 1.0 Hz, 1H) ESI$^+$ m/z 232 (100%) $[M + H]^+$ The experimental data obtained are in agreement with literature.[133]

6-(4-methylphenyl)-2,2'-bipyridine

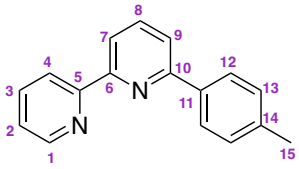

A mixture of 6-Bromo-2,2′-bipyridine (150 mg, 0.64 mmol), p-tolylboronic acid (87 mg, 0.64 mmol), Na_2CO_3 (541 mg, 5.10 mmol), DME (5 mL) and water (5 mL) was degassed by three freeze-pump-thaw cycles. $Pd(PPh_3)_4$ (37 mg, 0.032 mmol) was added under nitrogen and the mixture heated at reflux temperature for 72 h. After cooling down, water (10 mL) was added and the crude product was extracted into

DCM (3×15 mL). The organic phase was dried over $MgSO_4$, filtered and the solvent was removed under reduced pressure. The crude product was purified by gradient column chromatography from 100% hexane to 70% hexane / 30% ethyl acetate (R_f = 0.5 in EtOAc : hexane = 2 : 8) to yield an off-white solid (135 mg, 86% yield) ^{1}H NMR (400 MHz, $CDCl_3$) δ_H / ppm 8.72 (d, J = 5.0 Hz, 1H), 8.67 (d, J = 8.0 Hz, 1H), 8.37 (d, J = 8.0 Hz, 1H), 8.08 (d, J = 8.0 Hz, 2H), 7.93 – 7.83 (m, 2H), 7.77 (d, J = 8.0 Hz, 1H), 7.34 (d, J = 8.0 Hz, 3H), 2.46 (s, 3H) ESI$^+$ m/z 247 (100%) $[M + H]^+$ The experimental data obtained are in agreement with literature.[134]

6-(3-methoxyphenyl)-2,2'-bipyridine

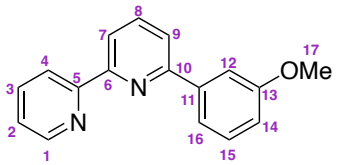

A mixture of 6-bromo-2,2-bipyridine (250 mg, 1.06 mmol), 3-methoxyphenylboronic acid (162 mg, 1.06 mmol), Na_2CO_3 (902 mg, 8.57 mmol), $Pd(PPh_3)_4$ (61 mg, 0.05 mmol), DME (9 mL) and water (9 mL) were reacted according to the general procedure for Suzuki cross-coupling. The product was obtained as an off-white solid (197 mg, 66% yield) (R_f = 0.3 in EtOAc : hexane = 1 : 9) ^{1}H NMR (400 MHz, $CDCl_3$) δ_H / ppm 8.72 (ddd, J = 5.0, 2.0, 1.0 Hz, 1H), 8.69 – 8.62 (m, 1H), 8.40 (dd, J = 8.0, 1.0 Hz, 1H), 7.96 – 7.83 (m, 2H), 7.83 – 7.76 (m, 2H), 7.73 (ddd, J = 8.0, 2.0, 1.0 Hz, 1H), 7.49 – 7.41 (m, 1H), 7.35 (ddd, J = 8.0, 5.0, 1.0 Hz, 1H), 7.02 (ddd, J = 8.0, 2.0, 1.0 Hz, 1H), 3.95 (s, 3H) ESI$^+$ m/z 262 (100%) $[M + H]^+$ The experimental data obtained are in agreement with literature.[64]

6-(4-methoxyphenyl)-2,2'-bipyridine

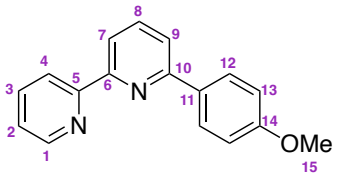

A mixture of 6-bromo-2,2-bipyridine (83 mg, 0.35 mmol), 4-methoxyphenylboronic acid (54 mg, 0.35 mmol), Na_2CO_3 (300 mg, 2.83 mmol), $Pd(PPh_3)_4$ (20 mg, 0.02 mmol), DME (20 mL) and water (20 mL) were reacted according to the general procedure for Suzuki cross-coupling. The product was obtained as an off-white solid (79

mg, 85% yield) (R_f = 0.3 in EtOAc : hexane = 2 : 8) ^{1}H NMR (400 MHz, $CDCl_3$) δ_H / ppm 8.72 (ddd, J = 5.0, 2.0, 1.0 Hz, 1H), 8.68 – 8.62 (m, 1H), 8.34 (dd, J = 8.0, 1.0 Hz, 1H), 8.19 – 8.10 (m, 2H), 7.92 – 7.83 (m, 2H), 7.74 (dd, J = 8.0, 1.0 Hz, 1H), 7.35 (ddd, J = 7.5, 5.0, 1.0 Hz, 1H), 7.10 – 7.02 (m, 2H), 3.91 (s, 3H) ESI$^+$ m/z 262 (100%) $[M + H]^+$ The experimental data obtained are in agreement with literature.[135]

6-[4-(trifluoromethyl)phenyl]-2,2'-bipyridine

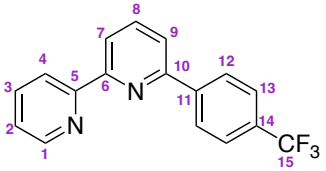

A mixture of 6-bromo-2,2-bipyridine (300 mg, 1.28 mmol), 4-(trifluoromethyl)phenylboronic acid (244 mg, 1.28 mmol), Na_2CO_3 (1.082 g, 10.21 mmol), $Pd(PPh_3)_4$ (74 mg, 0.06 mmol), DME (10 mL) and water (10 mL) were reacted according to the general procedure for Suzuki cross-coupling. The product was obtained as an off-white solid (334 mg, 87% yield) (R_f = 0.4 in EtOAc : hexane = 2 : 8) ^{1}H NMR (400 MHz, $CDCl_3$) δ_H / ppm 8.73 (ddd, J = 5.0, 2.0, 1.0 Hz, 1H), 8.68 – 8.61 (m, 1H), 8.47 (dd, J = 8.0, 1.0 Hz, 1H), 8.32 – 8.25 (m, 2H), 8.00 – 7.93 (m, 1H), 7.92 – 7.87 (m, 1H), 7.83 (dd, J = 8.0, 1.0 Hz, 1H), 7.81 – 7.77 (m, 2H), 7.37 (ddd, J = 7.5, 5.0, 1.0 Hz, 1H) ^{19}F NMR (376 MHz, $CDCl_3$) δ_F / ppm -62.5 ESI$^+$ m/z 300 (100%) $[M + H]^+$ The experimental data obtained are in agreement with literature.[135]

6-(thiophen-2-yl)-2,2'-bipyridine

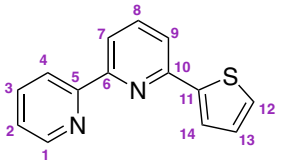

6-Bromo-2,2-bipyridine (200 mg, 0.85 mmol) and 2-(tributylstannyl)thiophene (270 µL, 0.85 mmol) were dissolved in toluene (10 mL) and degassed by three freeze-pump-thaw cycles. $Pd(PPh_3)_4$ (30 mg, 0.04 mmol) was added under nitrogen and the resulting yellow solution was heated at reflux temperature overnight. After cooling down, saturated aqueous KF (10 mL) was added and the mixture was stirred for 30 min. The precipitate was filtered off and then the solvent was removed under reduced pressure. The crude product was extracted into DCM (3×15 mL), washed with 5% $NaHCO_3$(aq)

(3×15 mL), dried over $MgSO_3$ and purified by gradient column chromatography on silica with hexane / ethyl acetate as the mobile phase (R_f = 0.3 in EtOAc : hexane = 2 : 8) to yield a white solid (178 mg, 88% yield) ^{1}H NMR (400 MHz, $CDCl_3$) δ_H / ppm 8.70 (ddd, *J* = 5.0, 2.0, 1.0 Hz, 1H), 8.63 – 8.58 (m, 1H), 8.32 (dd, *J* = 7.5, 1.0 Hz, 1H), 7.88 (ddd, *J* = 8.0, 7.5, 2.0 Hz, 1H), 7.87 – 7.81 (m, 1H), 7.72 – 7.66 (m, 2H), 7.44 (dd, *J* = 5.0, 1.0 Hz, 1H), 7.35 (ddd, *J* = 7.5, 5.0, 1.0 Hz, 1H), 7.16 (dd, *J* = 5.0, 3.5 Hz, 1H) ESI$^+$ m/z 238 (100%) $[M + H]^+$ The experimental data obtained are in agreement with literature.[136]

2-bromo-5-(8-quinolinyl)pyridine

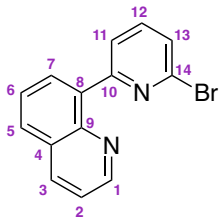

A mixture of 6-bromo-2,2-bipyridine (205 mg, 0.87 mmol), 8-quinolinyl boronic acid (150 mg, 0.87 mmol), Na_2CO_3 (740 mg, 6.96 mmol), $Pd(PPh_3)_4$ (50 mg, 0.043 mmol), DME (7 mL) and water (7 mL) were reacted according to the general procedure for Suzuki cross-coupling. The product was obtained as a white solid (166 mg, 67% yield) (R_f = 0.3 in EtOAc : hexane = 2 : 8) ^{1}H NMR (400 MHz, $CDCl_3$) δ_H / ppm 8.98 (dd, *J* = 4.0, 2.0 Hz, 1H), 8.27 – 8.20 (m, 3H), 7.92 (dd, *J* = 8.0, 2.0 Hz, 1H), 7.72 – 7.66 (m, 2H), 7.52 (dd, *J* = 8.0, 1.0 Hz, 1H), 7.47 (dd, *J* = 8.0, 4.0 Hz, 1H) HRMS (ES$^+$) m/z 285.0023 $[M+H^+]$ calcd for $[C_{14}H_{10}N_2Br]^+$ 285.0027

8-(6-phenylpyridin-2-yl)quinoline

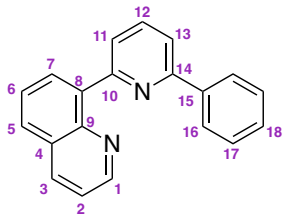

A mixture 2-bromo-5-(8-quinolinyl)pyridine (100 mg, 0.35 mmol), phenylboronic acid (43 mg, 0.35 mmol), Na_2CO_3 (297 mg, 2.31 mmol), $Pd(PPh_3)_4$ (20 mg, 0.018 mmol), DME (6 mL) and water (6 mL) were reacted according to the general procedure for Suzuki cross-coupling. The product was obtained as an off-white solid (98 mg, 99%

yield) (R_f = 0.6 in EtOAc : hexane = 3 : 7) ^{1}H NMR (400 MHz, $CDCl_3$) δ_H / ppm 8.98 (dd, J = 4.0, 2.0 Hz, 1H, H^1), 8.34 (dd, J = 7.0, 1.5 Hz, 1H, H^7), 8.23 (dd, J = 8.5, 2.0 Hz, 1H, H^3), 8.13 – 8.10 (m, 3H, H^{13} and H^{16}), 7.91 – 7.85 (m, 2H, H^5 and H^{12}), 7.75 (dd, J = 8.0, 1.0 Hz, 1H, H^{11}), 7.70 (dd, J = 8.0, 7.0 Hz, 1H, H^6), 7.50 – 7.45 (m, 2H, H^{17}), 7.43 (dd, J = 8.5, 4.0 Hz, 1H, H^2), 7.42 – 7.39 (m, 1H, H^{18}) ^{13}C NMR (151 MHz, $CDCl_3$) δ_C / ppm 157.1 (C^{14}), 156.5 (C^{10}), 150.2 (C^1), 145.9 (C^4), 139.9 (C^{15}), 139.0 (C^8), 136.5 (C^3), 136.1 (C^{12}), 131.6 (C^7), 128.7 (C^5), 128.7 (C^{18}), 128.7 (C^9), 128.6 (C^{17}), 127.1 (C^{16}), 126.6 (C^6), 126.0 (C^{13}), 121.0 (C^2), 118.9 (C^{11}) HRMS (ES$^+$) m/z 283.1230 [M+H$^+$] calcd for $[C_{20}H_{15}N_2]^+$ 283.1235

2-(3-methoxyphenyl)pyridine

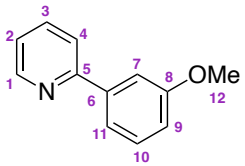

A mixture of 2-bromopyridine (61 µL, 0.63 mmol), 3-methoxyphenylboronic acid (96 mg, 0.63 mmol), Na_2CO_3 (537 mg, 5.06 mmol), $Pd(PPh_3)_4$ (37 mg, 0.032 mmol), DME (5 mL) and water (5 mL) were reacted according to the general procedure for Suzuki cross-coupling. The product was obtained as a colourless liquid (54 mg, 67% yield) (R_f = 0.2 in EtOAc : hexane = 2 : 8) ^{1}H NMR (400 MHz, $CDCl_3$) δ_H / ppm 8.72 (ddd, J = 5.0, 2.0, 1.0 Hz, 1H), 7.81 – 7.72 (m, 2H), 7.61 (dd, J = 2.5, 1.5 Hz, 1H), 7.57 (ddd, J = 7.5, 1.5, 1.0 Hz, 1H), 7.41 (dd, J = 8.0, 7.5 Hz, 1H), 7.30 – 7.22 (m, 2H), 7.00 (ddd, J = 8.0, 2.5, 1.0 Hz, 1H), 3.93 (s, 3H) ESI$^+$ m/z 185 (100%) [M + H]$^+$ The experimental data obtained are in agreement with literature.[137]

2-(4-methoxyphenyl)pyridine

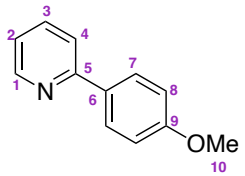

A mixture of 2-bromopyridine (82 µL, 0.86 mmol), 4-methoxyphenylboronic acid (135 mg, 0.86 mmol), Na_2CO_3 (697 mg, 6.54 mmol), $Pd(PPh_3)_4$ (50 mg, 0.42 mmol), DME (7 mL) and water (7 mL) were reacted according to the general procedure for Suzuki cross-coupling. The product was obtained as a colourless liquid (70 mg, 62% yield)

(R_f = 0.2 in EtOAc : hexane = 2 : 8) ^{1}H NMR (400 MHz, $CDCl_3$) δ_H / ppm 8.68 (ddd, J = 5.0, 2.0, 1.0 Hz, 1H), 8.02 – 7.93 (m, 2H), 7.76 – 7.67 (m, 2H), 7.19 (ddd, J = 7.0, 5.0, 1.0 Hz, 1H), 7.05 – 6.99 (m, 2H), 3.89 (s, 3H) ESI$^+$ m/z 185 (100%) $[M + H]^+$ The experimental data obtained are in agreement with literature.[138]

2-(4-(trifluoromethyl)phenyl)pyridine

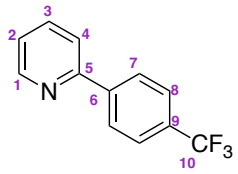

A mixture of 2-bromopyridine (50 µL, 0.52 mmol), (trifluoromethyl)phenylboronic acid (109 mg, 0.52 mmol), CsF (198 mg, 1.31 mmol), $Pd(PPh_3)_4$ (25 mg, 0.02 mmol) and DME (5 mL) were mixed in a microwave vial and degassed by three freeze-pump-thaw cycles. The reaction was heated in the microwave for 1h at 120 °C. Water was added to the mixture and the crude product was extracted into DCM. The organic phase was dried over $MgSO_4$, filtered and the solvent was removed under reduced pressure. The crude product was purified by gradient column chromatography on silica with hexane / ethyl acetate. The product was obtained as an colourless liquid (88 mg, 76% yield) (R_f = 0.2 in EtOAc : hexane = 2 : 8) ^{1}H NMR (400 MHz, $CDCl_3$) δ_H / ppm 8.76 (ddd, J = 5.0, 2.0, 1.0 Hz, 1H), 8.18 – 8.09 (m, 2H), 7.86 – 7.72 (m, 4H), 7.35 – 7.29 (m, 1H) ESI$^+$ m/z 223 (100%) $[M + H]^+$ The experimental data obtained are in agreement with literature.[139]

8.5.2 Pt^{II} complexes

PtL^7Cl

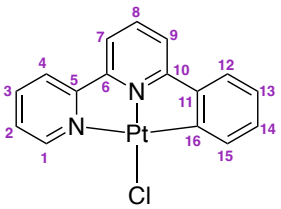

Method 1

K_2PtCl_4 (306 mg, 0.74 mmol) and 6-phenyl-2,2'-bipyridine (150 mg, 0.65 mmol) were reacted according to the general procedure. The product was obtained as a yellow solid (250 mg, 83% yield)

Method 2

A solution of 6-phenyl-2,2'-bipyridine (38 mg, 0.16 mmol) in MeCN (3 mL) was degassed by three freeze-pump-thaw cycles and was added to a degassed solution of K_2PtCl_4 (64 mg, 0.15 mmol) in water (3 mL). The mixture was heated to 100 °C overnight. After cooling down, the solvent was removed under reduced pressure. The crude product was washed successively with water (5 mL), MeOH (5 mL) and diethyl ether (5 mL), and extracted into DCM. The solvent was removed under reduced pressure to yield an orange solid (46 mg, 66% yield)

^{1}H NMR (400 MHz, DMSO-d_6) δ_H / ppm 8.91 (ddd, J = 5.5, 1.5, 1.0 Hz, 1H), 8.55 – 8.50 (m, 1H), 8.39 – 8.33 (m, 1H), 8.23 – 8.10 (m, 2H), 8.00 – 7.89 (m, 2H), 7.62 (dd, J = 7.5, 1.5 Hz, 1H), 7.51 (dd, $^3J_{^{195}Pt-^1H} \approx$ 34 Hz, J = 7.5, 1.5 Hz, 1H), 7.19 – 7.13 (m, 1H), 7.12 – 7.06 (m, 1H) ASAP$^+$ *m/z* 468 (100%) [M – Cl^- + MeCN]$^+$

The experimental data obtained for both methods are in agreement with the literature.[140]

PtL^{8}Cl

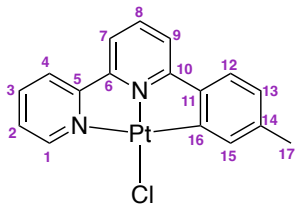

K_2PtCl_4 (259 mg, 0.63 mmol) and 6-(4-methylphenyl)-2,2'-bipyridine (135 mg, 0.55 mmol) were dissolved in acetic acid (18 mL) and degassed by three freeze-pump-thaw cycles. The mixture was heated to reflux temperature for 72 h. After cooling down, water was added. The resulting precipitate was isolated, washed successively with water (5 mL), MeOH (5 mL) and diethyl ether (5 mL), and extracted into DCM. The solvent was removed under reduced pressure to yield a red solid (250 mg, 95% yield). ^{1}H NMR (400 MHz, DMSO-d_6) δ_H / ppm 8.93 – 8.86 (m, 1H), 8.52 – 8.45 (m, 1H), 8.38 – 8.29 (m, 2H), 8.16 – 8.04 (m, 2H), 7.95 – 7.85 (m, 3H), 7.48 (d, J = 8.0 Hz, 2H), 7.30 (d, J = 2.0 Hz, 1H), 6.93 – 6.86 (m, 1H), 2.29 (s, 4H). The experimental data obtained are in agreement with literature.[141]

PtL^{9}Cl

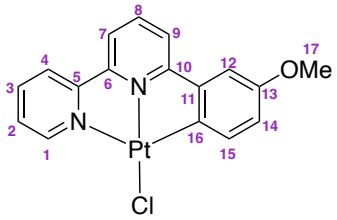

K_2PtCl_4 (235 mg, 0.57 mmol) and 6-(3-methoxyphenyl)-2,2'-bipyridine (130 mg, 0.50 mmol) were reacted according to the general procedure. The product was obtained as an orange solid (200 mg, 82% yield) ^{1}H NMR (599 MHz, DMSO-d_6) δ_H / ppm 8.90 (d, *J* = 5.5 Hz, 1H, H^{1}), 8.49 (d, *J* = 8.0 Hz, 1H, H^{4}), 8.33 (dd, *J* = 8.5, 7.0 Hz, 1H, H^{3}), 8.18 – 8.09 (m, 2H, H^{7} and H^{8}), 8.00 (d, *J* = 8.0 Hz, 1H, H^{9}), 7.92 – 7.87 (m, 1H, H^{2}), 7.34 (d, $^{3}J_{^{195}Pt-^{1}H} \approx$ 38 Hz, *J* = 8.5 Hz, 1H, H^{15}), 7.26 (d, *J* = 3.0 Hz, 1H, H^{12}), 6.83 (dd, *J* = 8.0, 3.0 Hz, 1H, H^{14}), 3.76 (s, 2H, H^{17}) ^{13}C NMR (151 MHz, DMSO-d_6) δ_C / ppm 148.53 (C^{1}), 140.89 (C^{3}), 140.11 (C^{8}), 135.36 (C^{15}), 128.82 (C^{2}), 124.39 (C^{4}), 120.00 (C^{7}), 120.00 (C^{9}), 116.89 (C^{14}), 111.21 (C^{12}), 55.63 (C^{17}) HRMS (ASAP^{+}) m/z 491.0422 [M]$^{+}$ calcd for [$C_{17}H_{14}N_2OCl^{194}Pt$]$^{+}$ 491.0421

PtL^{10}Cl

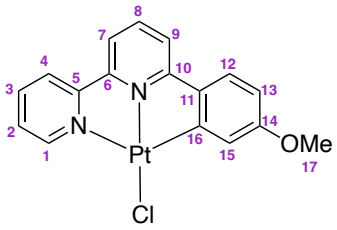

K_2PtCl_4 (88 mg, 0.21 mmol) and 6-(3-methoxyphenyl)-2,2'-bipyridine (49 mg, 0.19 mmol) were reacted according to the general procedure. The product was obtained as an orange solid (70 mg, 77% yield) ^{1}H NMR (599 MHz, DMSO-d_6) δ_H / ppm 8.91 – 8.85 (m, 1H, H^{1}), 8.49 – 8.44 (m, 1H, H^{4}), 8.35 – 8.28 (m, 1H, H^{3}), 8.08 – 8.01 (m, 2H, H^{7} and H^{8}), 7.88 (ddd, *J* = 7.5, 5.5, 1.5 Hz, 1H, H^{2}), 7.81 (dd, *J* = 7.5, 1.5 Hz, 1H, H^{9}), 7.55 (d, *J* = 8.5 Hz, 1H, H^{12}), 7.02 (d, $^{3}J_{^{195}Pt-^{1}H} \approx$ 47 Hz, *J* = 2.5 Hz, 1H, H^{15}), 6.64 (dd, *J* = 8.5, 2.5 Hz, 1H, H^{13}), 3.75 (s, 3H, H^{17}) ^{13}C NMR (151 MHz, DMSO-d_6) δ_C / ppm 148.8 (C^{1}), 141.1 (C^{3}), 140.0 (C^{8}), 128.7 (C^{2}), 127.2 (C^{12}), 124.3 (C^{4}), 119.5 (C^{15}), 119.1 (C^{9}), 118.6 (C^{7}), 109.9, 55.4 (C^{13}) HRMS (ASAP^{+}) m/z 491.0422 [M]$^{+}$ calcd for [$C_{17}H_{14}N_2OCl^{194}Pt$]$^{+}$ 491.0421

PtL^{11}Cl

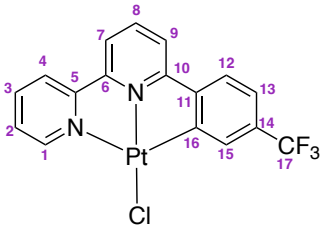

K_2PtCl_4 (142 mg, 0.34 mmol) and 6-[4-(trifluoromethyl)phenyl]-2,2'-bipyridine (90 mg, 0.30 mmol) were reacted according to the general procedure. The product was obtained as a yellow solid (140 mg, 88% yield) ^{1}H NMR (599 MHz, DMSO-d_6) δ_H / ppm 8.86 – 8.80 (m, 1H, H^1), 8.51 – 8.46 (m, 1H, H^4), 8.35 – 8.29 (m, 1H, H^3), 8.23 (dd, *J* = 8.0, 1.0 Hz, 1H, H^7), 8.19 – 8.12 (m, 1H, H^8), 8.03 (dd, *J* = 8.0, 1.0 Hz, 1H, H^9), 7.89 (ddd, *J* = 7.5, 5.5, 1.0 Hz, 1H, H^2), 7.77 (d, *J* = 8.0 Hz, 1H, H^{12}), 7.71 (d, *J* = 2.0 Hz, 1H, H^{15}), 7.40 – 7.35 (m, 1H, H^{13}) ^{13}C NMR (151 MHz, DMSO-d_6) δ_C / ppm 148.9 (C^1), 141.3 (C^3), 140.5 (C^8), 130.0 (C^{15}), 128.9 (C^2), 125.3 (C^{12}), 124.6 (C^4), 121.3 (C^7), 121.1 (C^9), 121.1 (C^{13}) HRMS (ASAP$^+$) m/z 570.0461 [M + MeCN]$^+$ calcd for $[C_{19}H_{14}N_3Cl^{194}PtF_3]^+$ 570.0455

PtL^{12}Cl

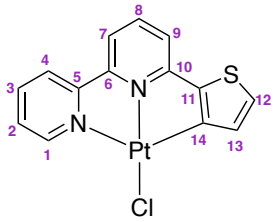

K_2PtCl_4 (72 mg, 0.17 mmol) and 6-(thiophen-2-yl)-2,2'-bipyridine (36 mg, 0.15 mmol) were reacted according to the general procedure. The product was obtained as an orange solid (40 mg, 57% yield) ^{1}H NMR (599 MHz, DMSO-d_6) δ_H / ppm 8.84 (d, *J* = 5.5 Hz, 1H, H^1), 8.45 (d, *J* = 8.0 Hz, 1H, H^4), 8.35 – 8.30 (m, 1H, H^3), 7.98 – 7.92 (m, 2H, H^7 and H^8 or H^9), 7.92 – 7.86 (m, 1H, H^2), 7.83 – 7.78 (m, 1H, H^{12}), 7.56 – 7.51 (m, 1H, H^8 or H^9), 6.96 (dd, *J* = 4.6, 0.9 Hz, 1H, H^{13}) ^{13}C NMR (151 MHz, DMSO-d_6) δ_C / ppm 148.7 (C^1), 141.3 (C^3), 141.3 (C^7, C^8 or C^9),133.1 (C^{13}), 130.4 (C^{12}), 128.9 (C^2), 124.6 (C^4), 117.3 (C^8 or C^9), 116.8 (C^7, C^8 or C^9) ASAP$^+$ m/z 467 (100%) [M]$^+$

PtL^{13}Cl

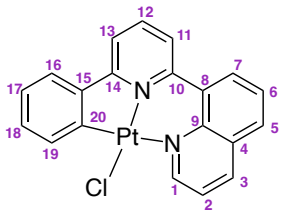

K_2PtCl_4 (59 mg, 0.14 mmol) and HL^{13} (35 mg, 0.12 mmol) were reacted according to the general procedure. The product was obtained as a yellow solid (46 mg, 73% yield) ^{1}H NMR (599 MHz, $CDCl_3$) δ_H / ppm 10.35 (dd, $^3J_{^{195}Pt-^1H} \approx 21$, J = 5.0, 1.5 Hz, 1H, H^1), 8.48 (dd, J = 8.0, 1.5 Hz, 1H, H^3), 8.32 (d, J = 7.5 Hz, 1H, H^7), 8.14 (dd, $^3J_{^{195}Pt-^1H} \approx 32$, J = 7.5, 1.5 Hz, 1H, H^{19}), 8.06 (d, J = 8.0 Hz, 1H, H^5), 8.01 – 7.94 (m, 1H, H^{12}), 7.75 – 7.68 (m, 2H, H^6 and H^{13}), 7.69 – 7.61 (m, 2H, H^{11} and H^2), 7.48 (dd, J = 7.5, 1.5 Hz, 1H, H^{16}), 7.26 – 7.23 (m, 1H, H^{18}), 7.17 – 7.10 (m, 1H, H^{17}) ^{13}C NMR (151 MHz, $CDCl_3$) δ_C / ppm 168.2 Cquat , 155.0 C^1 , 151.9 Cquat , 140.4 Cquat, 139.7 (C^3), 137.8 C^{12}, 135.7 C^{19}, 134.8 C^7, 133.5 Cquat, 132.4 C^5, 129.8 C^{18}, 129.4 Cquat, 127.0 C^6, 124.1 C^{17}, 123.3 C^{16}, 122.8 C^{11}, 122.4 C^2, 117.4 C^{13} HRMS (ES$^+$) m/z 516.0977 [M – Cl$^-$ + MeCN]$^+$ calcd for [$C_{22}H_{16}N_3{}^{194}Pt$]$^+$ 516.0971

8.5.3 Pt^{IV} complexes

Pt^{IV}Cl$_3$ complexes

PtL^{7}Cl$_3$

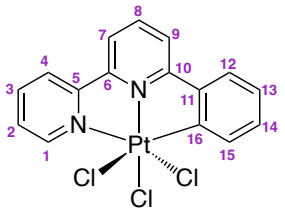

PtL^{7}Cl (250 mg, 0.54 mmol) was oxidised according to method 1 from the general procedure outlined above. The product was extracted into DCM and the solvent removed under reduced pressure to yield a pale yellow solid (189 mg, 90% yield) ^{1}H NMR (599 MHz, DMSO-d_6) δ_H / ppm 9.10 (dd, J = 5.5, 1.5 Hz, 1H, H^1), 8.85 (d, J = 8.0 Hz, 1H, H^4), 8.63 (d, J = 8.0 Hz, 1H, H^7), 8.49 – 8.44 (m, 2H, H^3 and H^9), 8.44 – 8.39 (m, 1H, H^8), 8.06 (dd, J = 8.0, 5.5 Hz, 1H, H^2), 7.97 (dd, J = 8.0, 1.5 51 Hz, 1H, H^{12}), 7.59 (dd, J = 8.0, 1.0 Hz, 1H, H^{15}), 7.41 – 7.35 (m, 1H, H^{14}), 7.31 – 7.25 (m, 1H,

H^{13}) ^{13}C NMR (151 MHz, DMSO-d_6) δ_C / ppm 148.8 (C^1), 144.1 (C^8), 142.4 (C^3 or C^9), 133.0 (C^{14}), 132.6 (C^{15}), 129.6 (C^2), 127.7 (C^{12}), 127.0 (C^{13}), 126.4 (C^4), 123.1 (C^3, C^9 or C^7) HRMS (ES^+) m/z 536.0192 $[M - Cl^- + MeCN]^+$ calcd for $[C_{18}H_{14}N_3Cl_2{}^{194}Pt]^+$ 536.0212

PtL^8Cl_3

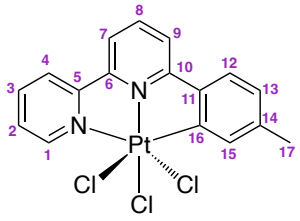

PtL^8Cl (231 mg, 0.42 mmol) was oxidised according to the general procedure outlined above. The product was extracted into DCM and the solvent removed under reduced pressure to yield a pale yellow solid (244 mg, 92% yield) ^1H NMR (599 MHz, DMSO-d_6) δ_H / ppm 9.10 (ddd, *J* = 5.0, 1.5, 0.5 Hz, 1H, H^1), 8.84 – 8.81 (m, 1H, H^4), 8.57 (dd, *J* = 7.0, 2.0 Hz, 1H, H^7), 8.48 – 8.42 (m, 1H, H^3), 8.41 – 8.34 (m, 2H, H^9 and H^8), 8.05 (ddd, *J* = 7.5, 5.0, 1.5 Hz, 1H, H^2), 7.85 (d, *J* = 8.0 Hz, 1H, H^{12}), 7.41 (dd, *J* = 1.5, 1.0 Hz, 1H, H^{15}), 7.11 (ddd, *J* = 8.0, 1.5, 1.0 Hz, 1H, H^{13}), 2.40 (s, 3H, H^{17}) ^{13}C NMR (151 MHz, DMSO-d_6) δ_C / ppm 161.6 (C^{10}), 154.9 (C^5), 151.4 (C^6), 148.8 (C^1), 143.9 (C^8), 143.6 (C^{14} or C^{16}), 142.4 (C^3), 141.4 (C^{14} or C^{16}), 134.6 (C^{11}), 133.0 (C^{15}), 129.5 (C^2), 127.6 (C^{13}), 127.5 (C^{12}), 126.3 (C^4), 122.7 (C^9), 122.5 (C^7), 22.1 (C^{17}) *m/z* 551 (100%) $[M - Cl^- + MeCN]^+$

PtL^9Cl_3

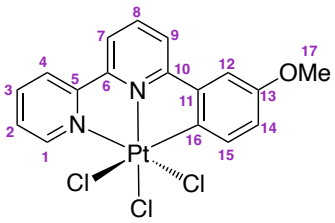

PtL^9Cl (200 mg, 0.41 mmol) and $PhICl_2$ (224 mg, 0.82 mmol) were reacted according to method 2 from the general procedure. The product was washed with DCM (10 mL) and then extracted into DCM to yield a pale yellow solid (160 mg, 70% yield) ^1H NMR (599 MHz, DMSO-d_6) δ_H / ppm 9.10 (ddd, *J* = 5.0, 1.5, 1.0 Hz, 1H, H^1), 8.88 – 8.83 (m, 1H, H^4), 8.63 (dd, *J* = 8.0, 1.0 Hz, 1H, H^7), 8.54 (dd, *J* = 8.0, 1.0 Hz, 1H, H^9),

8.50 – 8.40 (m, 2H, H^3 and H^8), 8.07 (ddd, J = 7.5, 5.0, 1.0 Hz, 1H, H^2), 7.65 (d, J = 3.0 Hz, 1H, H^{12}), 7.46 (d, J = 8.5 Hz, 1H, H^{15}), 7.08 (dd, J = 8.5, 3.0 Hz, 1H, H^{14}), 3.86 (s, 3H, H^{17}) ^{13}C NMR (151 MHz, DMSO-d_6) δ_C / ppm 148.8 (C^1), 144.0 (C^8), 142.4 (C^3), 132.7 (C^{15}), 129.6 (C^2), 126.4 (C^4), 123.3 (C^9), 123.1 (C^7), 119.0 (C^{14}), 113.1 (C^{12}), 56.2 (C^{17}) HRMS (ES$^+$) m/z 566.0297 [M – Cl$^-$ + MeCN]$^+$ calcd for [$C_{19}H_{16}N_3OCl_2{}^{194}Pt$]$^+$ 566.0297

PtL^{9Cl}Cl$_3$

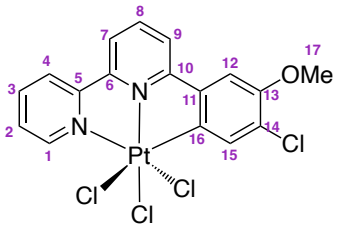

PtL^{9}Cl (175 mg, 0.36 mmol) was reacted according to method 1 from the general procedure outlined above. The product was extracted into DCM and the solvent removed under reduced pressure. The product was recrystallised from DCM / diethyl ether to yield a pale yellow solid (60 mg, 28% yield) ^{1}H NMR (599 MHz, DMSO-d_6) δ_H / ppm 9.12 – 9.08 (m, 1H, H^1), 8.86 (d, J = 8.0 Hz, 1H, H^4), 8.64 (dd, J = 8.0, 1.0 Hz, 1H, H^7), 8.62 (dd, J = 8.0, 1.0 Hz, 1H, H^9), 8.51 – 8.44 (m, 2H, H^8 and H^3), 8.08 (ddd, J = 7.5, 5.5, 1.0 Hz, 1H, H^2), 7.85 (s, 1H, H^{12}), 7.49 (s, 1H, H^{13}), 3.99 (s, 3H, H^{17}) ^{13}C NMR (151 MHz, DMSO-d_6) δ_C / ppm 149.0 (C^1), 144.2 (C^3 or C^8), 142.6 (C^3 or C^8), 132.0 (C^{13}), 129.5 (C^2), 126.6 (C^4), 123.8 (C^9), 123.5 (C^7), 112.1 (C^{12}), 57.3 (C^{17}) HRMS (ES$^+$) m/z 599.9902 [M – Cl$^-$ + MeCN]$^+$ calcd for [$C_{19}H_{15}N_3OCl_3{}^{194}Pt$]$^+$ 599.9907

PtL^{10}Cl$_3$

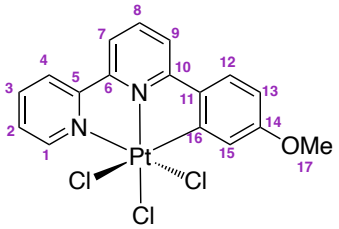

PtL^{10}Cl (70 mg, 0.14 mmol) and $PhICl_2$ (39 mg, 0.14 mmol) were reacted according to method 2 from the general procedure. The product was purified by gradient column chromatography on silica with hexane : ethyl acetate to yield a pale-yellow solid (30

mg, 38% yield) ^{1}H NMR (599 MHz, DMSO-d_6) δ_H / ppm 9.13 (ddd, *J* = 5.5, 1.5, 1.0 Hz, 1H, H^1), 8.89 – 8.82 (m, 1H, H^4), 8.54 (dd, *J* = 5.5, 3.5 Hz, 1H, H^7), 8.52 – 8.45 (m, 1H, H^3), 8.39 – 8.34 (m, 2H, H^8 and H^9), 8.07 (ddd, *J* = 7.5, 5.5, 1.0 Hz, 1H, H^2), 7.97 (d, *J* = 8.5 Hz, 1H, H^{12}), 7.13 (d, *J* = 2.5 Hz, 1H, H^{15}), 6.93 (dd, *J* = 8.5, 2.5 Hz, 1H, H^{13}), 3.90 (s, 3H, H^{17}) ^{13}C NMR (151 MHz, DMSO-d_6) δ_C / ppm 148.9 (C^1), 143.6 (C^9), 142.4 (C^3), 129.5 (C^2), 129.2 (C^{12}), 126.2 (C^4), 122.3 (C^8), 121.7 (C^7), 117.6 (C^{15}), 112.3 (C^{13}), 56.1 (C^{17}) HRMS (ASAP$^+$) m/z 525.0016 [M – Cl]$^+$ calcd for [$C_{17}H_{13}Cl_2N2O^{194}Pt$]$^+$ 525.0032

PtL^{10Cl}Cl$_3$

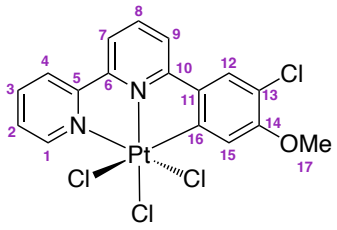

PtL^{10}Cl (65 mg, 0.13 mmol) was reacted according to method 1 from the general procedure outlined above. The product was extracted into DCM and the solvent removed under reduced pressure. The product was recrystallised from DCM / diethyl ether to yield a pale yellow solid (70 mg, 89% yield) ^{1}H NMR (599 MHz, DMSO-d_6) δ_H / ppm 9.11 (ddd, *J* = 5.5, 1.5, 1.0 Hz, 1H, H^1), 8.87 8.80 (m, 1H, H^4), 8.55 (dd, *J* = 8.5, 1.0 Hz, 1H, H^7), 8.50 – 8.44 (m, 1H, H^3), 8.42 (dd, *J* = 8.5, 1.0 Hz, 1H, H^9), 8.41 – 8.35 (m, 1H, H^8), 8.22 (s, 1H, H^{12}), 8.05 (ddd, *J* = 7.5, 5.5, 1.0 Hz, 1H, H^2), 7.26 (s, 1H, H^{15}), 3.96 (s, 3H, H^{17}) ^{13}C NMR (151 MHz, DMSO-d_6) δ_C / ppm 149.0 (C^1), 144.0 (C^8), 142.6 (C^3), 129.7 (C^2), 128.7 (C^{12}), 126.5 (C^4), 122.9 (C^9), 122.4 (C^7), 115.1 (C^{15}), 57.1 (C^{17}) HRMS (ES$^+$) m/z 599.9917 [M – Cl$^-$ + MeCN]$^+$ calcd for [$C_{19}H_{15}N_3OCl_3{}^{194}Pt$]$^+$ 599.9907

PtL^{11}Cl$_3$

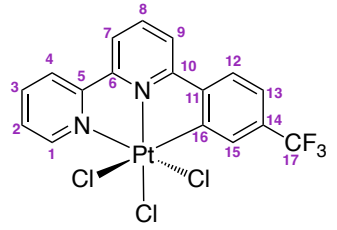

PtL^{11}Cl (138 mg, 0.26 mmol) and $PhICl_2$ (72 mg, 0.26 mmol) were reacted according

to method 2 from the general procedure. The product was purified by gradient column chromatography on silica with hexane : ethyl acetate to yield a pale-yellow solid (78 mg, 50% yield) ^{1}H NMR (599 MHz, DMSO-d_6) δ_H / ppm 9.14 – 9.11 (m, 1H, H^1), 8.92 – 8.87 (m, 1H, H^4), 8.75 (dd, *J* = 8.0, 1.0 Hz, 1H, H^7), 8.64 (dd, *J* = 8.0, 1.0 Hz, 1H, H^9), 8.56 – 8.47 (m, 2H, H^8 and H^3), 8.26 (d, *J* = 8.0 Hz, 1H, H^{12}), 8.09 (ddd, *J* = 8.0, 5.5, 1.0 Hz, 1H, H^2), 7.86 – 7.82 (m, 1H, H^{15}), 7.74 – 7.69 (m, 1H, H^{13}) ^{13}C NMR (151 MHz, DMSO-d_6) δ_C / ppm 149.1 (C^1), 144.7 (C^8), 142.8 (C^3), 130.0 (C^2), 128.3 (C^{12}), 127.9 (C^{15}), 126.9 (C^4), 124.6 (C^7), 124.4 (C^9), 124.2 (C^{13}) HRMS (ASAP$^+$) m/z 562.9792 [M – Cl]$^+$ calcd for $[C_{17}H_{10}N_2F_3Cl_2{}^{194}Pt]^+$ 562.9800

PtL^{12}Cl$_3$

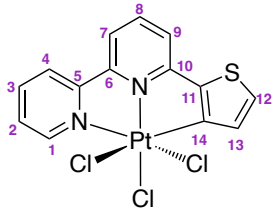

PtL^{12}Cl (220 mg, 0.47 mmol) and $PhICl_2$ (129 mg, 0.47 mmol) were reacted according to method 2 from the general procedure. The product was washed with DCM (10 mL) and then extracted into DCM to yield a yellow solid (238 mg, 94% yield) ^{1}H NMR (599 MHz, DMSO-d_6) δ_H / ppm 9.08 – 9.04 (m, 1H, H^1), 8.82 (d, *J* = 8.0 Hz, 1H, H^4), 8.49 – 8.44 (m, 1H, H^3), 8.44 – 8.40 (m, 1H, H^7), 8.32 – 8.27 (m, 1H, H^8), 8.11 (d, *J* = 5.0 Hz, 1H, H^{12}), 8.09 (dd, *J* = 8.0, 1.0 Hz, 1H, H^9), 8.06 (ddd, *J* = 8.0, 5.5, 1.0 Hz, 1H, H^2), 7.25 (d, *J* = 5.0 Hz, 1H, H^{13}) HRMS (ES$^+$) m/z 541.9771 [M – Cl$^-$ + MeCN]$^+$ calcd for $[C_{16}H_{12}N_3SCl_2{}^{194}Pt]^+$ 541.9756

PtL^{13}Cl$_3$

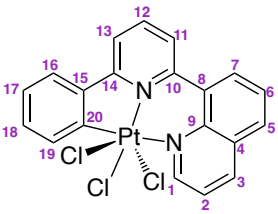

YD046 (50 mg, 0.10 mmol) was oxidised according to method 1 from the general procedure outlined above. The product was obtained as a pale yellow solid (54 mg, 95% yield) ^{1}H NMR (599 MHz, DMSO-d_6) δ_H / ppm 10.03 (dd, *J* = 5.0, 1.5 Hz, 1H, H^1), 9.00 (dd, *J* = 8.0, 1.5 Hz, 1H, H^3), 8.67 (dd, *J* = 7.5, 1.5 Hz, 1H, H^7), 8.54 – 8.48

(m, 2H, H^5 and H^{13}), 8.40 – 8.34 (m, 1H, H^{12}), 8.30 – 8.26 (m, 1H, H^{11}), 8.09 (dd, *J* = 8.0, 5.0 Hz, 1H, H^2), 8.04 – 7.99 (m, 2H, H^6 and H^{16}), 7.86 (dd, *J* = 8.0, 1.5 Hz, 1H, H^{19}), 7.38 (ddd, *J* = 8.0, 7.5, 1.5 Hz, 1H, H^{18}), 7.34 – 7.29 (m, 1H, H^{17}) ^{13}C NMR (151 MHz, DMSO-d_6) δ_C / ppm 155.1 (C^1), 143.3 (C^{12}), 143.1 (C^3), 138.1 (C^7), 134.5 (C^5), 133.4 (C^{19}), 131.8 (C^{18}), 128.7 (C^6 or C^{16}), 127.1 (C^{11}), 127.0 (C^{17}), 126.3 (C^6 or C^{16}), 123.5 (C^2), 121.3 (C^{13}) HRMS (ES$^+$) m/z 586.0375 [M – Cl^- + MeCN]$^+$ calcd for $[C_{22}H_{16}N_3Cl_2{}^{194}Pt]^+$ 586.0348

3 + 2 + 1 Pt^{IV} complexes

$[PtL^7L^4][PF_6]$

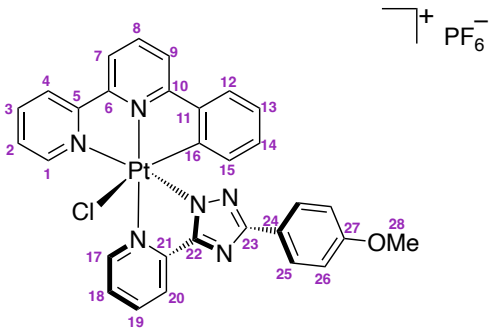

PtL^7Cl_3 (30 mg, 0.06 mmol), L^4 (14 mg, 0.06 mmol) and AgOTf (29 mg, 0.11 mmol) were reacted according to the general procedure outlined above. The complex was purified by gradient column chromatography on silica with MeCN, water and saturated aqueous KNO_3 (100 : 0 : 0 to 80 : 19.5 : 0.5) yielding a pale yellow solid (11 mg, 23% yield) ^{1}H NMR (599 MHz, acetone-d_6) δ_H / ppm 9.80 – 9.73 (m, $^3J_{^{195}Pt-^1H} \approx$ 26 Hz, 1H, H^{17}), 8.97 (d, *J* = 8.0 Hz, 1H, H^4), 8.89 – 8.82 (m, 1H, H^7), 8.83 – 8.77 (m, 2H, H^{19} and H^8), 8.69 (d, *J* = 8.0 Hz, 1H, H^9), 8.67 – 8.62 (m, 1H, H^1), 8.56 – 8.50 (m, 2H, H^{20} and H^3), 8.26 – 8.19 (m, 1H, H^{18}), 8.08 (dd, *J* = 8.0, 1.5 Hz, 1H, H^{12}), 7.92 (dd, *J* = 8.0, 5.5 Hz, 1H, H^2), 7.76 – 7.70 (m, 2H, H^{25}), 7.39 – 7.33 (m, 1H, H^{13}), 7.25 – 7.19 (m, 1H, H^{14}), 6.89 – 6.83 (m, 2H, H^{26}), 6.40 – 6.30 (m, $^3J_{^{195}Pt-^1H} \approx$ 25 Hz, 1H, H^{15}), 3.76 (s, 3H, H^{28}), 2.77 (d, *J* = 1.0 Hz, 3H, H^1). ^{13}C NMR (151 MHz, acetone-d_6) δ_C / ppm 160.7 (C^{quat}), 150.1 (C^1), 149.0 (C^{17}), 145.1 (C^{quat}), 144.9 (C^{19} or C^8), 143.0 (C^3), 133.7 (C^{14}), 129.9 (C^2), 128.9 (C^{15}), 128.2 (C^{12}), 128.2 (C^{13}), 127.6 (C^{18}), 127.2 (C^{25}), 126.6 (C^4), 123.8 (C^{quat}), 123.7 (C^7), 123.4 (C^9), 123.2 (C^{20}), 113.7 (C^{26}), 65.2 (C^{quat}), 54.7 (C^{27}) HRMS (ES$^+$) *m/z* 711.1168 [M – PF_6]$^+$ calcd for $[C_{30}H_{22}N_6ClO^{194}Pt]^+$ 711.1170

[PtL^{7}L^5][PF$_6$]

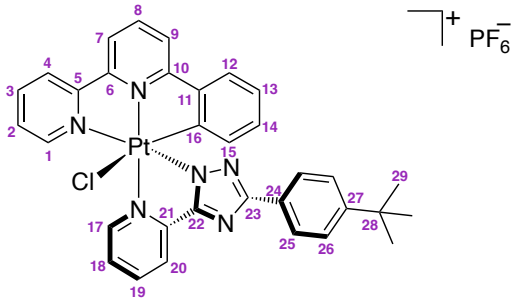

PtL^{7}Cl$_3$ (30 mg, 0.06 mmol), L^5 (16 mg, 0.06 mmol) and AgOTf (29 mg, 0.11 mmol) were reacted according to the general procedure outlined above. The crude product was recrystallised from DCM/ diethyl ether, yielding a pale yellow solid (13 mg, 26% yield) ^{1}H NMR (599 MHz, acetone-d$_6$) δ_H / ppm 9.82 – 9.73 (m, $^3J_{^{195}Pt-^1H} \approx$ 26 Hz, 1H, H^{17}), 8.96 (dd, J = 8.0, 1.0 Hz, 1H, H^4), 8.87 – 8.83 (m, 1H, H^7), 8.83 – 8.77 (m, 2H, H^{19} and H^8), 8.83 – 8.77 (m, 1H, H^9), 8.65 (d, J = 5.5 Hz, 1H, H^1), 8.55 (d, J = 8.0 Hz, 1H, H^{20}), 8.54 – 8.50 (m, 1H, H^3), 8.26 – 8.19 (m, 1H, H^{18}), 8.13 – 8.05 (m, 1H, H^{12}), 7.96 – 7.87 (m, 1H, H^2), 7.77 – 7.70 (m, 2H, H^{25}), 7.39 – 7.32 (m, 3H, H^{13} and H^{26}), 7.25 – 7.19 (m, 1H, H^{14}), 6.41 – 6.30 (m, $^3J_{^{195}Pt-^1H} \approx$ 22 Hz, 1H, H^{15}), 1.24 (s, 1H, H^{29}) ^{13}C NMR (151 MHz, acetone-d$_6$) δ_C / ppm 163.4 (C^{23}), 162.0 (C^{10}), 158.9 (C^{24}), 154.3 (C^5), 152.2 (C^{27}), 152.1 (C^6), 150.1 (C^1), 149.0 (C^{17}), 147.9 (C^{22}), 145.1 (C^8 or C^{19}), 144.9 (C^{21}), 143.3 (C^{11}), 143.0 (C^3), 133.9 (C^{16}), 133.7 (C^{14}), 129.9 (C^2), 128.9 (C^{15}), 128.4 (C^{26}), 128.2 (C^{13}), 128.2 (C^{12}), 127.7 (C^{18}), 126.6 (C^4), 125.5 (C^{25}), 125.2 (C^{26}), 123.8 (C^{20}), 123.4 (C^9), 123.2 (C^7), 34.3 (C^{23}), 30.5 (C^{29}) HRMS (ES$^+$) *m/z* 737.1685 [M – PF$_6$]$^+$ calcd for [C$_{33}$H$_{28}$N$_6$Cl^{194}Pt]$^+$ 737.1691

[PtL^{7}L^6][PF$_6$]

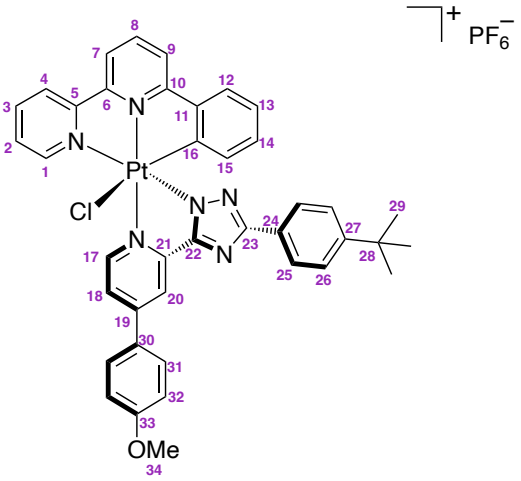

PtL^7Cl_3 (30 mg, 0.06 mmol), L^6 (22 mg, 0.06 mmol) and AgOTf (29 mg, 0.11 mmol) were reacted according to the general procedure outlined above. The complex was purified by gradient column chromatography on silica with MeCN, water and saturated aqueous KNO_3 (100 : 0 : 0 to 80 : 19.5 : 0.5) yielding a pale yellow solid (9 mg, 16% yield) ^{1}H NMR (599 MHz, acetone-d_6) δ_H / ppm 9.64 (d, $^3J_{^{195}Pt-^1H} \approx$ 26 Hz, J = 6.5 Hz, 1H, H^{17}), 8.98 (d, J = 8.0 Hz, 1H, H^4), 8.86 (dd, J = 8.0, 1.0 Hz, 1H, H^7), 8.83 – 8.79 (m, 1H, H^8), 8.75 – 8.67 (m, 3H, H^1, H^9 and H^{20}), 8.56 – 8.50 (m, 1H, H^3), 8.46 (dd, J = 6.5, 2.5 Hz, 1H, H^{18}), 8.29 – 8.22 (m, 2H, H^{31}), 8.09 (dd, J = 8.0, 1.5 Hz, 1H, H^{12}), 7.98 – 7.89 (m, 1H, H^2), 7.79 – 7.71 (m, 2H, H^{25}), 7.40 – 7.34 (m, 3H, H^{26} and H^{13}), 7.34 – 7.25 (m, 2H, H^{32}), 7.25 – 7.18 (m, 1H, H^{14}), 6.51 (dd, $^3J_{^{195}Pt-^1H} \approx$ 25 Hz, J = 8.0, 1.0 Hz, 1H, H^{15}), 3.98 (s, 3H, H^{34}), 1.25 (s, 9H, H^{29}) ^{13}C NMR (151 MHz, acetone-d_6) δ_C / ppm 163.3 (C^{33}), 152.2 (C^{27}), 150.0 (C^1), 148.4 (C^{17}), 145.0 (C^8), 143.0 (C^3), 133.7 (C^{14}), 129.8 (C^2), 129.7 (C^{31}), 129.1 (C^{15}), 128.2 (C^{13}), 128.1 (C^{12}), 126.6 (C^4), 125.5 (C^{25}), 125.2 (C^{26}), 123.4 (C^9), 123.2 (C^7), 123.2 (C^{18}), 119.2 (C^{20}), 115.2 (C^{32}), 55.2 (C^{34}), 34.3 (C^{28}), 30.5 (C^{29}) HRMS (ES$^+$) *m/z* 843.2120 $[M - PF_6]^+$ calcd for $[C_{40}H_{34}N_6ClO^{194}Pt]^+$ 843.2109

$[PtL^7(bpy)][PF_6]$

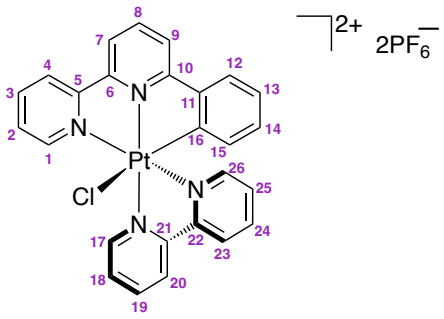

PtL^7Cl_3 (25 mg, 0.05 mmol), 2,2'-bipyridine (9 mg, 0.05 mmol) and AgOTf (24 mg, 0.09 mmol) were reacted according to the general procedure outlined above. The crude product was recrystallised from acetone/ diethyl ether, yielding a pale yellow solid (10 mg, 23% yield) ^{1}H NMR (599 MHz, acetone-d_6) δ_H / ppm 9.96 (d, $^3J_{^{195}Pt-^1H} \approx$ 25 Hz, J = 6.0 Hz, 1H, H^{17}), 9.22 (d, J = 8.0 Hz, 1H, H^{25}), 9.06 – 8.99 (m, 3H, H^{18}, H^{26} and H^4), 8.93 (d, J = 8.0 Hz, 1H, H^7), 8.89 – 8.84 (m, 1H, H^8), 8.78 (d, J = 8.0 Hz, 2H, H^9), 8.65 (d, J = 5.5 Hz, 1H, H^{23}), 8.60 – 8.51 (m, 3H, H^3, H^{19} and H^{24}), 8.43 (d, $^3J_{^{195}Pt-^1H} \approx$ 32 Hz, J = 6.0 Hz, 1H, H^1), 8.19 (d, J = 8.0 Hz, 1H, H^{12}), 7.97 – 7.86 (m, 1H, H^{20}), 7.80 – 7.73 (m, 1H, H^2), 7.46 – 7.39 (m, 1H, H^{13}), 7.30 – 7.23 (m, 1H, H^{14}),

6.47 – 6.40 (m, $^{3}J_{^{195}Pt\text{-}^{1}H} \approx 23$ Hz, 1H, H^{15}) HRMS (ES^{+}) *m/z* 308.0435 $[M]^{2+}/2$ calcd for $[C_{26}H_{17}N_4Cl^{194}Pt]^{2+}/2$ 308.0462

$[PtL^{7}(phpy)Cl]PF_6$

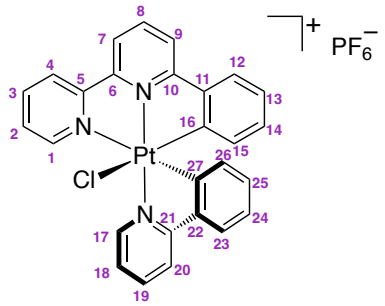

$PtL^{7}Cl_3$ (25 mg, 0.05 mmol), 2-phenylpyridine (6.7 L, 0.05 mmol) and AgOTf (24 mg, 0.09 mmol) were reacted according to the general procedure outlined above. The complex was purified by two recrystallisations from acetone/ diethyl ether, yielding a pale yellow solid (5 mg, 14% yield) ^{1}H NMR (599 MHz, acetone-d_6) δ_H / ppm 10.04 – 9.99 (m, $^{3}J_{^{195}Pt\text{-}^{1}H} \approx 27$ Hz, 1H, H^{17}), 8.92 – 8.86 (m, 1H, H^{4}), 8.79 – 8.75 (m, 1H, H^{7}), 8.74 – 8.69 (m, 1H, H^{8}), 8.65 – 8.57 (m, 3H, H^{9}, H^{20} and H^{18}), 8.47 – 8.43 (m, 1H, H^{3}), 8.41 (ddd, J = 5.5, 1.5, 0.5 Hz, 1H, H^{1}), 8.06 – 7.97 (m, 3H, H^{19}, H^{12} and H^{23}), 7.80 (ddd, J = 7.5, 5.5, 1.0 Hz, 1H, H^{2}), 7.29 – 7.22 (m, 2H, H^{13} and H^{24}), 7.13 – 7.06 (m, 1H, H^{19}), 7.01 (ddd, J = 8.0, 7.5, 1.5 Hz, 1H, H^{25}), 6.34 (dd, $^{3}J_{^{195}Pt\text{-}^{1}H} \approx 33$ Hz, J = 8.0, 1.0 Hz, 1H, H^{26}), 6.22 (dd, $^{3}J_{^{195}Pt\text{-}^{1}H} \approx 32$ Hz, J = 8.0, 1.0 Hz, 1H, H^{15}) HRMS (ES^{+}) m/z 614.0903 $[M]^{+}$ calcd for $[C_{27}H_{19}N_3Cl^{194}Pt]^{+}$ 614.0894

$[PtL^{9Cl}(phpy)Cl]PF_6$

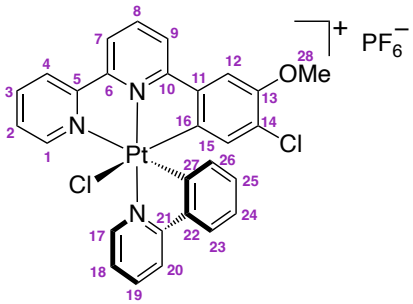

$Pt(3\text{-}OMe\text{-}4\text{-}Cl\text{-}phbpy)Cl_3$ (36 mg, 0.06 mmol), 2-phenylpyridine (9 mg, 0.06 mmol) and AgOTf (31 mg, 0.12 mmol) were reacted according to the general procedure outlined above. The complex was purified column chromatography on silica with MeCN : water : saturated aqueous KNO_3 (100 : 0 : 0 to 80 : 19.5 : 0.5), yielding an orange

solid (2 mg, 4% yield) ^{1}H NMR (599 MHz, acetone-d$_6$) δ_H / ppm 10.00 (d, $^{3}J_{^{195}Pt\text{-}^{1}H} \approx$ 26 Hz, J = 6.0 Hz, 1H, H^{17}), 9.05 (d, J = 8.0 Hz, 1H, H^{4}), 8.94 (d, J = 8.0 Hz, 1H, H^{7}), 8.86 (d, J = 8.0 Hz, 1H, H^{9}), 8.76 – 8.68 (m, 1H, H^{8}), 8.65 – 8.59 (m, 2H, H^{19} and H^{20}), 8.45 (d, J = 8.0 Hz, 1H, H^{3}), 8.37 (d, J = 5.0 Hz, 1H, H^{1}), 8.07 (d, J = 7.5 Hz, 1H, H^{23}), 8.03 – 7.97 (m, 1H, H^{18}), 7.95 (s, 1H, H^{12}), 7.83 – 7.78 (m, 1H, H^{2}), 7.29 – 7.22 (m, 1H, H^{24}), 7.07 – 6.99 (m, 1H, H^{25}), 6.34 (d, $^{3}J_{^{195}Pt\text{-}^{1}H} \approx$ 34, J = 8.0 Hz, 1H, H^{26}), 6.18 (s, $^{3}J_{^{195}Pt\text{-}^{1}H} \approx$ 35, 1H, H^{15}), 4.00 (s, 3H, H^{28}) HRMS (ES$^+$) m/z 678.0631 [M]$^+$ calcd for [$C_{28}H_{20}N_3OCl_2{}^{194}Pt$]$^+$ 678.0610

[PtL^{9}(3-OMe-phpy)Cl]PF$_6$

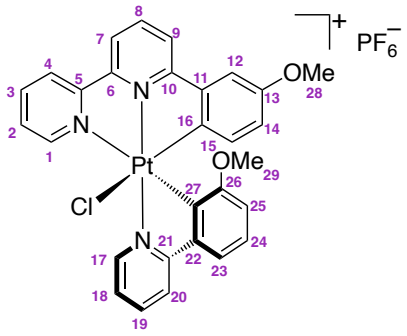

PtL^{9}Cl$_3$ (40 mg, 0.07 mmol), 2-(3-methoxyphenyl)pyridine (13 mg, 0.07 mmol) and AgOTf (37 mg, 0.14 mmol) were reacted according to the general procedure outlined above. The complex was purified by gradient column chromatography on C18 reverse-phase silica with water : MeCN, yielding a pale yellow solid (3 mg, 5% yield) ^{1}H NMR (599 MHz, acetone-d$_6$) δ_H / ppm 10.11 – 10.00 (m, $^{3}J_{^{195}Pt\text{-}^{1}H} \approx$ 26 Hz, 1H, H^{17}), 8.87 (d, J = 8.0 Hz, 1H, H^{4}), 8.68 (dd, J = 8.0, 1.0 Hz, 1H, H^{7}), 8.63 – 8.51 (m, 4H, H^{8}, H^{9}, H^{19} and H^{20}), 8.48 – 8.42 (m, 1H, H^{3}), 8.39 (d, J = 5.0 Hz, 1H, H^{1}), 7.96 – 7.88 (m, 1H, H^{18}), 7.79 (ddd, J = 7.5, 5.5, 1.5 Hz, 1H, H^{2}), 7.69 (dd, J = 8.0, 1.0 Hz, 1H, H^{23}), 7.63 – 7.57 (m, 1H, H^{12}), 7.26 – 7.20 (m, 1H, H^{24}), 6.72 (dd, J = 8.5, 3.0 Hz, 1H, H^{14}), 6.60 (d, J = 8.5 Hz, 1H, H^{25}), 6.05 – 5.95 (m, $^{3}J_{^{195}Pt\text{-}^{1}H} \approx$ 32 Hz, 1H, H^{15}), 3.81 (s, 3H, H^{28}), 3.16 (s, 3H, H^{29}) HRMS (ES$^+$) m/z 674.1118 [M]$^+$ calcd for [$C_{29}H_{23}N_3O_2Cl{}^{194}Pt$]$^+$ 674.1106

[PtL^{10}(4-OMe-phpy)Cl]PF$_6$

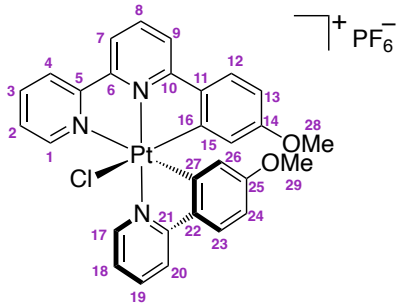

PtL^{10}Cl$_3$ (24 mg, 0.04 mmol), 2-(4-methoxyphenyl)pyridine (8 mg, 0.04 mmol) and AgOTf (22 mg, 0.09 mmol) were reacted according to the general procedure outlined above. The complex was purified by three fractional precipitations from DCM/ diethyl ether, yielding a yellow solid (5 mg, 14% yield) ^{1}H NMR (599 MHz, acetone-d$_6$) δ_H / ppm 9.95 – 9.86 (m, $^3J_{^{195}Pt-^1H} \approx$ 26 Hz, 1H, H^{17}), 8.85 (d, J = 8.0 Hz, 1H, H^4), 8.66 – 8.58 (m, 2H, H^7 and H^8), 8.51 – 8.41 (m, 4H, H^3,H^9, H^{19} and H^{20}), 8.39 (d, $^3J_{^{195}Pt-^1H} \approx$ 14 Hz, J = 5.0 Hz, 1H, H^1), 8.03 – 7.97 (m, 2H, H^{12} and H^{23}), 7.86 (ddd, J = 8.0, 6.0, 1.5 Hz, 1H, H^{18}), 7.79 (ddd, J = 7.5, 5.5, 1.0 Hz, 1H, H^2), 6.89 – 6.83 (m, 2H, H^{13} and H^{24}), 5.68 (d, $^3J_{^{195}Pt-^1H} \approx$ 39 Hz, J = 2.5 Hz, 1H, H^{26}), 5.62 (d, $^3J_{^{195}Pt-^1H} \approx$ 37 Hz, J = 2.5 Hz, 1H, H^{15}), 3.67 (s, 3H, H^{28}), 3.59 (s, 3H, H^{29}) ^{13}C NMR (151 MHz, acetone-d$_6$) δ_C / ppm 149.4 (C^1), 148.9 (C^{17}), 143.4 (C^8), 142.6 (C^{19}), 142.0 (C^3), 129.3 (C^{12}), 129.0 (C^2), 128.0 (C^{23}), 126.2 (C^4), 124.5 (C^{18}), 122.3 (C^9), 121.5 (C^{20}), 121.3 (C^7), 115.1 (C^{15}), 112.9 (C^{26}), 111.3 (C^{24}), 110.7 (C^{13}), 55.0 (C^{28}), 54.9 (C^{29}) HRMS (ES$^+$) m/z 674.1105 [M]$^+$ calcd for [C$_{29}$H$_{23}$N$_3$O$_2$Cl^{194}Pt]$^+$ 674.1106

bis-tridentate Pt^{IV} complexes

[PtL^7(tpy)][PF$_6$]$_3$

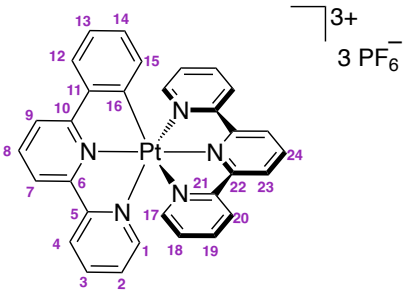

PtL^{7}Cl$_3$ (30 mg, 0.06 mmol), 2,2';6',2"-terpyridine (14 mg, 0.06 mmol) and AgOTf (44 mg, 0.17 mmol) were reacted according to the general procedure outlined above. The crude product was recrystallised from acetone/ diethyl ether, yielding a red solid (23

mg, 38% yield) ^{1}H NMR (599 MHz, acetone-d_6) δ_H / ppm 9.39 (d, *J* = 8.0 Hz, 2H, H^{23}), 9.26 (dd, *J* = 8.5, 8.0, 1H, H^{24}), 9.17 – 9.11 (m, 2H, H^{20}), 9.11 – 9.04 (m, 2H, H^{8} and H^{4}), 8.98 – 8.92 (m, 2H, H^{9} and H^{7}), 8.84 – 8.80 (m, $^{3}J_{^{195}Pt\text{-}^{1}H} \approx 14$ Hz, 1H, H^{1}), 8.67 – 8.61 (m, 2H, H^{19}), 8.57 – 8.47 (m, 3H, H^{17} and H^{3}), 8.30 – 8.26 (m, 1H, H^{12}), 7.89 – 7.83 (m, 2H, H^{18}), 7.81 – 7.76 (m, 1H, H^{2}), 7.49 – 7.43 (m, 1H, H^{13}), 7.23 – 7.18 (m, 1H, H^{14}), 6.60 – 6.54 (m, $^{3}J_{^{195}Pt\text{-}^{1}H} \approx 25$ Hz, 1H, H^{15}) ^{13}C NMR (151 MHz, acetone-d_6) δ_C / ppm 160.1 (C^{10}), 157.0 (C^{21}), 155.1 (C^{quat}), 152.5 (C^{22}), 152.2 (C^{1}), 151.7 (C^{17}), 147.1 (C^{24}), 147.0 (C^{7} or C^{9}), 145.5 (C^{19}), 143.8 (C^{3}), 143.2 (C^{quat}), 134.5 (C^{14}), 133.0 (C^{quat}), 131.6 (C^{18}), 130.2 (C^{13}), 130.0 (C^{2}), 130.0 (C^{12}), 129.8 (C^{20}), 129.3 (C^{23}), 129.0 (C^{15}), 127.8 (C^{4}), 125.9 (C^{8}), 125.8 (C^{7} or C^{9}) HRMS (ES$^+$) *m/z* 948.0795 $[M+2PF_6]^+$ calcd for $[C_{31}H_{22}P_2N_5{}^{194}PtF_{12}]^+$ 948.0786

$[PtL^{8}(tpy)][PF_6]_3$

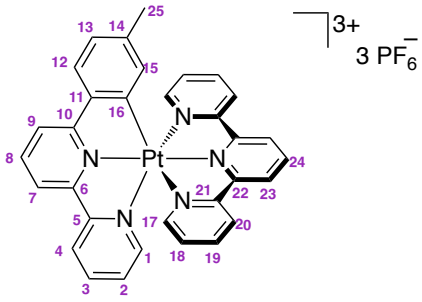

$PtL^{8}Cl_3$ (30 mg, 0.06 mmol), 2,2';6',2"-terpyridine (13 mg, 0.06 mmol) and AgOTf (43 mg, 0.17 mmol) were reacted according to the general procedure outlined above. The crude product was recrystallised from acetone/ diethyl ether, yielding a pale yellow solid (20 mg, 32% yield) ^{1}H NMR (599 MHz, acetone-d_6) δ_H / ppm 9.33 – 9.26 (m, 3H, H^{23} and H^{24}), 9.06 (ddd, *J* = 8.0, 1.5, 0.5 Hz, 2H, H^{20}), 9.02 – 8.97 (m, 2H, H^{4} and H^{7}), 8.96 – 8.92 (m, 1H, H^{8}), 8.85 (dd, *J* = 8.0, 1.0 Hz, 1H, H^{9}), 8.67 – 8.63 (m, 3H, H^{1} and H^{19}), 8.52 – 8.42 (m, 3H, H^{3} and H^{17}), 8.14 (d, *J* = 8.0 Hz, 1H, H^{12}), 7.85 (ddd, *J* = 8.0, 6.0, 1.5 Hz, 2H, H^{18}), 7.76 (ddd, *J* = 7.5, 5.5, 1.5 Hz, 1H, H^{2}), 7.29 (ddd, *J* = 8.0, 1.5, 1.0 Hz, 1H, H^{13}), 6.41 (dd, *J* = 1.5, 1.0 Hz, 1H, H^{15}), 2.06 (s, 3H, H^{25}) ^{13}C NMR (151 MHz, acetone-d_6) δ_C / ppm 160.5 (C^{10}), 157.0 (C^{21}), 155.0 (C^{5}), 152.5 (C^{22}), 151.9 (C^{quat}), 151.7 (C^{1}), 151.5 (C^{17}), 147.1 (C^{24}), 146.8 (C^{8}), 145.5 (C^{19}), 143.9 (C^{3}), 140.1 (C^{14}), 133.2 (C^{quat}), 131.6 (C^{18}), 130.8 (C^{13}), 130.0 (C^{2}), 129.7 (C^{12}), 129.6 (C^{20}), 129.3 (C^{15}), 129.1 (C^{23}), 127.6 (C^{4}), 125.3 (C^{9}), 125.0 (C^{7}), 20.9 (C^{25}) HRMS (ES$^+$) *m/z* 224.0520 $[M]^{3+}/3$ calcd for $[C_{32}H_{21}N_5{}^{194}Pt]^{3+}/3$ 224.0553, 962.0985 $[M+2PF_6]^+$ calcd for $[C_{32}H_{21}P_2N_5{}^{194}PtF_{12}]^+$ 962.0942

$[PtL^7{}_2][PF_6]_2$

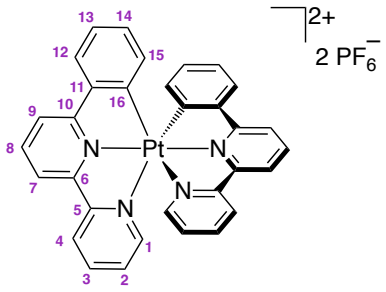

A mixture of PtL^7Cl_3 (30 mg, 0.06 mmol), 6-phenyl-2,2-bipyridine (13 mg, 0.06 mmol) and AgOTf (43 mg, 0.17 mmol) was suspended in dry toluene (3 mL) in a dry Schlenk flask. The mixture was degassed by three freeze-pump-thaw cycles and was heated at 125°C overnight, with the partial exclusion of light. The resulting precipitate was isolated by centrifugation, washed successively with toluene (5 mL), DCM (5 mL) and diethyl ether (5 mL), and extracted into acetone. The solvent was removed under reduced pressure. The crude product was dissolved in acetone and the solution was slowly added dropwise to a saturated aqueous solution of KPF_6 (20 mL). The precipitate was isolated, washed with water (10 mL) and dried. The crude product was purified by column chromatography on alumina with MeCN, water and saturated aqueous KNO_3 (100 : 0 : 0 to 80 : 19.5 : 0.5), followed by two recrystallisations from acetone/ diethyl ether, yielding a green solid (7 mg, 13% yield) ^{1}H NMR (599 MHz, acetone-d_6) δ_H / ppm 9.03 – 9.00 (m, 1H, H^4), 8.98 (dd, J = 8.0, 1.0 Hz, 1H, H^7), 8.89 – 8.84 (m, 1H, H^8), 8.83 – 8.79 (m, 1H, H^9), 8.63 (ddd, $^3J_{^{195}Pt-^1H} \approx$ 12 Hz, J = 5.5, 1.5, 1.0 Hz, 1H, H^1), 8.49 – 8.42 (m, 1H, H^3), 8.15 (dd, J = 8.0, 1.5 Hz, 1H, H^{12}), 7.75 (ddd, J = 7.5, 5.5, 1.5 Hz, 1H, H^2), 7.37 – 7.30 (m, 1H, H^{13}), 7.14 – 7.07 (m, 1H, H^{14}), 6.39 (dd, $^3J_{^{195}Pt-^1H} \approx$ 34 Hz, J = 8.0, 1.0 Hz, 1H, H^{15}) ^{13}C NMR (151 MHz, acetone-d_6) δ_C / ppm 161.5 (C^{10}), 155.3 (C^5), 152.2 (C^6), 150.6 (C^1), 144.9 (C^8), 143.5 (C^{11}), 143.0 (C^3), 134.6 (C^{16}), 133.3 (C^{14}), 129.5 (C^2), 128.5 (C^{15}), 128.4 (C^{12}), 128.1 (C^{13}), 127.0 (C^4), 124.1 (C^7), 124.0 (C^9) HRMS (ES$^+$) m/z 328.0712 $[M]^{2+}$/2 calcd for $[C_{32}H_{20}N_4{}^{194}Pt]^{2+}$/2 328.0736

8.6 Chapter 4 synthesis

8.6.1 Proligands and precursors

2-bromo-6-phenylpyridine

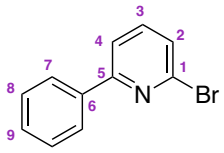

A mixture of 2,6-dibromopyridine (1.48 g, 6.25 mmol), phenylboronic acid (760 mg, 6.25 mmol), Na_2CO_3 (5.29 g, 50 mmol), $Pd(PPh_3)_4$ (361 mg, 0.31 mmol), DME (50 mL) and water (50 mL) were reacted according to the general procedure for Suzuki cross-coupling. The product was purified by gradient column chromatography on C18 reverse-phase silica with water : MeCN, yielding a white solid (665 mg, 45% yield) ^{1}H NMR (400 MHz, $CDCl_3$) δ_H / ppm 8.04 – 7.98 (m, 2H), 7.71 (dd, *J* = 7.5, 1.0 Hz, 1H), 7.66 – 7.58 (m, 1H), 7.52 – 7.42 (m, 4H) ESI$^+$ m/z 235 (100%) $[M + H]^+$

2-bromo-6-(4-(*tert*-butyl)phenyl)pyridine

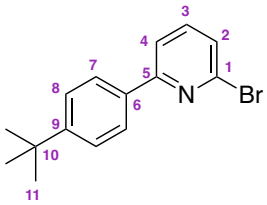

A mixture of 2,6-dibromopyridine (4.13 g, 17.42 mmol), 4-*tert*-butylphenylboronic acid (1.55 mg, 8.71 mmol), Na_2CO_3 (7.38 g, 69.66 mmol), $Pd(PPh_3)_4$ (503 mg, 0.43 mmol), DME (70 mL) and water (70 mL) were reacted according to the general procedure for Suzuki cross-coupling. The product was purified by gradient column chromatography on C18 reverse-phase silica with water : MeCN, yielding a white solid (1.934 mg, 77% yield) ^{1}H NMR (400 MHz, $CDCl_3$) δ_H / ppm 7.96 – 7.91 (m, 2H), 7.68 (dd, *J* = 7.5, 1.0 Hz, 1H), 7.62 – 7.56 (m, 1H), 7.54 – 7.48 (m, 2H), 7.40 (dd, *J* = 7.5, 1.0 Hz, 1H), 1.38 (s, 9H) ESI$^+$ m/z 292 (100%) $[M + H]^+$

2-phenyl-6-(tributylstannyl)pyridine

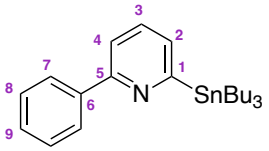

Method 1

A solution of 2-dimethylaminoethanol (0.8 mL, 8 mol) in hexane (10 mL) was cooled at 0°C and treated dropwise with n-BuLi (10 mL, 16 mmol). After 30 min at 0°C, a solution of 2-phenylpyridine (412 mg, 2.66 mmol) in hexane (5 mL) was added dropwise. After 1 h at 0°C , the mixture was cooled to –78°C and treated with a solution of tributyltin chloride (9.6 mmol) in hexane (5 mL). After 1 h at –78°C the temperature was allowed to rise to room temperature. The hydrolysis was then performed at 0°C with H_2O. The organic layer was then extracted twice with diethyl ether, dried over $MgSO_4$, and evaporated under vacuum. The crude product was dissolved in hexane and filtered through a plug of silica to yield a yellow oil (446 mg, 38% yield)[142]

Method 2

n-BuLi (1.22 mL, 1.6 M in hexane, 1.95 mmol) was added dropwise to a solution of 2-bromo-6-phenylpyridine (456 mg, 1.95 mmol) in dry THF (3 mL) at –78°C, and the mixture was stirred for 1 h. Tributyltin chloride (582 µL, 2.14 mmol) was added to the solution at –78°C , and stirring continued for 3 h at –78°C, then 30 min at room temperature. The reaction was quenched with saturated aqueous NH_4Cl solution (5 mL) and extracted with ethylacetate (3 × 25 mL). The organic layer was washed with brine, then water and finally dried over anhydrous $MgSO_4$. The solvent was evaporated under reduced pressure to give 2-phenyl-6-(tributylstannyl)pyridine in quantitative yield (989 mg) as a pale yellow oil.[143]

^{1}H NMR (400 MHz, $CDCl_3$) δ_H / ppm 8.12 – 8.07 (m, 2H), 7.61 – 7.56 (m, 2H), 7.52 – 7.45 (m, 2H), 7.44 – 7.40 (m, 1H), 7.35 (dd, *J* = 7.0, 1.5 Hz, 1H) ESI$^+$ m/z 445 (100%) $[M + H]^+$

2-(4-(*tert*-butyl)phenyl)-6-(tributylstannyl)pyridine

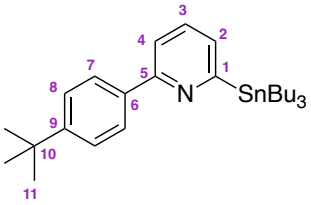

n-BuLi (3.23 mL, 1.6 M in hexane, 5.17 mmol) was added dropwise to a solution of 2-bromo-6-(4-(*tert*-butyl)phenyl)pyridine (1.5 g, 5.17 mmol) in dry THF (4 mL) at –78°C, and the mixture was stirred for 1 h. Tributyltin chloride (1.5 mL, 5.69 mmol) was added to the solution at –78°C, and stirring continued for 3 h at –78°C, then 30 min at room temperature. The reaction was quenched with saturated aqueous NH_4Cl solution (5 mL) and extracted with ethylacetate (3 × 25 mL). The organic layer was washed with brine, then water and finally dried over anhydrous $MgSO_4$. The solvent was evaporated under reduced pressure to give the product in quantitative yield (2.8 g) as a yellow oil. ^{1}H NMR (400 MHz, $CDCl_3$) δ_H / ppm 8.06 – 7.99 (m, 2H), 7.58 – 7.54 (m, 2H), 7.53 – 7.48 (m, 2H), 7.30 – 7.34 (m, 1H), 1.39 (s, 9H) ESI$^+$ m/z 502 (100%) $[M + H]^+$

6,6'-diphenyl-2,2'-bipyridine (HL^{15})

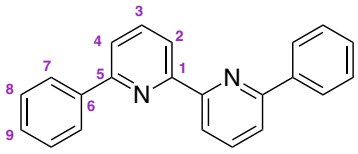

A mixture of 2-bromo-6-phenylpyridine (165 mg, 0.705 mmol) and 2-phenyl-6-(tributylstannyl)pyridine(313 mg, 0.705 mmol) were dissolved in toluene (8 mL) and degassed by three freeze-pump-thaw cycles. $Pd(PPh_3)_4$ (41 mg, 0.035 mmol) was added under nitrogen and the resulting yellow solution was heated at reflux temperature overnight. After cooling down, saturated aqueous KF (5 mL) was added and the mixture was stirred for 30 min. The precipitate was filtered off and then the solvent was removed under reduced pressure. The crude product was extracted into DCM (3×20 mL), washed with 5% $NaHCO_3$(aq) (3×15 mL), dried over $MgSO_3$ and purified by gradient column chromatography on silica with hexane / ethyl acetate as the mobile phase (R_f = 0.5 in EtOAc : hexane = 1 : 9) to yield a white solid (82 mg, 38% yield) ^{1}H NMR (599 MHz, $CDCl_3$) δ_H / ppm 8.60 (dd, J = 8.0, 1.0 Hz, 2H, H^2), 8.20 – 8.14 (m, 4H, H^7), 7.89 – 7.92 (m, 2H, H^3), 7.78 (dd, J = 8.0, 1.0 Hz, 2H, H^4), 7.55 – 7.48 (m, 4H, H^8), 7.47 – 7.41 (m, 2H, H^9) ^{13}C NMR (151 MHz, $CDCl_3$) δ_C / ppm 156.3 C^5, 155.9 C^1, 139.4 C^6, 137.6 C^3, 129.0 C^9, 128.7 C^8, 126.9 C^7, 120.3 C^4, 119.5 C^2 ESI$^+$ m/z 309 (100%) $[M + H]^+$ The experimental data obtained are in agreement with literature.[144]

6,6'-bis(4-(*tert*-butyl)phenyl)-2,2'-bipyridine (HL^{16})

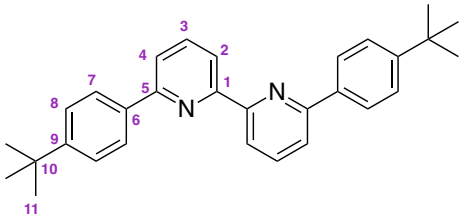

A mixture of 2-bromo-6-(4-(*tert*-butyl)phenyl)pyridine (306 mg, 1.054 mmol) and 2-(4-(*tert*-butyl)phenyl)-6-(tributylstannyl)pyridine(528 g, 1.054 mmol) were dissolved in toluene (10 mL) and degassed by three freeze-pump-thaw cycles. $Pd(PPh_3)_4$ (61 mg, 0.053 mmol) was added under nitrogen and the resulting yellow solution was heated at reflux temperature overnight. After cooling down, saturated aqueous KF (5 mL) was added and the mixture was stirred for 30 min. The precipitate was filtered off and then the solvent was removed under reduced pressure. The crude product was extracted into DCM (3×20 mL), washed with 5% $NaHCO_3$(aq) (3×15 mL), dried over $MgSO_3$ and purified by gradient column chromatography on silica with hexane / ethyl acetate as the mobile phase (R_f = 0.6 in EtOAc : hexane = 1 : 9) to yield a white solid (225 mg, 51% yield) ^{1}H NMR (400 MHz, $CDCl_3$) δ_H / ppm 8.62 (dd, J = 8.0, 1.0 Hz, 2H), 8.17 – 8.06 (m, 4H), 7.96 – 7.90 (m, 2H), 7.80 (dd, J = 8.0, 1.0 Hz, 2H), 7.61 – 7.53 (m, 4H), 1.42 (s, 18H) ESI$^+$ m/z 421 (100%) $[M + H]^+$ The experimental data obtained are in agreement with literature.[145]

8.6.2 Pt^{II} complexes

$PtL^{15}Cl$

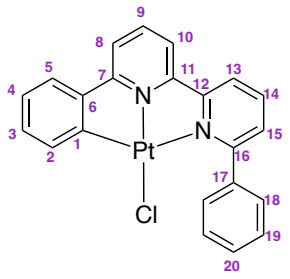

K_2PtCl_4 (126 mg, 0.303 mmol) and LH (82 mg, 0.266 mmol) were dissolved in acetic acid (5 mL) and degassed by three freeze-pump-thaw cycles. The mixture was heated to reflux temperature for 72 h. After cooling down, water (5 mL) was added. The resulting precipitate was isolated and washed with water (20 mL). The product was dried under reduced pressure and purified by gradient column chromatography on

silica with hexane : ethyl acetate to yield a red solid (40 mg, 28% yield) ^{1}H NMR (400 MHz, $CDCl_3$) δ_H / ppm 8.11 – 8.04 (m, 1H), 7.98 (d, *J* = 7.5 Hz, 1H), 7.94 – 7.87 (m, 1H), 7.82 (d, *J* = 7.0 Hz, 1H), 7.78 – 7.70 (m, 3H), 7.67 (d, *J* = 8.0 Hz, 1H), 7.59 – 7.49 (m, 4H), 7.35 (d, *J* = 7.5 Hz, 1H), 7.22 – 7.15 (m, 1H), 7.12 – 7.05 (m, 1H) ASAP^{+} m/z 542 (100%) $[M - Cl^{-} + MeCN]^{+}$ The experimental data obtained are in agreement with literature.

PtL^{16}Cl

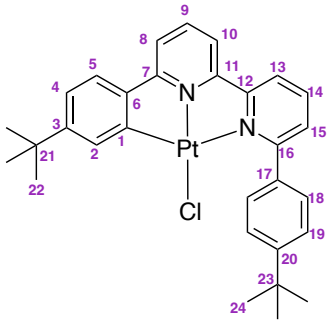

K_2PtCl_4 (191 mg, 0.461 mmol) and LH (170 mg, 0.404 mmol) were dissolved in acetic acid (20 mL) and degassed by three freeze-pump-thaw cycles. The mixture was heated to reflux temperature for 72 h. After cooling down, water (5 mL) was added. The resulting precipitate was isolated and washed with water (20 mL). The product was dried under reduced pressure and purified by fractional precipitation from DCM/hexane (25 mg, 10% yield) ^{1}H NMR (700 MHz, $CDCl_3$) δ_H / ppm 7.86 – 7.82 (m, 1H, H^{14}), 7.81 – 7.77 (m, 2H, H^{13} and H^{2}), 7.64 – 7.60 (m, 1H, H^{9}), 7.54 (dd, *J* = 7.5, 2.0 Hz, 1H, H^{15}), 7.52 – 7.49 (m, 2H, H^{18}), 7.46 – 7.41 (m, 3H, H^{10} and H^{19}), 7.27 (dd, *J* = 8.0, 1.0 Hz, 1H, H^{8}), 7.11 (d, *J* = 8.0 Hz, 1H, H^{5}), 7.01 (dd, *J* = 8.0, 2.0 Hz, 1H, H^{4}), 1.34 (d, *J* = 1.0 Hz, 9H, H^{24}), 1.24 (d, *J* = 1.0 Hz, 9H, H^{22}) ^{13}C NMR (176 MHz, $CDCl_3$) δ_C / ppm 165.9 C^{7}, 164.1 C^{16}, 157.3 C^{11} or C^{12}, 154.7 C^{11} or C^{12}, 153.9 C^{3}, 152.9 C^{20}, 142.6 C^{1} or C^{6}, 138.7 C^{14}, 137.7 C^{9}, 136.9 C^{1} or C^{6}, 136.1 C^{17}, 131.4 C^{2}, 129.2 C^{18}, 128.9 C^{15}, 125.1 C^{19}, 123.7 C^{5}, 121.1 C^{4}, 120.4 C^{13}, 118.1 C^{10}, 117.9 C^{8}, 35.3 C^{21}, 34.8 C^{23}, 31.4 C^{24}, 31.3 C^{22} HRMS (ASAP^{+}) m/z 654.2391 $[M - Cl^{-} + MeCN]^{+}$ calcd for $[C_{32}H_{34}N_3{}^{194}Pt]^{+}$ 654.2380

8.6.3 Pt^{IV} complexes

$PtL^{15}Cl_3$

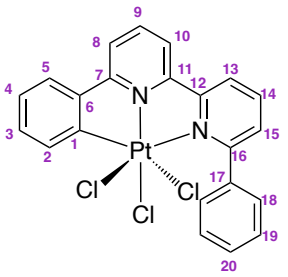

$L(PtCl_3)(PtCl)$ (41 mg, 0.078 mmol) and $PhICl_2$ (32 mg, 0.117 mmol) were dissolved in $CHCl_3$ (15 mL) and the mixture was left to stir overnight, with the partial exclusion of light. The solvent was removed under reduced pressure and the resulting solid washed with diethyl ether (30 mL). The product was purified by gradient column chromatography on silica with hexane : ethyl acetate to yield a yellow solid (24 mg, 51%yield) ^{1}H NMR (599 MHz, DMSO-d_6) δ_H / ppm 8.81 (dd, J = 8.0, 1.0 Hz, 1H, H^{13}), 8.70 – 8.64 (m, 1H, H^{10}), 8.51 – 8.46 (m, 1H, H^8), 8.46 – 8.38 (m, 2H, H^9 and H^{14}), 7.93 (dd, J = 7.5, 1.5 Hz, 1H, H^5), 7.89 (dd, J = 8.0, 1.0 Hz, 1H, H^{15}), 7.75 – 7.65 (m, 2H, H^{18}), 7.51 – 7.41 (m, 4H, H^2, H^{19} and H^{20}), 7.31 – 7.26 (m, 1H, H^3), 7.26 – 7.21 (m, 1H, H^4) ^{13}C NMR (151 MHz, DMSO-d_6) δ_C / ppm 163.6 C^{16}, 160.5 C^7, 155.0 C^{12}, 152.4 C^{11}, 143.8 C^9, 143.2, 141.8 C^{14}, 138.4, 135.0, 134.5 , 132.4 , 131.9 , 131.0, 130.3 , 129.7, 128.2, 127.3 C^5, 124.9 C^{13}, 123.6 C^{10}, 122.8 C^8, 122.8, 120.6 HRMS (ASAP$^+$) m/z 613.0551 $[M - Cl^- + MeCN]^+$ calcd for $[C_{25}H_{16}N_3Cl_2{}^{195}Pt]^+$ 613.0435

$PtL^{16}Cl_3$

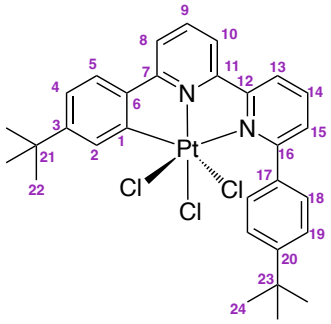

$L(PtCl_3)(PtCl)$ (61 mg, 0.093 mmol) and $PhICl_2$ (38 mg, 0.140 mmol) were dissolved in $CHCl_3$ (15 mL) and the mixture was left to stir overnight, with the partial exclusion of light. The solvent was removed under reduced pressure and the resulting

solid washed with diethyl ether (30 mL).The product was purified by gradient column chromatography on silica with hexane : ethyl acetate to yield a yellow solid (18 mg, 27%yield) ^{1}H NMR (599 MHz, $CDCl_3$) δ_H / ppm 8.15 (dd, J = 8.0, 1.5 Hz, 1H, H^{13}), 8.11 – 8.08 (m, 1H, H^{14}), 8.06 – 8.02 (m, 1H, H^{9}), 7.96 (dd, J = 8.0, 1.0 Hz, 1H, H^{10}), 7.86 (dd, J = 8.0, 1.0 Hz, 1H, H^{8}), 7.81 (d, J = 2.0 Hz, 1H, H^{2}), 7.73 (dd, J = 7.5, 1.5 Hz, 1H, H^{15}), 7.70 – 7.66 (m, 2H, H^{18}), 7.56 – 7.53 (m, 2H, H^{19}), 7.43 (d, J = 8.0 Hz, 1H, H^{5}), 7.22 (dd, J = 8.0, 2.0 Hz, 1H, H^{4}), 1.40 (s, 9H, H^{24}), 1.30 (s, 9H, H^{22}) ^{13}C NMR (151 MHz, $CDCl_3$) δ_C / ppm 141.2 C^{9}, 139.4 C^{14}, 130.0 C^{15}, 129.5 C^{18}, 129.3 C^{2}, 125.7 C^{5}, 125.2 C^{19}, 124.2 C^{4}, 122.2 C^{13}, 120.5 C^{8}, 120.1 C^{10}, 36.0 C^{21}, 34.8 C^{23}, 31.3 C^{24}, 31.1 C^{22} HRMS (ASAP$^+$) m/z 726.1818 [M – Cl^- + MeCN]$^+$ calcd for $[C_{32}H_{34}N_3Cl_2{}^{195}Pt]^+$ 726.1859

[PtL^{15}(ppy)Cl]PF_6

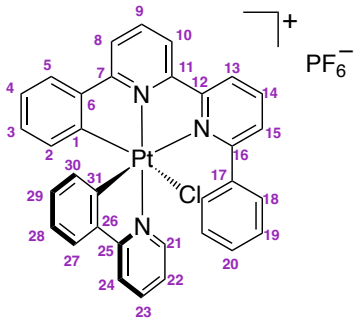

$PtLCl_3$ (16 mg, 0.026 mmol), 2-phenylpyridine (20 µL, 0.052 mmol) and AgOTf (13 mg, 0.052 mmol) were reacted according to the general procedure for synthesis of 3+2+1 Pt^{IV} complexes. The complex was purified by fractional precipitation from DCM/ diethyl ether, yielding a pale yellow solid (11 mg, 51% yield) ^{1}H NMR (599 MHz, acetone-d_6) δ_H / ppm 9.33 (ddd, $^{3}J_{^{195}Pt-^{1}H} \approx$ 28 Hz, J = 6.0, 1.5, 0.5 Hz, 1H, H^{21}), 8.94 (dd, J = 8.0, 1.0 Hz, 1H, H^{13}), 8.89 – 8.85 (m, 1H, H^{10}), 8.74 – 8.70 (m, 1H, H^{9}), 8.61 – 8.57 (m, 1H, H^{8}), 8.50 – 8.46 (m, 1H, H^{14}), 8.25 – 8.21 (m, 1H, H^{23}), 8.19 (dd, J = 8.0, 1.5 Hz, 1H, H^{24}), 7.96 – 7.92 (m, 1H, H^{5}), 7.90 (dd, J = 7.5, 1.5 Hz, 1H, H^{27}), 7.72 – 7.67 (m, 1H, H^{15}), 7.58 (ddd, J = 8.0, 5.0, 1.5 Hz, 1H, H^{22}), 7.53 (br s, 1H, H^{18}), 7.34 (br s, 1H, H^{19}), 7.30 – 7.24 (m, 1H, H^{28}), 7.22 – 7.15 (m, 2H, H^{4} and H^{20}), 7.06 – 7.00 (m, 1H, H^{29}), 6.94(br s, 1H, H^{19}), 6.99 – 6.91 (m, 1H, H^{3}), 6.53 (br s, 1H, H^{18}), 6.41 (dd, $^{3}J_{^{195}Pt-^{1}H} \approx$ 32 Hz, J = 8.0, 1.0 Hz, 1H, H^{30}), 5.32 (dd, $^{3}J_{^{195}Pt-^{1}H} \approx$ 36 Hz, J = 8.0, 1.0 Hz, 1H, H^{2}) ^{13}C NMR (151 MHz, acetone-d_6) δ_C / ppm 163.7, 154.6, 150.1 C^{21}, 143.7 C^{9}, 142.7, 141.7 C^{23}, 141.7 C^{14}, 141.6, 139.0, 137.1, 132.6 C^{3}, 132.2 C^{29}, 130.4 C^{20},

130.2 C^{15}, 128.5, 127.4 C^{28}, 127.2 C^{5}, 127.0 C^{4}, 127.0 C^{30}, 126.7 C^{2}, 126.1 C^{27}, 125.5 C^{22}, 125.1 C^{13}, 123.1 C^{10}, 122.8 C^{8}, 121.9 C^{24} HRMS (ESI^+) m/z 690.1223 [M – PF_6]$^+$ calcd for [$C_{33}H_{23}N_3Cl^{195}Pt$]$^+$ 690.1207

[PtL^{16}(ppy)Cl]PF_6

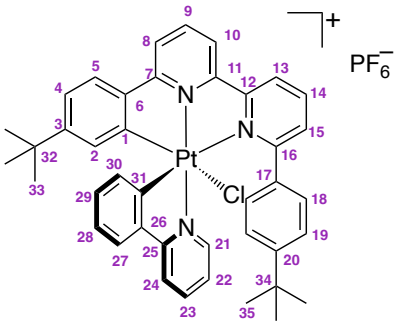

$PtLCl_3$ (58 mg, 0.080 mmol), 2-phenylpyridine (25 µL, 0.160 mmol) and AgOTf (41 mg, 0.161 mmol) were were reacted according to the general procedure for the synthesis of 3+2+1 Pt^{IV} complexes. The complex was purified by fractional precipitation from DCM/ diethyl ether, yielding a pale yellow solid (5 mg, 7% yield) ^{1}H NMR (700 MHz, $CDCl_3$) δ_H / pp 9.48 (ddd, $^3J_{^{195}Pt-^1H} \approx 28$ Hz, J = 6.0, 1.5, 0.5 Hz, 1H, H^{21}), 8.96 (dd, J = 8.0, 1.0 Hz, 1H, H^{13}), 8.89 – 8.84 (m, 1H, H^{10}), 8.73 – 8.69 (m, 1H, H^{9}), 8.59 – 8.54 (m, 1H, H^{8}), 8.50 – 8.43 (m, 1H, H^{14}), 8.43 – 8.35 (m, 1H, H^{23}), 8.33 – 8.29 (m, 1H, H^{24}), 7.95 (dd, J = 8.0, 1.5 Hz, 1H, H^{27}), 7.86 (dd, J = 8.0, 3.0 Hz, 1H, H^{5}), 7.72 – 7.68 (m, 2H, H^{22} and H^{15}), 7.59 (br s, 1H, H^{18} and H^{19}), 7.41 (br s, 1H, H^{18} and H^{19}), 7.32 – 7.25 (m, 2H, H^{28} and H^{4}), 7.10 – 7.04 (m, 1H, H^{29}), 7.03 (br s, 1H, H^{18} and H^{19}) 6.52 (br s, 1H, H^{18} and H^{19}), 6.46 (dd, $^3J_{^{195}Pt-^1H} \approx 33$ Hz, J = 8.0, 1.0 Hz, 1H, H^{30}), 5.22 (d, $^3J_{^{195}Pt-^1H} \approx 38$ Hz, J = 1.5 Hz, 1H, H^{2}), 1.31 (s, 9H, H^{35}), 0.96 (s, 9H, H^{33}) ^{13}C NMR (151 MHz, acetone-d_6) δ_C / ppm 164.2, 163.1, 161.3, 156.4 C^{3}, 152.4 C^{20}, 152.3, 150.2 C^{21}, 143.6 C^{9}, 142.2 C^{23}, 141.6, 141.5 C^{14}, 140.0, 139.2, 134.8, 134.8, 132.3 C^{29}, 130.5 C^{15} or C^{22}, 127.4 C^{28}, 127.0 C^{30}, 126.9 C^{5}, 126.1 C^{27}, 125.1 C^{15} or C^{22}, 125.0 C^{13}, 124.1 C^{4}, 123.1 C^{2}, 122.7 C^{10}, 122.5, 122.4 C^{8}, 121.7 C^{24}, 34.8 C^{32}, 34.4 C^{34}, 30.6 C^{35}, 30.0 C^{33} HRMS (ESI^+) m/z 802.2465 [M – PF_6]$^+$ calcd for [$C_{41}H_{39}N_3Cl^{195}Pt$]$^+$ 802.2459

8.7 Chapter 5 synthesis

8.7.1 Proligands and precursors

2-bromo-6-phenylpyridine

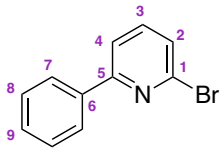

A mixture of 2,6-dibromopyridine (1.48 g, 6.25 mmol), phenylboronic acid (760 mg, 6.25 mmol), Na_2CO_3 (5.29 g, 50 mmol), $Pd(PPh_3)_4$ (361 mg, 0.31 mmol), DME (50 mL) and water (50 mL) were reacted according to the general procedure for Suzuki cross-coupling. The product was purified by gradient column chromatography on C18 reverse-phase silica with water : MeCN, yielding a white solid (665 mg, 45% yield) ^{1}H NMR (400 MHz, $CDCl_3$) δ_H / ppm 8.04 – 7.98 (m, 2H), 7.71 (dd, *J* = 7.5, 1.0 Hz, 1H), 7.66 – 7.58 (m, 1H), 7.52 – 7.42 (m, 4H) ESI$^+$ m/z 235 (100%) $[M + H]^+$

2-bromo-6-(4-(*tert*-butyl)phenyl)pyridine

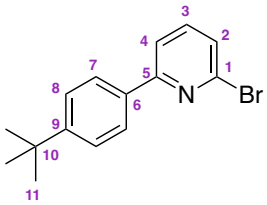

A mixture of 2,6-dibromopyridine (4.13 g, 17.42 mmol), 4-*tert*-butylphenylboronic acid (1.55 mg, 8.71 mmol), Na_2CO_3 (7.38 g, 69.66 mmol), $Pd(PPh_3)_4$ (503 mg, 0.43 mmol), DME (70 mL) and water (70 mL) were reacted according to the general procedure for Suzuki cross-coupling. The product was purified by gradient column chromatography on C18 reverse-phase silica with water : MeCN, yielding a white solid (1.934 mg, 77% yield) ^{1}H NMR (400 MHz, $CDCl_3$) δ_H / ppm 7.96 – 7.91 (m, 2H), 7.68 (dd, *J* = 7.5, 1.0 Hz, 1H), 7.62 – 7.56 (m, 1H), 7.54 – 7.48 (m, 2H), 7.40 (dd, *J* = 7.5, 1.0 Hz, 1H), 1.38 (s, 9H) ESI$^+$ m/z 292 (100%) $[M + H]^+$

2-bromo-6-(4-(trifluoromethyl)phenyl)pyridine

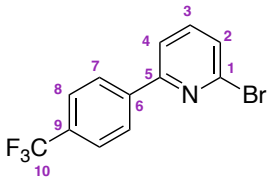

A mixture of 2,6-dibromopyridine (3.741 g, 15.80 mmol), 4-(trifluoromethyl)phenylboronic acid (1.500 mg, 7.90 mmol), Na_2CO_3 (6.696 g, 63.18 mmol), $Pd(PPh_3)_4$ (456 mg, 0.395 mmol), DME (63 mL) and water (63 mL) were reacted according to the general procedure for Suzuki cross-coupling. The product was purified by gradient column chromatography on C18 reverse-phase silica with water : MeCN, yielding a white solid (1.203 mg, 50% yield) ^{1}H NMR (400 MHz, $CDCl_3$) δ_H / ppm 8.16 – 8.10 (m, 2H), 7.78 – 7.72 (m, 3H), 7.71 – 7.64 (m, 1H), 7.51 (dd, J = 8.0, 1.0 Hz, 1H) ESI$^+$ m/z 302 (100%) $[M + H]^+$

2-phenyl-6-(tributylstannyl)pyridine

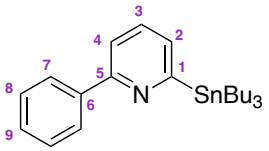

Method 1

A solution of 2-dimethylaminoethanol (0.8 mL, 8 mol) in hexane (10 mL) was cooled at 0 °C and treated dropwise with n-BuLi (10 mL, 16 mmol). After 30 min at 0 °C, a solution of 2-phenylpyridine (412 mg, 2.66 mmol) in hexane (5 mL) was added dropwise. After 1 h at 0 °C, the mixture was cooled to –78 °C and treated with a solution of tributyltin chloride (9.6 mmol) in hexane (5 mL). After 1 h at –78 °C the temperature was allowed to raise to room temperature. The hydrolysis was then performed at 0 °C with H_2O. The organic layer was then extracted twice with diethyl ether, dried over $MgSO_4$, and evaporated under vacuum. The crude product was dissolved in hexane and filtered through a plug of silica to yield a yellow oil (446 mg, 38% yield)[142]

Method 2

n-BuLi (1.22 mL, 1.6 M in hexane, 1.95 mmol) was added dropwise to a solution of 2-bromo-6-phenylpyridine (456 mg, 1.95 mmol) in dry THF (3 mL) at –78 °C, and the mixture was stirred for 1 h. Tributyltin chloride (582 µL, 2.14 mmol) was added to the solution at –78 °C, and stirring continued for 3 h at –78 °C, then 30 min at room temper-

ature. The reaction was quenched with saturated aqueous NH_4Cl solution (5 mL) and extracted with ethylacetate (3 × 25 mL). The organic layer was washed with brine, then water and finally dried over anhydrous $MgSO_4$. The solvent was evaporated under reduced pressure to give 2-phenyl-6-(tributylstannyl)pyridine in quantitative yield (989 mg) as a pale yellow oil.[143]

^{1}H NMR (400 MHz, $CDCl_3$) δ_H / ppm 8.12 – 8.07 (m, 2H), 7.61 – 7.56 (m, 2H), 7.52 – 7.45 (m, 2H), 7.44 – 7.40 (m, 1H), 7.35 (dd, *J* = 7.0, 1.5 Hz, 1H) ESI$^+$ m/z 445 (100%) $[M + H]^+$

2-(4-(*tert*-butyl)phenyl)-6-(tributylstannyl)pyridine

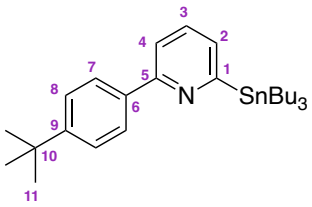

n-BuLi (3.23 mL, 1.6 M in hexane, 5.17 mmol) was added dropwise to a solution of 2-bromo-6-(4-(*tert*-butyl)phenyl)pyridine (1.5 g, 5.17 mmol) in dry THF (4 mL) at –78 °C, and the mixture was stirred for 1 h. Tributyltin chloride (1.5 mL, 5.69 mmol) was added to the solution at –78 °C, and stirring continued for 3 h at –78 °C, then 30 min at room temperature. The reaction was quenched with saturated aqueous NH_4Cl solution (5 mL) and extracted with ethylacetate (3 × 25 mL). The organic layer was washed with brine, then water and finally dried over anhydrous $MgSO_4$. The solvent was evaporated under reduced pressure to give the product in quantitative yield (2.8 g) as a yellow oil. ^{1}H NMR (400 MHz, $CDCl_3$) δ_H / ppm 8.06 – 7.99 (m, 2H), 7.58 – 7.54 (m, 2H), 7.53 – 7.48 (m, 2H), 7.30 – 7.34 (m, 1H), 1.39 (s, 9H) ESI$^+$ m/z 502 (100%) $[M + H]^+$

2-(tributylstannyl)-6-(4-(trifluoromethyl)phenyl)pyridine

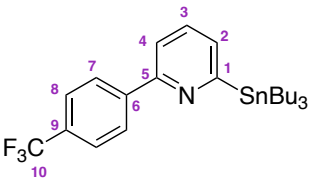

n-BuLi (2.35 mL, 1.6 M in hexane, 3.77 mmol) was added dropwise to a solution of 2-bromo-6-(4-(trifluoromethyl)phenyl)pyridine (1.14 g, 3.77 mmol) in dry THF (3 mL)

at –78 °C, and the mixture was stirred for 1 h. Tributyltin chloride (1.12 mL, 4.14 mmol) was added to the solution at –78 °C, and stirring continued for 3 h at –78 °C, then 30 min at room temperature. The reaction was quenched with saturated aqueous NH_4Cl solution (5 mL) and extracted with ethylacetate (3 × 25 mL). The organic layer was washed with brine, then water and finally dried over anhydrous $MgSO_4$. The solvent was evaporated under reduced pressure to give the product in quantitative yield (1.99 g) as a yellow oil. ^{1}H NMR (400 MHz, $CDCl_3$) δ_H / ppm 8.20 (d, J = 8.0 Hz, 2H), 7.75 – 7.71 (m, 2H), 7.66 – 7.58 (m, 2H), 7.41 (dd, J = 6.5, 2.0 Hz, 1H) ESI$^+$ m/z 514 (100%) $[M + H]^+$

4,6-bis(6-phenylpyridin-2-yl)pyrimidine (H_2L^{17})

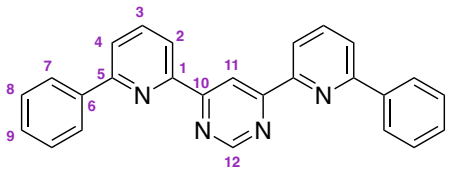

A mixture of 2-phenyl-6-(tributylstannyl)pyridine (1.60 g, 3.602 mmol), 4,6-dichloro-pyrimidine (179 mg, 1.201 mmol) and LiCl (255 mg, 6.005 mmol) were dissolved in toluene (10 mL) and degassed by three freeze-pump-thaw cycles. $Pd(PPh_3)_4$ (208 mg, 0.180 mmol) was added under nitrogen and the resulting yellow solution was heated at reflux temperature overnight. After cooling down, saturated aqueous KF (10 mL) was added and the mixture was stirred for 30 min. The precipitate was filtered off and then the solvent was removed under reduced pressure. The crude product was extracted into DCM (3×20 mL), washed with 5% $NaHCO_3$(aq) (3×15 mL), dried over $MgSO_3$ and purified by gradient column chromatography on silica with hexane / ethyl acetate as the mobile phase (R_f = 0.4 in EtOAc : hexane = 2 : 8) to yield a white solid (100 mg, 22% yield) ^{1}H NMR (599 MHz, $CDCl_3$) δ_H / ppm 9.86 (d, J = 1.5 Hz, 1H, H^{11}), 9.37 (d, J = 1.5 Hz, 1H, H^{12}), 8.48 (dd, J = 7.5, 1.0 Hz, 2H, H^2), 8.32 – 8.28 (m, 4H, H^7), 7.95 – 7.99 (m, 2H, H^3), 7.92 (dd, J = 8.0, 1.0 Hz, 2H, H^4), 7.56 (dd, J = 8.5, 7.0 Hz, 4H, H^8), 7.53 – 7.45 (m, 2H, H^9) ^{13}C NMR (151 MHz, $CDCl_3$) δ_C / ppm 164.1 C^{10}, 158.5 C^{12}, 156.7 C^5, 153.7 C^1, 138.8 C^6, 138.0 C^3, 129.4 C^9, 128.8 C^8, 127.0 C^7, 121.6 C^4, 119.9 C^2, 114.3 C^{11} HRMS (ESI$^+$) m/z 387.1604 $[M+H]^+$ calcd for $[C_{26}H_{19}N_4]^+$ 387.1610

4,6-bis(6-(4-(*tert*-butyl)phenyl)pyridin-2-yl)pyrimidine (H_2L^{18})

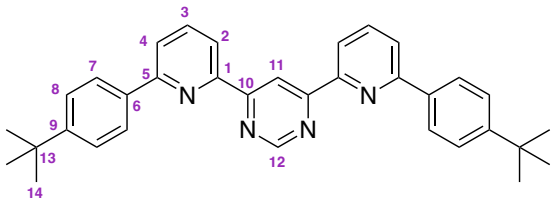

A mixture of 2-(4-(*tert*-butyl)phenyl)-6-(tributylstannyl)pyridine (1 g, 1.999 mmol), 4,6-dichloropyrimidine (119 mg, 0.799 mmol) and LiCl (169 mg, 3.994 mmol) were dissolved in toluene (7 mL) and degassed by three freeze-pump-thaw cycles. $Pd(PPh_3)_4$ (138 mg, 0.120 mmol) was added under nitrogen and the resulting yellow solution was heated at reflux temperature overnight. After cooling down, saturated aqueous KF (10 mL) was added and the mixture was stirred for 30 min. The precipitate was filtered off and then the solvent was removed under reduced pressure. The crude product was extracted into DCM (3×20 mL), washed with 5% $NaHCO_3$(aq) (3×15 mL), dried over $MgSO_3$ and purified by gradient column chromatography on silica with hexane / ethyl acetate as the mobile phase (R_f = 0.4 in EtOAc : hexane = 1 : 9) to yield a white solid (206 mg, 52% yield) ^{1}H NMR (599 MHz, $CDCl_3$) δ_H / ppm 9.87 (d, J = 1.5 Hz, 1H, H^{11}), 9.36 (d, J = 1.5 Hz, 1H, H^{12}), 8.45 (dd, J = 7.5, 1.0 Hz, 2H, H^2), 8.26 – 8.22 (m, 4H, H^7), 7.92 – 7.95 (m, 2H, H^3), 7.90 (dd, J = 8.0, 1.0 Hz, 2H, H^4), 7.61 – 7.58 (m, 4H, H^8), 1.41 (s, 18H, H^{14}) ^{13}C NMR (151 MHz, $CDCl_3$) δ_C / ppm 164.1 C^{10}, 158.4 C^{12}, 156.6 C^5, 153.6 C^1, 152.6 C^6, 137.8 C^3, 136.1 C^9, 126.7 C^7, 125.7 C^8, 121.4 C^4, 119.6 C^2, 114.2 C^{11}, 34.7 C^{14}, 31.3 C^{13} HRMS (ESI$^+$) m/z 499.2903 $[M+H]^+$ calcd for $[C_{34}H_{34}N_4]^+$ 499.2862

4,6-bis(6-(4-(trifluoromethyl)phenyl)pyridin-2-yl)pyrimidine (H_2L^{19})

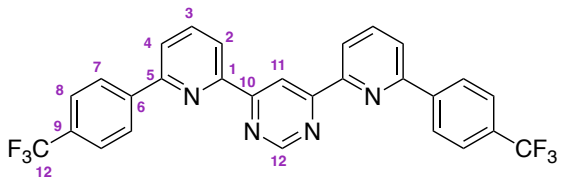

A mixture of 2-(tributylstannyl)-6-(4-(trifluoromethyl)phenyl)pyridine (1.00 g, 1.952 mmol), 4,6-dichloropyrimidine (116 mg, 0.781 mmol) and LiCl (166 g, 3.904 mmol) were dissolved in toluene (5 mL) and degassed by three freeze-pump-thaw cycles. $Pd(PPh_3)_4$ (135 mg, 0.117 mmol) was added under nitrogen and the resulting yellow solution was heated at reflux temperature overnight. After cooling down, saturated

aqueous KF (5 mL) was added and the mixture was stirred for 30 min. The precipitate was filtered off and then the solvent was removed under reduced pressure. The crude product was extracted into DCM (3×20 mL), washed with 5% $NaHCO_3$(aq) (3×15 mL), dried over $MgSO_3$ and washed with acetone (3×15 mL) to yield a white solid (227 mg, 56% yield) ^{1}H NMR (700 MHz, $CDCl_3$) δ_H / ppm 9.71 (d, *J* = 1.5 Hz, 1H, H^{11}), 9.32 (d, *J* = 1.5 Hz, 1H, H^{12}), 8.46 (d, *J* = 7.5 Hz, 2H, H^2), 8.29 (d, *J* = 8.0 Hz, 4H, H^7), 7.97 – 7.92 (m, 2H H^3), 7.88 (d, *J* = 8.0 Hz, 2H, H^4), 7.72 (d, *J* = 8.0 Hz, 4H, H^8) ^{13}C NMR (176 MHz, $CDCl_3$) δ_C / ppm 163.9 C^{10}, 158.6 C^{12}, 155.3 C^5, 154.0 C^1, 142.2 C^6, 138.3 C^3, 131.4 (q, *J* = 32.5 Hz, C^9), 127.3 C^7, 125.7 (q, *J* = 3.5 Hz, C^8), 124.4 (q, *J* = 271.0 Hz, C^{12}), 122.1 C^4, 120.8 C^2, 114.3 C^{11} HRMS (ESI$^+$) m/z 523.1357 $[M+H]^+$ calcd for $[C_{28}H_{17}N_4F_6]^+$ 523.1358

8.7.2 Platinum complexes

PtHL^{17}Cl

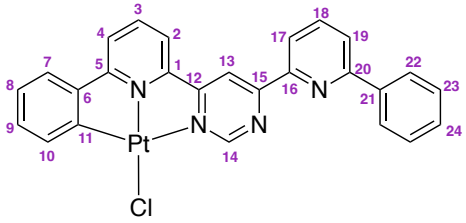

K_2PtCl_4 (68 mg, 0.176 mmol) and H_2L^{17} (161 mg, 0.387 mmol) were dissolved in acetic acid (25 mL) and degassed by three freeze-pump-thaw cycles. The mixture was heated to reflux temperature for 72 h. After cooling down, water (25 mL) was added. The resulting precipitate was isolated, washed successively with water (20 mL), MeOH (20 mL) and diethyl ether (20 mL), and extracted into DCM. The solvent was removed under reduced pressure to yield the product as a dark brown solid (51 mg, 47% yield) ^{1}H NMR (599 MHz, DMSO-d_6) δ_H / ppm 9.43 (s, 1H, H^{13}), 9.24 (s, 1H, H^{14}), 8.64 (d, *J* = 8.0 Hz, 1H, H^2), 8.49 (d, *J* = 7.5 Hz, 1H, H^{17}), 8.42 – 8.37 (m, 2H, H^{22}), 8.29 (d, *J* = 8.0 Hz, 1H, H^{19}), 8.26 – 8.21 (m, 1H, H^3), 8.20 – 8.16 (m, 1H, H^{18}), 8.10 (d, *J* = 8.0 Hz, 1H, H^4), 7.63 (d, *J* = 7.5 Hz, 1H, H^7), 7.60 – 7.55 (m, 3H, H^{23}), 7.53 (d, *J* = 7.5 Hz, 1H, H^{24}), 7.47 (d, *J* = 7.5 Hz, 1H, H^{10}), 7.15 (d, *J* = 7.0 Hz, 1H, H^9), 7.10 – 7.04 (m, 1H, H^8) HRMS (ASAP$^+$) m/z 615.0868 $[M]^+$ calcd for $[C_{26}H_{18}N_4Cl^{194}Pt]^+$ 615.0847

$PtHL^{17}Cl_3$

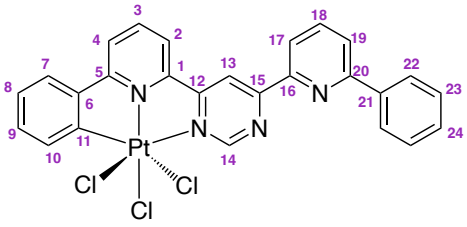

$PtHL^{17}Cl$ (40 mg, 0.064 mmol) and $PhICl_2$ (18 mg, 0.064 mmol) were dissolved in $CHCl_3$ (25 mL) and the mixture was left to stir overnight, with the partial exclusion of light. The solvent was removed under reduced pressure and the resulting solid washed with diethyl ether(25 mL) to yield the final product as an orange solid (22 mg, 50% yield)^{1}H NMR (599 MHz, DMSO-d_6) δ_H / ppm 9.70 (s, 1H, H^{13} or H^{14}), 9.63 (s, 1H, H^{13} or H^{14}), 9.12 (d, J = 8.0 Hz, 1H, H^2), 8.65 (d, J = 8.0 Hz, 1H, H^4), 8.58 – 8.53 (m, 2H, H^{17} and H^3), 8.42 (d, J = 8.0 Hz, 2H, H^{22}), 8.32 (d, J = 8.0 Hz, 1H, H^{19}), 8.26 – 8.21 (m, 1H, H^{18}), 8.03 (d, J = 7.5 Hz, 1H, H^7), 7.62 – 7.56 (m, 3H, H^{10} and H^{23}), 7.56 – 7.49 (m, 1H, H^{24}), 7.46 – 7.40 (m, 1H, H^9), 7.36 – 7.29 (m, 1H, H^8)

$(PtCl_3)(PtCl)L^{17}$

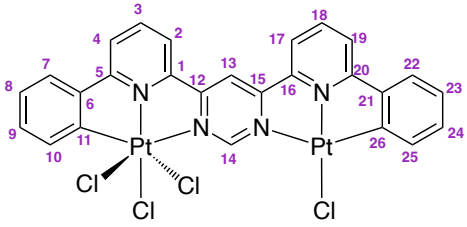

$PtHL^{17}Cl_3$ (15 mg, 0.022 mmol) and K_2PtCl_4 (10 mg, 0.027 mmol) were dissolved in acetic acid (2 mL) and degassed by three freeze-pump-thaw cycles. The mixture was heated to reflux temperature for 72 h. After cooling down, water (2 mL) was added. The resulting precipitate was isolated, washed successively with water (10 mL), MeOH (10 mL) and diethyl ether (10 mL), and extracted into DCM. The solvent was removed under reduced pressure to yield the final product (11 mg, 55% yield) ^{1}H NMR (400 MHz, DMSO-d_6) δ_H / ppm 9.80 (s, 1H, H^{13} or H^{14}), 9.73 (s, 1H, H^{13} or H^{14}), 9.04 (d, J = 7.5 Hz, 1H), 8.80 (d, J = 8.5 Hz, 1H), 8.74 – 8.68 (m, 1H), 8.61 (d, J = 8.0 Hz, 1H), 8.44 – 8.38 (m, 1H), 8.26 (d, J = 8.0 Hz, 1H), 8.09 (d, J = 7.5 Hz, 1H), 7.70 (d, J = 7.5 Hz, 1H), 7.61 (d, J = 8.0 Hz, 1H), 7.53 – 7.42 (m, 2H), 7.41 – 7.36 (m, 1H), 7.25 – 7.18 (m, 1H), 7.17 – 7.10 (m, 1H)

$(PtCl_3)_2L^{17}$

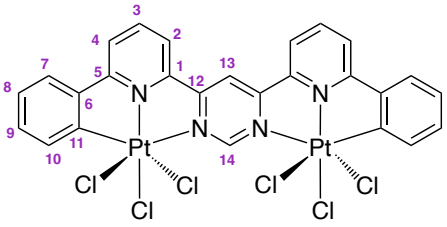

$L(PtCl_3)(PtCl)$ (6 mg, 0.007 mmol) and $PhICl_2$ (2 mg, 0.007 mmol) were dissolved in $CHCl_3$ (10 mL) and the mixture was left to stir overnight, with the partial exclusion of light. The solvent was removed under reduced pressure and the resulting solid washed with diethyl ether (20 mL), dissolved in DCM and filtered through a silica plug to yield the final product as a dark orange solid (5 mg, 78% yield) ^{1}H NMR (599 MHz, DMSO-d_6) δ_H / ppm 10.32 (s, 1H, H^{13} or H^{14}), 9.73 (s, 1H, H^{13} or H^{14}), 9.13 (d, J = 8.0 Hz, 2H, H^2), 8.79 (d, J = 8.0 Hz, 2H, H^4), 8.76 – 8.70 (m, 2H, H^3), 8.07 (d, J = 8.0 Hz, 2H, H^7), 7.58 (d, J = 8.0 Hz, 2H, H^{10}), 7.50 – 7.43 (m, 2H, H^9), 7.39 – 7.33 (m, 2H, H^8)

$PtHL^{18}Cl$

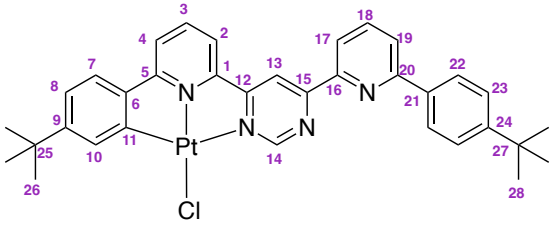

H_2L^{18} (198 mg, 0.387 mmol) were dissolved in acetic acid (25 mL) and degassed by three freeze-pump-thaw cycles. The mixture was heated to reflux temperature for 72 h. After cooling down, water (25 mL) was added. The resulting precipitate was isolated, washed successively with water (20 mL), MeOH (20 mL) and diethyl ether (20 mL). The solid was extracted into DCM and filtered through a plug of silica. The solvent was removed under reduced pressure to yield the final product as a red solid (265 mg, 80% yield) ^{1}H NMR (599 MHz, $CDCl_3$) δ_H / ppm 9.65 (d, J = 1.0 Hz, 1H, H^{14}), 8.99 (d, J = 1.0 Hz, 1H, H^{13}), 8.51 (dd, J = 7.5, 1.0 Hz, 1H, H^{17}), 8.08 – 8.03 (m, 2H, H^{22}), 8.00 – 7.95 (m, 1H, H^{18}), 7.93 (dd, J = 8.0, 1.0 Hz, 1H, H^{19}), 7.91 – 7.86 (m, 1H, H^3), 7.79 (dd, J = 8.0, 1.0 Hz, 1H, H^2), 7.75 (d, J = 2.0 Hz, 1H, H^{10}), 7.61 – 7.57 (m, 2H, H^{23}), 7.56 – 7.52 (m, 1H, H^4), 7.23 (d, J = 8.0 Hz, 1H, H^7), 7.10 (dd, J = 8.0, 2.0 Hz, 1H, H^8), 1.40 (s, 9H, H^{28}), 1.33 (s, 9H, H^{26}) ^{13}C NMR (151 MHz, $CDCl_3$) δ_C /

ppm 157.5 C^{14}, 138.2 C^{3}, 131.6 C^{10}, 126.8 C^{22}, 125.9 C^{23}, 123.9 C^{19}, 121.4 C^{8}, 121.2 C^{17}, 120.1 C^{4}, 118.7 C^{2}, 113.4 C^{13}, 31.3 C^{28}, 31.2 C^{26} HRMS (ASAP$^+$) m/z 727.2084 $[M]^+$ calcd for $[C_{34}H_{34}N_4Cl^{194}Pt]^+$ 727.2099

$PtHL^{18}Cl_3$

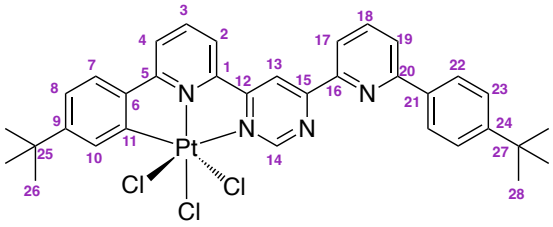

$PtHL^{18}Cl$ (265 mg, 0.386 mmol) and $PhICl_2$ (106 mg, 0.386 mmol) were dissolved in $CHCl_3$ (30 mL) and the mixture was left to stir overnight, with the partial exclusion of light. The solvent was removed under reduced pressure and the resulting solid washed with diethyl ether (30 mL) to yield the final product as a yellow solid (210 mg, 72% yield) ^{1}H NMR (599 MHz, $CDCl_3$) δ_H / ppm 9.89 (d, *J* = 1.0 Hz, 1H, H^{14}), 9.30 (d, *J* = 1.0 Hz, 1H, H^{13}), 8.61 (d, *J* = 7.5 Hz, 1H, H^{17}), 8.21 (d, *J* = 7.5 Hz, 1H, H^{2}), 8.15 – 8.09 (m, 1H, H^{3}), 8.06 – 8.00 (m, 3H, H^{18} and H^{23}), 8.00 – 7.93 (m, 2H, H^{4} and H^{19}), 7.90 (d, *J* = 2.0 Hz, 1H, H^{10}), 7.59 (d, *J* = 8.5 Hz, 2H, H^{13}), 7.51 (d, *J* = 8.0 Hz, 1H, H^{4}), 7.30 (dd, *J* = 8.0, 2.0 Hz, 1H, H^{3}), 1.41 (s, 9H, H^{17}), 1.41 (s, 9H, H^{16}) ^{13}C NMR (151 MHz, $CDCl_3$) δ_C / ppm 157.6 C^{14}, 141.6 C^{3}, 138.4 C^{18}, 129.5 C^{10}, 127.1 C^{23}, 126.5 C^{7}, 125.9 C^{22}, 124.4 C^{8}, 124.2 C^{19}, 122.8 C^{4}, 121.6 C^{17}, 121.4 C^{2}, 115.4 C^{13}, 31.2 C^{17} and C^{16}

$(PtCl_3)(PtCl)L^{18}$

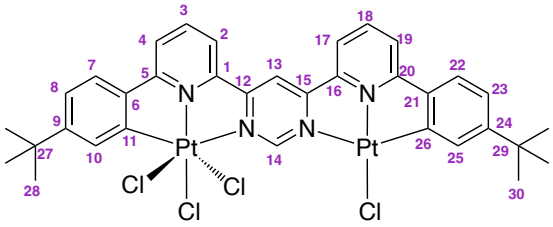

$LHPtCl_3$ (210 mg, 0.277 mmol) and K_2PtCl_4 (131 mg, 0.316 mmol) were dissolved in acetic acid (25 mL) and degassed by three freeze-pump-thaw cycles. The mixture was heated to reflux temperature for 72 h. After cooling down, water (25 mL) was added. The resulting precipitate was isolated, washed successively with water (30 mL), MeOH (30 mL) and diethyl ether (30 mL), and extracted into DCM. The solvent

was removed under reduced pressure to yield the final product.

$(PtCl_3)_2L^{18}$

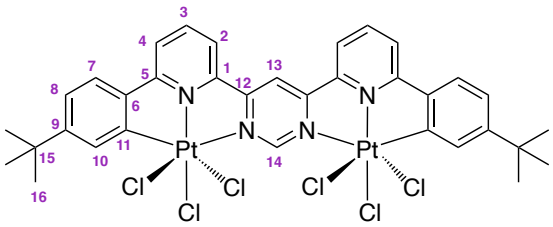

$L(PtCl_3)(PtCl)$ (200 mg, 0.194 mmol) and $PhICl_2$ (53 mg, 0.194 mmol) were dissolved in $CHCl_3$ (30 mL) and the mixture was left to stir overnight, with the partial exclusion of light. The solvent was removed under reduced pressure and the resulting solid washed with diethyl ether (30 mL).The product was purified by gradient column chromatography on silica with hexane : ethyl acetate to yield an orange solid (23 mg, 11%yield) ^{1}H NMR (400 MHz, CD_2Cl_2) δ_H / ppm 10.23 (d, J = 1.0 Hz, 1H, H^{14}), 8.98 (s, 1H, H^{13}), 8.42 (dd, J = 6.0, 3.0 Hz, 2H, H^2), 8.15 – 8.03 (m, 4H, H^3 and H^4), 7.85 (d, J = 1.5 Hz, 2H, H^{10}), 7.51 (d, J = 8.0 Hz, 2H, H^8), 7.43 (dd, J = 8.0, 1.5 Hz, 2H, H^7), 1.49 (s, 18H, H^{16})

8.8 Chapter 6 synthesis

8.8.1 Proligands and precursors

2-(3-bromo-5-(*tert*-butyl)phenyl)pyridine

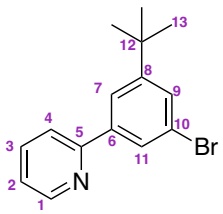

A mixture of 1,3-dibromo-5-(*tert*-butyl)benzene (451 mg, 1.544 mmol) and 2-(tributylstannyl)pyridine (0.5 mL, 569 mg, 1.544 mmol) were dissolved in toluene (15 mL) and degassed by three freeze-pump-thaw cycles. $Pd(PPh_3)_4$ (89 mg, 0.077 mmol) was added under nitrogen and the resulting yellow solution was heated at reflux temperature overnight. After cooling down, saturated aqueous KF (5 mL) was added and the mixture was stirred for 30 min. The precipitate was filtered off and then the solvent was removed under reduced pressure. The crude product was extracted into DCM

(3×20 mL), washed with 5% $NaHCO_3$(aq) (3×15 mL), dried over $MgSO_3$ and purified by gradient column chromatography on silica with hexane / ethyl acetate as the mobile phase (R_f = 0.6 in EtOAc : hexane = 2 : 8) to yield a white solid (196 mg, 44% yield) ^{1}H NMR (400 MHz, $CDCl_3$) δ_H / ppm 8.72 (ddd, J = 5.0, 2.0, 1.0 Hz, 1H), 7.99 – 7.92 (m, 2H), 7.79 (ddd, J = 8.0, 7.5, 2.0 Hz, 1H), 7.76 – 7.69 (m, 1H), 7.60 – 7.55 (m, 1H), 7.32 – 7.23 (m, 1H), 1.40 (s, 9H) The experimental data obtained are in agreement with literature.[146]

8-(3-bromo-5-(*tert*-butyl)phenyl)quinoline

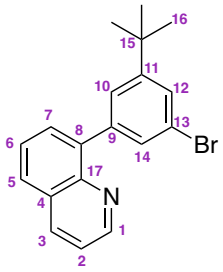

A mixture of 8-quinolinylboronic acid (300 mg, 1.734 mmol), 1,3-dibromo-5-(*tert*-butyl)benzene (506 mg, 1.734 mmol), Na_2CO_3 (1.470 g, 13.874 mmol), $Pd(PPh_3)_4$ (100 mg, 0.087 mmol), DME (14 mL) and water (14 mL) were reacted according to the general procedure for Suzuki cross-coupling. The product was obtained as a colourless oil (423 mg, 72% yield) (R_f = 0.5 in EtOAc : hexane = 1 : 9) ^{1}H NMR (700 MHz, $CDCl_3$) δ_H / ppm 8.99 – 8.92 (m, 1H, H^1), 8.21 (d, J = 8.0 Hz, 1H, H^3), 7.83 – 7.78 (m, 1H, H^5), 7.67 (dd, J = 7.0, 1.5 Hz, 1H, H^7), 7.61 – 7.59 (m, 1H, H^{14}), 7.59 – 7.55 (m, 1H, H^6), 7.54 – 7.52 (m, 1H, H^{10}), 7.52 – 7.50 (m, 1H, H^{12}), 7.41 (dd, J = 8.0, 4.0 Hz, 1H, H^2), 1.30 (s, 9H, H^{16}) ^{13}C NMR (176 MHz, $CDCl_3$) δ_C / ppm 153.0 C^{11}, 150.1 C^1, 130.7 C^{14}, 128.8, 128.0 C^{12}, 126.6 C^{10}, 122.1, 121.2 C^2, 35.0 C^{15} 31.3 C^{16} HRMS (ESI$^+$) m/z 340.0701 $[M+H]^+$ calcd for $[C_{19}H_{19}NBr]^+$ 340.0714

2-(3-(*tert*-butyl)-5-(4,4,5,5-tetramethyl-1,3,2-dioxaborolan-2-yl)phenyl)pyridine

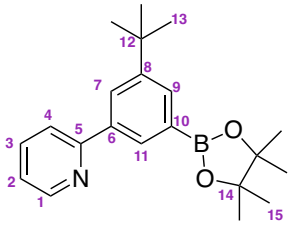

A mixture of 2-(3-bromo-5-(tert-butyl)phenyl)pyridine (140 mg, 0.482 mmol), bis(pina-

colato)diboron (135 mg, 0.531 mmol) and KOAc (254 mg, 2.895 mmol) were dissolved in 1,4-dioxane (5 mL) and degassed by three freeze-pump-thaw cycles. $PdCl_2(dppf)_2$ (39 mg, 0.048 mmol) was added under nitrogen and the resulting solution was heated at reflux temperature overnight. The solvent was removed under reduced pressure and the crude product was dissolved in DCM, filtered and washed with water, dried over $MgSO_4$ and purified by gradient column chromatography on silica with hexane / ethyl acetate as the mobile phase (R_f = 0.2 in EtOAc : hexane = 1 : 9) to yield a white solid (129 mg, 92% yield) ^{1}H NMR (700 MHz, $CDCl_3$) δ_H / ppm 8.67 – 8.62 (m, 1H, H^1), 8.15 – 8.12 (m, 1H, H^7), 8.10 (dd, J = 2.0, 1.0 Hz, 1H, H^{11}), 7.83 (dd, J = 2.0, 1.0 Hz, 1H, H^9), 7.74 (d, J = 8.0 Hz, 1H, H^4), 7.71 – 7.65 (m, 1H, H^3), 7.18 – 7.14 (m, 1H, H^2), 1.35 (s, 9H, H^{13}), 1.29 (s, 12H, H^{15}) ^{13}C NMR (176 MHz, $CDCl_3$) δ_C / ppm 157.9 C^5, 151.0 C^8, 149.2 C^1, 138.2 C^6, 132.4 C^9, 130.7 C^{11}, 129.2 C^{10}, 127.2 C^7, 122.0 C^2, 121.2 C^4, 83.8 C^{14}, 34.9 C^{12}, 31.5 C^{13}, 24.9 C^{15} HRMS (ESI$^+$) m/z 337.2336 $[M+H]^+$ calcd for $[C_{21}H_{19}NO_2{}^{10}B]^+$ 337.2328

8-(3-(*tert*-butyl)-5-(4,4,5,5-tetramethyl-1,3,2-dioxaborolan-2-yl)phenyl)quinoline

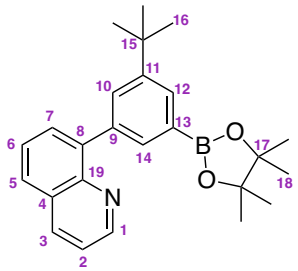

A mixture of 8-(3-bromo-5-(tert-butyl)phenyl)quinoline (122 mg, 0.359 mmol), bis(pinacolato)diboron (100 mg, 0.394 mmol) and KOAc (211 mg, 2.151 mmol) were dissolved in 1,4-dioxane (5 mL) and degassed by three freeze-pump-thaw cycles. $PdCl_2(dppf)_2$ (29 mg, 0.036 mmol) was added under nitrogen and the resulting solution was heated at reflux temperature overnight. The solvent was removed under reduced pressure and the crude product was dissolved in DCM, filtered and washed with water, dried over $MgSO_4$ and purified by gradient column chromatography on silica with hexane / ethyl acetate as the mobile phase (R_f = 0.2 in EtOAc : hexane = 1 : 9) to yield a white solid (86 mg, 62% yield) ^{1}H NMR (700 MHz, $CDCl_3$) δ_H / ppm 9.04 (s, 1H, H^1), 8.30 – 8.24 (m, 1H, H^3), 7.96 – 7.89 (m, 2H, H^{10} and H^{14}), 7.85 (d, J = 8.0 Hz, 1H, H^5), 7.83 (s, 1H, H^{12}), 7.79 (d, J = 7.0 Hz, 1H, H^7), 7.66 – 7.59 (m, 1H, H^6), 7.47 (s, 1H, H^2), 1.44 (d, J = 1.0 Hz, 9H, H^{16}), 1.37 (s, 12H, H^{18}) ^{13}C NMR (176

MHz, $CDCl_3$) δ_C / ppm 150.0 C^1, 149.8 C^{11}, 134.2 C^{12} and C^{14}, 131.0 C^{10}, 128.7, 127.3 C^5, 126.5 C^6, 120.9 C^2, 83.6 C^{17}, 34.8 C^{13}, 31.6 C^{16}, 24.9 C^{18} HRMS (ESI^+) m/z 387.2504 $[M+H]^+$ calcd for $[C_{25}H_{31}NO_2{}^{10}B]^+$ 387.2484

2,2'-(5,5'-di-*tert*-butyl-[1,1'-biphenyl]-3,3'-diyl)dipyridine (H_2L^{21})

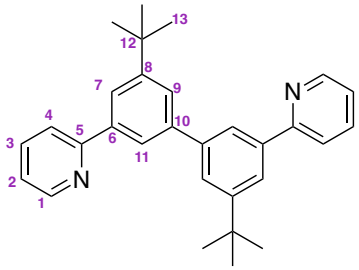

A mixture of 2-(3-(*tert*-butyl)-5-(4,4,5,5-tetramethyl-1,3,2-dioxaborolan-2-yl)phenyl)-pyridine (150 mg, 0.445 mmol), 2-(3-bromo-5-(*tert*-butyl)phenyl)pyridine (129 mg, 0.445 mmol), Na_2CO_3 (337 mg, 3.56 mmol), $Pd(PPh_3)_4$ (26 mg, 0.022 mmol), DME (3.5 mL) and water (3.5 mL) were reacted according to the general procedure for Suzuki cross-coupling. The product was obtained as a colourless oil (174 mg, 93% yield) (R_f = 0.3 in EtOAc : hexane = 2 : 8) ^1H NMR (400 MHz, $CDCl_3$) δ_H / ppm 8.78 – 8.74 (m, 1H, H^1), 8.09 – 8.06 (m, 1H, H^{11}), 8.06 – 8.02 (m, 1H, H^7), 7.85 – 7.76 (m, 2H, H^3 and H^4), 7.76 – 7.71 (m, 1H, H^9), 7.32 – 7.24 (m, 1H, H^2), 1.49 (s, 9H, H^{13}) ^{13}C NMR (176 MHz, $CDCl_3$) δ_C / ppm 157.1 C^5, 152.6, 148.0 C^1, 142.1, 138.6, 126.2 C^9, 124.0 C^{11}, 123.6 C^7, 122.5 C^2, 122.0 C^4, 35.2 C^{12}, 30.9 C^{13} HRMS (ESI^+) m/z 421.2639 $[M+H]^+$ calcd for $[C_{30}H_{33}N_2]^+$ 421.2644

8-(3',5-di-*tert*-butyl-5'-(pyridin-2-yl)-[1,1'-biphenyl]-3-yl)quinoline (H_2L^{22})

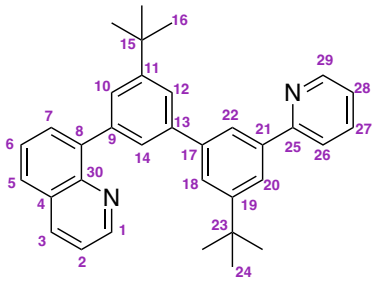

A mixture of 2-(3-(*tert*-butyl)-5-(4,4,5,5-tetramethyl-1,3,2-dioxaborolan-2-yl)phenyl)-pyridine (72 mg, 0.214 mmol), 8-(3-bromo-5-(*tert*-butyl)phenyl)quinoline (73 mg, 0.214 mmol), Na_2CO_3 (181 mg, 1.708 mmol), $Pd(PPh_3)_4$ (12 mg, 0.011 mmol), DME (2 mL) and water (2 mL) were reacted according to the general procedure for Suzuki

cross-coupling. The product was obtained as a white solid (89 mg, 89% yield) (R_f = 0.2 in EtOAc : hexane = 1 : 9) ^{1}H NMR (700 MHz, $CDCl_3$) δ_H / ppm 8.89 (dd, J = 4.0, 2.0 Hz, 1H, H^1), 8.67 – 8.65 (m, 1H, H^{29}), 8.15 (dd, J = 8.5, 2.0 Hz, 1H, H^3), 8.00 – 7.96 (m, 1H, H^{20}), 7.94 – 7.90 (m, 1H, H^{22}), 7.78 (dd, J = 8.0, 1.5 Hz, 1H, H^5), 7.75 (dd, J = 7.0, 1.5 Hz, 1H, H^7), 7.73 – 7.70 (m, 3H, H^{14}, H^{26} and H^{27}), 7.66 – 7.65 (m, 1H, H^{18}), 7.68 – 7.67 (m, 1H, H^{10}), 7.64 – 7.62 (m, 1H, H^{12}), 7.56 (dd, J = 8.0, 7.0 Hz, 1H, H^6), 7.35 (dd, J = 8.5, 4.0 Hz, 1H, H^2), 7.18 (s, 1H, H^{28}), 1.39 (s, 9H, H^{16}), 1.37 (s, 9H, H^{24}) ^{13}C NMR (176 MHz, $CDCl_3$) δ_C / ppm 158.0 C^{25}, 152.1 C^{19}, 151.0 C^{11}, 150.3 C^1, 149.2 C^{29}, 146.2 C^{30}, 142.7 C^{13} or C^{17}, 141.4 C^8, 141.1 C^{13} or C^{17}, 139.5 C^9, 137.2 C^{26} or C^{27}, 136.2 C^3, 130.4 C^7, 128.8 C^4, 127.5 C^5, 127.4 C^{14}, 127.1 C^{10}, 126.3 C^6, 126.1 C^{18}, 123.9 C^{12}, 123.8 C^{22}, 123.0 C^{20}, 122.1 C^{28}, 121.3 C^{26} or C^{27}, 121.0 C^2, 35.1 C^{23}, 35.0 C^{15}, 31.6 C^{16}, 31.5 C^{24} HRMS (ESI$^+$) m/z 471.2783 $[M+H]^+$ calcd for $[C_{34}H_{35}N_2]^+$ 471.2800

8,8'-(5,5'-di-*tert*-butyl-[1,1'-biphenyl]-3,3'-diyl)diquinoline (H_2L^{23})

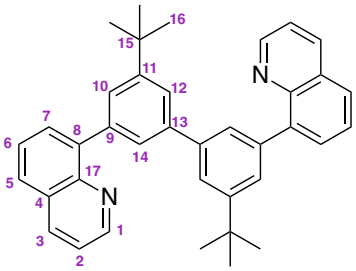

A mixture of 8-(3-(*tert*-butyl)-5-(4,4,5,5-tetramethyl-1,3,2-dioxaborolan-2-yl)phenyl)-quinoline (75 mg, 0.194 mmol), 8-(3-bromo-5-(*tert*-butyl)phenyl)quinoline (66 mg, 0.194 mmol), Na_2CO_3 (164 mg, 1.552 mmol), $Pd(PPh_3)_4$ (11 mg, 0.010 mmol), DME (1.5 mL) and water (1.5 mL) were reacted according to the general procedure for Suzuki cross-coupling. The product was obtained as a colourless oil (72 mg, 71% yield) (R_f = 0.5 in EtOAc : hexane = 2 : 8) ^{1}H NMR (700 MHz, $CDCl_3$) δ_H / ppm 9.02 – 8.99 (m, 2H, H^1), 8.26 (d, J = 8.5 Hz, 2H, H^3), 7.84 (ddd, J = 8.7, 7.6, 1.5 Hz, 4H, H^5 and H^7), 7.81 – 7.78 (m, 2H, H^{14}), 7.74 – 7.69 (m, 4H, H^{10} and H^{12}), 7.69 – 7.63 (m, 2H, H^6), 7.46 (dd, J = 8.5, 4.0 Hz, 2H, H^2), 1.46 (s, 18H, H^{16}) ^{13}C NMR (176 MHz, $CDCl_3$) δ_C / ppm 150.8 C^{11}, 150.2 C^1, 145.8 C^{17}, 141.8 C^{13}, 141.4 C^4 or C^8, 139.1 C^9, 136.5 C^3, 130.6 C^7, 128.8 C^4 or C^8, 127.4 C^{14}, 127.4 C^5, 126.8 C^{10} or C^{12}, 126.4 C^6, 124.4 C^{10} or C^{12}, 121.0 C^2, 35.0 C^{15}, 31.6 C^{16} HRMS (ESI$^+$) m/z 521.2957 $[M+H]^+$ calcd for $[C_{38}H_{37}N_2]^+$ 521.2957

8.8.2 Platinum complexes

$Pt_2L^{21}{}_2Cl_2$

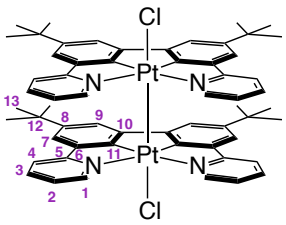

K_2PtCl_4 (87 mg, 0.209 mmol) and $L^{21}H_2$ (77 mg, 0.183 mmol) were dissolved in acetic acid (8 mL) and degassed by three freeze-pump-thaw cycles. The mixture was heated to reflux temperature for 72 h. After cooling down, water (5 mL) was added. The resulting precipitate was isolated and washed with water (20 mL). The product was dried under reduced pressure and purified by recrystallisation from DCM/Et_2O (101 mg, 85% yield) ^{1}H NMR (700 MHz, CD_2Cl_2) δ_H / ppm 7.86 (d, J = 5.0 Hz, 1H, H^1), 7.56 – 7.51 (m, 1H, H^3), 7.35 – 7.31 (m, 1H, H^4), 7.24 (d, J = 2.0 Hz, 1H, H^7), 7.07 (ddd, J = 7.5, 5.0, 1.5 Hz, 1H, H^2), 7.03 (d, J = 2.0 Hz, 1H, H^9), 1.41 (s, 9H, H^{13}) ^{13}C NMR (176 MHz, CD_2Cl_2) δ_C / ppm 162.7, 149.8 C^1, 149.3, 147.1 C^8, 137.7 C^3, 121.8 C^2, 119.4 C^9, 119.0 C^4, 118.8 C^7, 34.7 C^{12}, 31.8 C^{13}

$PtL^{22}Cl_2$

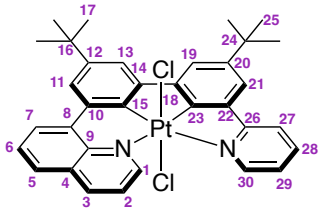

K_2PtCl_4 (89 mg, 0.213 mmol) and $L^{22}H_2$ (88 mg, 0.187 mmol) were dissolved in acetic acid (8 mL) and degassed by three freeze-pump-thaw cycles. The mixture was heated to reflux temperature for 72 h. After cooling down, water (5 mL) was added. The resulting precipitate was isolated and washed with water (20 mL). The product was dried under reduced pressure and purified by gradient column chromatography on silica with hexane : ethyl acetate to yield a yellow solid (80 mg, 58% yield) ^{1}H NMR (599 MHz, CD_2Cl_2) δ_H / ppm 9.69 (dd, J = 5.0, 2.0 Hz, 1H, H^1), 8.82 (d, J = 5.5 Hz, 1H, H^{30}), 8.64 (dd, J = 8.0, 2.0 Hz, 1H, H^3), 8.53 (dd, J = 8.0, 1.5 Hz, 1H, H^7), 8.17 (d, J = 8.0 Hz, 1H, H^{27}), 8.06 – 8.00 (m, 2H, H^5 and H^{28}), 7.92 – 7.86 (m, 2H, H^2 and H^6), 7.82 (d, J = 2.0 Hz, 1H, H^{11}), 7.75 (d, J = 2.0 Hz, 1H, H^{19}), 7.74 – 7.72 (m, 2H,

H^{13} and H^{21}), 7.56 (ddd, *J* = 8.0, 5.5, 1.5 Hz, 1H, H^{29}), 1.53 (s, 9H, H^{17}), 1.53 (s, 9H, H^{25}) ^{13}C NMR (151 MHz, CD_2Cl_2) δ_C / ppm 162.7 C^{26}, 152.1 C^1, 150.6, 149.7 C^{12}, 149.3 C^{20}, 147.5 C^{30}, 145.8, 144.8, 141.5, 141.2 C^3, 139.5 C^{28}, 136.7, 133.0, 132.2 C^7, 130.7, 129.6, 129.3 C^5, 128.1 C^6, 123.6 C^{11}, 123.3 C^{29}, 121.5 C^2, 121.2 C^{27}, 120.8 C^{19}, 119.9 C^{13} and C^{21}, 119.8 C^{13} and C^{21}, 34.9 C^{24}, 34.6 C^{16}, 31.6 C^{25}, 31.4 C^{17} HRMS (ESI^+) m/z 733.1619 $[M]^+$ calcd for $[C_{34}H_{33}N_2Cl_2{}^{194}Pt]^+$ 733.1648

$PtL^{23}Cl_2$

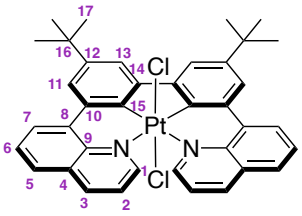

K_2PtCl_4 (56 mg, 0.136 mmol) and $L^{23}H_2$ (62 mg, 0.119 mmol) were dissolved in acetic acid (6 mL) and degassed by three freeze-pump-thaw cycles. The mixture was heated to reflux temperature for 72 h. After cooling down, water (5 mL) was added. The resulting precipitate was isolated and washed with water (20 mL). The complex was purified fractional precipitations from DCM/ diethyl ether, yielding a yellow solid (39 mg, 42% yield) ^1H NMR (599 MHz, $CDCl_3$) δ_H / ppm 8.82 (dd, $^3J_{^{195}Pt-^1H} \approx 14$ Hz, *J* = 5.0, 1.5 Hz, 1H, H^1), 8.52 – 8.46 (m, 2H, H^3 and H^7), 7.92 (dd, *J* = 8.0, 1.5 Hz, 1H, H^5), 7.86 – 7.81 (m, 1H, H^6), 7.78 – 7.74 (m, 2H, H^{11} and H^{13}), 7.55 (dd, *J* = 8.0, 5.0 Hz, 1H, H^2), 1.50 (s, 9H, H^{17}) ^{13}C NMR (151 MHz, $CDCl_3$) δ_C / ppm 153.9 C^1, 149.0, 148.4, 142.2 C^9, 141.1 C^3, 136.8, 132.9, 131.9 C^7, 131.1, 129.8 C^4, 128.3 C^5 or C^6, 128.2 C^5 or C^6, 123.8 C^{11}, 120.7 C^2, 119.4 C^{13}, 34.6 C^{16}, 31.8 C^{17} HRMS (ESI^+) m/z 783.1816 $[M]^+$ calcd for $[C_{38}H_{35}N_2Cl_2{}^{194}Pt]^+$ 783.1804

PtL^{21}

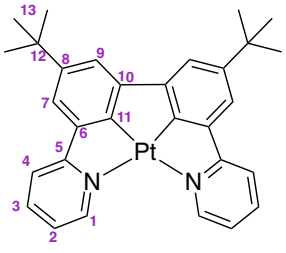

$PtL^{21}Cl_2$ (10 mg, 0.015 mmol) and activated Zn^0 (20 mg) were mixed in dry DCM (3 mL) and degassed by three freeze-pump-thaw cycles. The suspension was heated

at reflux temperature for 5 d under N_2. After cooling down, the mixture was filtrated through celite and the solvent evaporated under reduced pressure to yield the product as a red solid (7 mg, 79% yield) ^{1}H NMR (400 MHz, CD_2Cl_2) δ_H / ppm 8.88 (ddd, $^3J_{^{195}Pt-^1H} \approx 15$ Hz, J = 5.5, 1.5, 1.0 Hz, 1H, H^1), 7.97 (ddd, J = 8.0, 7.0, 1.5 Hz, 1H, H^3), 7.91 (d, J = 8.0, 1.5, 1.0 Hz, 1H, H^4), 7.53 – 7.47 (m, 1H, H^7), 7.47 – 7.39 (m, 2H, H^2 and H^9), 1.47 (s, 9H, H^{13}). ^{13}C NMR (151 MHz, $CDCl_3$) δ_C / ppm 150.7 C^1, 138.4 C^3, 122.4 C^9, 119.2 C^4, 118.6 C^2, 117.2 C^7, 33.2 C^{13}. HRMS (ESI$^+$) m/z 613.2115 $[M]^+$ calcd for $[C_{30}H_{31}N_2{}^{194}Pt]^+$ 613.2114

PtL^{22}

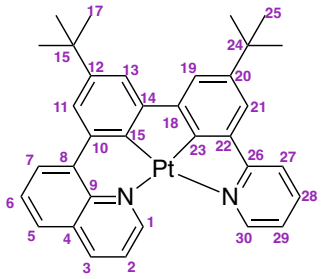

PtL^{22}Cl$_2$ (10 mg, 0.014 mmol) and activated Zn^0 (20 mg) were mixed in dry DCM (3 mL) and degassed by three freeze-pump-thaw cycles. The suspension was heated at reflux temperature for 5 d under N_2. After cooling down, the mixture was filtrated through celite and the solvent evaporated under reduced pressure to yield the product as a red solid (5 mg, 54% yield) ^{1}H NMR (599 MHz, CD_2Cl_2) δ_H / ppm 9.56 (dd, J = 5.0, 2.0 Hz, 1H, H^1), 8.60 (dd, J = 8.0, 2.0 Hz, 1H, H^3), 8.58 – 8.53 (m, 2H, H^7 and H^{30}), 7.97 – 7.89 (m, 3H, H^5, H^{27} and H^{28}), 7.83 – 7.76 (m, 2H, H^6 and H^{11}), 7.66 (dd, J = 8.0, 5.0 Hz, 1H, H^2), 7.52 (d, J = 2.0 Hz, 1H, H^{13}), 7.49 (d, J = 1.5 Hz, 1H, H^{21}), 7.48 (d, J = 1.5 Hz, 1H, H^{19}), 7.39 (ddd, J = 7.0, 5.5, 1.5 Hz, 1H, H^{29}), 1.49 (s, 9H, H^{17}), 1.47 (s, 9H, H^{25}) ^{13}C NMR (151 MHz, CD_2Cl_2) δ_C / ppm 167.5 C^{26}, 163.5, 156.6, 152.5 C^1, 152.2, 148.3 C^{30}, 147.2 C^{12}, 146.3 C^{20}, 145.1, 141.3, 141.2, 139.7 C^3, 139.4, 138.1 C^{28}, 134.0, 130.7, 130.7 C^7, 127.8, 127.5 C^6, 122.0 C^{29}, 120.7 C^2, 120.5 C^{11}, 119.3 C^{27}, 117.7 C^{19}, 117.1 C^{13}, 116.9 C^{21}, 34.9 C^{24}, 34.7 C^{24}, 31.5 C^{25}, 31.4 C^{17} HRMS (ASAP$^+$) m/z 662.2202 $[M]^+$ calcd for $[C_{34}H_{32}N_2{}^{194}Pt]^+$ 662.2192

PtL^{23}

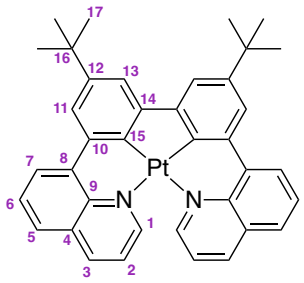

PtL^{23}Cl$_2$ (10 mg, 0.013 mmol) and activated Zn^0 (20 mg) were mixed in dry DCM (3 mL) and degassed by three freeze-pump-thaw cycles. The suspension was heated at reflux temperature for 5 d under N_2. After cooling down, the mixture was filtrated through celite and the solvent evaporated under reduced pressure to yield the product as a red solid (6 mg, 65% yield) ^{1}H NMR (599 MHz, CD_2Cl_2) δ_H / ppm 8.65 (d, J = 8.0 Hz, 2H, H^7), 8.56 (dd, J = 8.0, 1.5 Hz, 2H, H^3), 8.36 (dd, $^3J_{^{195}Pt\text{-}^1H} \approx$ 19 Hz, J = 5.0, 1.5 Hz, 2H, H^1), 7.92 (d, J = 8.0 Hz, 2H, H^5), 7.87 – 7.80 (m, 4H, H^6 and H^{11}), 7.61 (d, J = 2.0 Hz, 2H, H^{13}), 7.44 (dd, J = 8.0, 5.0 Hz, 2H, H^2), 1.50 (s, 18H, H^{17}). ^{13}C NMR (151 MHz, CD_2Cl_2) δ_C / ppm 155.4 C^{15}, 153.7 C^1, 147.3 C^{14}, 147.0 C^{12}, 141.7 C^9, 139.2 C^8, 138.8 C^3, 133.3 C^{10}, 129.7 C^7, 129.7 C^4, 127.5 C^6, 127.2 C^5, 121.0 C^2, 120.2 C^{11}, 116.3 C^{13}, 34.6 C^{16}, 31.4 C^{17} HRMS (ASAP$^+$) m/z 713.2420 [M]$^+$ calcd for [$C_{38}H_{35}N_2{}^{194}Pt$]$^+$ 713.2427

References

Bibliography

[1] V. Balzani and S. Campagna, *Photochemistry and Photophysics of Coordination Compounds I*, Springer-Verlag Berlin Heidelberg, Berlin, 1st edn., 2007, p. 9.

[2] M. Cocchi, D. Virgili, V. Fattori, D. L. Rochester and J. A. G. Williams, *Adv. Funct. Mater.*, 2007, **17**, 285–289.

[3] J. A. G. Williams, S. Develay, D. L. Rochester and L. Murphy, *Coord. Chem. Rev.*, 2008, **252**, 2596–2611.

[4] S. W. Botchway, M. Charnley, J. W. Haycock, A. W. Parker, D. L. Rochester, J. A. Weinstein and J. A. G. Williams, *Proc. Natl. Acad. Sci. U. S. A.*, 2008, **105**, 16071–16076.

[5] P. Wu, E. L.-M. Wong, D.-L. Ma, G. S.-M. Tong, K.-M. Ng and C.-M. Che, *Chem. Eur. J.*, 2009, **15**, 3652–3656.

[6] P. H. Lanoë, J. L. Fillaut, L. Toupet, J. A. G. Williams, H. L. Bozec and V. Guerchais, *Chem. Commun.*, 2008, 4333–4335.

[7] C. Kreitner, A. K. C. Mengel, T. K. Lee, W. Cho, K. Char, Y. S. Kang and K. Heinze, *Chem. Eur. J.*, 2016, **22**, 8915–8928.

[8] L. K. McKenzie, H. E. Bryant and J. A. Weinstein, *Coord. Chem. Rev.*, 2019, **379**, 2–29.

[9] V. L. Whittle and J. A. G. Williams, *Inorg. Chem.*, 2008, **47**, 6596–6607.

[10] P. I. Djurovich, D. Murphy, M. E. Thompson, B. Hernandez, R. Gao, P. L. Hunt and M. Selke, *Dalton Trans.*, 2007, 3763–3770.

[11] J. A. G. Williams, A. J. Wilkinson and V. L. Whittle, *Dalton Trans.*, 2008, 2081–2099.

[12] J. A. G. Williams, *Chem. Soc. Rev.*, 2009, **38**, 1783–1801.

[13] L. Chassot, E. Mueller and A. Von Zelewsky, *Inorg. Chem.*, 1984, **23**, 4249–4253.

[14] L. Chassot, A. Von Zelewsky, D. Sandrini, M. Maestri and V. Balzani, *J. Am. Chem. Soc.*, 1986, **108**, 6084–6085.

[15] A. von Zelewsky, A. P. Suckling and H. Stoeckli-Evans, *Inorg. Chem.*, 1993, **32**, 4585–4593.

[16] C. P. Newman, K. Casey-Green, G. J. Clarkson, G. W. V. Cave, W. Errington and J. P. Rourke, *Dalton Trans.*, 2007, 3170–3182.

[17] S. R. Whitfield and M. S. Sanford, *Organometallics*, 2008, **27**, 1683–1689.

[18] J. Mamtora, S. H. Crosby, C. P. Newman, G. J. Clarkson and J. P. Rourke, *Organometallics*, 2008, **27**, 5559–5565.

[19] P. Reveco, J. H. Medley, A. R. Garber, N. S. Bhacca and J. Selbin, *Inorg. Chem.*, 1985, **24**, 1096–1099.

[20] R. R. Parker, J. P. Sarju, A. C. Whitwood, J. A. G. Williams, J. M. Lynam and D. W. Bruce, *Chem. Eur. J.*, 2018, **24**, 19010–19023.

[21] J. Terheljden, G. van Koten, J. L. de Booys, H. J. Ubbeis and C. H. Stam, *Organometallics*, 1983, **2**, 1882–1883.

[22] G. V. Koten, J. Terheijden, J. A. Van Beek, I. C. Wehman-Ooyevaar, F. Muller and C. H. Stam, *Organometallics*, 1990, **9**, 903–912.

[23] G. D. Batema, M. Lutz, A. L. Spek, C. A. van Walree, C. M. De Donegá, A. Meijerink, R. W. A. Havenith, J. Pérez-Moreno, K. Clays, M. Büchel, A. Van Dijken, D. L. Bryce, G. P. M. Van Klink and G. Van Koten, *Organometallics*, 2008, **27**, 1690–1701.

[24] F. Juliá, D. Bautista, J. M. Fernández-Hernández and P. González-Herrero, *Chem. Sci.*, 2014, **5**, 1875–1880.

[25] F. Juliá, M.-D. García-Legaz, D. Bautista and P. González-Herrero, *Inorg. Chem.*, 2016, **55**, 7647–7660.

[26] F. Juliá, D. Bautista and P. González-Herrero, *Chem. Commun.*, 2016, **52**,

1657–1660.

[27] Á. Vivancos, D. Poveda, A. Munõz, J. Moreno, D. Bautista and P. González-Herrero, *Dalton Trans.*, 2019, **48**, 14367–14382.

[28] Á. Vivancos, A. Jiménez-García, D. Bautista and P. González-Herrero, *Inorg. Chem.*, 2021, **60**, 7900–7913.

[29] Y. Unger, D. Meyer, O. Molt, C. Schildknecht, I. Münster, G. Wagenblast and T. Strassner, *Angew. Chem. Int. Ed.*, 2010, **49**, 10214–10216.

[30] T. Sajoto, P. I. Djurovich, A. B. Tamayo, J. Oxgaard, W. A. Goddard and M. E. Thompson, *J. Am. Chem. Soc.*, 2009, **131**, 9813–9822.

[31] D. M. Jenkins and S. Bernhard, *Inorg. Chem.*, 2010, **49**, 11297–11308.

[32] A. Corral-Zorzano, D. Gómez de Segura, E. Lalinde and M. T. Moreno, *Dalton Trans.*, 2023, **52**, 6543–6550.

[33] F. Juliá and P. González-Herrero, *Dalton Trans.*, 2016, **45**, 10599–10608.

[34] F. Juliá, G. Aullón, D. Bautista and P. González-Herrero, *Chem. Eur. J.*, 2014, **20**, 17346–17359.

[35] Á. Vivancos, D. Bautista and P. González-Herrero, *Inorg. Chem.*, 2022, **61**, 12033–12042.

[36] J. C. López-López, D. Bautista, P. González-Herrero, J. C. LópezLópez, D. Bautista and P. GonzálezHerrero, *Chem. Eur. J.*, 2020, **26**, 11307–11315.

[37] A. Tlahuext-Aca, M. N. Hopkinson, C. G. Daniliuc and F. Glorius, *Chem. Eur. J.*, 2016, **22**, 11587–11592.

[38] G. Albertin, S. Antoniutti, M. Bortoluzzi, J. Castro-Fojo and S. Garcia-Fontán, *Inorg. Chem.*, 2004, **43**, 4511–4522.

[39] Á. Vivancos, D. Bautista and P. González-Herrero, *Chem. Eur. J.*, 2019, **25**, 6014–6025.

[40] S. W. Thomas, K. Venkatesan, P. Müller and T. M. Swager, *J. Am. Chem. Soc.*, 2006, **128**, 16641–16648.

[41] B. Rosenberg, L. Van Camp and T. Krigas, *Nature*, 1965, **205**, 698–699.

[42] D. Gibson, *Dalton Trans.*, 2016, **45**, 12983–12991.

[43] F. Reeßing and W. Szymanski, *Curr. Med. Chem.*, 2018, **24**, year.

[44] G. Canil, S. Braccini, T. Marzo, L. Marchetti, A. Pratesi, T. Biver, T. Funaioli, F. Chiellini, J. D. Hoeschele and C. Gabbiani, *Dalton Trans.*, 2019, **48**, 10933–10944.

[45] M. T. Walden, *PhD Thesis*, Durham University, 2018.

[46] G. Freeman, *PhD Thesis*, Durham University, 2014.

[47] L. Murphy, *PhD Thesis*, Durham University, 2010.

[48] N. Miyaura and A. Suzuki, *Chem. Rev.*, 1995, **95**, 2457.

[49] M. Mydlak, M. Mauro, F. Polo, M. Felicetti, J. Leonhardt, G. Diener, L. De Cola and C. A. Strassert, *Chem. Mater.*, 2011, **23**, 3659–3667.

[50] D. J. Cárdenas, A. M. Echavarren and M. C. Ramírez De Arellano, *Organometallics*, 1999, **18**, 3337–3341.

[51] S. Develay and J. A. G. Williams, *Dalton Trans.*, 2008, 4562–4564.

[52] R. Muñoz-Rodríguez, E. Buñuel, J. A. G. Williams and D. J. Cárdenas, *Chem. Commun.*, 2012, **48**, 5980–5982.

[53] P. Pander, M. T. Walden, R. J. Salthouse, A. Sil, D. S. Yufit, F. B. Dias and J. A. G. Williams, *J. Mater. Chem. C*, 2023, **11**, 15335–15346.

[54] A. J. Wilkinson, H. Puschmann, J. A. K. Howard, C. E. Foster and J. A. G. Williams, *Inorg. Chem.*, 2006, **45**, 86858699.

[55] P. Brulatti, R. J. Gildea, J. A. Howard, V. Fattori, M. Cocchi and J. A. G. Williams, *Inorg. Chem.*, 2012, **51**, 3813–3826.

[56] E. W. Abel, K. G. Orrell, A. G. Osborne, H. M. Pain and V. Šik, *J. Chem. Soc., Dalton Trans.*, 1994, 111–116.

[57] K. L. Garner, L. F. Parkes, J. D. Piper and J. A. G. Williams, *Inorg. Chem.*, 2010,

49, 476–487.

[58] M. Abrahamsson, M. Jäger, T. O. Sterman, L. Eriksson, P. Persson, H.-C. Becker, O. Johansson and L. Hammarström, *J. Am. Chem. Soc.*, 2006, **128**, 12616–12617.

[59] J.-R. Jiménez, B. Doistau, C. M. Cruz, C. Besnard, J. M. Cuerva, A. G. Campaña and C. Piguet, *J. Am. Chem. Soc.*, 2019, **141**, 13244–13252.

[60] S. D. Taylor, V. M. Shingade, R. Muvirimi, S. D. Hicks, J. A. Krause and W. B. Connick, *Inorg. Chem.*, 2019, **58**, 16364–16371.

[61] J. K. Stille, *Angew. Chem. Int. Ed.*, 1986, **25**, 508–524.

[62] A. F. Littke and G. C. Fu, *Angew. Chem. Int. Ed.*, 2002, **41**, 4176–4211.

[63] K. Billingsley and S. L. Buchwald, *Journal of the American Chemical Society*, 2007, **129**, 3358–3366.

[64] A. K. Sharma, K. Gowdahalli, J. Krzeminski and S. Amin, *J. Org. Chem.*, 2007, **72**, 8987–8989.

[65] E. C. Constable, R. P. Henney, T. A. Leese and D. A. Tocher, *J. Chem. Soc., Dalton Trans.*, 1990, 443–449.

[66] S. R. Whitfield and M. S. Sanford, *Organometallics*, 2008, **27**, 1683–1689.

[67] T. G. Appleton and J. R. Hall, *Inorg. Chem.*, 1971, **10**, 1717–1725.

[68] L. M. Pregosin, P. S.; Omura, H.; Venanzi, *J. Am. Chem. Soc.*, 1973, **95**, 2047–2048.

[69] K. J. Arm and J. A. G. Williams, *Chem. Commun.*, 2005, 230–232.

[70] T. Yutaka, S. Obara, S. Ogawa, K. Nozaki, N. Ikeda, T. Ohno, Y. Ishii, K. Sakai and M. A. Haga, *Inorg. Chem.*, 2005, **44**, 4737–4746.

[71] C.-W. Chan, Luk-Ki Cheng and C.-M. Che, *Coord. Chem. Rev.*, 1994, **132**, 87–97.

[72] D. N. Kozhevnikov, V. N. Kozhevnikov, M. Z. Shafikov, A. M. Prokhorov, D. W. Bruce and J. A. G. Williams, *Inorg. Chem.*, 2011, **50**, 3804–3815.

[73] S. J. Farley, D. L. Rochester, A. L. Thompson, J. A. Howard and J. A. G. Williams, *Inorg. Chem.*, 2005, **44**, 9690–9703.

[74] W. A. Tarran, G. R. Freeman, L. Murphy, A. M. Benham, R. Kataky and J. A. Williams, *Inorg. Chem.*, 2014, **53**, 5738–5749.

[75] R. J. Salthouse, A. Sil, L. F. Gildea, D. S. Yufit and J. A. G. Williams, *Inorg. Chem.*, 2023, **62**, 12356–12371.

[76] D. N. Kozhevnikov, V. N. Kozhevnikov, M. Z. Shafikov, A. M. Prokhorov, D. W. Bruce and J. A. Williams, *Inorg. Chem.*, 2011, **50**, 3804–3815.

[77] A. M. Bünzli, E. C. Constable, C. E. Housecroft, A. Prescimone, J. A. Zampese, G. Longo, L. Gil-Escrig, A. Pertegás, E. Ortí and H. J. Bolink, *Chem. Sci.*, 2015, **6**, 2843–2852.

[78] E. V. Puttock, M. T. Walden and J. A. G. Williams, *Coord. Chem. Rev.*, 2018, **367**, 127–162.

[79] M. Z. Shafikov, R. Daniels, P. Pander, F. B. Dias, J. A. G. Williams and V. N. Kozhevnikov, *ACS Appl. Mater. Interfaces*, 2019, **11**, 8182–8193.

[80] M. Z. Shafikov, P. Pander, A. V. Zaytsev, R. Daniels, R. Martinscroft, F. B. Dias, J. A. G. Williams and V. N. Kozhevnikov, *J. Mater. Chem*, 2021, **9**, 127–135.

[81] M. Z. Shafikov, A. V. Zaytsev and V. N. Kozhevnikov, *Inorg. Chem.*, 2024, **63**, 1317–1327.

[82] R. E. Daniels, S. Culham, M. Hunter, M. C. Durrant, M. R. Probert, W. Clegg, J. A. G. Williams and V. N. Kozhevnikov, *Dalton Trans.*, 2016, **45**, 6949–6962.

[83] P. H. Lanoë, C. M. Tong, R. W. Harrington, M. R. Probert, W. Clegg, J. A. G. Williams and V. N. Kozhevnikov, *Chem. Commun.*, 2014, **50**, 6831–6834.

[84] M. Z. Shafikov, R. Martinscroft, C. Hodgson, A. Hayer, A. Auch and V. N. Kozhevnikov, *Inorg. Chem.*, 2021, **60**, 1780–1789.

[85] E. V. Puttock, A. Sil, D. S. Yufit and J. A. G. Williams, *Dalton Trans.*, 2020, **49**, 10463–10476.

[86] Z. Guo, S. M. Yiu and M. C. Chan, *Chem. Eur. J.*, 2013, **19**, 8937–8947.

[87] E. A. Katlenok, A. A. Zolotarev and K. P. Balashev, *Russ. J. Gen. Chem.*, 2014, **84**, 1593–1598.

[88] P. Pander, A. V. Zaytsev, A. Sil, J. A. G. Williams, P. H. Lanoe, V. N. Kozhevnikov and F. B. Dias, *J. Mater. Chem. C*, 2021, **9**, 10276–10287.

[89] E. V. Puttock, *Ph.D. thesis*, 2017.

[90] P. Pander, A. V. Zaytsev, A. Sil, J. A. G. Williams, V. N. Kozhevnikov and F. B. Dias, *J. Mater. Chem. C*, 2022, **10**, 4851–4860.

[91] D. A. Vezzu, J. C. Deaton, J. S. Jones, L. Bartolotti, C. F. Harris, A. P. Marchetti, M. Kondakova, R. D. Pike and S. Huo, *Inorg. Chem.*, 2010, **49**, 5107–5119.

[92] S. Huo, C. F. Harris, D. A. Vezzu, J. P. Gagnier, M. E. Smith, R. D. Pike and Y. Li, *Polyhedron*, 2013, **52**, 1030–1040.

[93] A. I. Solomatina, E. E. Galenko, D. O. Kozina, A. A. Kalinichev, V. A. Baigildin, N. A. Prudovskaya, J. R. Shakirova, A. F. Khlebnikov, V. V. Porsev, R. A. Evarestov and S. P. Tunik, *Chem. Eur. J.*, 2022, **28**, 27–29.

[94] C. Wu, Y. Zhang, J. Miao, K. Li, W. Zhu and C. Yang, *Chin. Chem. Lett.*, 2023, **34**, 107445.

[95] L. Wang, J. Miao, Y. Zhang, C. Wu, H. Huang, X. Wang and C. Yang, *Adv. Mater.*, 2023, **35**, 1–9.

[96] K. Feng, C. Zuniga, Y. D. Zhang, D. Kim, S. Barlow, S. R. Marder, J. L. Brédas and M. Weck, *Macromolecules*, 2009, **42**, 6855–6864.

[97] K. Y. Liao, C. W. Hsu, Y. Chi, M. K. Hsu, S. W. Wu, C. H. Chang, S. H. Liu, G. H. Lee, P. T. Chou, Y. Hu and N. Robertson, *Inorg. Chem.*, 2015, **54**, 4029–4038.

[98] X. C. Hang, T. Fleetham, E. Turner, J. Brooks and J. Li, *Angew. Chem. Int. Ed.*, 2013, **52**, 6753–6756.

[99] T. Fleetham, G. Li, L. Wen and J. Li, *Adv. Mater.*, 2014, **26**, 7116–7121.

[100] T. Fleetham, L. Huang and J. Li, *Adv. Funct. Mater.*, 2014, **24**, 6066–6073.

[101] G. E. Norby, C. D. Park, B. O'Brien, G. Li, L. Huang and J. Li, *Org. Electron.*,

2016, **37**, 163–168.

[102] M. A. Soto, V. Carta, R. J. Andrews, M. T. Chaudhry and M. J. MacLachlan, *Angew. Chem. Int. Ed.*, 2020, **59**, 10348–10352.

[103] M. A. Soto, V. Carta, M. T. Cano, R. J. Andrews, B. O. Patrick and M. J. MacLachlan, *Inorg. Chem.*, 2022, **61**, 2999–3006.

[104] M. A. Soto, M. T. Chaudhry, G. K. Matharu, F. Lelj and M. J. MacLachlan, *Angew. Chem. Int. Ed.*, 2023, **62**, 1–7.

[105] R. J. Ortiz, J. D. Braun, J. A. G. Williams and D. E. Herbert, *Inorg. Chem.*, 2021, **60**, 16881–16894.

[106] F. Mongin, A.-S. Rebstock, F. Trécourt, Q. Guy and F. Marsais, *J. Org. Chem.*, 2004, **69**, 6766–6771.

[107] M. A. Soto, V. Carta, R. J. Andrews, M. T. Chaudhry and M. J. MacLachlan, *Angew. Chem. Int. Ed.*, 2020, **59**, 10348–10352.

[108] A. Santoro, M. Wegrzyn, A. C. Whitwood, B. Donnio and D. W. Bruce, *J. Am. Chem. Soc.*, 2010, **132**, 10689–10691.

[109] E. Anger, M. Rudolph, L. Norel, S. Zrig, C. Shen, N. Vanthuyne, L. Toupet, J. A. G. Williams, C. Roussel, J. Autschbach, J. Crassous and R. Réau, *Chem. Eur. J.*, 2011, **17**, 14178–14198.

[110] M. A. Bennett, S. K. Bhargava, A. M. Bond, A. J. Edwards, S. X. Guo, S. H. Privér, A. D. Rae and A. C. Willis, *Inorg. Chem.*, 2004, **43**, 7752–7763.

[111] M. A. Bennett, S. K. Bhargava, E. C. C. Cheng, W. H. Lam, T. K. M. Lee, S. H. Privér, J. Wagler, A. C. Willis and V. W. W. Yam, *J. Am. Chem. Soc.*, 2010, **132**, 7094–7103.

[112] K. Suzuki, A. Kobayashi, S. Kaneko, K. Takehira, T. Yoshihara, H. Ishida, Y. Shiina, S. Oishi and S. Tobita, *Phys. Chem. Chem. Phys.*, 2009, **11**, 9850–9860.

[113] F. Neese, *WIREs Comput. Mol. Sci.*, 2018, **8**, e1327.

[114] F. Neese, *WIREs Comput. Mol. Sci.*, 2012, **2**, 73–78.

[115] F. Neese, *WIREs Comput Mol Sci*, 2022, **12**, e1606.

[116] S. Lehtola, C. Steigemann, M. J. T. Oliveira and M. A. L. Marques, *SoftwareX*, 2018, **7**, 1–5.

[117] E. F. Pettersen, T. D. Goddard, C. C. Huang, E. C. Meng, G. S. Couch, T. I. Croll, J. H. Morris and T. E. Ferrin, *Protein Sci.*, 2021, **30**, 70–82.

[118] T. D. Goddard, C. C. Huang, E. C. Meng, E. F. Pettersen, G. S. Couch, J. H. Morris and T. E. Ferrin, *Protein Sci.*, 2018, **27**, 14–25.

[119] *Avogadro: an open-source molecular builder and visualization tool. Version 1.2.0*, `https://avogadro.cc`.

[120] M. D. Hanwell, D. E. Curtis, D. C. Lonie, T. Vandermeersch, E. Zurek and G. R. Hutchison, *J. Cheminform.*, 2012, **4**, 17.

[121] A. D. Becke, *J. Chem. Phys.*, 1993, **98**, 5648–5652.

[122] P. J. Stephens, F. J. Devlin, C. F. Chabalowski and M. J. Frisch, *J. Phys. Chem.*, 1994, **98**, 11623–11627.

[123] F. Weigend and R. Ahlrichs, *Phys. Chem. Chem. Phys.*, 2005, **7**, 3297–3305.

[124] A. D. Becke, *Phys. Rev. A*, 1988, **38**, 3098–3100.

[125] A. Hellweg, C. Hättig, S. Höfener and W. Klopper, *Theor. Chem. Acc.*, 2007, **117**, 587–597.

[126] F. Weigend, *Phys. Chem. Chem. Phys.*, 2006, **8**, 1057–1065.

[127] F. Neese, F. Wennmohs, A. Hansen and U. Becker, *Chem. Phys.*, 2009, **356**, 98–109.

[128] R. Izsák and F. Neese, *J. Chem. Phys.*, 2011, **135**, 144105.

[129] S. Grimme, S. Ehrlich and L. Goerigk, *J. Comput. Chem.*, 2011, **32**, 1456–1465.

[130] S. Grimme, J. Antony, S. Ehrlich and H. Krieg, *J. Chem. Phys.*, 2010, **132**, 154104.

[131] S. Stoccoro, G. Alesso, M. A. Cinellu, G. Minghetti, A. Zucca, M. Manassero

and C. Manassero, *Dalton Trans.*, 2009, 3467–3477.

[132] D. J. Cárdenas, A. M. Echavarren and M. C. Ramírez De Arellano, *Organometallics*, 1999, **18**, 3337–3341.

[133] D. A. Vezzu, Q. Lu, Y. H. Chen and S. Huo, *J. Inorg. Biochem.*, 2014, **134**, 49–56.

[134] J. M. Kelly, C. Long, C. M. O'Connell, J. G. Vos and A. H. Tinnemans, *Inorg. Chem.*, 1983, **22**, 2818–2824.

[135] Y. Yoshinaga, T. Yamamoto and M. Suginome, *Angew. Chem. Int. Ed.*, 2020, **59**, 7251–7255.

[136] L. J. Nurkkala, R. O. Steen, H. K. Friberg, J. A. Häggström, P. V. Bernhardt, M. J. Riley and S. J. Dunne, *Eur. J. Inorg. Chem.*, 2008, 4101–4110.

[137] W. C. Chen, Y. C. Hsu, W. C. Shih, C. Y. Lee, W. H. Chuang, Y. F. Tsai, P. P. Y. Chen and T. G. Ong, *Chem. Commun.*, 2012, **48**, 6702–6704.

[138] H. Zhao, J. Shen, J. Guo, R. Yea and H. Zeng, *Chem. Commun.*, 2013, **49**, 2323–2325.

[139] K. T. Hylland, I. L. Schmidtke, D. S. Wragg, A. Nova and M. Tilset, *Dalton Trans.*, 2022, **51**, 5082–5097.

[140] R. Romeo, M. R. Plutino, L. M. Scolaro, S. Stoccoro and G. Minghetti, *Inorg. Chem.*, 2000, **39**, 4749–4755.

[141] W. Lu, V. A. Roy and C. M. Che, *Chem. Commun.*, 2006, 3972–3974.

[142] P. Gros, C. Viney and Y. Fort, *Synlett*, 2002, 628–630.

[143] T. N. Y. Hoang, M. Humbert-Droz, T. Dutronc, L. Guénée, C. Besnard and C. Piguet, *Inorg. Chem.*, 2013, **52**, 5570–5580.

[144] P. W. Antoni, C. Golz and M. M. Hansmann, *Angew. Chem. Int. Ed.*, 2022, **61**, e202203064.

[145] V. Blasczak, M. McKinnon, L. Suntrup, N. A. Aminudin, B. Reed, S. Groysman, M. Z. Ertem, D. C. Grills and J. Rochford, *Inorg. Chem.*, 2022, **61**, 15784–

15800.

[146] B. Wang, F. Liang, H. Hu, Y. Liu, Z. Kang, L. S. Liao and J. Fan, *J. Mater. Chem*, 2015, **3**, 8212–8218.

Appendix

Crystal structure data

Chapter 2

Crystal data and structure refinement for Pt(dpyb)Cl

Identification code	20srv299
Empirical formula	$C_{16}H_{11}ClN_2Pt$
Formula weight	461.81
Temperature/K	120.0
Crystal system	monoclinic
Space group	C2/c
a/Å	10.4452(4)
b/Å	14.2233(6)
c/Å	8.9323(4)
α/°	90
β/ °	97.6940(10)
γ/ °	90
Volume/Å^3	1315.08(10)
Z	4
ρ_{calc}g/cm^3	2.332
μ/ mm^{-1}	10.861
F(000)	864.0
Crystal size/mm^3	0.08 $\times$ 0.04 $\times$ 0.02
Radiation	Mo Kα(λ = 0.71073)
2Θ range for data collection/ °	4.868 to 59.99
Index ranges	-14 $\leq$ h $\leq$ 14, -20 $\leq$ k $\leq$20, -12 $\leq$ l $\leq$ 12
Reflections collected	11325
Independent reflections	1924 [R_{int} = 0.0454, R_{sigma} = 0.0302]
Data/restraints/parameters	1924/0/93
Goodness-of-fit on F^2	1.073
Final R indexes [I$\geq$2σ(I)]	R_1 = 0.0211, wR_2 = 0.0458
Final R indexes [all data]	R_1 = 0.0244, wR_2 = 0.0469
Largest diff. peak/hole / e Å^{-3}	1.36/-1.06

Crystal data and structure refinement for $Pt(dpyb)Cl_3$

Identification code	21srv009
Empirical formula	$C_{16}H_{11}Cl_3N_2Pt$
Formula weight	532.71
Temperature/K	120.0
Crystal system	monoclinic
Space group	P21/n
a/Å	8.2237(3)
b/Å	14.2988(5)
c/Å	13.6888(5)
$\alpha/^\circ$	90
$\beta/^\circ$	104.9550(10)
$\gamma/^\circ$	90
Volume/Å^3	1555.13(10)
Z	4
ρ_{calc}g/cm^3	2.275
μ/ mm^{-1}	9.533
F(000)	1000.0
Crystal size/mm^3	$0.11 \times 0.1 \times 0.03$
Radiation	Mo Kα(λ = 0.71073)
2Θ range for data collection/ $^\circ$	4.196 to 59.996
Index ranges	$-11 \leq h \leq 11$, $-20 \leq k \leq 20$, $-19 \leq l \leq 19$
Reflections collected	27134
Independent reflections	4527 [R_{int} = 0.0316, R_{sigma} = 0.0224]
Data/restraints/parameters	4527/0/199
Goodness-of-fit on F^2	1.065
Final R indexes [$I \geq 2\sigma(I)$]	R_1 = 0.0176, wR_2 = 0.0343
Final R indexes [all data]	R_1 = 0.0236, wR_2 = 0.0359
Largest diff. peak/hole / e Å^{-3}	0.77/-0.83

Crystal data and structure refinement for [Pt(dpyb)(*N*-CH_3CN)]$^+$

Identification code	21srv028
Empirical formula	$C_{18}H_{14}F_6N_3PPt$ x 0.25 CH_2Cl_2
Formula weight	633.61
Temperature/K	120.0
Crystal system	monoclinic
Space group	P21/c
a/Å	6.7209(4)
b/Å	22.4679(14)
c/Å	25.6208(15)
α/°	90
β/ °	92.089(2)
γ/ °	90
Volume/Å^3	3866.3(4)
Z	8
ρ_{calc}g/cm^3	2.177
μ/ mm^{-1}	7.477
F(000)	2404.0
Crystal size/mm^3	0.19 $\times$ 0.04 $\times$ 0.01
Radiation	Mo Kα(λ = 0.71073)
2Θ range for data collection/ °	3.96 to 57.992
Index ranges	$-9 \leq h \leq 9$, $-30 \leq k \leq 30$, $-34 \leq l \leq 34$
Reflections collected	82719
Independent reflections	10264 [R_{int} = 0.1397, R_{sigma} = 0.0873]
Data/restraints/parameters	10264/114/588
Goodness-of-fit on F^2	1.113
Final R indexes [I$\geq$2σ(I)]	R_1 = 0.0767, wR_2 = 0.1257
Final R indexes [all data]	R_1 = 0.1176, wR_2 = 0.1388
Largest diff. peak/hole / e Å^{-3}	4.40/-2.64

Crystal data and structure refinement for [Pt(dpyb)(*N*-HL^7)]$^+$

Identification code	21srv013
Empirical formula	$C_{33}H_{25}Cl_2F_6N_4PPt$
Formula weight	888.53
Temperature/K	120.0
Crystal system	triclinic
Space group	P-1
a/Å	9.8456(4)
b/Å	12.2628(4)
c/Å	14.7246(5)
α/°	109.2870(10)
β/ °	96.4410(10)
γ/ °	109.8480(10)
Volume/Å^3	1527.10(10)
Z	2
ρ_{calc}g/cm^3	1.932
μ/ mm^{-1}	4.891
F(000)	864.0
Crystal size/mm^3	0.19 × 0.11 × 0.05
Radiation	Mo Kα(λ = 0.71073)
2Θ range for data collection/ °	4.546 to 59.996
Index ranges	-13 ≤ h ≤ 13, -17 ≤ k ≤ 17, -20 ≤ l ≤ 20
Reflections collected	36821
Independent reflections	8865 [R_{int} = 0.0283, R_{sigma} = 0.0247]
Data/restraints/parameters	8865/0/424
Goodness-of-fit on F^2	1.043
Final R indexes [I≥2σ(I)]	R_1 = 0.0177, wR_2 = 0.0402
Final R indexes [all data]	R_1 = 0.0193, wR_2 = 0.0407
Largest diff. peak/hole / e Å^{-3}	0.79/-0.79

Crystal data and structure refinement for $[\{Pt(dpyb)\}_3L^3]^{2+}$

Identification code	21srv018
Empirical formula	$C_{62}H_{44}F_{12}N_{10}OP_2Pt_3$ x 2 PF_6 x 2.25 CH_2Cl_2
Formula weight	2011.36
Temperature/K	120.0
Crystal system	monoclinic
Space group	C2/c
a/Å	36.7956(9)
b/Å	14.9943(4)
c/Å	30.2648(11)
α/°	90
β/ °	126.6340(10)
γ/ °	90
Volume/Å^3	13399.4(7)
Z	8
ρ_{calc}g/cm^3	1.994
μ/ mm^{-1}	6.561
F(000)	7684.0
Crystal size/mm^3	0.28 $\times$ 0.14 $\times$ 0.03
Radiation	Mo Kα(λ = 0.71073)
2Θ range for data collection/ °	3.874 to 59.998
Index ranges	-51 $\leq$ h $\leq$ 51, -21 $\leq$ k $\leq$ 21, -42 $\leq$ l $\leq$ 42
Reflections collected	160081
Independent reflections	19506 [R_{int} = 0.0524, R_{sigma} = 0.0314]
Data/restraints/parameters	19506/19/875
Goodness-of-fit on F^2	1.084
Final R indexes [I$\geq$2σ(I)]	R_1 = 0.0397, wR_2 = 0.0914
Final R indexes [all data]	R_1 = 0.0597, wR_2 = 0.1045
Largest diff. peak/hole / e Å^{-3}	2.40/-1.46

Crystal data and structure refinement for $[Pt(dpyb)L^3Cl]^+$

Identification code	21srv097
Empirical formula	$C_{31}H_{24}Cl_3F_6N_6OPPt$
Formula weight	942.97
Temperature/K	120.0
Crystal system	triclinic
Space group	P-1
a/Å	10.3306(5)
b/Å	12.7476(6)
c/Å	13.3490(6)
α/°	100.457(2)
β/ °	107.310(2)
γ/ °	90.091(2)
Volume/Å^3	1647.54(14)
Z	2
ρ_{calc}g/cm^3	1.901
μ/ mm^{-1}	4.622
F(000)	916.0
Crystal size/mm^3	0.24 × 0.02 × 0.01
Radiation	Mo Kα(λ = 0.71073)
2Θ range for data collection/ °	4.138 to 59.996
Index ranges	-14 ≤ h ≤ 14, -17 ≤ k ≤ 17, -18 ≤ l ≤ 18
Reflections collected	39507
Independent reflections	9591 [R_{int} = 0.0635, R_{sigma} = 0.0545]
Data/restraints/parameters	9591/0/443
Goodness-of-fit on F^2	1.064
Final R indexes [I≥2σ(I)]	R_1 = 0.0290, wR_2 = 0.0606
Final R indexes [all data]	R_1 = 0.0347, wR_2 = 0.0625
Largest diff. peak/hole / e Å^{-3}	1.65/-1.14

Crystal data and structure refinement for $[Pt(dpyb)L^6Cl]^+$

Identification code	21srv208
Empirical formula	$C_{47}H_{51}ClF_6N_6OPPt$
Formula weight	1091.44
Temperature/K	120.0
Crystal system	triclinic
Space group	P-1
a/Å	11.6608(6)
b/Å	13.1573(7)
c/Å	17.1026(9)
α/°	95.332(2)
β/ °	103.245(2)
γ/ °	111.7660(10)
Volume/Å^3	2325.7(2)
Z	2
ρ_{calc}g/cm^3	1.559
μ/ mm^{-1}	3.175
F(000)	1094.0
Crystal size/mm^3	0.03 $\times$ 0.01 $\times$ 0.001
Radiation	Mo Kα(λ = 0.71073)
2Θ range for data collection/ °	4.006 to 54
Index ranges	-14 $\leq$ h $\leq$ 14, -16 $\leq$ k $\leq$ 16, -21 $\leq$ l $\leq$ 21
Reflections collected	40773
Independent reflections	10147 [R_{int} = 0.1095, R_{sigma} = 0.1165]
Data/restraints/parameters	10147/37/583
Goodness-of-fit on F^2	1.002
Final R indexes [I$\geq$2σ(I)]	R_1 = 0.0547, wR_2 = 0.1022
Final R indexes [all data]	R_1 = 0.0925, wR_2 = 0.1166
Largest diff. peak/hole / e Å^{-3}	2.25/-1.20

Crystal data and structure refinement for $[Pt(dpyb)(bpy)Cl]^{2+}$

Identification code	21srv188
Empirical formula	$C_{28}H_{22}ClF_{12}N_5P_2Pt$
Formula weight	948.98
Temperature/K	120.0
Crystal system	monoclinic
Space group	P21/n
a/Å	17.4548(6)
b/Å	8.5700(3)
c/Å	21.2471(7)
α/°	90
β/ °	100.7950(10)
γ/ °	90
Volume/Å^3	3122.06(18)
Z	4
ρ_{calc}g/cm^3	2.019
μ/ mm^{-1}	4.785
F(000)	1832.0
Crystal size/mm^3	0.12 × 0.08 × 0.005
Radiation	Mo Kα(λ = 0.71073)
2Θ range for data collection/ °	4.752 to 59.996
Index ranges	-24 ≤ h ≤ 24, -12 ≤ k ≤ 11, -29 ≤ l ≤ 29
Reflections collected	53438
Independent reflections	9101 [R_{int} = 0.0588, R_{sigma} = 0.0429]
Data/restraints/parameters	9101/0/443
Goodness-of-fit on F^2	1.085
Final R indexes [I≥2σ(I)]	R_1 = 0.0380, wR_2 = 0.0586
Final R indexes [all data]	R_1 = 0.0562, wR_2 = 0.0626
Largest diff. peak/hole / e Å^{-3}	1.18/-2.36

Crystal data and structure refinement for [Pt(dpyb)(*NN*-tpy)Cl]$^{2+}$

Identification code	21srv039
Empirical formula	$C_{31}H_{22}ClF_{12}N_5P_2Pt$
Formula weight	985.01
Temperature/K	200.0
Crystal system	triclinic
Space group	P-1
a/Å	9.1893(3)
b/Å	14.0243(4)
c/Å	14.1376(4)
α/°	91.7730(10)
β/ °	108.5000(10)
γ/ °	104.9990(10)
Volume/Å^3	1656.18(9)
Z	2
ρ_{calc}g/cm^3	1.975
μ/ mm^{-1}	4.515
F(000)	952.0
Crystal size/mm^3	0.21 $\times$ 0.19 $\times$ 0.01
Radiation	Mo Kα(λ = 0.71073)
2Θ range for data collection/ °	4.804 to 59.994
Index ranges	-12 $\leq$ h $\leq$ 12, -19 $\leq$ k $\leq$ 19, -19 $\leq$ l $\leq$ 19
Reflections collected	39800
Independent reflections	9589 [R_{int} = 0.0336, R_{sigma} = 0.0306]
Data/restraints/parameters	9589/66/462
Goodness-of-fit on F^2	1.028
Final R indexes [I$\geq$2σ(I)]	R_1 = 0.0334, wR_2 = 0.0849
Final R indexes [all data]	R_1 = 0.0371, wR_2 = 0.0872
Largest diff. peak/hole / e Å^{-3}	1.79/-1.23

Crystal data and structure refinement for $[Pt(dpyb)(azbpy)]^{3+}$

Identification code	21srv247
Empirical formula	$C_{36.75}H_{30.75}F_{18}N_6O_{1.25}P_3Pt$
Formula weight	1206.42
Temperature/K	296.15
Crystal system	triclinic
Space group	P-1
a/Å	12.3894(3)
b/Å	18.8217(5)
c/Å	22.3306(6)
α/°	69.0880(10)
β/ °	74.4130(10)
γ/ °	79.1750(10)
Volume/Å^3	4660.9(2)
Z	4
ρ_{calc}g/cm^3	1.719
μ/ mm^{-1}	3.223
F(000)	2353.0
Crystal size/mm^3	0.1 $\times$ 0.06 $\times$ 0.04
Radiation	Mo Kα(λ = 0.71073)
2Θ range for data collection/ °	4.336 to 55
Index ranges	-16 $\leq$ h $\leq$ 16, -24 $\leq$ k $\leq$ 24, -29 $\leq$ l $\leq$ 29
Reflections collected	96068
Independent reflections	21360 [R_{int} = 0.0550, R_{sigma} = 0.0517]
Data/restraints/parameters	21360/663/1282
Goodness-of-fit on F^2	1.086
Final R indexes [I$\geq$2σ(I)]	R_1 = 0.0707, wR_2 = 0.1758
Final R indexes [all data]	R_1 = 0.0934, wR_2 = 0.1884
Largest diff. peak/hole / e Å^{-3}	3.00/-2.38

Crystal data and structure refinement for $[Pt(dpyb)(tpy)]^{3+}$

Identification code	21srv251
Empirical formula	$C_{31}H_{22}F_{18}N_5P_3Pt$
Formula weight	1094.53
Temperature/K	120.0
Crystal system	monoclinic
Space group	P21/c
a/Å	19.2463(7)
b/Å	16.4628(6)
c/Å	11.0670(4)
$\alpha/^\circ$	90
$\beta/^\circ$	98.442(2)
$\gamma/^\circ$	90
Volume/Å^3	3468.6(2)
Z	4
ρ_{calc}g/cm^3	2.096
μ/ mm^{-1}	4.316
F(000)	2112.0
Crystal size/mm^3	0.078 × 0.065 × 0.044
Radiation	Mo Kα(λ = 0.71073)
2Θ range for data collection/ $^\circ$	4.278 to 59.996
Index ranges	$-27 \leq h \leq 26$, $0 \leq k \leq 23$, $0 \leq l \leq 15$
Reflections collected	14263
Independent reflections	14263 [R_{int} = 0.0900, R_{sigma} = 0.0776]
Data/restraints/parameters	14263/222/593
Goodness-of-fit on F^2	1.029
Final R indexes [$I \geq 2\sigma(I)$]	R_1 = 0.0499, wR_2 = 0.0972
Final R indexes [all data]	R_1 = 0.0763, wR_2 = 0.1045
Largest diff. peak/hole / e Å^{-3}	1.44/-1.56

Crystal data and structure refinement for $[Pt(dpyb)(HL^7)Cl]^{2+}$

Identification code	21srv311
Empirical formula	$C_{37}H_{29}ClF_6N_4O_7PtS_2$
Formula weight	1050.30
Temperature/K	120.0
Crystal system	monoclinic
Space group	P21/n
a/Å	14.8499(11)
b/Å	12.5801(10)
c/Å	20.5936(16)
α/°	90
β/ °	90.020(3)
γ/ °	90
Volume/Å^3	3847.2(5)
Z	4
ρ_{calc}g/cm^3	1.813
μ/ mm^{-1}	3.909
F(000)	2064.0
Crystal size/mm^3	0.26 × 0.05 × 0.04
Radiation	Mo Kα(λ = 0.71073)
2Θ range for data collection/ °	3.794 to 59.984
Index ranges	-20 ≤ h ≤ 20, -17 ≤ k ≤ 17, -28 ≤ l ≤ 28
Reflections collected	65339
Independent reflections	11186 [R_{int} = 0.0480, R_{sigma} = 0.0356]
Data/restraints/parameters	11186/0/525
Goodness-of-fit on F^2	1.029
Final R indexes [I≥2σ(I)]	R_1 = 0.0248, wR_2 = 0.0452
Final R indexes [all data]	R_1 = 0.0349, wR_2 = 0.0482
Largest diff. peak/hole / e Å^{-3}	0.70/-1.00

Crystal data and structure refinement for $[Pt(dpyb)(HL^7)Cl]^{2+}$

Identification code	21srv314
Empirical formula	$C_{32}H_{23}ClN_4Pt \times 2(O_3SCF_3) \times 0.35\ H_2O$
Formula weight	998.53
Temperature/K	120.0
Crystal system	triclinic
Space group	P-1
a/Å	9.8904(3)
b/Å	12.2240(3)
c/Å	28.9149(8)
α/°	90.0290(10)
β/ °	92.0690(10)
γ/ °	99.6740(10)
Volume/Å^3	3443.78(17)
Z	4
ρ_{calc}g/cm^3	1.926
μ/ mm^{-1}	4.361
F(000)	1950.0
Crystal size/mm^3	0.24 × 0.14 × 0.07
Radiation	Mo Kα(λ = 0.71073)
2Θ range for data collection/ °	1.41 to 60
Index ranges	-13 ≤ h ≤ 13, -17 ≤ k ≤ 17, -40 ≤ l ≤ 40
Reflections collected	59517
Independent reflections	19924 [R_{int} = 0.0330, R_{sigma} = 0.0400]
Data/restraints/parameters	19924/106/1066
Goodness-of-fit on F^2	1.194
Final R indexes [I≥2σ(I)]	R_1 = 0.0365, wR_2 = 0.0668
Final R indexes [all data]	R_1 = 0.0446, wR_2 = 0.0687
Largest diff. peak/hole / e Å^{-3}	0.96/-1.98

Crystal data and structure refinement for Pt(dpyb)Cl_2(*O*-PO_2F_2)

Identification code	21srv242
Empirical formula	$C_{16}H_{11}Cl_2F_2N_2O_2PPt$
Formula weight	598.23
Temperature/K	120.0
Crystal system	monoclinic
Space group	C2/c
a/Å	13.2663(4)
b/Å	10.6712(3)
c/Å	24.6213(7)
α/°	90
β/ °	100.9310(10)
γ/ °	90
Volume/Å^3	3422.33(17)
Z	8
ρ_{calc}g/cm^3	2.322
μ/ mm^{-1}	8.641
F(000)	2256.0
Crystal size/mm^3	0.09 × 0.04 × 0.02
Radiation	Mo Kα(λ = 0.71073)
2Θ range for data collection/ °	4.934 to 59.996
Index ranges	-18 ≤ h ≤ 18, -14 ≤ k ≤ 14, -34 ≤ l ≤ 34
Reflections collected	30227
Independent reflections	4955 [R_{int} = 0.0412, R_{sigma} = 0.0293]
Data/restraints/parameters	4955/0/235
Goodness-of-fit on F^2	1.094
Final R indexes [I≥2σ(I)]	R_1 = 0.0248, wR_2 = 0.0435
Final R indexes [all data]	R_1 = 0.0300, wR_2 = 0.0448
Largest diff. peak/hole / e Å^{-3}	0.96/-1.92

Chapter 3

Crystal data and structure refinement for PtL^7Cl_3

Identification code	21srv196
Empirical formula	$C_{16}H_{11}Cl_3N_2Pt$
Formula weight	532.71
Temperature/K	120.0
Crystal system	monoclinic
Space group	P21/n
a/Å	8.2970(2)
b/Å	14.3443(4)
c/Å	13.5758(3)
α/°	90
β/ °	105.3560(10)
γ/ °	90
Volume/Å^3	1558.04(7)
Z	4
ρ_{calc}g/cm^3	2.271
μ/ mm^{-1}	9.516
F(000)	1000.0
Crystal size/mm^3	0.18 $\times$ 0.09 $\times$ 0.04
Radiation	Mo Kα(λ = 0.71073)
2Θ range for data collection/ °	4.212 to 59.994
Index ranges	-11 $\leq$ h $\leq$ 11, -20 $\leq$ k $\leq$ 20, -19 $\leq$ l $\leq$ 19
Reflections collected	26205
Independent reflections	4517 [R_{int} = 0.0264, R_{sigma} = 0.0186]
Data/restraints/parameters	4517/0/199
Goodness-of-fit on F^2	1.082
Final R indexes [I$\geq$2σ(I)]	R_1 = 0.0140, wR_2 = 0.0292
Final R indexes [all data]	R_1 = 0.0166, wR_2 = 0.0300
Largest diff. peak/hole / e Å^{-3}	0.43/-0.60

Crystal data and structure refinement for PtL^9Cl

Identification code	21srv436
Empirical formula	$C_{18}H_{16}ClN_2O_{1.5}PtS_{0.5}$
Formula weight	530.90
Temperature/K	120.0
Crystal system	monoclinic
Space group	C2/c
a/Å	26.5322(6)
b/Å	8.0304(2)
c/Å	16.1422(4)
α/°	90
β/ °	108.4900(10)
γ/ °	90
Volume/Å^3	3261.78(14)
Z	8
ρ_{calc}g/cm^3	2.162
μ/ mm^{-1}	8.842
F(000)	2024.0
Crystal size/mm^3	0.14 × 0.08 × 0.06
Radiation	Mo Kα(λ= 0.71073)
2Θ range for data collection/ °	5.322 to 59.998
Index ranges	-37 ≤ h ≤ 37, -11 ≤ k ≤ 11, -22 ≤ l ≤ 22
Reflections collected	38081
Independent reflections	4738 [R_{int} = 0.0314, R_{sigma} = 0.0184]
Data/restraints/parameters	4738/2/238
Goodness-of-fit on F^2	1.040
Final R indexes [I≥2σ(I)]	R_1 = 0.0143, wR_2 = 0.0306
Final R indexes [all data]	R_1 = 0.0165, wR_2 = 0.0313
Largest diff. peak/hole / e Å^{-3}	0.69/-0.52

Crystal data and structure refinement for $PtL^{10}Cl$

Identification code	22srv085
Empirical formula	$C_{19}H_{18.5}Cl_3.5N_2O_2PtS$
Formula weight	658.08
Temperature/K	120.00
Crystal system	monoclinic
Space group	P21/n
a/Å	13.0190(3)
b/Å	7.7027(2)
c/Å	21.5171(6)
α/°	90
β/ °	93.4060(10)
γ/ °	90
Volume/Å^3	2153.95(10)
Z	4
ρ_{calc}g/cm^3	2.029
μ/ mm^{-1}	7.064
F(000)	1264.0
Crystal size/mm^3	0.08 × 0.07 × 0.01
Radiation	Mo Kα(λ = 0.71073)
2Θ range for data collection/ °	3.758 to 59.994
Index ranges	-18 ≤ h ≤ 18, -10 ≤ k ≤ 10, -30 ≤ l ≤ 30
Reflections collected	51957
Independent reflections	6276 [R_{int} = 0.0420, R_{sigma} = 0.0253]
Data/restraints/parameters	6276/0/266
Goodness-of-fit on F^2	1.301
Final R indexes [I≥2σ(I)]	R_1 = 0.0352, wR_2 = 0.0685
Final R indexes [all data]	R_1 = 0.0395, wR_2 = 0.0698
Largest diff. peak/hole / e Å^{-3}	2.31/-1.39

Crystal data and structure refinement for $PtL^{10Cl}Cl$

Identification code	22srv111
Empirical formula	$C_{17}H_{12}Cl_2N_2OPt$
Formula weight	526.28
Temperature/K	120.00
Crystal system	triclinic
Space group	P-1
a/Å	8.1312(5)
b/Å	9.7780(6)
c/Å	9.9408(6)
α/°	101.229(2)
β/ °	102.073(2)
γ/ °	90.519(2)
Volume/Å^3	757.06(8)
Z	2
ρ_{calc}g/cm^3	2.309
μ/ mm^{-1}	9.624
F(000)	496.0
Crystal size/mm^3	0.12 × 0.03 × 0.01
Radiation	Mo Kα(λ = 0.71073)
2Θ range for data collection/ °	4.252 to 59.992
Index ranges	-11 ≤ h ≤ 11, -13 ≤ k ≤ 13, -13 ≤ l ≤ 13
Reflections collected	16311
Independent reflections	4404 [R_{int} = 0.0433, R_{sigma} = 0.0449]
Data/restraints/parameters	4404/0/209
Goodness-of-fit on F^2	1.116
Final R indexes [I≥2σ(I)]	R_1 = 0.0392, wR_2 = 0.0775
Final R indexes [all data]	R_1 = 0.0454, wR_2 = 0.0795
Largest diff. peak/hole / e Å^{-3}	7.61/-2.34

Crystal data and structure refinement for $PtL^{13}Cl$

Identification code	21srv046
Empirical formula	$C_{20}H_{13}ClN_2Pt$
Formula weight	511.86
Temperature/K	120.0
Crystal system	orthorhombic
Space group	P212121
a/Å	7.0237(3)
b/Å	13.5522(5)
c/Å	16.3885(7)
α/°	90
β/ °	90
γ/ °	90
Volume/Å^3	1559.97(11)
Z	4
ρ_{calc}g/cm^3	2.179
μ/ mm^{-1}	9.168
F(000)	968.0
Crystal size/mm^3	0.06 × 0.02 × 0.01
Radiation	Mo Kα(λ = 0.71073)
2Θ range for data collection/ °	4.972 to 55
Index ranges	-9 ≤ h ≤ 9, -17 ≤ k ≤ 17, -21 ≤ l ≤ 21
Reflections collected	23405
Independent reflections	3576 [R_{int} = 0.0633, R_{sigma} = 0.0463]
Data/restraints/parameters	3576/6/217
Goodness-of-fit on F^2	1.099
Final R indexes [I≥2σ(I)]	R_1 = 0.0302, wR_2 = 0.0549
Final R indexes [all data]	R_1 = 0.0369, wR_2 = 0.0571
Largest diff. peak/hole / e Å^{-3}	0.98/-0.66
Flack parameter	-0.009(7)

Crystal data and structure refinement for PtL^8Cl_3

Identification code	21srv272
Empirical formula	$C_{17}H_{13}Cl_3.2N_2Pt$
Formula weight	553.82
Temperature/K	296.15
Crystal system	monoclinic
Space group	P21/n
a/Å	8.9671(2)
b/Å	25.1355(6)
c/Å	14.9470(4)
α/°	90
β/ °	91.3380(10)
γ/ °	90
Volume/Å^3	3368.02(14)
Z	8
ρ_{calc}g/cm^3	2.184
μ/ mm^{-1}	8.839
F(000)	2091.0
Crystal size/mm^3	0.1 $\times$ 0.05 $\times$ 0.02
Radiation	Mo Kα(λ = 0.71073)
2Θ range for data collection/ °	4.234 to 57.996
Index ranges	-12 $\leq$ h $\leq$ 12, -34 $\leq$ k $\leq$ 34, -20 $\leq$ l $\leq$ 20
Reflections collected	57444
Independent reflections	8945 [R_{int} = 0.0463, R_{sigma} = 0.0337]
Data/restraints/parameters	8945/0/435
Goodness-of-fit on F^2	1.205
Final R indexes [I$\geq$2σ(I)]	R_1 = 0.0572, wR_2 = 0.1060
Final R indexes [all data]	R_1 = 0.0664, wR_2 = 0.1092
Largest diff. peak/hole / e Å^{-3}	4.52/-3.37

Crystal data and structure refinement for PtL^9Cl_3

Identification code	21srv459
Empirical formula	$C_{17}H_{13}Cl_3N_2OPt$
Formula weight	562.73
Temperature/K	120.0
Crystal system	monoclinic
Space group	P21/n
a/Å	8.3128(2)
b/Å	14.3004(4)
c/Å	14.4137(4)
α/°	90
β/ °	94.5381(10)
γ/ °	90
Volume/Å^3	1708.08(8)
Z	4
ρ_{calc}g/cm^3	2.188
μ/ mm^{-1}	8.690
F(000)	1064.0
Crystal size/mm^3	0.11 $\times$ 0.06 $\times$ 0.01
Radiation	Mo Kα(λ = 0.71073)
2Θ range for data collection/ °	4.018 to 60
Index ranges	-11 $\leq$ h $\leq$ 11, -20 $\leq$ k $\leq$ 20, -20 $\leq$ l $\leq$ 20
Reflections collected	40074
Independent reflections	4977 [R_{int} = 0.0339, R_{sigma} = 0.0201]
Data/restraints/parameters	4977/0/218
Goodness-of-fit on F^2	1.043
Final R indexes [I$\geq$2σ(I)]	R_1 = 0.0180, wR_2 = 0.0371
Final R indexes [all data]	R_1 = 0.0231, wR_2 = 0.0388
Largest diff. peak/hole / e Å^{-3}	1.34/-0.58

Crystal data and structure refinement for $PtL^{9Cl}Cl_3$

Identification code	21srv410
Empirical formula	$C_{18}H_{15}Cl_4N_2O_{1.5}PtS_{0.5}$
Formula weight	636.24
Temperature/K	120.0
Crystal system	monoclinic
Space group	P21/n
a/Å	8.1467(2)
b/Å	18.5442(5)
c/Å	13.3755(4)
α/°	90
β/ °	103.8530(10)
γ/ °	90
Volume/Å^3	1961.91(9)
Z	4
ρ_{calc}g/cm^3	2.154
μ/ mm^{-1}	7.764
F(000)	1212.0
Crystal size/mm^3	0.15 × 0.03 × 0.01
Radiation	Mo Kα(λ= 0.71073)
2Θ range for data collection/ °	3.828 to 59.998
Index ranges	-11 ≤ h ≤ 11, -26 ≤ k ≤ 26, -18 ≤ l ≤ 18
Reflections collected	46848
Independent reflections	5712 [R_{int} = 0.0511, R_{sigma} = 0.0291]
Data/restraints/parameters	5712/12/254
Goodness-of-fit on F^2	1.055
Final R indexes [I≥2σ(I)]	R_1 = 0.0348, wR_2 = 0.0800
Final R indexes [all data]	R_1 = 0.0409, wR_2 = 0.0831
Largest diff. peak/hole / e Å^{-3}	2.96/-1.63

Crystal data and structure refinement for $PtL^{10Cl}Cl_3$

Identification code	22srv129
Empirical formula	$C_{19}H_{18}Cl_4N_2O_2PtS$
Formula weight	675.30
Temperature/K	120.00
Crystal system	monoclinic
Space group	P21/n
a/Å	13.1070(4)
b/Å	7.8011(2)
c/Å	21.3095(6)
α/°	90
β/ °	93.2290(10)
γ/ °	90
Volume/Å^3	2175.42(11)
Z	4
ρ_{calc}g/cm^3	2.062
μ/ mm^{-1}	7.057
F(000)	1296.0
Crystal size/mm^3	0.11 × 0.04 × 0.01
Radiation	Mo Kα(λ = 0.71073)
2Θ range for data collection/ °	5.562 to 59.994
Index ranges	-18 ≤ h ≤ 18, -10 ≤ k ≤ 10, -29 ≤ l ≤ 29
Reflections collected	50536
Independent reflections	6335 [R_{int} = 0.0381, R_{sigma} = 0.0229]
Data/restraints/parameters	6335/0/265
Goodness-of-fit on F^2	1.189
Final R indexes [I≥2σ(I)]	R_1 = 0.0288, wR_2 = 0.0544
Final R indexes [all data]	R_1 = 0.0329, wR_2 = 0.0555
Largest diff. peak/hole / e Å^{-3}	1.52/-1.36

Crystal data and structure refinement for $PtL^{11}Cl_3$

Identification code	22srv138
Empirical formula	$C_{17}H_{10}Cl_3F_3N_2Pt$
Formula weight	600.71
Temperature/K	120.00
Crystal system	triclinic
Space group	P-1
a/Å	8.9786(2)
b/Å	9.1735(2)
c/Å	10.6655(3)
α/°	73.9860(10)
β/ °	87.5650(10)
γ/ °	89.5740(10)
Volume/Å^3	843.61(4)
Z	2
ρ_{calc}g/cm^3	2.365
μ/ mm^{-1}	8.826
F(000)	564.0
Crystal size/mm^3	0.11 × 0.03 × 0.007
Radiation	Mo Kα(λ = 0.71073)
2Θ range for data collection/ °	3.976 to 59.998
Index ranges	-12 ≤ h ≤ 12, -12 ≤ k ≤ 12, -14 ≤ l ≤ 14
Reflections collected	30252
Independent reflections	4901 [R_{int} = 0.0366, R_{sigma} = 0.0251]
Data/restraints/parameters	4901/0/235
Goodness-of-fit on F^2	1.078
Final R indexes [I≥2σ(I)]	R_1 = 0.0227, wR_2 = 0.0469
Final R indexes [all data]	R_1 = 0.0250, wR_2 = 0.0477
Largest diff. peak/hole / e Å^{-3}	2.91/-1.27

Crystal data and structure refinement for $PtL^{12}Cl_3$

Identification code	21srv447
Empirical formula	$C_{15}H_{12}Cl_3N_2O_2PtS_2$
Formula weight	617.83
Temperature/K	120.0
Crystal system	triclinic
Space group	P-1
a/Å	8.3113(2)
b/Å	10.6355(3)
c/Å	11.0657(3)
α/°	82.1790(10)
β/ °	83.5440(10)
γ/ °	88.0070(10)
Volume/Å^3	962.72(4)
Z	2
ρ_{calc}g/cm^3	2.131
μ/ mm^{-1}	7.932
F(000)	586.0
Crystal size/mm^3	0.12 $\times$ 0.04 $\times$ 0.005
Radiation	Mo Kα(λ = 0.71073)
2Θ range for data collection/ °	3.738 to 59.998
Index ranges	-11 $\leq$ h $\leq$ 11, -14 $\leq$ k $\leq$ 14, -15 $\leq$ l $\leq$ 15
Reflections collected	23142
Independent reflections	5606 [R_{int} = 0.0353, R_{sigma} = 0.0329]
Data/restraints/parameters	5606/0/246
Goodness-of-fit on F^2	1.086
Final R indexes [I$\geq$2σ(I)]	R_1 = 0.0337, wR_2 = 0.0699
Final R indexes [all data]	R_1 = 0.0417, wR_2 = 0.0738
Largest diff. peak/hole / e Å^{-3}	2.70/-2.42

Crystal data and structure refinement for $PtL^{13}Cl_3$

Identification code	21srv392
Empirical formula	$C_{20}H_{13}Cl_3N_2Pt$
Formula weight	582.76
Temperature/K	120.0
Crystal system	monoclinic
Space group	C2/c
a/Å	13.3498(3)
b/Å	13.4416(3)
c/Å	19.5197(5)
α/°	90
β/ °	90.2106(9)
γ/ °	90
Volume/Å^3	3502.64(14)
Z	8
ρ_{calc}g/cm^3	2.210
μ/ mm^{-1}	8.476
F(000)	2208.0
Crystal size/mm^3	0.2 × 0.18 × 0.06
Radiation	Mo Kα(λ= 0.71073)
2Θ range for data collection/ °	4.174 to 59.996
Index ranges	-18 ≤ h ≤ 18, -18 ≤ k ≤ 18, -27 ≤ l ≤ 27
Reflections collected	41377
Independent reflections	5111 [R_{int} = 0.0327, R_{sigma} = 0.0184]
Data/restraints/parameters	5111/0/235
Goodness-of-fit on F^2	1.041
Final R indexes [I≥2σ(I)]	R_1 = 0.0176, wR_2 = 0.0391
Final R indexes [all data]	R_1 = 0.0203, wR_2 = 0.0401
Largest diff. peak/hole / e Å^{-3}	1.92/-0.89

Crystal data and structure refinement for $[PtL^7(bpy)Cl]^{2+}$

Identification code	21srv231
Empirical formula	$C_{29}H_{25}ClF_{12}N_4OP_2Pt$
Formula weight	966.01
Temperature/K	120.0
Crystal system	monoclinic
Space group	P21/c
a/Å	17.5046(4)
b/Å	8.5916(2)
c/Å	23.1168(6)
α/°	90
β/ °	109.5820(10)
γ/ °	90
Volume/Å^3	3275.52(14)
Z	4
ρ_{calc}g/cm^3	1.959
μ/ mm^{-1}	4.564
F(000)	1872.0
Crystal size/mm^3	0.12 × 0.03 × 0.02
Radiation	Mo Kα(λ = 0.71073)
2Θ range for data collection/ °	3.728 to 59.998
Index ranges	-24 ≤ h ≤ 24, -12 ≤ k ≤ 12, -32 ≤ l ≤ 32
Reflections collected	58257
Independent reflections	9552 [R_{int} = 0.0603, R_{sigma} = 0.0439]
Data/restraints/parameters	9552/0/452
Goodness-of-fit on F^2	1.161
Final R indexes [I≥2σ(I)]	R_1 = 0.0456, wR_2 = 0.0794
Final R indexes [all data]	R_1 = 0.0577, wR_2 = 0.0827
Largest diff. peak/hole / e Å^{-3}	1.79/-2.81

Crystal data and structure refinement for $[PtL^7(tpy)]^{3+}$

Identification code	21srv215
Empirical formula	$C_{31}H_{22}N_5Pt \times 2(CF_3SO_3) \times 4\ C_3H_6O$
Formula weight	935.02
Temperature/K	296.15
Crystal system	triclinic
Space group	P-1
a/Å	9.2077(4)
b/Å	20.4814(8)
c/Å	22.8017(9)
α/°	89.238(2)
β/ °	89.211(2)
γ/ °	79.762(2)
Volume/Å^3	4231.0(3)
Z	4
ρ_{calc}g/cm^3	1.468
μ/ mm^{-1}	3.468
F(000)	1827.0
Crystal size/mm^3	0.16 × 0.04 × 0.04
Radiation	Mo Kα(λ = 0.71073)
2Θ range for data collection/ °	4.438 to 52
Index ranges	-11 ≤ h ≤ 11, -25 ≤ k ≤ 25, -28 ≤ l ≤ 28
Reflections collected	77164
Independent reflections	16606 [R_{int} = 0.0520, R_{sigma} = 0.0471]
Data/restraints/parameters	16606/88/991
Goodness-of-fit on F^2	1.084
Final R indexes [I≥2σ(I)]	R_1 = 0.0641, wR_2 = 0.1459
Final R indexes [all data]	R_1 = 0.0759, wR_2 = 0.1515
Largest diff. peak/hole / e Å^{-3}	2.83/-2.46

Crystal data and structure refinement for $[PtL^8(tpy)]^{3+}$

Identification code	21srv310
Empirical formula	$C_{37}H_{33}F_{18}N_6OP_3Pt$
Formula weight	1207.69
Temperature/K	120.0
Crystal system	orthorhombic
Space group	P212121
a/Å	13.5539(4)
b/Å	13.7166(4)
c/Å	22.2917(7)
α/°	90
β/ °	90
γ/ °	90
Volume/Å^3	4144.3(2)
Z	4
ρ_{calc}g/cm^3	1.936
μ/ mm^{-1}	3.625
F(000)	2360.0
Crystal size/mm^3	0.14 × 0.11 × 0.04
Radiation	Mo Kα(λ = 0.71073)
2Θ range for data collection/ °	4.604 to 59.996
Index ranges	-19 ≤ h ≤ 19, -19 ≤ k ≤ 19, -31 ≤ l ≤ 31
Reflections collected	99776
Independent reflections	12081 [R_{int} = 0.0509, R_{sigma} = 0.0317]
Data/restraints/parameters	12081/82/635
Goodness-of-fit on F^2	1.206
Final R indexes [I≥2σ(I)]	R_1 = 0.0490, wR_2 = 0.1036
Final R indexes [all data]	R_1 = 0.0541, wR_2 = 0.1057
Largest diff. peak/hole / e Å^{-3}	2.30/-3.67
Flack parameter	0.006(2)

Crystal data and structure refinement for $[PtL^7(ppy)Cl]^+$

Identification code	21srv448
Empirical formula	$C_{29}H_{21}Cl_3F_3N_3O_3PtS$
Formula weight	849.99
Temperature/K	120.0
Crystal system	monoclinic
Space group	P21/c
a/Å	15.1961(6)
b/Å	13.4215(5)
c/Å	15.8875(6)
α/°	90
β/ °	111.904(3)
γ/ °	90
Volume/Å^3	3006.4(2)
Z	4
ρ_{calc}g/cm^3	1.878
μ/ mm^{-1}	5.059
F(000)	1648.0
Crystal size/mm^3	0.11 × 0.08 × 0.01
Radiation	Mo Kα(λ = 0.71073)
2Θ range for data collection/ °	4.104 to 59.994
Index ranges	21 ≤ h ≤ -21, 18 ≤ k ≤ -18, 22 ≤ l ≤ -22
Reflections collected	8629
Independent reflections	8629 [R_{int} = 0.0518, R_{sigma} = 0.0500]
Data/restraints/parameters	8629/6/388
Goodness-of-fit on F^2	1.051
Final R indexes [I≥2σ(I)]	R_1 = 0.0390, wR_2 = 0.0888
Final R indexes [all data]	R_1 = 0.0641, wR_2 = 0.0936
Largest diff. peak/hole / e Å^{-3}	1.44/-2.81

Crystal data and structure refinement for $[PtL^9(3\text{-OMe-ppy})Cl]^+$

Identification code	21srv455
Empirical formula	$C_{31}H_{25}Cl_3F_3N_3O_5PtS$
Formula weight	910.04
Temperature/K	120.0
Crystal system	triclinic
Space group	P-1
a/Å	10.5820(4)
b/Å	11.8805(4)
c/Å	13.0407(4)
α/°	88.2460(10)
β/ °	76.3250(10)
γ/ °	86.5130(10)
Volume/Å^3	1589.82(9)
Z	2
ρ_{calc}g/cm^3	1.901
μ/ mm^{-1}	4.795
F(000)	888.0
Crystal size/mm^3	0.07 × 0.06 × 0.03
Radiation	Mo Kα(λ = 0.71073)
2Θ range for data collection/ °	4.482 to 57.998
Index ranges	-14 ≤ h ≤ 14, -16 ≤ k ≤ 16, -17 ≤ l ≤ 17
Reflections collected	38914
Independent reflections	8443 [R_{int} = 0.0676, R_{sigma} = 0.0643]
Data/restraints/parameters	8443/0/430
Goodness-of-fit on F^2	1.064
Final R indexes [I≥2σ(I)]	R_1 = 0.0458, wR_2 = 0.1011
Final R indexes [all data]	R_1 = 0.0605, wR_2 = 0.1074
Largest diff. peak/hole / e Å^{-3}	1.66/-1.90

Crystal data and structure refinement for $[PtL^{10}(4\text{-OMe-ppy})Cl]^+$

Identification code	22srv026
Empirical formula	$C_{29.5}H_{24}Cl_2F_6N_3O_2PPt$
Formula weight	863.48
Temperature/K	120.00
Crystal system	triclinic
Space group	P-1
a/Å	13.8190(6)
b/Å	15.4968(6)
c/Å	15.5042(6)
α/°	87.5698(16)
β/ °	83.6170(16)
γ/ °	87.6078(16)
Volume/Å^3	3294.4(2)
Z	4
ρ_{calc}g/cm^3	1.741
μ/ mm^{-1}	4.535
F(000)	1676.0
Crystal size/mm^3	0.34 × 0.04 × 0.01
Radiation	Mo Kα(λ = 0.71073)
2Θ range for data collection/ °	3.802 to 59.998
Index ranges	-19 ≤ h ≤ 19, -21 ≤ k ≤ 21, -21 ≤ l ≤ 21
Reflections collected	73924
Independent reflections	19211 [R_{int} = 0.0721, R_{sigma} = 0.0764]
Data/restraints/parameters	19211/192/860
Goodness-of-fit on F^2	1.021
Final R indexes [I≥2σ(I)]	R_1 = 0.0521, wR_2 = 0.1107
Final R indexes [all data]	R_1 = 0.0880, wR_2 = 0.1245
Largest diff. peak/hole / e Å^{-3}	1.97/-1.75

Crystal data and structure refinement for $[PtL^{10Cl}(ppy)Cl]^+$

Identification code	22srv141
Empirical formula	$C_{29.5}H_{23}Cl_2F_6N_3O_{1.5}PPt$
Formula weight	854.47
Temperature/K	120.00
Crystal system	triclinic
Space group	P-1
a/Å	11.6681(4)
b/Å	13.1112(5)
c/Å	13.7379(5)
α/°	112.7128(11)
β/ °	104.4060(11)
γ/ °	102.3458(11)
Volume/Å^3	1761.17(11)
Z	2
ρ_{calc}g/cm^3	1.611
μ/ mm^{-1}	4.240
F(000)	828.0
Crystal size/mm^3	0.09 × 0.05 × 0.01
Radiation	Mo Kα(λ = 0.71073)
2Θ range for data collection/ °	4.252 to 59.994
Index ranges	-16 ≤ h ≤ 16, -18 ≤ k ≤ 18, -19 ≤ l ≤ 19
Reflections collected	37817
Independent reflections	10264 [R_{int} = 0.0575, R_{sigma} = 0.0648]
Data/restraints/parameters	10264/19/418
Goodness-of-fit on F^2	1.039
Final R indexes [I≥2σ(I)]	R_1 = 0.0417, wR_2 = 0.0937
Final R indexes [all data]	R_1 = 0.0546, wR_2 = 0.0980
Largest diff. peak/hole / e Å^{-3}	1.51/-1.17

Crystal data and structure refinement for $[PtL^{12}(thpy)Cl]^+$

Identification code	22srv110
Empirical formula	$C_{23.5}H_{16}Cl_2F_6N_3PPtS_2$
Formula weight	815.47
Temperature/K	120.00
Crystal system	triclinic
Space group	P-1
a/Å	9.8398(4)
b/Å	12.5659(6)
c/Å	12.9285(6)
α/°	76.0700(10)
β/ °	71.2540(10)
γ/ °	84.3930(10)
Volume/Å^3	1468.88(12)
Z	2
ρ_{calc}g/cm^3	1.844
μ/ mm^{-1}	5.212
F(000)	782.0
Crystal size/mm^3	0.08 × 0.06 × 0.01
Radiation	Mo Kα(λ = 0.71073)
2Θ range for data collection/ °	4.212 to 54.998
Index ranges	-12 ≤ h ≤ 12, -16 ≤ k ≤ 16, -16 ≤ l ≤ 16
Reflections collected	24245
Independent reflections	6742 [R_{int} = 0.0564, R_{sigma} = 0.0637]
Data/restraints/parameters	6742/114/424
Goodness-of-fit on F^2	1.042
Final R indexes [I≥2σ(I)]	R_1 = 0.0471, wR_2 = 0.1159
Final R indexes [all data]	R_1 = 0.0671, wR_2 = 0.1260
Largest diff. peak/hole / e Å^{-3}	1.72/-1.18

Chapter 4

Crystal data and structure refinement for $[PtL^{15}(ppy)Cl]PF_6$

Identification code	23srv087
Empirical formula	$C_{33}H_{23}ClF_6N_3PPt$
Formula weight	837.05
Temperature/K	120.00
Crystal system	monoclinic
Space group	P21/n
a/Å	8.8761(5)
b/Å	19.1326(9)
c/Å	16.9874(8)
α/°	90
β/ °	98.222(2)
γ/ °	90
Volume/Å^3	2855.2(2)
Z	4
ρ_{calc}g/cm^3	1.947
μ/ mm^{-1}	5.134
F(000)	1624.0
Crystal size/mm^3	0.28 $\times$ 0.006 $\times$ 0.004
Radiation	Mo Kα(λ = 0.71073)
2Θ range for data collection/ °	4.258 to 55.996
Index ranges	-11 $\leq$ h $\leq$ 11, -25 $\leq$ k $\leq$ 25, -22 $\leq$ l $\leq$ 22
Reflections collected	60583
Independent reflections	6894 [R_{int} = 0.1401, R_{sigma} = 0.0910]
Data/restraints/parameters	6894/6/407
Goodness-of-fit on F^2	1.113
Final R indexes [I$\geq$2σ(I)]	R_1 = 0.0605, wR_2 = 0.1276
Final R indexes [all data]	R_1 = 0.0932, wR_2 = 0.1408
Largest diff. peak/hole / e Å^{-3}	6.86/-2.96

Crystal data and structure refinement for $[PtL^{16}(ppy)Cl]PF_6$

Identification code	23srv186
Empirical formula	$C_{41}H_{41}ClF_6N_3OPPt$
Formula weight	967.28
Temperature/K	120.00
Crystal system	monoclinic
Space group	P21/c
a/Å	9.7403(3)
b/Å	15.8106(4)
c/Å	26.6637(7)
α/°	90
β/ °	96.9954(10)
γ/ °	90
Volume/Å^3	4075.64(19)
Z	4
ρ_{calc}g/cm^3	1.576
μ/ mm^{-1}	3.610
F(000)	1920.0
Crystal size/mm^3	0.11 × 0.03 × 0.01
Radiation	Mo Kα(λ = 0.71073)
2Θ range for data collection/ °	4.014 to 58
Index ranges	-13 ≤ h ≤ 13, -21 ≤ k ≤ 21, -36 ≤ l ≤ 36
Reflections collected	139676
Independent reflections	11036 [R_{int} = 0.0691, R_{sigma} = 0.0325]
Data/restraints/parameters	11036/216/587
Goodness-of-fit on F^2	1.190
Final R indexes [I≥2σ(I)]	R_1 = 0.0781, wR_2 = 0.1684
Final R indexes [all data]	R_1 = 0.0903, wR_2 = 0.1754
Largest diff. peak/hole / e Å^{-3}	3.69/-2.92

Chapter 5

Crystal data and structure refinement for $HL^{18}PtCl$

Identification code	22srv297
Empirical formula	$C_{27}H_{19}Cl_3N_4Pt$
Formula weight	700.90
Temperature/K	120.00
Crystal system	monoclinic
Space group	P21/n
a/Å	17.2820(10)
b/Å	7.6243(4)
c/Å	19.6406(11)
α/°	90
β/ °	111.7168(14)
γ/ °	90
Volume/Å^3	2404.2(2)
Z	4
ρ_{calc}g/cm^3	1.936
μ/ mm^{-1}	6.195
F(000)	1352.0
Crystal size/mm^3	0.27 $\times$ 0.02 $\times$ 0.01
Radiation	Mo Kα(λ= 0.71073)
2Θ range for data collection/ °	4.464 to 59.996
Index ranges	-24 $\leq$ h $\leq$ 23, -10 $\leq$ k $\leq$ 10, -27 $\leq$ l $\leq$ 27
Reflections collected	49370
Independent reflections	7018 [R_{int} = 0.0706, R_{sigma} = 0.0467]
Data/restraints/parameters	7018/0/317
Goodness-of-fit on F^2	1.144
Final R indexes [I$\geq$2σ(I)]	R_1 = 0.0434, wR_2 = 0.0741
Final R indexes [all data]	R_1 = 0.0589, wR_2 = 0.0787
Largest diff. peak/hole / e Å^{-3}	1.64/-2.18

Chapter 6

Crystal data and structure refinement for $Pt_2L^{21}{}_2Cl_2$

Identification code	23srv390_abs
Empirical formula	$C_{61}H_{62}Cl_4N_4Pt_2$
Formula weight	1383.12
Temperature/K	120.00
Crystal system	monoclinic
Space group	P21
a/Å	10.3330(7)
b/Å	10.3055(7)
c/Å	25.7800(16)
α/ °	90
β/ °	95.731(2)
γ/ °	90
Volume/Å^3	2731.5(3)
Z	2
ρ_{calc}g/cm^3	1.682
μ/ mm^{-1}	5.355
F(000)	1360.0
Crystal size/mm^3	0.113 $\times$ 0.032 $\times$ 0.016
Radiation	Mo Kα(λ = 0.71073)
2Θ range for data collection/ °	3.962 to 54.426
Index ranges	-13 $\leq$ h $\leq$ 13, -13 $\leq$ k $\leq$ 13, -33 $\leq$ l $\leq$ 33
Reflections collected	74616
Independent reflections	12146 [R_{int} = 0.1114, R_{sigma} = 0.0852]
Data/restraints/parameters	12146/1113/653
Goodness-of-fit on F^2	1.163
Final R indexes [I$\geq$2σ(I)]	R_1 = 0.0769, wR_2 = 0.1696
Final R indexes [all data]	R_1 = 0.0958, wR_2 = 0.1770
Largest diff. peak/hole / e Å^{-3}	3.34/-5.53
Flack parameter	0.04(2)

Crystal data and structure refinement for $PtL^{22}Cl_2$

Identification code	23srv299
Empirical formula	$C_{34}H_{32}Cl_2N_2Pt$
Formula weight	734.60
Temperature/K	120.00
Crystal system	orthorhombic
Space group	P212121
a/Å	12.1298(5)
b/Å	13.2304(6)
c/Å	17.6483(8)
α/ °	90
β/ °	90
γ/ °	90
Volume/Å^3	2832.2(2)
Z	4
ρ_{calc}g/cm^3	1.723
μ/ mm^{-1}	5.170
F(000)	1448.0
Crystal size/mm^3	0.18 $\times$ 0.14 $\times$ 0.06
Radiation	Mo Kα(λ = 0.71073)
2Θ range for data collection/ °	3.848 to 64.998
Index ranges	-18 $\leq$ h $\leq$ 17, -20 $\leq$ k $\leq$ 20, -26 $\leq$ l $\leq$ 26
Reflections collected	119186
Independent reflections	10246 [R_{int} = 0.0529, R_{sigma} = 0.0251]
Data/restraints/parameters	10246/0/358
Goodness-of-fit on F^2	1.138
Final R indexes [I$\geq$2σ(I)]	R_1 = 0.0446, wR_2 = 0.1041
Final R indexes [all data]	R_1 = 0.0475, wR_2 = 0.1058
Largest diff. peak/hole / e Å^{-3}	7.73/-2.98
Flack parameter	0.014(3)

Crystal data and structure refinement for $PtL^{23}Cl_2$

Identification code	23srv192
Empirical formula	$C_{40}H_{38}Cl_6N_2Pt$
Formula weight	954.51
Temperature/K	120.00
Crystal system	triclinic
Space group	P-1
a/Å	9.8883(3)
b/Å	13.6503(4)
c/Å	14.8785(4)
α/°	70.6418(11)
β/ °	81.2945(11)
γ/ °	79.5201(11)
Volume/Å^3	1854.13(9)
Z	2
ρ_{calc}g/cm^3	1.710
μ/ mm^{-1}	4.249
F(000)	944.0
Crystal size/mm^3	0.14 × 0.06 × 0.03
Radiation	Mo Kα(λ = 0.71073)
2Θ range for data collection/ °	4.21 to 63.998
Index ranges	-14 ≤ h ≤ 14, -19 ≤ k ≤ 20, -22 ≤ l ≤ 22
Reflections collected	76877
Independent reflections	12887 [R_{int} = 0.0392, R_{sigma} = 0.0278]
Data/restraints/parameters	12887/33/478
Goodness-of-fit on F^2	1.031
Final R indexes [I≥2σ(I)]	R_1 = 0.0212, wR_2 = 0.0453
Final R indexes [all data]	R_1 = 0.0244, wR_2 = 0.0464
Largest diff. peak/hole / e Å^{-3}	1.30/-1.47

Crystal data and structure refinement for PtL[21]

Identification code	23srv403
Empirical formula	$C_{30}H_{30}N_2Pt$
Formula weight	613.65
Temperature/K	120
Crystal system	monoclinic
Space group	P21/n
a/Å	14.1941(5)
b/Å	10.9744(4)
c/Å	15.9505(5)
α/ °	90
β/ °	107.5540(10)
γ/ °	90
Volume/Å^3	2368.93(14)
Z	4
ρ_{calc}g/cm^3	1.721
μ/ mm^{-1}	5.944
F(000)	1208.0
Crystal size/mm^3	0.168 $\times$ 0.166 $\times$ 0.036
Radiation	Mo Kα(λ = 0.71073)
2Θ range for data collection/ °	4.578 to 59.236
Index ranges	-19 $\leq$ h $\leq$ 19, -15 $\leq$ k $\leq$ 15, -22 $\leq$ l $\leq$ 22
Reflections collected	58520
Independent reflections	6658 [R_{int} = 0.0473, R_{sigma} = 0.0280]
Data/restraints/parameters	6658/0/304
Goodness-of-fit on F^2	1.073
Final R indexes [I$\geq$2σ(I)]	R_1 = 0.0239, wR_2 = 0.0436
Final R indexes [all data]	R_1 = 0.0331, wR_2 = 0.0461
Largest diff. peak/hole / e Å^{-3}	0.76/-0.91

Crystal data and structure refinement for PtL[22]

Identification code	23srv191
Empirical formula	$C_{34}H_{32}N_2Pt$
Formula weight	663.70
Temperature/K	120.00
Crystal system	triclinic
Space group	P-1
a/Å	13.2316(3)
b/Å	13.7483(4)
c/Å	15.6441(4)
α/°	68.3692(10)
β/ °	87.8420(10)
γ/ °	85.1322(11)
Volume/Å^3	2635.84(12)
Z	4
ρ_{calc}g/cm^3	1.672
μ/ mm^{-1}	5.349
F(000)	1312.0
Crystal size/mm^3	0.09 × 0.05 × 0.01
Radiation	Mo Kα(λ = 0.71073)
2Θ range for data collection/ °	4.156 to 55
Index ranges	-17 ≤ h ≤ 17, -17 ≤ k ≤ 17, -20 ≤ l ≤ 20
Reflections collected	67710
Independent reflections	12091 [R_{int} = 0.0627, R_{sigma} = 0.0472]
Data/restraints/parameters	12091/57/709
Goodness-of-fit on F^2	1.106
Final R indexes [I≥2σ(I)]	R_1 = 0.0477, wR_2 = 0.0923
Final R indexes [all data]	R_1 = 0.0629, wR_2 = 0.0972
Largest diff. peak/hole / e Å^{-3}	5.74/-2.67

Crystal data and structure refinement for PtL[23]

Identification code	23srv309
Empirical formula	$C_{38}H_{34}N_2Pt$
Formula weight	713.76
Temperature/K	120.00
Crystal system	triclinic
Space group	P-1
a/Å	7.9225(11)
b/Å	13.1739(18)
c/Å	13.6608(19)
α/ °	87.845(4)
β/ °	89.704(4)
γ/ °	84.084(4)
Volume/Å^3	1417.2(3)
Z	2
ρ_{calc}g/cm^3	1.673
μ/ mm^{-1}	4.981
F(000)	708.0
Crystal size/mm^3	0.146 × 0.032 × 0.027
Radiation	Mo Kα(λ = 0.71073)
2Θ range for data collection/ °	4.23 to 60.504
Index ranges	-11 ≤ h ≤ 11, -18 ≤ k ≤ 18, -19 ≤ l ≤ 19
Reflections collected	36889
Independent reflections	8208 [R_{int} = 0.0687, R_{sigma} = 0.0588]
Data/restraints/parameters	8208/759/407
Goodness-of-fit on F^2	1.144
Final R indexes [I≥2σ(I)]	R_1 = 0.0791, wR_2 = 0.1829
Final R indexes [all data]	R_1 = 0.0862, wR_2 = 0.1866
Largest diff. peak/hole / e Å^{-3}	7.58/-8.01